# NONLINEAR AEROELASTIC COUPLED TRIM MODELING OF CYCLOIDAL ROTOR BASED MICRO AIR VEHICLE

A Dissertation

by

ATANU HALDER

Submitted to the Office of Graduate and Professional Studies of
Texas A&M University
in partial fulfillment of the requirements for the degree of

DOCTOR OF PHILOSOPHY

| | |
|---|---|
| Chair of Committee, | Moble Benedict |
| Committee Members, | John E. Hurtado |
| | Thomas Strganac |
| | Sivakumar Rathinam |
| Head of Department, | Rodney Bowersox |

August 2019

Major Subject: Aerospace Engineering

# ABSTRACT

Present generation of hover-capable micro air vehicles (MAVs) based on conventional rotors have shown poor performance in terms of endurance (<15 minutes), agility, and disturbance-rejection capability. Developing next generation of MAVs would require radical improvements in propulsion systems as well as control and guidance strategies. Cycloidal rotor is one such novel propulsion concept, which has huge potential due to its higher efficiency and maneuverability (instantaneous 360° thrust vectoring capability). Cycloidal rotor is a horizontal-axis rotary wing system which utilizes cyclic blade pitching to generate lift and thrust. A crucial step towards building efficient MAVs utilizing cycloidal rotor systems involves developing an aeroelastic framework and a coupled trim methodology, which could be utilized for design optimization and this is the main objective of the present dissertation.

To obtain instantaneous blade aerodynamic forces and performance (cycle-averaged thrust and power) of cycloidal rotor, an unsteady aerodynamic model is developed. Towards this, aerodynamics of cycloidal rotor is investigated thoroughly and various underlying physical phenomena such as dynamic virtual camber, effects of near and shed wake, leading edge vortices are rigorously modeled. All these detail modeling helped the aerodynamic model to systematically validate with not only time averaged forces, but also time-history of aerodynamic forces obtained from in-house experiments. Once validated, the aerodynamic model is utilized to understand the physics behind the force production of cycloidal rotor. Through systematic investigation, it was observed that the dynamic virtual camber effect plays a very important role in this aspect. Dynamic virtual camber due to pitch rate creates asymmetry in side-force between the right and the left halves, which in turn causes net time averaged side force on a cycloidal propeller in hover even with zero phase offset. Moreover, it is found extremely crucial for a cycloidal rotor to rotate in opposite direction (back-spin) with respect to the incoming flow in order to produce an upward vertical force in forward flight. This is due to the dynamic nature of virtual camber effect.

Although the above mentioned lower order model is computationally inexpensive and capable

of predicting rotor performance with sufficient accuracy, it cannot accurately capture the complex flow-field of cycloidal rotor, specifically the blade vortex interaction and geometry of trailing vortices. For this reason, a high-fidelity model of cycloidal rotor based on free-wake is developed to further investigate aerodynamics of cycloidal rotor in more detail. The prediction of the developed free wake model shows even better correlation with in-house experimental data compared to that of a lower model. Although, wake model is much more expensive from computational point of view which limits its application for preliminary design optimization of cycloidal rotor.

Experimental study shows that cycloidal rotor goes through large blade deflections mainly due to centrifugal force which decreases thrust production and increases power requirement of the rotor. To capture these deflections, a fully nonlinear geometrically exact model is developed which shows much better prediction compared to a traditional $2^{nd}$ order nonlinear model. To investigate effect of blade deflections on cycloidal rotor performance an aeroelastic framework of cycloidal rotor is developed by coupling lower order unsteady aerodynamic model with the structural model. The experimental validation shows inclusion of geometrically exact model is crucial for accurate performance prediction of flexible cycloidal rotors. Through systematic investigation utilizing the aeroelastic model, it is observed that nonlinear moment, arising due to coupling of bending curvatures in two orthogonal directions, is the key reason behind performance drop of flexible rotors.

To obtain performance of conventional nose rotor in low Reynolds number regime, a modified blade element momentum theory based model is developed which utilizes look-up table obtained from CFD study. Both CFD look-up table and model predictions are validated with previously published experimental data.

Control strategy of a cycloidal rotor based MAV, known as 'Cyclocopter' is developed for different flight conditions. Based on that, a coupled trim analysis of cyclocopter is performed for by simultaneously solving blade response equations and vehicle trim equations. Once systematically validated with in-house experimental data, the coupled trim model is utilized to investigate effect of several design parameters on the control inputs of the vehicle.

# DEDICATION

This dissertation is dedicated to my mother for all her care and support throughout my life.

# ACKNOWLEDGMENTS

I am extremely thankful to my dissertation advisor, Dr. Moble Benedict for all this support and guidance during my PhD life. He is an exceptional teacher and always has been an inspiration for me. He has a major contribution to my professional development. It has been a great pleasure to work with him.

I would like to thank my committee members, Dr. John E. Hurtado, Dr. Thomas Strganac and Dr. Sivakumar Rathinam for their guidance and priceless suggestions. I would specifically like to thank Dr. John E. Hurtado for his extraordinary teaching skills. The 'Spacecraft Dynamics' course taught by him is one of the best courses I have ever attended.

I would like to thank Carolyn Walther, Loic Barett and Adam Kellen for their assistance in the experimental study. My special thanks go towards James Lankford, Ananth Sridharan, Eric Greenwood, Vinod Laxminarayan, Bharath Govindarajan for their guidance and help over the course of my PhD.

I have greatest sense of appreciation to my friends and colleagues David Coleman and Aswathi Sudhir for their assistance. I would also like to thank every member in our research team. I would specifically like to mention Xuan Yang, Carl Runco, Farid Saemi, Bochan Lee, Hunter Denton, Vishaal Subramanian. I would also like to thank my other friends at Texas A&M for their support. Special mention goes to Shubhadeep Chakraborty, Samayita Guha, Niladri Das, Vinicius Goecks, Dipanjan Saha, Mayukh Majumdar, Raman Goyal, Utkarsh Mishra, Vishala, Aman Rana.

I would like to thank the Texas A&M University Office of Graduate and Professional Studies to allow me to construct this LaTeX thesis template. Special thanks to JaeCee Crawford, Amy Motquin, Ashley Schmitt, Rachel Krolczyk, and Roberta Caton for carefully reviewing this material.

I am extremely grateful towards all my relatives who supported me throughout my career.

Lastly, the acknowledgement will not be complete without the mention of my mother. This thesis is dedicated to her.

# NOMENCLATURE

| | |
|---|---|
| $c$ | Chord length |
| $C_d$ | Drag coefficient |
| $C_{d_{le}}$ | Drag coefficient with leading edge vortex |
| $C_{d_{wole}}$ | Drag coefficient without leading edge vortex |
| $cg$ | center of gravity |
| $C_l$ | Lift coefficient |
| $C_{l_{le}}$ | Lift coefficient with leading edge vortex |
| $C_{l_o}$ | Additional lift coefficient due to virtual camber effect |
| $C_{l_{quasi\_steady}}$ | Quasi-steady lift coefficient |
| $C_{l_{unsteady}}$ | Unsteady lift coefficient |
| $C_{l_{wole}}$ | Lift coefficient without leading edge vortex |
| $d$ | Drag |
| $e_g$ | Chord-wise location of blade cg ahead of elastic axis |
| $F_u$ | Force on the blade along the flow direction at upstream |
| $F_d$ | Force on the blade along the flow direction at downstream |
| $f_u$ | Force per unit area along the flow direction at upstream |
| $f_d$ | Force per unit area along the flow direction at downstream |
| $k_f$ | Reduced Frequency |
| $K_v$ | Non-dimensional coefficient due to extra vortex lift by leading edge suction |
| $l$ | Lift |
| $L$ | Blade length |
| $\dot{m}$ | Mass Flow Rate |

| | |
|---|---|
| $N_b$ | Number of blades in cyclorotor |
| $\vec{r}$ | Position vector of local blade element |
| $R$ | Radius of cyclorotor |
| $T$ | Kinetic Energy |
| $T_{DU}$ | Transformation matrix between deformed and un-deformed frame |
| $T_{DI}$ | Transformation matrix between deformed and inertial frame |
| $T_{RI}$ | Transformation matrix between rotating and inertial frame |
| $T_{UI}$ | Transformation matrix between undeformed and inertial frame |
| $u$ | Axial elongation |
| $U$ | Potential energy |
| $U_P$ | Component of resultant flow velocity along the perpendicular direction of blade |
| $U_T$ | Component of resultant flow velocity along the direction of blade |
| $v$ | Tangential bending deflection |
| $\vec{V}_b(x)$ | Blade velocity at a particular chord-wise location(x) on rotor blade |
| $V_d$ | Downstream inflow velocity |
| $V_{d\_wake}$ | Downstream wake velocity |
| $\vec{V}_i(x)$ | Inflow velocity at a particular chord-wise location (x) on rotor blade |
| $\vec{V}_p(x)$ | Relative flow velocity at a particular chord-wise location (x) on rotor blade due to blade pitching |
| $\vec{V}(x)$ | Resultant flow velocity at a particular chord-wise location (x) on rotor blade |
| $V_u$ | Upstream inflow velocity |
| $V_{u\_wake}$ | Upstream wake velocity |

| | |
|---|---|
| $V_\infty$ | Free stream velocity |
| $W$ | Virtual work done by the external forces |
| $w$ | Radial bending deflection |
| $\alpha_{eff}$ | Effective angle of attack |
| $\alpha_i$ | Induced angle of attack |
| $\alpha_x$ | Angle of attack at a particular chord-wise location (x) on rotor blade |
| $\beta$ | Angle between inflow velocity and vertical axis |
| $\Gamma$ | Circulation |
| $\gamma_d$ | Inflow angle at downstream locations |
| $\gamma_u$ | Inflow angle at upstream locations |
| $\phi$ | Axial twist |
| $\theta$ | Prescribed blade pitch |
| $\theta_{off}$ | Pitch phase offset of cyclorotor |
| $\theta_{trim}$ | Pitch phase offset of cyclorotor need to generate zero side force |
| $\rho$ | Fluid density |
| $\sigma$ | Solidity |
| $\Psi$ | Azimuthal location of blade in a cycle |
| $\vec{\Omega}$ | Rotational speed of cyclorotor |
| $\vec{\omega}^{dur}$ | Angular velocity of deformed blade frame with respect to inertial frame |
| $\vec{\omega}^{r}$ | Angular velocity of rotating frame with respect to inertial frame |
| $\vec{\omega}^{ur}$ | Angular velocity of un-deformed blade frame with respect to inertial frame |

TABLE OF CONTENTS

Page

LIST OF FIGURES

FIGURE Page

LIST OF TABLES

TABLE Page

# 1. INTRODUCTION

## 1.1 Micro Air Vehicles

Due to rapid advancements in miniaturized electronic systems and increased demand for smaller scale aerial platforms, a new class of flying vehicle known as Micro Air Vehicles (MAVs) has emerged rapidly in last few decades. The concept of such mobile micro-robots was first introduced in 1992 in a DARPA (Defense Advanced Research Projects Agency) / RAND (Research And Development) corporation workshop on "Future Technology Driven Revolutions in Military Operations" [1]. After some feasibility studies, DARPA created Small Business Innovation Research (SBIR) program to develop miniature flying vehicles [2]. According to this program, an MAV is defined to be a micro scale flying vehicle with no dimension exceeding 6 inches (15cm), having weight no more than 100 grams including payload of 20 grams and having endurance of one hour. The size constraints put MAVs orders of magnitude smaller compared to traditional Unmanned Aerial Vehicles (UAVs).

Initially MAVs were envisioned mainly for military applications. The changing dynamics of conflicts of modern era has greatly influenced and motivated the development of this new class of smaller scale aerial vehicles. In the post cold war period, there was been significant shift towards the characteristics of military operations which often includes small numbers of soldiers operating in non-traditional environments such as urban areas or unknown enemy territories. MAVs would highly reduce the latency in present reconnaissance methods in these types of situations. In contrast to higher level reconnaissance assets such as high amplitude UAVs and satellites, MAVs can be operated by an individual soldier in the field as a platoon-level asset. MAVs would provide individual soldiers real-time information regarding their surroundings, and other sensory data on demand. This local reconnaissance would result in unprecedented situational awareness, greater effectiveness and fewer casualties in critical missions such as hostage rescue, counter-drug operations etc. These local reconnaissance applications has been the primary driver for the first

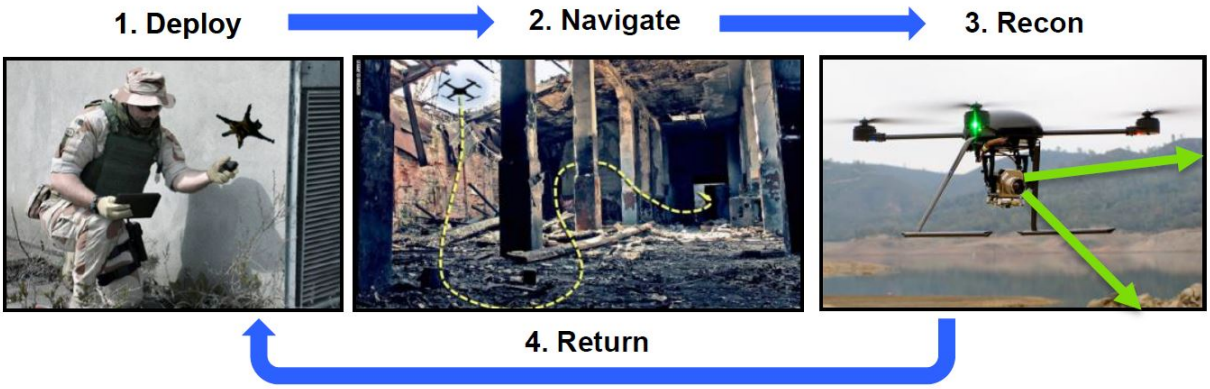


Figure 1.1: MAV application: local reconnaissance mission [4].

generation of MAVs [3]. This is partly attributed to the direct connectivity envisioned between these systems and the soldiers in emerging operational concepts. Direct connectivity means the soldier has to carry it. So the MAVs must be extremely portable compared to other soldier assets - like ammunition, food, water. All these requirements point to a highly compact, small and light system that could be easily transported and rapidly deployed by a single person.

Although local reconnaissance applications has been the primary motivator, lots of other military as well as civilian applications of MAVs are also explored in the successive period. Potential military applications include surveillance, demining, aerial offense etc. Potential civilian applications include traffic monitoring, rescue missions, biochemical sensing, power-line inspection, wildlife surveys etc. Recent advances in miniaturization of electronic, mechanical as well as electromechanical systems (MEMS) have heavily influenced these wide varieties of MAV applications. Chip-sized hazardous substance detectors, tiny infra red sensors and CCD-array cameras and various other small sensors can be integrated into the MAV system to obtain wide varieties of information useful for different missions. Using advance control algorithms, swarms of MAVs could be utilized to carry out complex missions that would have been otherwise impossible to solve for a single platform. Moreover, MAV's ability to operate in highly constrained environments like interior of buildings, caves and forests gives these systems a level of uniqueness unmatched by other concepts.

## 1.2 Challenges of Conventional MAVs

Although MAVs have significant future potential, there are significant technical barriers to be overcome. For last few decades lots of attempts were made to develop different types of MAV platforms. Present generation of MAVs based on conventional concepts have shown poor performance in terms of endurance (<30 minutes), agility, and disturbance-rejection capability. Most of the conventional MAVs built so far, can be categorized into two major sections: fixed wing MAVs and rotary wing MAVs. Among them fixed wing MAVs are comparatively most efficient in terms of aerodynamic performance and endurance. For this reason, several fixed wing MAVs are developed in last few decades [5, 6, 7, 8, 9]. Even though, these fixed wing MAVs are comparatively more efficient, they are still well short of endurance and payload objectives. Moreover, their incapability to hover and fly at smaller speeds restricts themselves from several desired MAV applications such as surveillance, monitoring etc. On the other hand, they can not take off and land vertically, which limits their usefulness in constrained environments and indoor applications.

On the other hand, rotary wing MAVs are hover capable and highly maneuverable which makes them ideal for majority of MAV applications. Their vertical takeoff and landing capability leads to minimal takeoff and landing zone which makes them extremely useful in indoor and constrained environments. For these advantageous reasons, lots of attempts were made to develop rotary wing MAVs based on conventional rotors [5, 6, 10, 11, 12, 13]. Although, these rotary wing MAVs based on conventional rotors are extremely inefficient just like full-scale rotorcrafts are much less efficient compared to full-scale fixed-wing aircrafts. Moreover, the scaling also has a very adverse effect on rotor performance mainly due to two reasons: decrease in rotor disk area and decrease in Reynolds number. Based on simple momentum theory computations, it can be easily shown that a rotor with smaller disk area is much less efficient from aerodynamic point of view compared to a rotor with larger disk area producing same amount of thrust. The aerodynamic efficiency of a rotor in hover is generally represented by power loading ($PL = T/A$), which is thrust ($T$) produced by the rotor using unit power ($P$). Utilizing actuator disk theory [14] and conservation of momentum,

power loading can be expressed as following.

$$PL = FM\sqrt{\frac{2\rho}{DL}} \tag{1.1}$$

In the above equation, $DL$ denotes disk loading which is thrust produced by unit actuator area ($DL = T/A$). $FM$ is figure of merit due to non-ideal effects and $\rho$ is fluid density. It is observed from Eq. 1.1, that as the disk loading of a rotor increases, it becomes less efficient in terms of power loading. Now full-scale conventional helicopters utilize large rotors to maximize disk area ($A$) which minimizes disk loading ($DL = T/A$) which in turn increases power loading ($PL$). On the other hand, rotary wing MAVs are equipped with very small rotors compared to their thrust requirements due to the additional size constraints. So, their disk loading ($DL$) is much larger compared to full-scale counterparts. This leads to much smaller power loading ($PL$) for rotary wing MAVs based on conventional rotor. Moreover, hover is a high-power flight condition which consumes significantly more power compared to forward flight. For MAV applications, long hover endurance is one of the key desirable aspects. On top of that, low aerodynamic performance of scaled down concepts poses additional challenges to attain desirable endurance objectives.

Another major challenge that all types of MAVs face is that they operate at a much smaller Reynolds number (<50,000) compared to their full-scale counterparts which generally operates at Reynolds number in the tens of millions. The smaller size and smaller velocity of the MAVs lead to this very low Reynolds number aerodynamic regime. Airfoil and lifting surface characteristics change significantly in low Reynolds number due to increased viscous drag. Even most optimized airfoils have very low lift-to-drag ratios in low Reynolds number. this can be realized from non-dimensional Navier-Stokes equation (Eq. 1.3). The incompressible Navier-Stokes equation can be expressed as following [15].

$$\frac{\partial \vec{u}}{\partial t} + (\vec{u} \cdot \vec{\nabla})\vec{u} = \vec{g} - \frac{\vec{\nabla} p}{\rho} + \nu \nabla^2 \vec{u} \tag{1.2}$$

The above equation can be non-dimensionalized based on characteristic length and speed which

would give following non-dimensional equation.

$$\frac{\partial \vec{u}^*}{\partial t^*} + (\vec{u}^* \cdot \vec{\nabla}^*)\vec{u}^* = \frac{1}{Fr^2}\vec{g}^* - \vec{\nabla}^* p^* + \frac{1}{Re}\nabla^{*2}\vec{u}^* \tag{1.3}$$

The last term on the right hand side of the equation denotes viscous dissipation. It can be observed that if Reynolds number decreases this viscous term $\frac{1}{Re}\nabla^{*2}\vec{u}^*$ becomes more dominant causing more viscous dissipation. This is one of the major reasons of aerodynamic inefficiency of MAVs.

Several studies are carried out in the past to investigate this low Reynolds number aerodynamics. One study by Schmitz [15] in 1930 showed that the performance of thick cambered airfoil changes drastically at certain Reynolds number, which was denoted as critical Reynolds number. Several other studies [17, 18, 19] in the next few decades also showed existence of such critical Reynolds number in the range of $10^4$-$10^6$, around which significant changes in airfoil performance occurs. In 1980, McMasters and Henderson [20] showed that maximum lift coefficient of airfoil drops suddenly around critical Reynolds number while minimum drag coefficient rises steeply around this point. The smooth airfoils have shown better lift to drag ratio at higher Reynolds number compared to rough airfoils. Although, performance drop around the critical Reynolds number is steeper for smooth airfoils. On the other hand, rough airfoils at low Reynolds number perform almost similar to high Reynolds number. This roughness might be desirable at lower Reynolds number to delay in flow separation.

From 1982 to 1999, Mueller did several systematic experimental study to investigate the performance of airfoil with variation of Reynolds number [21, 22, 23, 24, 25]. These studies showed that the sudden rise in lift coefficient after critical Reynolds number is due to formation of a Laminar Separation Bubble. As the Reynolds number decreases this separation bubble becomes longer which in turn decrease the lift-curve slope causing reduction of lift coefficient for certain angle of attack. In 1997, Laitone [26] did several study to investigate low Reynolds number performance of several types of airfoil such as airfoils with sharp trailing edge, sharp leading edge, elliptical

airfoil etc. For last few decades, Selig conducted extensive wind-tunnel studies to measure lift and drag coefficients of over 200 airfoils at low and moderate Reynolds number [27]. This extensive study showed that drag polar remains more or less same after Reynolds number greater than $10^5$ for majority of the airfoils. Specifically, the drag coefficient corresponding to moderate lift coefficients increases significantly for Reynolds number below $10^5$. On the other hand, drag coefficients corresponding to low and high lift coefficients remain almost low. In 2008, McArthur [28] demonstrated how Laminar Separation Bubble (LSB) is created which in turn decreases performance of airfoil at certain angle of attack at lower Reynolds number. This phenomenon starts with a laminar boundary layer which goes through adverse pressure gradient. This adverse pressure gradient causes boundary layer to separate somewhere after leading edge of airfoil. This separated flow gets unstable and transitions into a turbulent separated shear flow. The turbulence transports momentum from free-stream which in turn causes re-attachment of turbulence boundary layer to the surface at some later point close to trailing edge. Thus, a separation bubble is generated.

The performance of airfoils operating at different Reynolds number regime are summarized by Muller [25] and Carmichael [29]. From 1,000 and 10,000 Reynolds number regime, flow in boundary layer remains laminar which makes it difficult to transition to turbulent flow. Although many large insects fly in this aerodynamic regime, their specific structures help them to delay flow separation. From 10,000 and 30,000 Reynolds number regime also, boundary layer flow remains laminar and does not reattach if it separates. Several mechanism to reattach the flow has not been successful. From 30,000 to 70,000 Reynolds number regime, laminar separation transitions to turbulent flow. Although late onset of this transition might make it difficult for the turbulent flow to reattach. At Reynolds number above 70,000 airfoil performance improves drastically.

It is observed in the this section that MAVs based on conventional concepts are extremely inefficient compared to their full-scale counterparts. Although fixed wing MAVs are somewhat better performer, their hover/low speed incapability restricts them from many of the MAV applications. On the other hand, rotary wing MAVs based on conventional rotor are extremely power hungry and are well short of desirable performance numbers. None of the small helicopters can fly for more

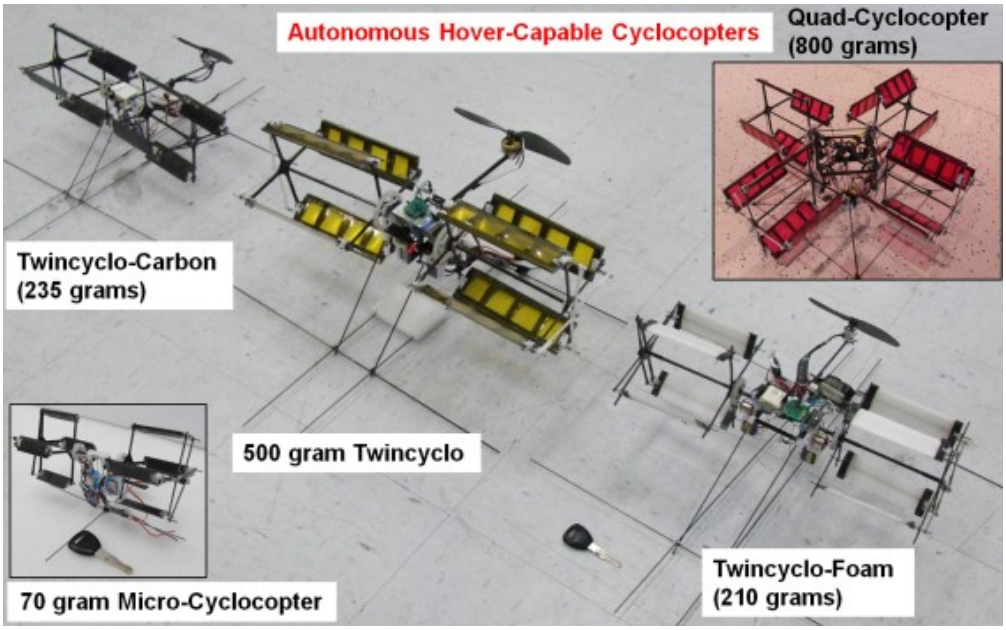


Figure 1.2: Hover-capable cyclocopters [30].

than 15 minutes, while the original objective of DARPA was to attain 60 minutes of endurance. Low Reynolds number aerodynamic regime of MAVs poses significant challenge to this aspect. Thrust production of conventional rotors relies on steady aerodynamic mechanisms, and it is challenging to keep a steady flow attached to the airfoil surface, especially at low Reynolds numbers. Therefore, a conventional rotor blade can only operate over a narrow range of angle of attack if the flow has to stay attached. This leads to small stall margins, and the slightest perturbation could cause the flow to separate. On the other hand, in nature, large insects and small birds operate in a highly unsteady aerodynamic regime with large variations in angle of attack and are more robust to perturbations. Therefore, scaling down of the conventional concepts might not be only right approach to solve the MAV problem. For this reason, various unconventional concepts and out-of-box solutions are getting lots of attention lately. Cycloidal rotor is one such novel propulsion system that exploits unsteady aerodynamics for efficient thrust production while they also offer high maneuverability through instantaneous thrust vectoring which could be extremely beneficial towards developing next generation MAVs.

## 1.3 Cycloidal Rotor and Cyclocopter

In the present dissertation, a novel cycloidal rotor based platform called 'Cyclocopter' (shown in Fig. 1) is proposed as an alternative to conventional rotorcraft based MAVs. The key difference between a cycloidal rotor and conventional rotor is that the blades of cycloidal rotor rotate along a horizontal axis and this axis of rotation is parallel to blade span. Moreover, a cyclic blade pitching mechanism is necessary for a cycloidal rotor to produce net time-averaged thrust at any direction. Figure 1.3 shows that the pitch angle of the blade is cyclically changed in such a way that rotor blade experiences positive geometric angles of attack at both the upstream and downstream halves of its circular trajectory, which causes a resultant thrust that can be resolved into a vertical force to balance the weight and horizontal propulsive force to overcome the drag. Magnitude of the resultant thrust vector is altered by changing pitch amplitude of cycloidal rotor and the direction of thrust vector is altered by introducing phase offset in the cyclic blade pitching mechanism of cycloidal rotor. Primary advantage of this concept is that a complete 360° instantaneous thrust vectoring can be obtained by altering phase of cyclic blade pitching mechanism. Instantaneous thrust vectoring enables the aircraft to become more maneuverable, gust tolerant and seamlessly transition from hover to high-speed forward flight. Few previous studies [31, 32, 33] have shown that an optimized cycloidal rotor can attain much higher aerodynamic efficiency in terms of power loading compared to a conventional helicopter rotor of same disk loading. The primary reason behind this may be the fact that the load distribution of a cycloidal rotor is more uniform along blade span compared to a conventional rotor which lowers induced power. Moreover, cycloidal rotor, being a very compact rotor system, utilizes the 3D space more efficiently compared to a conventional rotor which only occupies 2D circular space. An equivalent cycloidal rotor of same solidity and foot-print would have four times more blade area compared to that of a conventional rotor. Particle Image Velocimetry (PIV) studies show that another reason for the improved performance of cycloidal rotor is the favorable unsteady aerodynamic mechanisms such as leading-edge vortex formation [31, 32] which delays onset of blade stall and enables cycloidal rotor blades to operate at very high pitch angles.

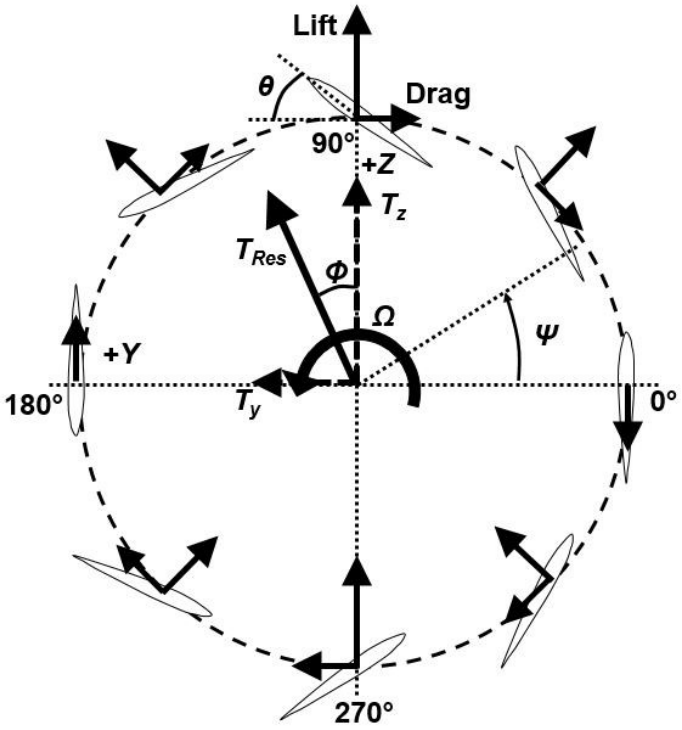


(a) Hover kinematics.

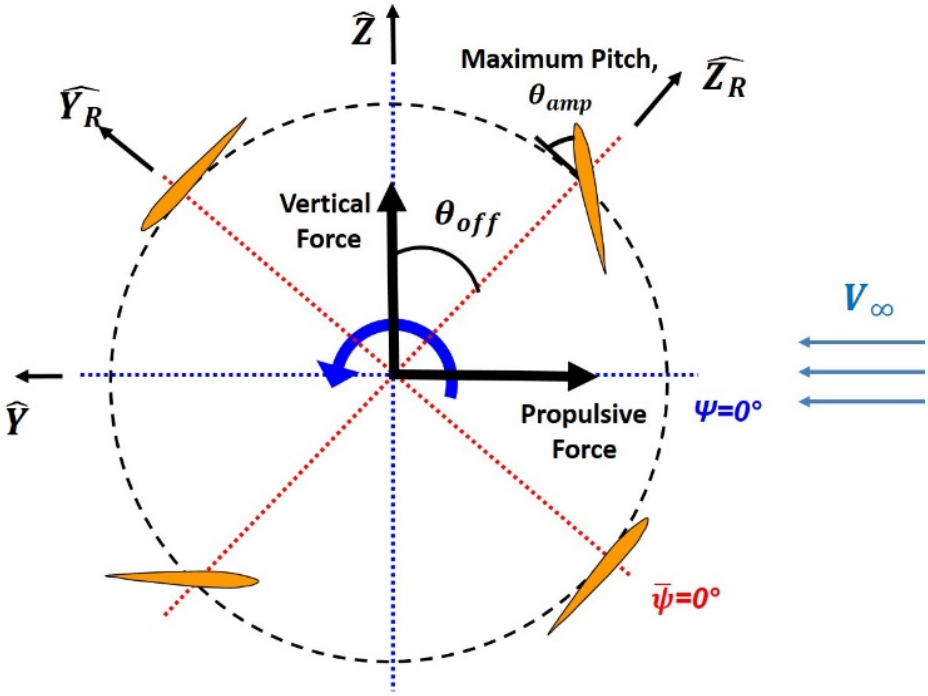


(b) Forward flight kinematics

Figure 1.3: Cycloidal rotor blade kinematics [34, 35].

Figure 1.4: Kirsten-Boeing propeller [40].

The concept of cycloidal rotor originated much earlier in the 19th century. More than a dozen studies on cycloidal rotors were conducted from 1910-1940 [36, 37]. These studies were mostly focused on building a flying vehicle, but all of them eventually failed. One of the key reason behind that was lack of systematic scientific study to understand this concept and its operating principles.

Professor Kurt Kirsten from University of Washington was one of the pioneers of this concept. During 1920s, Kirsten developed first cycloidal propeller in collaboration with Mr. W. E. Boeing [38, 39, 40]. These propellers are known as 'Kirsten-Boeing' propellers. Initially, a small propeller with 5.9 inches blade span and 10.23 inches diameter was developed. The experimental testing of this propeller at the wind tunnel of University of Washington was very satisfactory which led to the foundation of 'Kirsten-Boeing Engineering Company' in Seattle, Washington for the purpose of further improving these types of propellers.

Kirsten recognized the advantages of the thrust vectoring capability of this concept and envisioned to utilize these propellers for airship applications. If the cycloidal propellers are placed

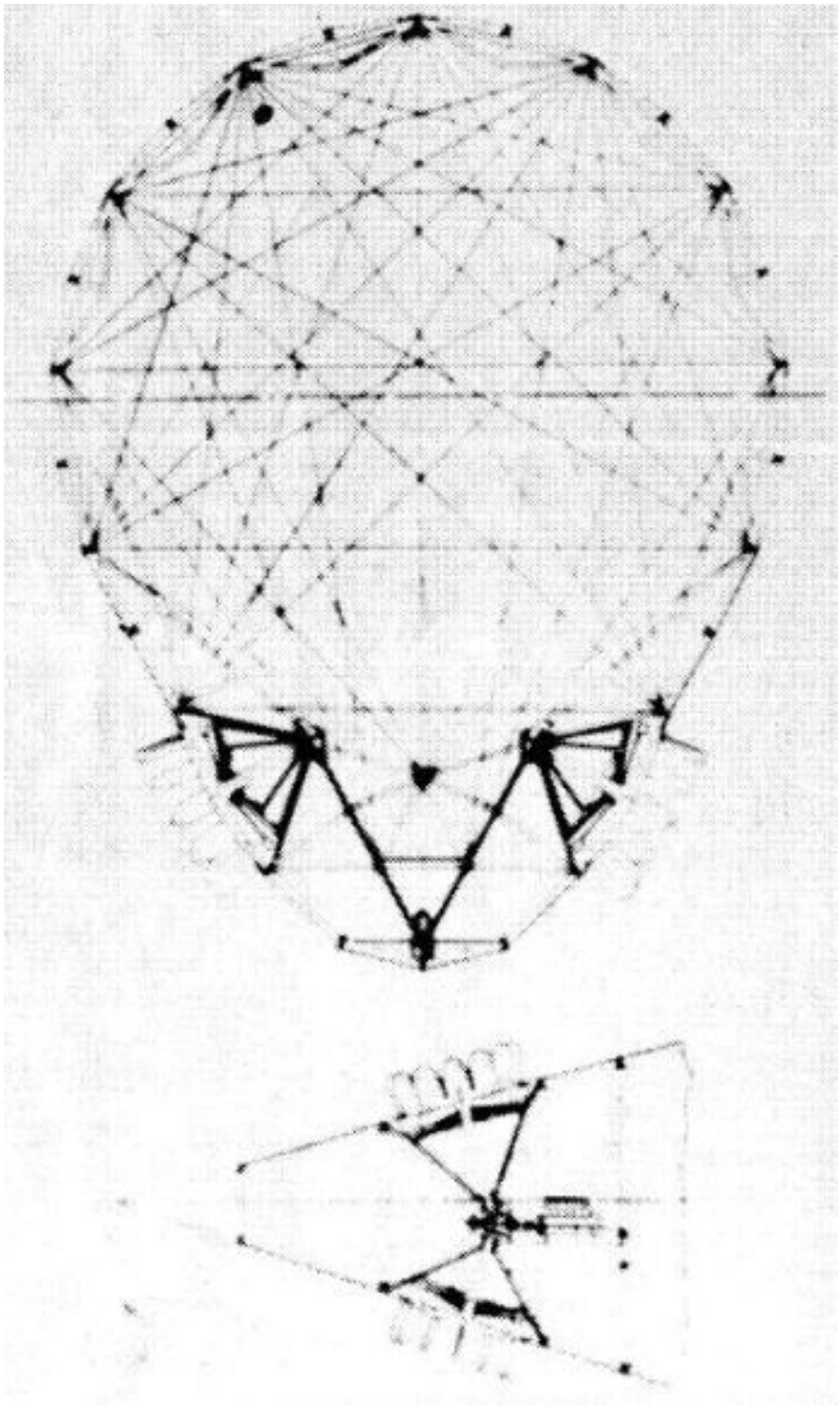

Figure 1.5: Proposed installation of Kristen-Boeing propeller on airship [38].

such that the axis of rotation of blades are along horizontal direction, then the cycloidal propeller could produce force in upward, downward, forward or backward directions. Moreover, if the axis of rotation of propeller blades lie on vertical direction, then it could produce forces in any direction in horizontal plane. Thus, it would provide extreme three dimensional maneuverability to the airships. Towards, this a large airship propeller was developed which was 4.76 ft long and 1.83 ft wide and consisted of 24 blades. A 400 HP Wright airplane engine was utilized to drive this propeller. Utilizing gear reduction, the propeller was rotated only at 225 rpm and produced 212 pounds of thrust. Performance of this propeller in terms of efficiency, controllability and quietness was quiet satisfactory. Due to initial successful testing, this propeller was planned to be mounted on the airship 'Shenandoah'. To control this airship, six main propellers were designed such that the axis of blade rotation remains along 30°from horizontal plane [Fig. 1.5]. This would enable the airship to move in three dimensional space. The six main propellers were designed to produce combined thrust of 10,800 pounds. Additionally, two rear propellers were designed to be placed in vertical plane to replace the customary rudders. Although, the airship 'Shenandoah' unfortunately crashed just few weeks before installation of cycloidal propellers. Unavailability of airships stopped further development of these propellers.

Once the airship applications of cycloidal propellers failed, Kirsten attempted to utilize a modified version of this cycloidal propeller for marine applications. The propellers were tested while mounted on a experimental boat. The main challenge here was to keep the water away from driving mechanism. The first propeller consisted of 16 blades and each of the blade had a steel cog-wheel and ball bearings at its upper end. Although, it was unsuccessful to keep the water away from steel wheel and ball bearings. In the modified version, a bronze wheel meshed with a bronze central driving gear was utilized which was successful to meet the requirements although wheels were allowed to run directly in the water. Finally the propellers were installed in a 38 feet long and 6 feet 7 inches wide boat driven by 150 HP engine. The boat was able to attain speed of 25 nautical miles per hour in the trial trips and covered a distance of over 4000 nautical miles in both salt water and fresh water. Further experimental tests were carried out in the naval model testing basin

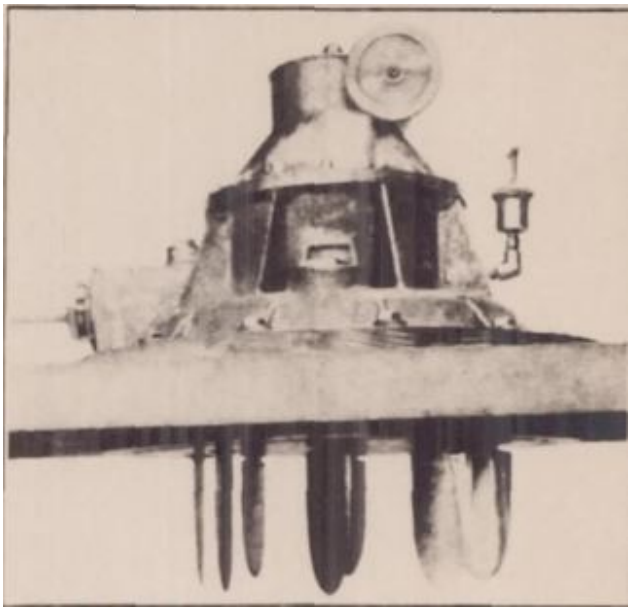

Figure 1.6: Kristen-Boeing boat propeller [38].

Figure 1.7: Voith-Schneider propeller [38].

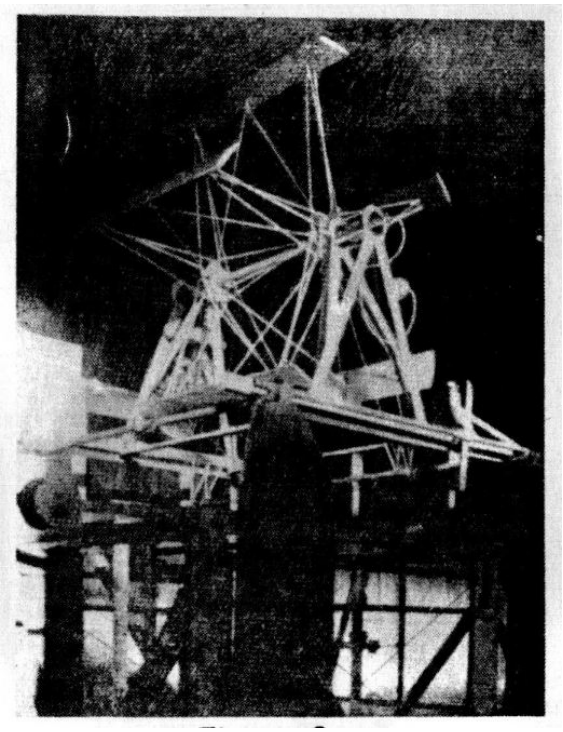

Figure 1.8: Strandgren's cyclogyro model [43].

of Washington and the propeller was found to have an efficiency of around $80\%$. Further results of the experiments are documented in Navy Yard publications which mentions that the boat equipped with Kirsten-Boeing propeller has exceptional maneuverability and does not require any rudder to adjust thrust vectoring. The boat can be shifted quickly from full speed ahead to full speed astern and can cover a 100 feet radius circle with full speed. Due to successful demonstration of this concept, Voith-Schneider Corp bought the patents from Kirsten. In the later period, improved versions of this propeller were built and utilized for marine applications [41, 42]. These propellers are known as 'Voith-Schneider propeller'. Till today, this has been only commercial application of this cycloidal rotor concept.

In 1933, Strandgren developed another cycloidal rotor based aircraft known as 'cyclogyro'. Strandgren was the first person to perform scientific study of this concept [43]. A simple quasi-steady aerodynamic analysis was carried out to determine thrust and lift produced by cyclogyro. The performance of the cyclogyro was computed purely from its kinematics without considering

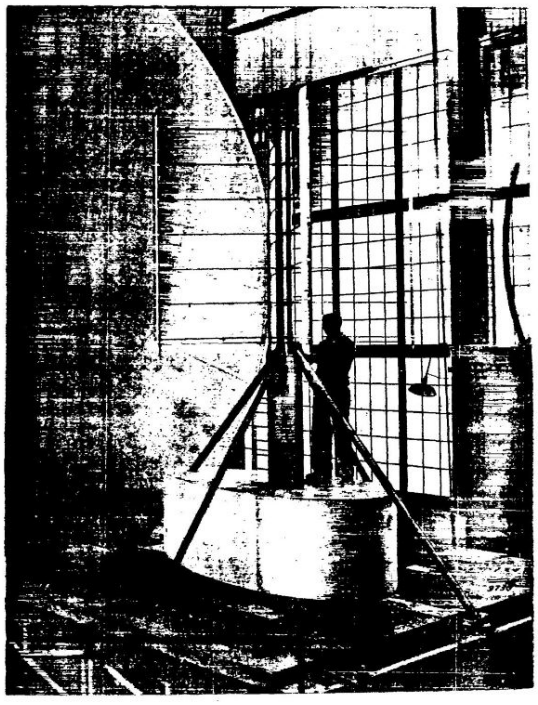

Figure 1.9: Wheatley's cyclogyro test setup [45].

any unsteady or virtual camber effects. The blade velocity was obtained from prescribed kinematics and flow velocity was obtained from forward speed. From these two information, relative air velocity and incident angle with respect to rotor blade was obtained. In the next step, instantaneous lift and drag are calculated based on steady aerodynamics. The lift and drag are resolved in blade normal and tangential direction and integrated to obtain time-averaged force and torque. Main objective of this study was to show feasibility of this concept as an aerial vehicle. The thrust vectoring capability of this concept was shown theoretically through his study. Although, this model was never validated.

From 1933 to 1935, Wheatley developed another simplified aerodynamic model of cycloidal rotor in forward flight [44]. This model was based on blade element theory theory and assumed an uniform inflow across the rotor disc. In this study constant drag model and linear lift model was considered while blade interference effects were neglected. Wheatley also conducted experimental study [45] to measure forces produced by cycloidal rotor. The prediction of Wheatley's model

showed poor correlation with experimental data obtained from wind-tunnel measurements due to lots of unrealistic assumptions to simplify the model. Although the experiments revealed some key features of cycloidal rotor. It was observed that the rotor produces non-zero side force at hover (zero forward speed) even while phase offset was kept to zero. Although in-depth explanation of this phenomenon was not given. The present thesis addresses this physics behind this phenomenon which is discussed at later chapter (Ch. 2).

Taniguchi performed experimental as well as analytical studies on cycloidal rotor during 1944 to 1960 [46, 47, 48, 49]. Taniguchi developed another quasi-steady aerodynamics model of cycloidal rotor in hover and forward flight. The induced flow was assumed to be constant along the azimuth of the rotor which is not practical. Taniguchi performed experiments to measure forces of cycloidal rotor. His model predictions showed good correlation with experiments only when a correction factor based on experimental results were included in the analytical model. This is a major limitation of the model.

After this, there has not been any research on cycloidal rotors for next two decades. The concept of cycloidal rotor was revived again by Bosch Aerospace in 1998 [50, 51, 52]. The advantages of instantaneous thrust vectoring of cycloidal rotor towards airship application was re-identified [50]. Towards this, first flight of an aerial object powered by cycloidal rotor was conducted in 2001 [51]. For this purpose two six-bladed cycloidal rotors were utilized (1.10a) which were attached with a 7 ft diameter balloon, 'The Big Orange' (1.10b). Successful flight test demonstrated that the balloon was controllable and maneuverable in all directions. Finally a 26 ft long, 500 cubic ft Blimp controlled by cycloidal rotor was successfully flight tested in 2003 (1.11) .

During this time, Bosch Aerospace collaborated with McNabb from Raspet Flight Research Laboratory at Mississippi State University and conducted experimental and analytical study of cycloidal rotor [52]. Experimental studies are carried out of demonstrate feasibility of this concept for UAV scale aerial vehicle. For this purpose 6-bladed cycloidal rotor with 4 ft diameter was designed and fabricated. Each of the blades were made of two sections having total 4 square ft area. Each section of the blades had 2 ft span and 1 ft chord. For blade cross sections, NACA 0012

(a) Cycloidal rotor.

(b) Balloon controlled by cycloidal rotor.

Figure 1.10: Cycloidal rotor powered vehicle at Bosch Aerospace [51].

Figure 1.11: Cycloidal rotor powered Blimp [51].

airfoil was chosen as a starting design point. Each section (half) of the rotor blades were built with 606 1 ribs welded to a main spar and covered with an aluminum 2024 skin, which was tack welded to the ribs. The central hub was CNC machined from mild steel stock. The test-rig was built using 3 inches 'C' section steel channel and heavy-duty pillow block bearings. Experiments confirmed significant aerodynamic and acoustic performance advantage of this new concept.Cycloidal rotor demonstrated aerodynamic performance of 11 lb/hp. The operation of cycloidal rotor was noticed to be extremely quiet compared to screw propellers.

In the meantime, McNabb in collaboration with Bosch Aerospace, developed a aerodynamic model of cycloidal rotor in hover and small forward flight speeds [53]. This model was based on simplified unsteady aerodynamics and Farrick's formulation [54]. This model predictions were compared with the results published by Wheatley in 1935 [45] and the experimental results obtained from Bosch Aerospace. The main limitation of this model was also inclusion of some correction factor which needs to be adjusted to match the experimental results. Once these cor-

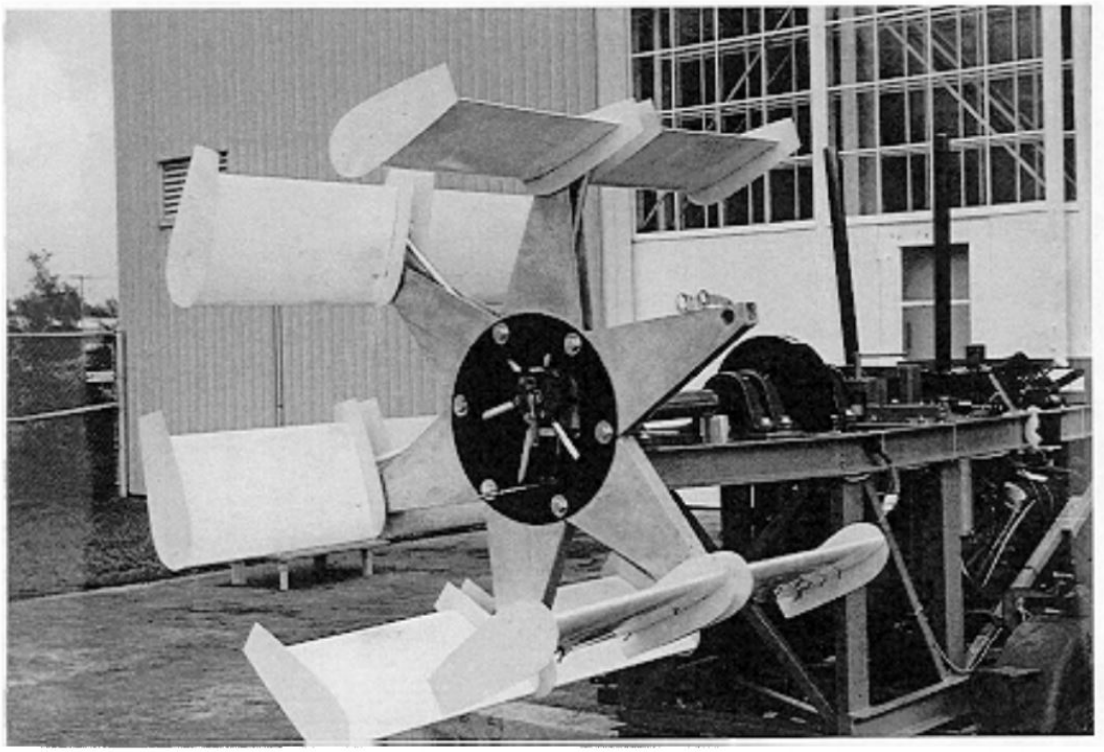

Figure 1.12: UAV scale cycloidal rotor designed and fabricated by Bosch Aerospace [52].

rection factors were adjusted, the model predictions showed reasonable correlation with all those experimental results.

From 2001 to 2006, Iosilevskii and Levy conducted experimental as well as computational study on cycloidal rotors operating at low Reynolds number [56, 57]. Experiments were conducted utilizing small, MAV scale cycloidal rotor of 55.8 mm radius. The cycloidal rotor was equipped with rectangular blades with 22 mm chord and 110 mm span and NACA 0015 cross section. For this purpose, 2, 4 and 6 bladed rotors were tested while varying the rpm from 4000 to 6000 (corresponding to chord-based Reynolds numbers of about 34,000 to 50,000). Time-averaged force and power were measured using a 5 component sting balance with its axis collinear with the axis of rotation of rotor. To develop further aerodynamic insight of cycloidal rotor, a 3D CFD study was carried out which showed reasonable correlation with the experimental results. In the numerical simulation, end plates were removed to simplify the problem and the blade span was doubled to

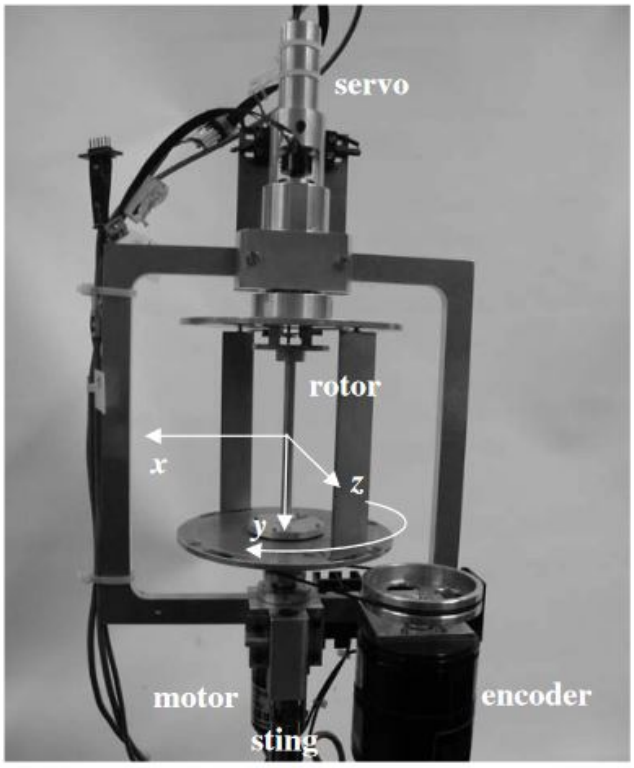


(a) Experimental test rig.

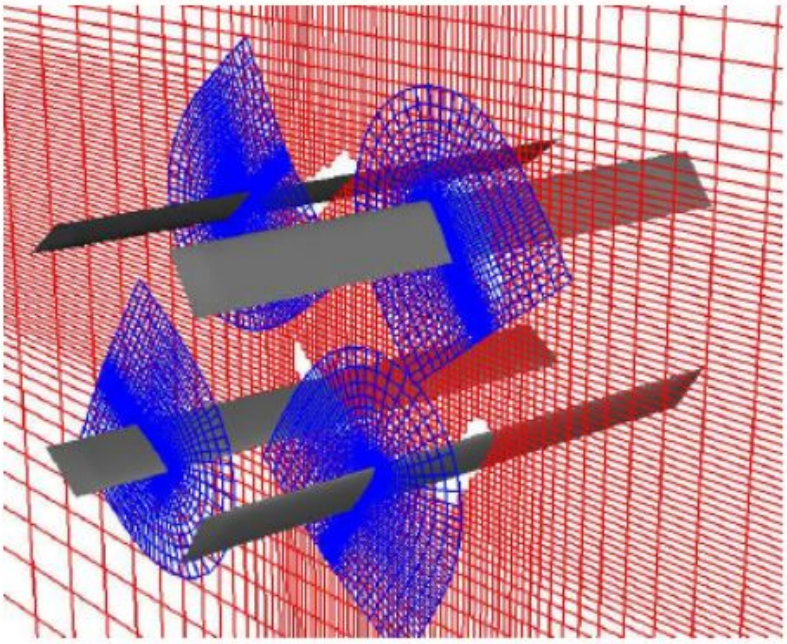

(b) Computational mesh.

Figure 1.13: Experimental and computational study by Iosilevskii and Levy [56, 57].

reduce the end effects. The EZNSS flow solver [57, 58, 59] was utilized for numerical simulation while the reference Reynolds number was kept at 40,000 and reference Mach number was kept at 0.12, roughly corresponding to actual test conditions. For each cycloidal rotor blade, 'D' shaped body-fixed meshes (Fig. 1.13b) were generated and embedded into the global mesh. The Chimera scheme [60] was utilized to account for the changes in mesh geometry due to the cyclic motion of rotor blades. In this study, complex interactions between blades and wakes of other blades were noticed. This phenomenon led to increasing propulsion losses as the number of blades were increased, as observed in both experimental and computational studies.

From 2003 to 2008, a series of thorough and systematic experimental, analytical and computational studies were carried out at the Seoul National University [61, 62, 63, 64, 65, 66, 67, 68, 69]. Kim et al. [61] measured time-averaged thrust and power of an UAV scale cycloidal rotor while varying several design parameters such as number of blades (2, 3 and 6), pitch amplitude (5°, 10°, 15°, 20°, 25°and 30°), rotor radius (0.4 m, 0.45 m and 0.5 m), pitch offset (-70°to 110°), rpm (0 to 600). For this purpose, composite blades were utilized to reduce the blade weight while increase the blade rigidity. Blade-skin was fabricated using 3 sheets of glass/epoxy pre-preg. The blade spar was composed of 3 tubular cells. 6 narrow strips of 0°carbon/epoxy were utilized as trailing stiffener. The test setup is shown in Fig. 1.14a. A 3-bladed cycloidal rotor was able to produce 4.6 kg force at an rpm of 500. Through extensive parametric study, effects of different design parameters on cycloidal rotor performance were observed. To investigate these phenomena, CFD analysis were carried out using commercial CFD software, Star-CD. The cyclic motion of the rotor blade was incorporated using sliding moving mesh (Fig. 1.14b). A global moving mesh which denotes the complete rotor system is taken as outer circle. 6 local moving meshes that denotes individual blades are placed inside smaller circles. The outer global mesh rotates with rpm of the rotor and 6 local mesh incorporates the pitching motion of rotor blades. The CFD simulations showed good correlation with the experiments.

The understanding and insight gained through these detail parametric experimental and computational studies led to the development of a cycloidal rotor based UAV in 2004 by Yun et al.

(a) Experimental setup.

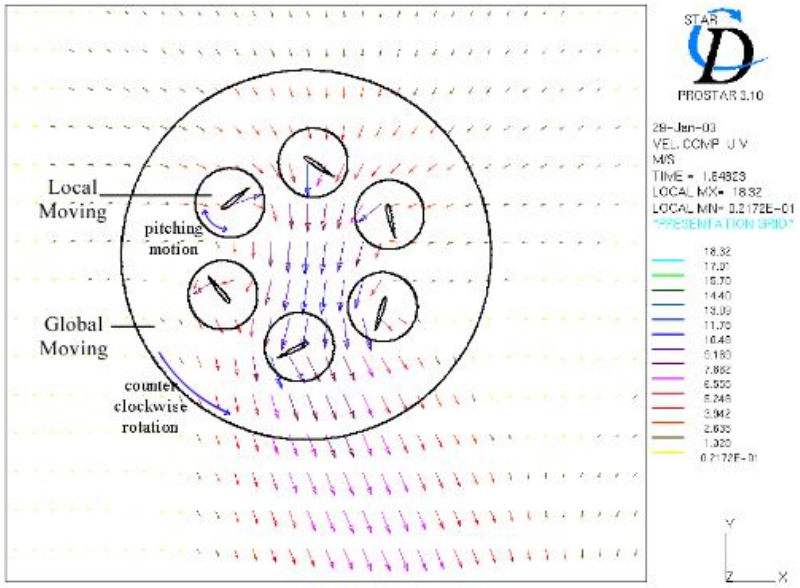


(b) Velocity vector components obtained from CFD.

Figure 1.14: Experimental and computational study by Kim et al. [61].

Figure 1.15: 46 kg cycloidal rotor based UAV built by Yun et al. [63].

[62, 63]. The vehicle, weighing 46 kg, was 1.65 meter long in longitudinal direction and 2.7 meter in lateral direction. In this vehicle two 4-bladed cycloidal rotors were utilized. Cycloidal rotor had a diameter of 1.4 meter, blade chord of 0.15 meter, blade span of 1 meter and NACA 0012 as blade cross-section. Two cycloidal rotors were able to produce 45 kg force together at 550 rpm while drawing 11 HP power. Although no flight test regarding this vehicle was informed. Another UAV was built by Yun et al. in 2007 [64]. Yun et al. [64] also developed a lower-order quasi-steady aerodynamic model for design and optimization of the cycloidal rotors. The aerodynamic model utilizes a double multiple streamtube model to capture the inflow. To capture blade loads BEMT based model was developed which assumes linear aerodynamics. The model showed reasonable correlation with cycle-averaged forces measured from experiments. Although instantaneous forces were not compared. Major limitation of the this analysis was lack of detail unsteady modeling. Moreover some key physical phenomena (such virtual camber) behind the operation of cycloidal rotor were also neglected.

In 2006, a 100 kg quad-cyclocopter was designed and built by Hwang et al. [66] at the Seoul National University. Each of the cycloidal rotors were equipped with 4 blades and had a diameter of 1.7 meter, blade chord of 0.22 meter and blade span of 1 meter. A 2D-CFD based parametric study

Figure 1.16: 100 kg quad-cyclocopter built by Hwang et al. [66].

was conducted to find optimum rotor parameters such as number of blades, airfoil, rotor radius, rotor speed, pitch amplitude, blade span and blade chord length. For the simulation purpose, commercial CFD software STAR-CD was utilized [70]. CFD mesh was generated by the PCL (Patran Command Language) of MSC.PATRAN [71]. To incorporate the cyclic motion of rotor blades, a moving mesh method was utilized. Furthermore, a 3D-CFD analysis was carried out for the detail analysis based on the preceding results of 2D-CFD study. For the structural analysis and optimization of rotor blade system, MSC.NASTRAN [72] was utilized. Servo-motor based control mechanism was developed to control the attitude of the vehicle. Although, no flight test/ tether test of the vehicle was documented.

In 2008, another quad-cyclocopter was designed and built by Hwang et al. [67]. The 4-bladed cycloidal rotors had diameter of 0.5 meter, blade chord of 0.105 meter and blade span of 0.5 meter. One key difference in this cyclocopter from the previous one is usage of elliptical blades to optimize blade aerodynamic performance. To optimize strength/weight ratio, composite blades are used as well as other blade parts and fuselage were also made of composite materials. For efficient control, a swash plate was incorporated in the rotor control mechanism. Experimentally, the cycloidal rotor was able to produce 157 N thrust at 1100 rpm with a power requirement of

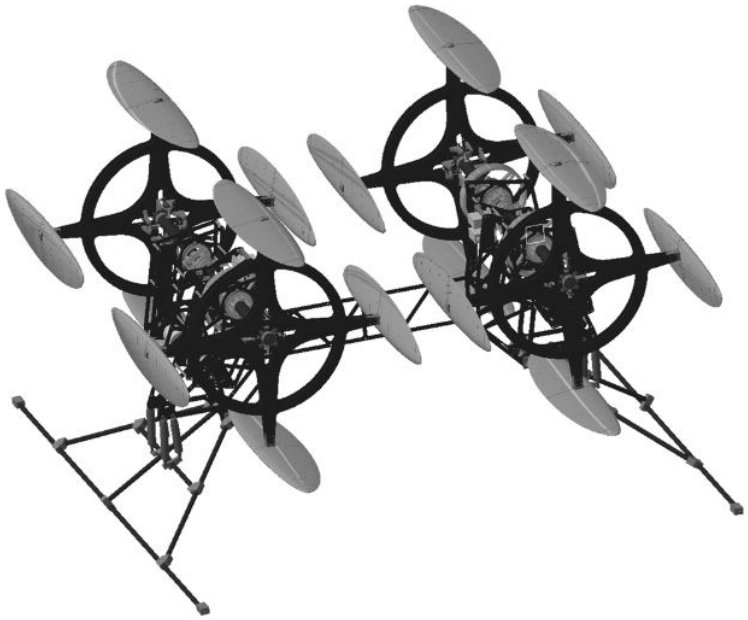

(a) Designed quad-cyclocopter.

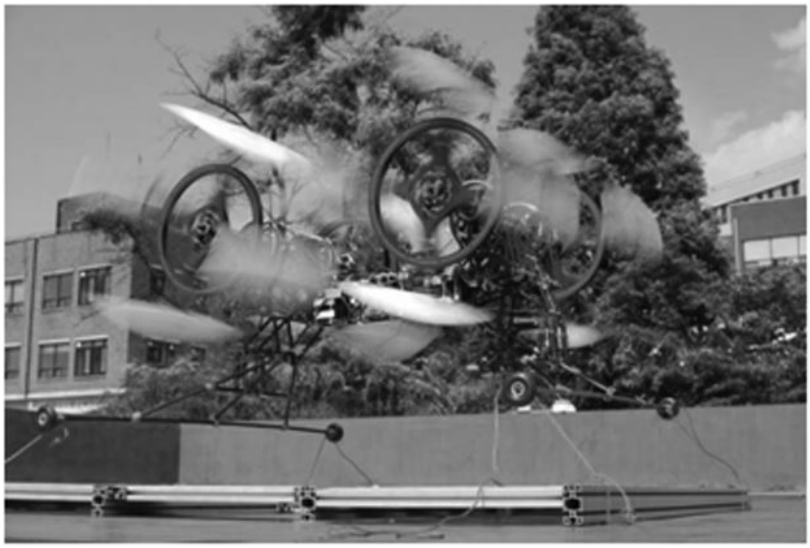

(b) Tether flight test of quad-cyclocopter.

Figure 1.17: 12 kg quad-cyclocopter developed by Hwang et al. [67].

2633 W. The experimental power consumption value came to be 15% more than expected from computational results. Although thrust was sufficient enough for the vehicle to take-off vertically, proceed to forward flight and land safely. A tethered flight test of the developed quad cyclocopter was conducted and vehicle was able to lift off the ground. Although due to lack of proper control strategy, it was unstable from attitude control point of view.

In the National University of Singapore, computational and experimental study on cycloidal rotor is conducted by Yu et.al [73, 74, 75] during 2006. For computational purpose, a 3-D Unsteady Vortex Lattice Method (UVLM) was utilized for performance prediction of cycloidal rotor in hover. Major limitation of this model is that it assumes flow to be inviscid and irrotational. Therefore, the model is incapable to predict the viscous effects which is very dominant for MAV scale cycloidal rotors. The experimental study includes development of a innovative 5-bar based pitching mechanism. An MAV scale cyclocopter was built based on above study. The tether hover testing of the vehicle was demonstrated.

In 2006, Sirohi et. al conducted experimental parametric studies on cycloidal rotors by varying different design parameters [76]. These studies showed promising performance from cycloidal rotor specially at MAV scale. In 2006, Acquity Technologies carried out both experimental and 2-D CFD studies of a model cycloidal rotor [77]. In this study active blade control was implemented to improve control authority of the rotor. In 2007, Siegel et. al. performed 2-D CFD analysis to investigate unsteady aerodynamic of cycloidal rotor [78]. This study showed that both thrust production and energy extraction is possible for a cycloidal rotor using suitable pitch kinematics. In 2007, Hara et. al. developed an innovative vehicle configuration based on cycloidal rotor [79]. The feasibility of this concept was also demonstrated. In 2007, Tanaka et. al. developed a new mechanism to alter blade pitch angle in a passive manner by inclusion of an eccentric rotational point [80]. In 2009, Nozaki et. al. performed experimental investigation on application of cycloidal rotor on an airship [81]. It was observed that inclusion of cycloidal propeller makes the airship much more maneuverable. In 2010 Kan et. al conducted 2-D and 3-D CFD studies of MAV scale cycloidal rotor in hover [82]. The flow field predicted by 3-D CFD was very similar to flow-field

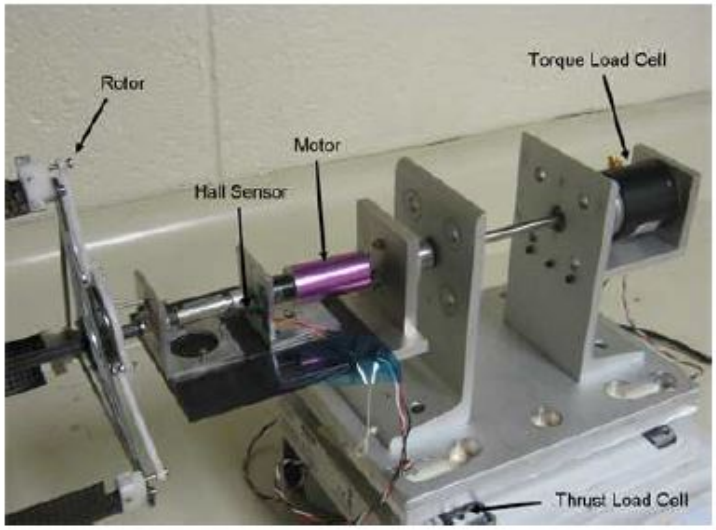


Figure 1.18: Hover test rig of cycloidal rotor at University of Maryland [31].

measured using PIV. In 2010, Nakai et al. performed PIV study to investigate flow field around a cycloidal rotor [83].

In university of Maryland, pioneering research were conducted on MAV scale applications of cycloidal rotor for last ten years. A combination of detailed and systematic experimental and computational studies are carried out to develop a fundamental understanding of the physics of cycloidal rotors at MAV scales by Benedict et. al. [31, 32, 33, 83, 84, 85, 86, 87, 88, 89]. The experimental studies include extensive parametric study to obtain an optimized cycloidal rotor configuration. Towards this, several design parameters such as rpm, pitch amplitude, airfoil profile, blade flexibility, blade planform shape, pitching kinematics were varied while measuring performance of cycloidal rotor. It is observed that chord-to radius ratio, location of pitching axis and asymmetry in pitch kinematics, significantly influences performance of cycloidal rotor. Studies with varying chord/radius ratio showed significant flow curvature associated with cycloidal rotor. Moreover, higher chord/radius ratio ($c/R >= 0.5$) was found to be beneficial to optimize rotor performance. Cycloidal rotor performance improved with solidity until 0.4 and increasing the chord was observed to be a better way to increase solidity rather than increasing number of blades. Pitching axis away from leading edge proved to improve performance, specially for blades with

larger chord/radius ratio where flow curvature effect is significant. Although in-depth reasoning behind these phenomena was lacking. From blade pitching kinematics point of view, an asymmetric pitching with slightly higher pitch at the top half of blade trajectory provided better power loading compared to symmetric pitching. Moreover, higher pitch amplitudes were observed to improve aerodynamic performance in terms of power loading. Although, higher pitch amplitudes led to significant bending and torsional deflections on the rotor blades which would have a detrimental effect on rotor performance. Camber of the blade section was found to decrease overall performance of cycloidal rotor, thus symmetric airfoil was utilized for later investigations. In-depth studies related to blade planform shape revealed that that trapezoidal blades with moderate taper ratios improved the power loading of the rotor slightly, although large taper was detrimental.

PIV studies were conducted to gain better understanding of the flow-field of MAV scale cycloidal rotor [31, 32]. Formation of large leading-edge vortex was observed in the PIV studies which is responsible for delaying onset of dynamic stall. Thus cycloidal rotor can operate at a much higher pitch amplitude upto 45°. Force measurements showed that cycloidal rotor in hover condition produces significant side force along with the vertical thrust force, as observed in Wheatley's experiments [44, 45]. To further investigate this phenomenon, PIV measurements were carried out in the wake of cycloidal rotor which showed significant wake skewness caused due to the side-ward force. Although in-depth reasoning behind this phenomenon was not clearly understood.

The forward flight studies conducted by Benedict et. al. [86, 87, 88] includes a combination of time-averaged force measurements, time-resolved PIV measurements and 2D CFD analyis. Flow field obtained from CFD analysis was very similar to that observed from PIV study. Moreover, it is observed that a cycloidal rotor would produce significant lift in forward flight even with 90°phase offset which would enable the vehicle to operate at high forward speed. It was also noted a backward spin of cycloidal rotor with respect to incoming flow is necessary to produce positive lift. While a a forward spin with respect to incoming flow would generate same amount of lift but in downward direction.

The insights from these studies along with autonomous flight control strategies, led to the de-

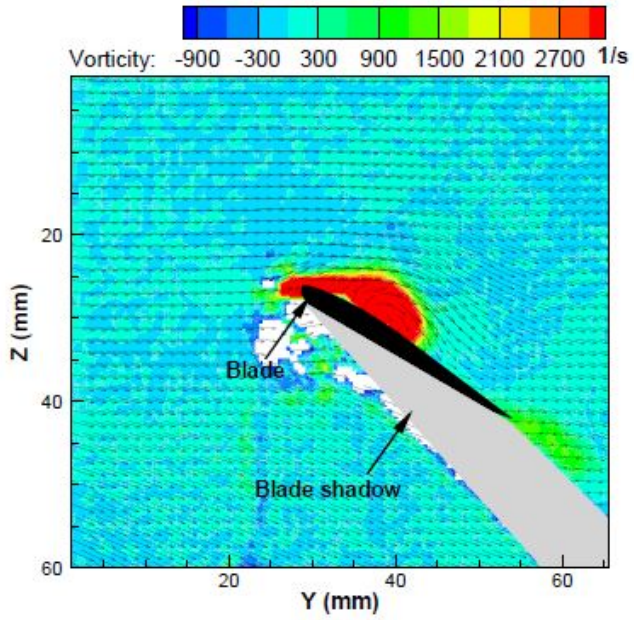


(a) Leading-edge vortex on top of cycloidal rotor blade.

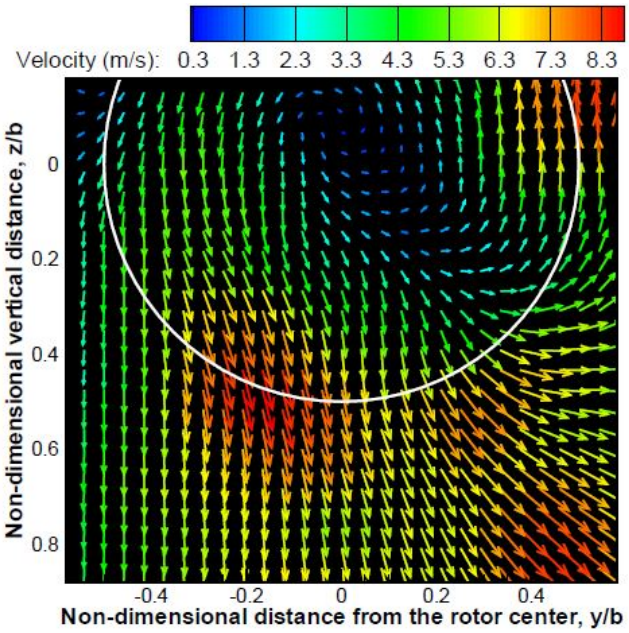


(b) Time averaged velocity measurements showing skewed wake of a cycloidal rotor.

Figure 1.19: PIV study by Benedict et al [31].

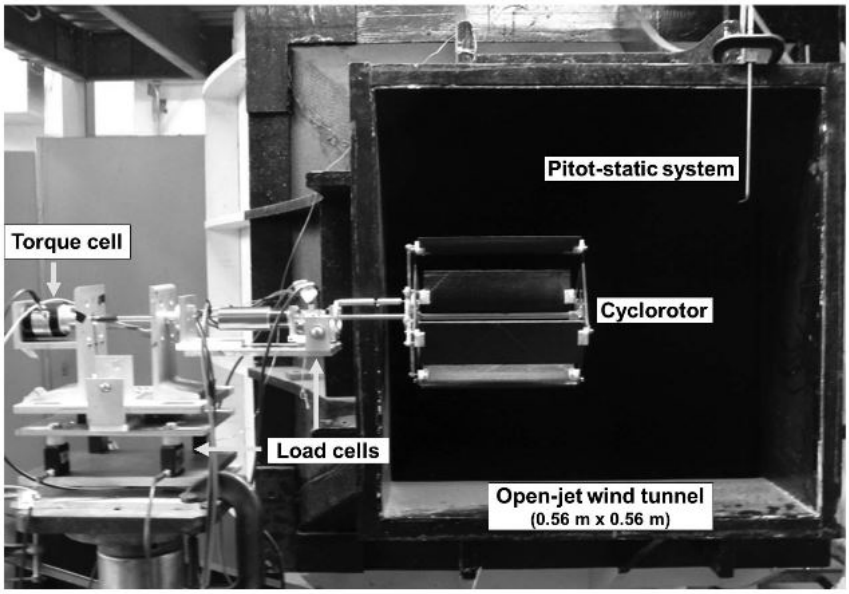


Figure 1.20: Open jet wind tunnel force balance setup at University of Maryland [88].

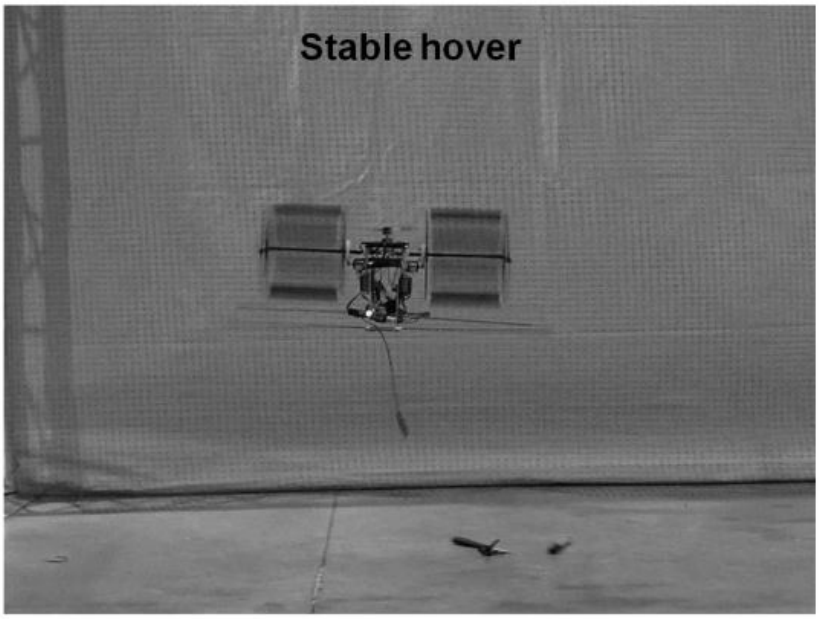


Figure 1.21: Autonomous stable hover of MAV scale cyclocopter [90].

velopment of the first open loop sustained hover of cyclocopter in the literature [90]. Since then different cyclocopter configurations at different scales (29 grams to 800 grams vehicle) were built and flight tested as shown in Fig. 1.2 [90, 91, 92, 93, 94, 95, 96, 97]. Identification of flight dynamics of a 500 grams MAV scale twin cyclocopter was carried out by Hrishikeshavan et. al. [95] at University of Maryland. Analysis based on a control-theoretic framework indicated sufficient maneuverability potential of cyclocopter in open-loop condition. Moreover, high gust tolerance capability of the vehicle was identified. Higher maneuverability and gust-tolerant capability enable this concept highly desirable for several MAV applications

It is observed that the concept of cycloidal rotor originated much earlier in the 20th century. Although, most of the practical implementations were unsuccessful due to lack of systematic scientific study. After few decades of no research, this concept was revived again by Bosh Aerospace. In the meantime, increasing demands of small scale aerial platforms and limitations of the conventional configurations led to increased interest in novel concepts like cycloidal rotor. Towards this, lots of researches on cycloidal rotor were conducted during last two decades. Although, there exist very limited efforts in the present literature to develop analytical models of cycloidal rotor. Most of the existing models are based on extremely simplified aerodynamics which can not capture complex flow features associated with cycloidal rotor and thus, show poor correlation with experimental results without any form of empirical corrections. The major reason behind this is lack of understanding and modeling of key aerodynamic phenomena (such as virtual camber, leading-edge vortex, effects of near and shed wake) behind the operation of cycloidal rotor. On the other hand, all these studies, except the one by Benedict et. al. [98], focused on modeling only the aerodynamic performance of cycloidal rotor while completely neglecting the effects of blade deflections. Moreover, none of the previous studies conducted trim analysis of cyclocopter at any flight conditions.

## 1.4 Motivation and Objective

Increased demand for unmanned aerial systems for both military and civilian applications has sparked lots of interest in MAV research in past few decades. Although fixed wing MAVs are com-

paratively more efficient in terms of performance and endurance, they can not be used for highly constrained environment or surveillance purposes due to their lack of hover/low-speed capability and maneuverability. On the other hand, present MAVs based on conventional rotors have shown very low performance capability, which are well short of the endurance (<15 minutes) and payload objectives as observed during literature review. Developing next generation of MAVs would require radical improvements in propulsion systems as well as control and guidance strategies. The limitations of MAVs based on conventional concept has led to lots of interest towards out-of-box solutions and novel configurations. Cycloidal rotor is one such novel propulsion concept, which has huge potential due to its higher aerodynamic efficiency and maneuverability (instantaneous 360° thrust vectoring capability).

Present MAVs based on cycloidal rotor are developed through extensive experimentation and not by utilizing traditional aircraft design techniques which is neither scientific nor practical. The reason for this is primarily the lack of design tools for these types of small-scale unconventional systems. A crucial step towards building efficient MAVs utilizing cycloidal rotor systems involves developing an aeroelastic framework and a coupled trim methodology, which could be utilized for design optimization and this is the main objective of the present dissertation.

However, physics behind the force production of cycloidal rotor is not well understood due to extremely complex flow-field associated with cycloidal rotor which is characterized by strong leading-edge vortex formation, nonlinear dynamic virtual camber effects, shed wake and blade-wake interactions. Moreover, its several key aerodynamic characteristics change with different flight conditions. For example the complex inflow characteristics and trajectory of blade wake is highly dependent on the forward speed and direction of it. The cycloidal rotor itself needs to alter its phase offset to produce positive propulsive force in forward speed. It is also observed that direction of rotation of cycloidal rotor in forward flight has a significant effect on its vertical force production capability. Although some of this phenomena are observed in previous in-house experiments and in literature review, the reasoning and physics behind those phenomena are not well understood. For this reason, it is extremely crucial to investigate the aerodynamics of cycloidal

rotor thoroughly in order to fully exploit the aerodynamic advantages of this configuration. One major step towards this is to develop an accurate physics based lower order model of cycloidal rotor by rigorously modeling the key aerodynamic phenomena. The next important step is to utilize the model to understand the force production principles of cycloidal rotor.

Another major improvement needed to develop efficient cycloidal rotor is development of light-weight rotor blades which would also reduce weight of all load bearing components of rotor hub since they have to withstand less blade inertial forces. On the other hand, considerable blade deflections are inevitable for a light-weight rotor blade. It is also observed from in-house experiments that cyclodial rotor blades go through very large bending and torsional deflections which significantly affect rotor performance. This demands development of an aeroelastic framework of cycloidal rotor that can be used to accurately predict large blade deflections and their effects on rotor performance. Moreover, detail aeroelastic investigation is needed to assess the nonlinear behaviour of blade deflections and how these deflections are affecting rotor performance.

Finally efficient control strategy of the entire vehicle needs to be developed. This includes coupling of individual thruster models with the trim model of the vehicle to obtain coupled trim solutions. In the present literature, there exists no study related to coupled trim modeling of MAVs based on cycloidal rotors. This coupled trim study is crucial to investigate the control inputs needed to sustain steady flight conditions.

## 1.5 Technical Challenges

Aeroelastic modeling of cycloidal rotor is the most challenging part of the present dissertation, containing both aerodynamic and structural challenges. Large amplitude, high reduced frequency pitching motion of cycloidal rotor blades results in highly complex unsteady aerodynamics characterized by strong leading-edge vortex formation, nonlinear dynamic virtual camber effects, shed wake and blade-wake interactions which makes it extremely challenging to come up with a lower order model. On the other hand, low Reynolds number operating regime of both cyclodial rotor and conventional rotor at MAV scale, poses additional modeling challenges. On the structural side, the cycloidal rotor blades go through very large bending and torsional deflections due to dom-

inant centrifugal force. Moreover, the cycloidal rotor blades being more constrained at both ends, start showing nonlinear behaviour at much earlier stages with can not be captured accurately by a traditional $2^{nd}$ order model. The key challenges of the present study is listed below in more detail.

### 1.5.1 Cycloidal Rotor Aerodynamic Challenges

1. The cycloidal rotor blades go through an unique aerodynamic phenomenon known as virtual camber. A symmetric airfoil in straight flow experiences same incident velocity angle (angle of attack) at different chord-wise location. On the other hand, a cambered airfoil in a straight flow experiences different incident velocity angle at different chord-wise location. Similarly, when a symmetric airfoil experiences variation of incident angle of attack along different chord locations due to various reasons, it shows cambered behaviour, which is known as virtual camber effect (symmetric airfoil behaving as cambered airfoil). This virtual camber effect is very predominant in cycloidal rotors because the flow over a cycloidal rotor blade is characterized by a pitching airfoil in a curvilinear flow in the presence of inflow that varies along with azimuth. A airfoil in a curvilinear flow experiences different flow velocity magnitude and direction along the chord due to geometry and the curvilinear nature of the flow; this manifests as an effective camber and incidence. Moreover, the non-uniform inflow distribution and flow velocity due to forward speed changes this curvilinear geometry which in turn changes virtual camber effect. Additionally, the pitch angle and pitch rate of cycloidal rotor blade influences chord-wise variation of flow incident angle and thus, virtual camber. Pitch angle and pitch rate of a cycloidal rotor changes continuously with azimuth so the virtual camber also changes with azimuth making it a dynamic virtual camber. This dynamic and non-linear nature of virtual camber due to multiple effects makes it extremely challenging to come up with a lower order model. This effect becomes more significant as the chord by radius ratio (c/R) of cycloidal rotor increases.

2. The lift generation for a pitching airfoil is very different from that of a static airfoil due to quasi-steady effects of pitching kinematics and unsteady effects from shed vortices. Oscil-

latory part of the lift produced by cycloidal rotor blade contains not just the first harmonic, rather it shows high frequency components with varying phase delays due to inclusion of virtual camber and its nonlinear behaviour. This phenomena makes it challenging to model the effects of shed wake.

3. Large amplitude, high reduced frequency pitching motion of cycloidal rotor blade causes formation of strong leading-edge vortex. These vortices delay the separation of flow over airfoils at higher angle of attack which causes higher lift-coefficient than steady state maximum values. Cycloidal rotors use cyclic blade pitching kinematic for net thrust generation. At higher angles of attack, these pitching blades show dynamic stall behavior which is very different from static stall and very difficult to model.

4. The inflow characteristics associated with cycloidal rotor is extremely complex and nowhere near uniform. The induced inflow interacts with the rotor twice, in upstream and downstream region. After interacting with the rotor blades at upstream location, the wake gets bent and accelerated before it interacts with rotor blades in the downstream. Due to this complex blade vortex interaction, trajectory of induced flow and trailing vortices becomes highly unpredictable which makes it very challenging for a lower order model to accurately capture the wake geometry. On the other hand, cycloidal rotor needs to change its phase offset in forward flight in order to produce positive propulsive force which alters upstream and downstream regions on cycloidal rotor blade. For this reason, the wake geometry gets highly influenced by direction and magnitude of flow due to forward speed.

### 1.5.2 Cycloidal Rotor Structural Challenges

1. In case of cycloidal rotor, the centrifugal force of rotor blade acts radially causing more deflections of the rotor blade unlike conventional rotor, where centrifugal force acts axially and causes axial stiffening of the blade. It is also observed from in-house experiments that cyclodial rotor blades go through very large bending and torsional deflections which significantly affect rotor performance.

2. The nonlinear coupling between bending curvatures in two orthogonal directions (i.e. radial and tangential) create large nonlinear moment. Blade twist due to this nonlinear moment is one of the major reasons of drop in performance of cycloidal rotor.

3. The cycloidal rotor blades are more constrained, fixed in bending at both side, unlike conventional rotor blades which are cantilever in nature. These extra bending constraints increase bending curvature and introduce nonlinearity at a much earlier stage. Specifically the nonlinear twist due to coupling of bending curvatures starts at very early stages of blade deflections. For this reason, even smaller blade deflections are not properly captured by traditional $2^{nd}$ order nonlinear model that are widely used in conventional rotorcraft structural analysis.

### 1.5.3 Conventional Rotor Aerodynamic Challenges

Conventional nose rotor of MAV scale cyclocopter operate at a very low Reynolds number compared to full-scale rotor. Aerodynamic behavior of airfoil changes significantly at very low Reynolds due to increased viscous effects. Due to this reason, the variation of Reynolds number at different span locations of rotor blade becomes more significant. Moreover, linear lift curve slope characteristic of airfoil does not hold true in this low Reynolds number regime. For this reason, traditional blade element momentum theory (BEMT), widely utilized for full scale rotor, is not applicable to these MAV scale rotors.

### 1.5.4 Challenges in Couple Trim Procedure

The nonlinear behaviour of coupled trim model of cycloidal rotor poses additional modeling challenges. Estimation of appropriate initial conditions and proper convergence scheme is essential for this purpose. Moreover, the control methodology of the vehicle changes based on flight conditions. For example, the control strategy for a twin-cyclocopter in forward flight is very different from hover because of the tilt of thrust vector.

## 1.6 Contributions of The Thesis

The main contribution of the thesis is development of an aeroelastic coupled trim model of a twin-cyclocopter at different flight conditions (i.e hover, forward flight). Twin-cyclocopter consists

of two cycloidal rotors as main thrusters and a conventional horizontal nose-rotor for pitch-torque balance. Coupled trim analysis requires simultaneous computation of trim controls, vehicle orientation and blade structural responses so that both blade response equations and vehicle trim equations are satisfied. To obtain the blade structural response and the rotor aerodynamic loads for a given set of control inputs, a nonlinear aeroelastic framework of the complete vehicle is developed. This framework consists of aeroelastic model of cycloidal rotor and aerodynamic model of conventional nose rotor. The nonlinear aeroelastic model of the cycloidal rotor is developed by coupling unsteady aerodynamic model with a fully nonlinear geometrically exact beam based structural framework capable of predicting large bending and torsional deflections of rotor blade. Towards this, complex aerodynamics of the cycloidal rotor is thoroughly investigated and various underlying phenomena, such as dynamic virtual camber, non-uniform inflow, effects of near and shed wake and leading-edge vortices are rigorously modeled. To obtain the performance of the conventional nose rotor, a modified BEMT based model with CFD-based airfoil lookup tables is developed. All the models and the sub-models are systematically validated with results obtained from in-house experiments. Once validated, the models are utilized to understand the physics behind the force production of cycloidal rotor. The key contributions of the developed models are listed below.

### 1.6.1 Cycloidal Rotor Aerodynamic Analysis

1. Cycloidal rotor blades go through an unique phenomenon known as virtual camber which is investigated in great detail and rigorously modeled. It is shown that the chord-wise variation of incidence velocity angle on cycloidal rotor blade is manifested as dynamic virtual camber, which depends on curvilinear flow geometry, pitch angle, pitch rate, inflow distribution and forward speed of vehicle. By including all these effects together, a generalized expression of additional lift due to virtual camber effect is developed.

2. Cycling pitching of cycloidal rotor blade creates shed wake along blade span. The oscillatory part of the lift of due to cyclic pitching contains higher frequency components with varying

phase delays. To handle this properly while modeling the effects of shed wake, an automated function has been developed that would perform Fourier series decomposition of oscillatory part of lift (due to shed wake) and compute corresponding frequency and Theodorsen's function to generate unsteady lift.

3. To capture the complex inflow characteristics of cycloidal rotor, a lower order computationally inexpensive model based on modified double multiple streamtube (D-MS) is developed which relaxes some of the unrealistic assumptions of traditional D-MS model and uniform inflow model. Moreover, effects of forward speed and cycloidal rotor phase offset on the inflow geometry is introduced in the proposed model.

4. To accurately capture blade-vortex interactions and its effect on wake geometry, a high-fidelity model based on free-wake is developed.

5. Once systematically validated with in-house experiments, the developed lower order model is utilized to understand physics behind the force production of cycloidal rotor.

### 1.6.2 Cycloidal Rotor Structural Analysis

1. To capture large bending and torsional deflections of cycloidal rotor blade a fully nonlinear geometrically exact model is developed. It is shown that the geometrically exact model gives much more better predictions compared to a traditional $2^{nd}$ order nonlinear model.

2. In-house experiments are carried out to investigate the effect of blade deflections on the performance of cycloidal rotor. It is observed that as the flexibility of blades increases, the thrust production of rotor decreases while power requirement increases. This leads to overall decrease in power loading.

3. An aeroelastic model of cycloidal rotor is developed by coupling unsteady aerodynamic model with the structural framework. It is also observed that the aeroelastic model based on geometrically exact structural framework gives very accurate prediction compared to the aeroelastic model based on $2^{nd}$ order nonlinear structural framework.

4. The fully nonlinear aeroelastic model is utilized to understand the reason behind performance drop of flexible cycloidal rotor.

### 1.6.3 Conventional Rotor Aerodynamic Analysis

At low Reynolds number operating regime of MAV scale rotor, aerodynamic behavior of airfoil changes significantly due to higher viscous losses. To model performance of such MAV scale conventional nose rotor, a modified blade element momentum theory (BEMT) model based on CFD lookup table is developed. The developed model relaxes few assumptions of traditional BEMT model which is not applicable to MAV scale rotor.

### 1.6.4 Coupled Trim Analysis

Control strategies of a twin cyclocopter at different steady state flight conditions (i.e. hover, forward flight) is developed. Base on that, a coupled trim analysis is carried out by simultaneously solving vehicle trim equations and blade response equations. This study is utilized to investigate effect of design parameters on control inputs of the vehicle.

## 1.7 Scope and Organization of Thesis

In the present chapter, a brief introduction to micro air vehicles or MAVs are provided. Although MAVs have significant potential applications in near future, the present MAVs based on conventional concepts are well short of desired performance in terms of endurance, agility and disturbance rejection capability. Challenges of present MAVs, specifically operation at low Reynolds number is discussed in detail. In the present thesis, cycloidal rotor based MAVs are proposed as an alternate solution. Towards this, thorough literature review of cycloidal rotor is carried out and advantages of this novel concept are explored. Finally specific issues crucial to the development of next generation cycloidal rotor based MAVs are addressed. In the existing literature, lack of accurate modeling tools of cycloidal rotor and cyclocopter is observed. The initial step towards building efficient cyclocopter is to develop an aeroelastic framework and coupled trim model of the vehicle which could be used for preliminary design and optimization, and this is the primary objective of the present dissertation. Technical challenges towards achieving these goals are addressed

and specific contribution of the thesis are listed. The remainder of the dissertation is organized into four chapters.

The $2^{nd}$ chapter discusses the detailed development of an unsteady aerodynamic model of an MAV scale cycloidal rotor, which is the first step towards modeling the entire vehicle. For this purpose, aerodynamics of a cycloidal rotor is investigated thoroughly and rigorous modeling of various underlying physical phenomena such as dynamic virtual camber, effects of near and shed wake, leading edge vortices are presented. After that, modeling of the complex inflow characteristics of cycloidal rotor is discussed. Initially, a lower order model based on modified double multiple streamtube (DMS) is developed. The systematic validation of the developed model with in-house experimental data of instantaneous forces produced by an MAV scale cycloidal rotor is presented. Once validated, the developed model is utilized to understand physics behind the force production of cycloidal rotor. Although the lower order model provides reasonable prediction of rotor performance, it cannot accurately capture the complex blade vortex interaction and the wake trajectory of cycloidal rotor. For this reason, high-fidelity free-wake based model of cycloidal rotor is developed which is shown to provide slightly better prediction compared to the lower order DMS model.

The $3^{rd}$ chapter discusses the detailed development of structural model of cycloidal rotor. Initially a $2^{nd}$ order nonlinear beam based model of cycloidal rotor is developed. Cycloidal rotor blade goes through large centrifugal load while being constrained at both ends which in turn results in large, nonlinear bending and torsional deflections. The $2^{nd}$ order nonlinear model is capable of predicting moderate deflection, but over-predicts the nonlinear deflections of cycloidal rotor blade. For this reason, a full nonlinear geometrically exact beam model of cycloidal rotor is developed. Next, validations of both the models with results from commercial software, Abaqus, are presented.

The $4^{th}$ chapter discusses the detailed development of vehicle response model of a twin cyclocopter which consists of modeling of individual rotors (cycloidal rotor and conventional nose rotor). The aeroelastic model of cycloidal rotor is developed by coupling the unsteady aerodynamic model with the structural framework. To further investigate the aeroelastic performance of

cycloidal rotor, experimental data utilizing moderately and highly flexible rotor blades are presented. Next, validation of aeroelastic model with these experimental data is presented. Once validated, the model is utilized to understand the effects of blade deflections on the performance of cycloidal rotor. On the other hand, a BEMT based aerodynamic model is developed to predict the performance of conventional nose rotor.

The $5^{th}$ chapter discusses coupled trim analysis of twin cyclocopter. The control strategy of the vehicle in hover and steady state forward flight is presented. After that, the development of the vehicle trim model at hover and forward flight is discussed. The trim model is coupled with the vehicle response model (developed in Chapter 4), to perform couple trim analysis. The validation of the developed model with in-house experiments is presented. Once validated, the model is utilized to understand the effect of different design parameters on control inputs required for vehicle trim and vehicle performance.

# 2. AERODYNAMIC MODELING OF CYCLOIDAL ROTOR*

## 2.1 Overview

In this chapter, development of an unsteady aerodynamic model of an MAV scale cycloidal rotor is discussed [99, 100, 101]. Large amplitude, high reduced frequency pitching motion of cycloidal rotor blades results in highly complex unsteady aerodynamics characterized by strong leading-edge vortex formation, nonlinear dynamic virtual camber effects, shed wake and blade-wake interactions. For accurate prediction of this complex physical system, detailed CFD modeling is necessary which is out of scope for the present application. The the main objective is to develop a computationally inexpensive model of a cycloidal rotor that could be utilized for design and optimization purposes. Therefore, a high fidelity lower-order model has been developed which can predict instantaneous blade aerodynamic forces and rotor performance (cycle-averaged thrust and power) with sufficient accuracy. Towards this, aerodynamics of a cycloidal rotor is investigated thoroughly and various underlying physical phenomena such as dynamic virtual camber, effects of near and shed wake, leading edge vortices are rigorously modeled. It is shown that the chord-wise variation of incidence velocity angle on cycloidal rotor blade is manifested as dynamic virtual camber, which depends on curvilinear flow geometry, pitch angle, pitch rate, inflow distribution and forward speed of vehicle. By including all these effects together, a generalized expression of additional lift due to virtual camber effect is developed. To capture the effects of near wake, a nonlinear lifting line model is incorporated. Rapid pitching of rotor blades produces unsteady phenomena such as strong leading edge vortices and shed wakes. Polhamus leading edge suction

*Part of the data reported in this chapter is reprinted with permission from "Unsteady Hydrodynamic Modeling of a Cycloidal Propeller" by Halder, A., Walther, C.M. and Benedict, M., *Fifth International Symposium on Marine Propulsion*, 2017 [99]; "Hydrodynamic Modeling and Experimental Validation of a Cycloidal Propeller" by Halder, A., Walther, C. M. and Benedict, M., *Ocean Engineering*, Vol. 154, 15 April 2018, Pages 94-105 [100]; "Nonlinear Aeroelastic Modeling of Cycloidal Rotor in Forward Flight" by Halder, A., and Benedict, M., *Proceedings of the AHS Technical Meeting on Aeromechanics Design for Transformative Vertical Lift*, 2018 [101] and "Free-wake Based Nonlinear Aeroelastic Modeling of Cycloidal Rotor" by Halder, A. and Benedict, M., *AIAA Aviation 2019 Forum*, 2019 [102].

analogy is applied to model leading edge vortex. To capture effects of shed wake, a method based on Theodorsen's approach has been developed. In this step, detailed Fourier analysis is carried out to properly calculate unsteady forces due to high frequency lift components, which mainly arise due to nonlinear virtual camber effects. A modified Double Multiple Streamtube (D-MS) model is used for modeling the complex inflow characteristics of a cycloidal rotor. All these detailed modeling helped the aerodynamic model to systematically validate with not only time averaged forces, but also time-history of aerodynamic forces obtained from in-house experiments at low Reynolds numbers.

Once validated, the model is utilized to understand several phenomena behind the force production of cycloidal rotor. It is observed the dynamic nature of virtual camber plays a significant role in this aspect. Dynamic virtual camber due to pitch rate creates asymmetry in side force between the right and the left halves, which in turn causes net time averaged side force on a cycloidal propeller in hover even with zero phase offset. Moreover, it is found extremely crucial for a cycloidal rotor to rotate in opposite direction (back-spin) with respect to the incoming flow in order to produce a upward vertical force in forward flight. In forward flight, a back-spinning cycloidal rotor experiences negative virtual camber near top of the cycle generating a small negative vertical force (retreating side), while it experiences positive virtual camber near bottom of the cycle generating a large positive vertical force (advancing side). This phenomena lead to net positive vertical force over a complete cycle. On the other hand, if the cycloidal rotor rotates in forward direction with respect to incoming flow (forward-spin) in forward flight, it would produce same amount of vertical force in downward direction since the top portion of cycle becomes advancing side producing large downward force and bottom portion becomes retreating side producing small upward force. These phenomena are explained in detail in later sections.

Although the above mentioned lower order model is computationally inexpensive and capable of predicting rotor performance with sufficient accuracy, it can not capture the complex flowfield of cycloidal rotor with extreme accuracy. Specifically, it is extremely challenging to the capture the complex inflow distribution, blade vortex interaction and geometry of trailing vortices

using a lower order model. For this reason, a high-fidelity model of cycloidal rotor based on free-wake is developed to further investigate aerodynamics of cycloidal rotor in more detail [102]. The wake model consists of multiple trailing vortices at near wake and only two trailing vortices in the far wake which are basically tip vortices. Moreover, there exists shed wake along the span of the blade which is generated and shed due to cyclic pitching of rotor blade. Initially a wake geometry is prescribed based on uniform inflow solution. Then, induced velocities are obtained on blade and wake locations using Biot-Savart law. Based on induced velocities wakes are convected and bound circulation of blades are updated. This procedure is continued until wake shape and bound circulation converges. The prediction of the developed free wake model shows even better correlation with in-house experimental data compared to that of the lower order model.

## 2.2 Aerodynamic Model in Hover

In this section, detail development and systematic experimental validation of a lower order aerodynamic model of cycloidal rotor in hover condition is discussed. Due to high reduced frequency and large amplitude pitching motion, cycloidal rotor blades results in highly complex unsteady aerodynamics characterized by strong dynamic-stall/leading-edge vortex formation, nonlinear dynamic virtual camber effects, shed wake and blade-wake interactions which makes it extremely challenging to develop with a lower order model. In the present study, aerodynamics of cycloidal rotor is investigated thoroughly and the underlying physical phenomena behind cycloidal rotor operation are rigorously modeled.

### 2.2.1 Modeling Methodology: Hover Model

A flow-chart of the developed aerodynamic model is shown in the Fig. 2.1. The first step in the proposed aerodynamic model is to compute the magnitude and incident angle of the resultant flow velocity at each local chord-wise location of cycloidal rotor blade. For this purpose, blade speed is obtained from prescribed kinematics and flow speed is obtained from inflow information. Chord-wise variation of incident flow angle is manifested as virtual camber effect which is discussed in detail in the subsequent sections. Once sectional angle of attack is obtained, sectional quasi-steady

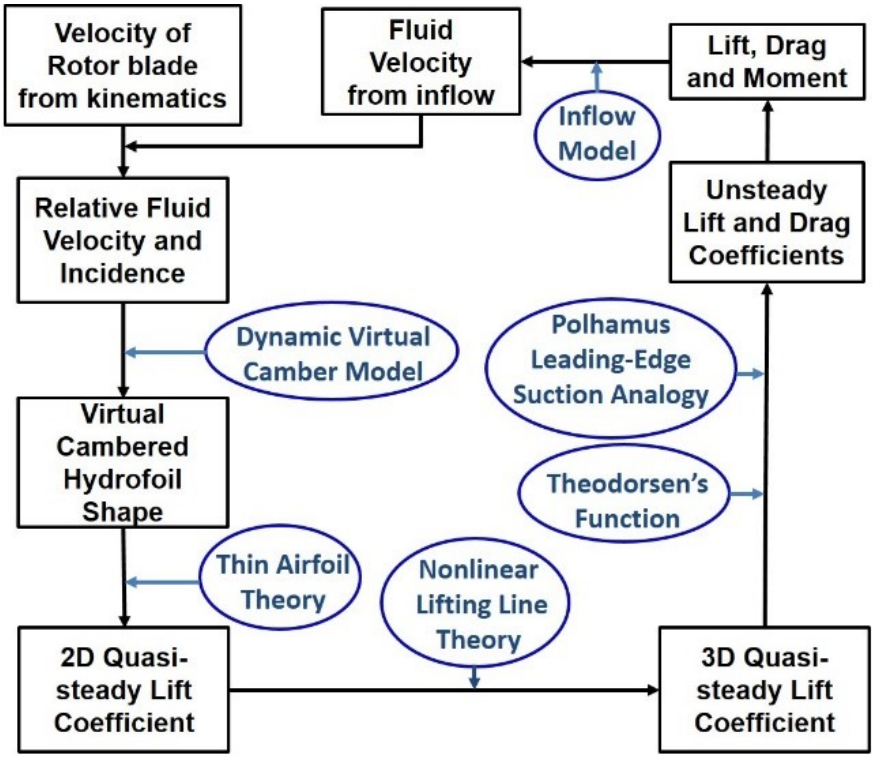


Figure 2.1: Flow chart of Aerodynamic Hover Model.

lift coefficients are computed from virtual shape of the airfoil using modified thin-airfoil theory. Small angle of attack assumption of thin-airfoil theory is not applicable to cycloidal rotor blades with large pitch amplitudes. This unrealistic assumption is relaxed while computing quasi-steady forces. In the next step, a non-linear lifting line model is developed to determine 3D aerodynamic forces. Rapid pitching of rotor blades create unsteady phenomena such as leading edge vortex and shed wake. Polhamus leading edge suction analogy is implemented to model additional vortex lift and vortex drag due to leading edge vortex. To capture effects of shed wake, a method based on Theodorsen's approach is implemented. During this procedure, Fourier analysis is carried out to account for high frequency force components, mainly arriving due to nonlinear virtual camber. All these modeling leads to unsteady force produced by cycloidal rotor blade. From the aerodynamic forces, inflow velocity is computed using proper inflow model. For inflow, a modified double multiple stream model (D-MS) is developed which relaxes some unrealistic assumptions of traditional D-MS model and uniform inflow model. Once inflow is obtained, the above mentioned cycle is

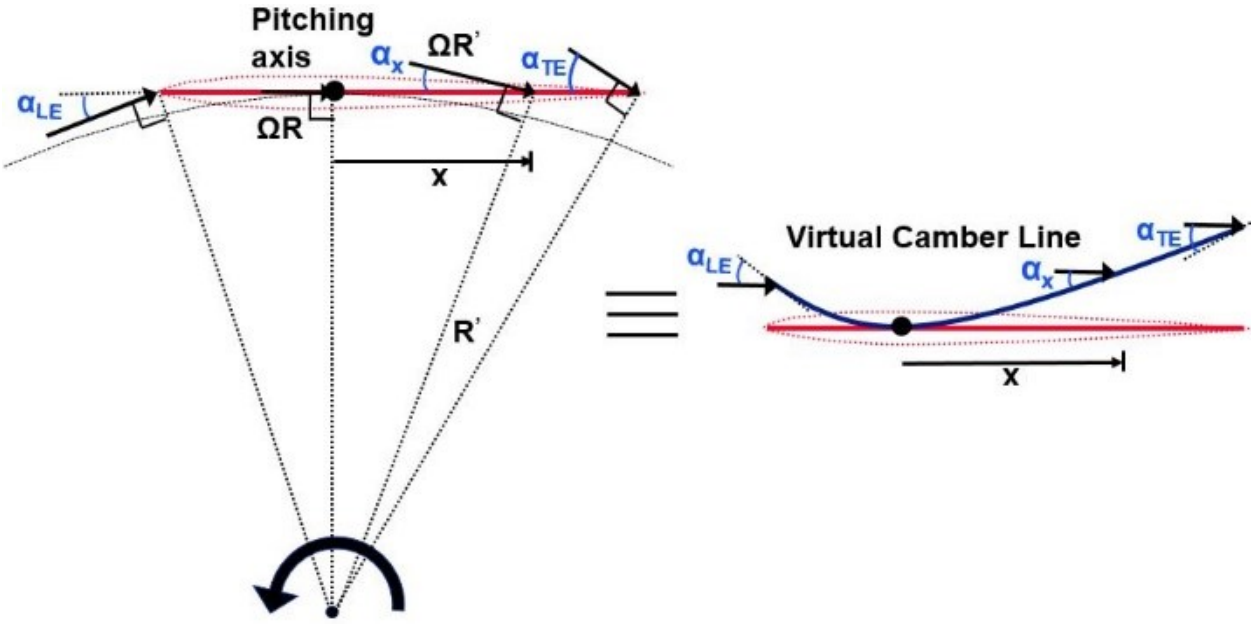


Figure 2.2: Negative virtual camber effect due to curvilinear flow.

repeated again in an iterative manner until both inflow and circulation converges together.

#### *2.2.1.1 Virtual Camber*

The cycloidal rotor blades experience a unique phenomenon known as virtual camber. A symmetric airfoil in straight flow experiences same incident velocity angle (angle of attack) at different chord-wise locations. On the other hand, a cambered airfoil in a straight flow experiences different incident velocity angle at different chord-wise locations. Similarly, when a symmetric airfoil experiences variation of incident angle of attack along different chord locations, it manifests as an effective camber, which is known as virtual camber effect (symmetric airfoil behaving as cambered airfoil). This virtual camber effect is very predominant in cycloidal rotors because the flow over a cycloidal rotor blade is characterized by a pitching airfoil in a curvilinear flow in the presence of inflow that varies along with azimuth. A airfoil in a curvilinear flow experiences different flow velocity magnitude and direction along the chord due to geometry and the curvilinear nature of the flow; this manifests as an effective camber and incidence. Figure 2.2 shows how curvilinear flow geometry creates a negative virtual camber effect for a blade at $0^\circ$ pitch angle. The left side of

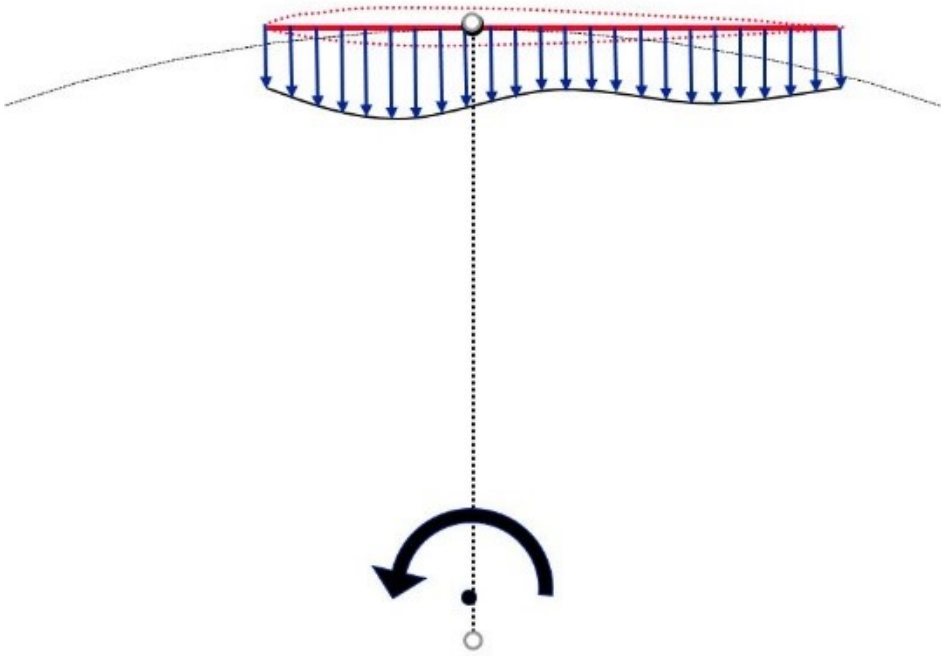

Figure 2.3: Chord-wise variation of flow velocity due to inflow distribution.

the figure shows that a symmetric airfoil on a curvilinear flow would experience a positive incident angle of attack ($\alpha_{LE}$) at the leading edge of the blade, while it would experience a negative incident angle of attack ($\alpha_{TE}$) at the trailing edge of the blade and incident angle is zero at pitching axis. The incident angle of attack at some other chord-location ($\alpha_x$) would be something different based on chord location, $x$. Right side of the figure shows that negative cambered airfoil immersed in a straight flow would experience similar variation of local incident angle of attack along its chord-wise locations. Therefore, a symmetric blade immersed in a curvilinear flow will behave like a cambered blade in a rectilinear flow as shown in Fig. 2.2 . This phenomenon is more significant for cycloidal rotors with a large chord-to-radius ratio (c/R) since it increases curvature of the flow. The local incident angle on cycloidal rotor blade depends on the parameter $R'$ which in turn depends on pitch angle of cycloidal rotor blade. Thus, virtual camber also depends on the pitch angle of cycloidal rotor blade. In case of cycloidal rotor, blade pitch changes cyclically as the blade goes through different azimuth location. Therefore, the virtual camber also changes cyclically making it a dynamic virtual camber effect.

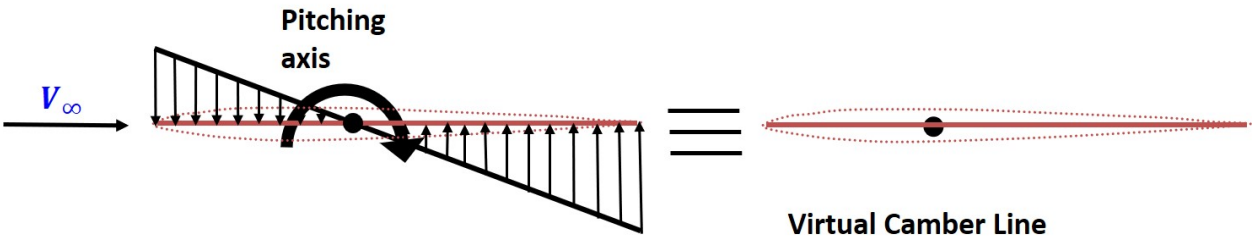


(a) Positive virtual camber effect due to pitch up motion.

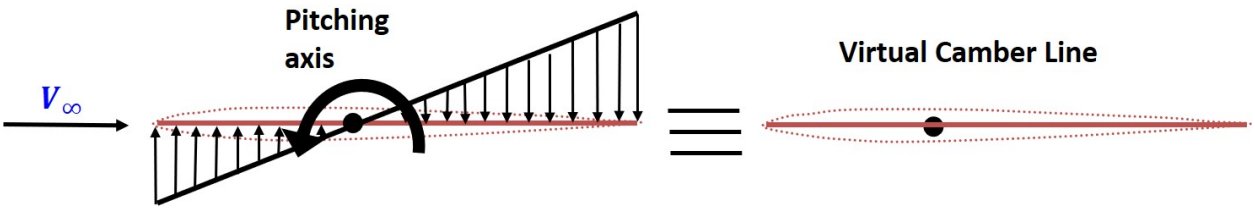


(b) Negative virtual camber effect due to pitch down motion.

Figure 2.4: Effect of pitch rate on virtual camber.

On the other hand, flow over a cycloidal rotor is not purely curvilinear. Thrust production of cycloidal rotor induces an inflow velocity opposite to the direction of thrust. Distribution of this inflow velocity (shown in Fig. 2.3) changes local variation of incident angle of attack along chord-wise direction, which in turn alters virtual camber effect.

Additionally, the blade pitch rate also affects the chord-wise variation of local incident angle of attack and therefore, alters virtual camber. An airfoil in an pitch-up moment would experience a negative incident angle of attack at leading edge, zero incident angle of attack at pitching axis and a positive incident angle of attack at trailing edge of the rotor blade. This is manifested as positive virtual camber effect as observed in Fig. 2.4a. Similarly, an opposite pitch rate (nose-down pitch) would cause a negative virtual camber effect (Fig. 2.4b). The pitch rate of cycloidal rotor blade also varies cyclically. Thus virtual camber effect due to pitch-rate of rotor blade would also vary in a cyclic manner. By considering all these effects together (effects of curvilinear geometry, inflow distribution, pitch and pitch-rate), a generalized expression has been derived to represent the variation of local incident angle of attack ($\alpha_x$) along the blade chord.

All the velocity components of fluid relative to rotor blade is shown in Fig. 2.5. The velocity

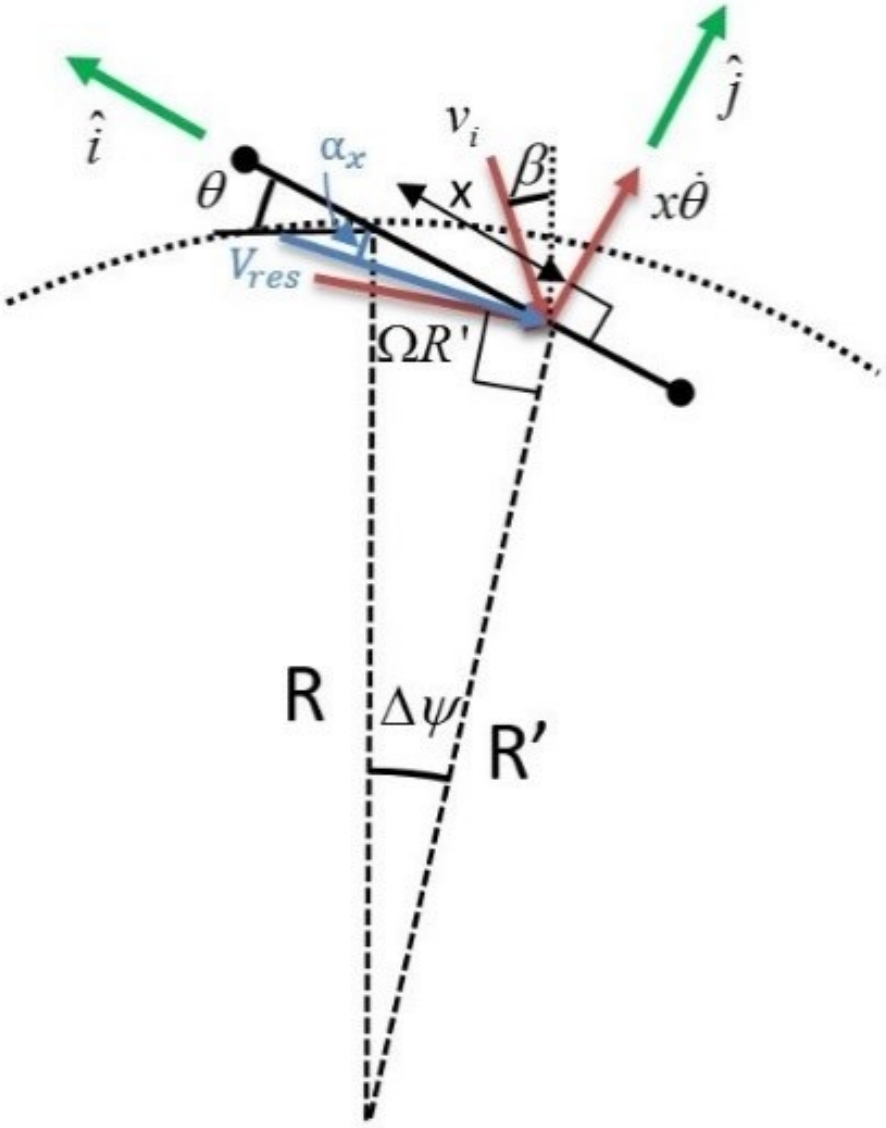


Figure 2.5: Velocity components at a local chord location on cycloidal rotor blade.

components are computed along tangential ($\hat{i}$) and normal ($\hat{j}$) to blade chord. Blade velocity ($\vec{V_b}$) at chord-wise location $x$ from pitching axis is obtained from prescribed kinematics of blade and can be expressed as following equation.

$$\vec{V_b}(x) = \Omega R' \cos(\theta - \Delta\psi)\ \hat{i} - \Omega R' \sin(\theta - \Delta\psi)\ \hat{j} \tag{2.1}$$

In the above equation, $\theta$ is geometric pitch angle of cycloidal rotor blade, $\psi$ is azimuth location of the blade in a cycle, $\Omega$ is rotational speed of rotor, $R'(x)$ is distance of local chord location ($x$) from center of cycloidal rotor. Using geometrical relations, blade velocity can be rewritten as following expression.

$$\vec{V_b}(x) = \Omega R \cos\theta\ \hat{i} - \Omega(R \sin\theta - x)\ \hat{j} \tag{2.2}$$

In the above equation, $R$ is the radius of cycloidal rotor. Flow velocity ($\vec{V_p}$) relative to rotor blade due to blade pitching is given as following.

$$\vec{V_p}(x) = x\dot{\theta}\ \hat{j} \tag{2.3}$$

The inflow speed is represented as $v_i(x)$ acting on rotor blade at an angle $\beta(x)$ w.r.t vertical axis. Thus, inflow velocity ($\vec{V_i}$) can be expressed as following.

$$\vec{V_i}(x) = -(v_i \sin(\beta + \theta)\ \hat{i} + v_i \cos(\beta + \theta)\ \hat{j}) \tag{2.4}$$

Considering all the velocity components described above, the net relative flow velocity ($\vec{V}$) with respect to rotor blade is calculated.

$$\vec{V}(x) = \vec{V_p}(x) + \vec{V_i}(x) - \vec{V_b}(x) \tag{2.5}$$

Substituting, Eqs. 2.2, 2.3 and 2.4 into Eq. 2.5, the net flow velocity can be expressed as following

equation.

$$\vec{V}(x) = -U_T\,\hat{i} - U_P\,\hat{j} \tag{2.6}$$

Where,

$$U_T = \Omega R\cos\theta + v_i\sin(\beta+\theta) \tag{2.7}$$

$$U_P = x(\Omega - \dot{\theta}) - \Omega R\sin\theta + v_i\cos(\beta+\theta) \tag{2.8}$$

This information all together gives net flow speed ($V(x)$) and incident angle of attack ($\alpha_x(x)$) at each local chord-wise location of the cycloidal rotor blade.

$$V(x) = \sqrt{U_T^2 + U_P^2} \tag{2.9}$$

$$\alpha_x = -\tan^{-1}\left(\frac{x(\Omega-\dot{\theta}) + v_i\cos(\beta-\theta) - \Omega R\sin\theta}{\Omega R\cos\theta + v_i\sin(\beta+\theta)}\right) \tag{2.10}$$

In the above expression, $v_i$ is assumed to be zero for the first iteration and updated using inflow model (modified D-MS model, discussed later) for subsequent iterations. For a cambered airfoil in straight flow, the local angle of attack varies along chord according to following equation.

$$\alpha_x = \theta - \frac{dy}{dx}(x) \tag{2.11}$$

By comparing, Eq. 2.10 and Eq. 2.11, expression for virtual camber line of cycloidal rotor blade is computed.

$$\frac{dy}{dx}(x) = \theta + \tan^{-1}\left(\frac{x(\Omega-\dot{\theta}) + v_i\cos(\beta-\theta) - \Omega R\sin\theta}{\Omega R\cos\theta + v_i\sin(\beta+\theta)}\right) \tag{2.12}$$

#### *2.2.1.2 Quasi-Steady Force Computation*

Modified thin airfoil theory has been used to calculate quasi-steady lift from the chord-wise variation of incident angle of attack. For this purpose, airfoil co-ordinates are transformed along chord line. Figure 2.6 shows co-ordinate transformation from actual chord-line ($x$, $y$) to virtual chord-line ($X$, $Y$) and Equations 2.13 and 2.14 provide expressions for this co-ordinate transfor-

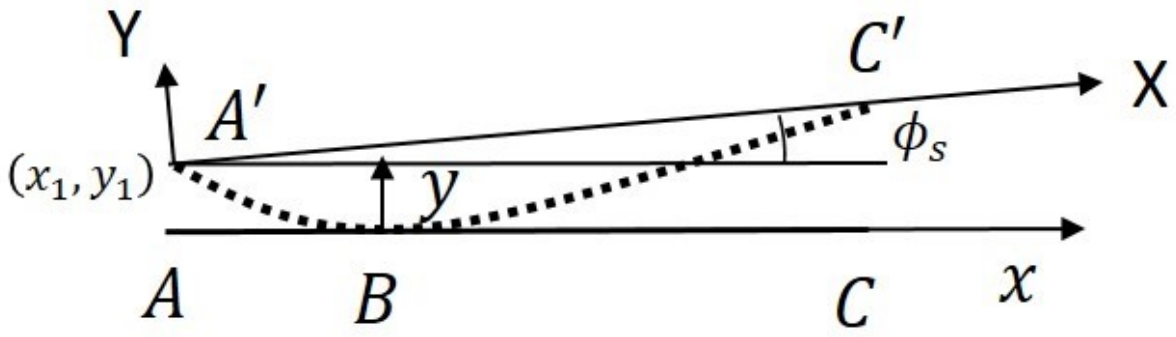


Figure 2.6: Co-ordinate transformation from physical airfoil co-ordinate to virtual cambered airfoil co-ordinate.

mation.

$$X = (y - y_1)\sin\phi + (x - x_1)\cos\phi \tag{2.13}$$

$$Y = (y - y_1)\cos\phi - (x - x_1)\sin\phi \tag{2.14}$$

One of the key assumptions of thin-airfoil theory is small angle of attack [15] which is not valid for cycloidal rotor blades. This is because the rotor blades go through large angles of attack due to higher operating pitch amplitude ($\sim$40°). For this reason, a modified thin-airfoil theory is derived by relaxing the small angle of attack assumption and a more general expression (Eq. 2.15) is developed.

$$C_L = K\sin\alpha + C_{L_0} \tag{2.15}$$

In the above equation, $K$ is a constant that represents lift-curve slope at small angle of attack, $C_{L_0}$ is additional lift due to the effects of virtual camber. $C_{L_0}$ is a complex function of incidence angle given by Eq. 2.16. In this equation, $dY/dX$ is computed from Eqs. 2.12, 2.13 and 2.14. $dY/dX$ represents slope of virtual camber line in transformed co-ordinate $X-Y$. Using numerical

integration procedure, $C_{L_0}$ is computed.

$$C_{L_0} = 2\cos\alpha \int_0^{\pi} \frac{dY}{dX}(\cos\eta - 1)d\eta \tag{2.16}$$

Where, $\eta$ is a non-dimensional parameter used for integration purposes. $\eta$ is chosen such that

$$x = \frac{c}{2}(1 - \cos\eta) \tag{2.17}$$

#### *2.2.1.3 Nonlinear Lifting Line Model*

A nonlinear lifting line theory [15] is implemented numerically to incorporate the effects of tip vortices in near wake region (finite-span effect). In this case, a linear geometry of trailing vortex lines is assumed. For this purpose, the wing is divided into number of span-wise elements. Nodal point is set to center of each element. Induced angle of attack at each nodal point is obtained using following expression (Eq. 2.18).

$$\alpha_i(y_0) = \frac{1}{4\pi V_\infty} \int_{-b/2}^{b/2} \frac{d\Gamma/dy}{y_0 - y} dy \tag{2.18}$$

Above integral is computed numerically using Gauss-quadrature integration rule. 11 Gauss quadrature points are used for this purpose. In the next step, effective angle of attack at each nodal point is computed using following expression.

$$\alpha_{eff}(y_0) = \alpha(y_0) - \alpha_i(y_0) \tag{2.19}$$

Effective angle of attack is used to calculate quasi-steady lift using Eq. 2.15. Circulation is computed at the center of each element from calculated lift, $L$ using following expression.

$$\Gamma(y_0) = \frac{L(y_0)}{\rho V_\infty} \tag{2.20}$$

For the first iteration, suitable values of circulation based on elliptical lift distribution are assumed and circulation is updated from lift calculated at each iteration until convergence is obtained. Circulation update law is given below

$$\Gamma_{new} = \Gamma_{old} + D(\Gamma_{new} - \Gamma_{old}) \tag{2.21}$$

Where, $D$ is an update parameter and suitably chosen for proper convergence ($0.05$ in present simulations).

#### *2.2.1.4 Shed Wake*

Cyclic pitching of rotor blade causes instantaneous changes in bound circulation which in-turn causes generation of shed-wake along blade span. To capture effect of shed wake, an unsteady model based on Theodorsen's approach has been developed [14]. Theodorsen's function has been originally developed to calculate circulatory lift produced by sinusoidal variation of angle of attack and pitch angle. Due to inclusion of virtual camber and its nonlinear behavior, the oscillatory part of the lift on a cycloidal rotor blade contains not just the first harmonic, rather it shows high frequency components with varying phase delays. To handle this, an automated function has been developed that would perform Fourier series decomposition of oscillatory part of lift (due to shed wake) and compute corresponding frequency and Theodorsen's function to generate unsteady lift. Fourier decomposition of quasi-steady lift coefficient can be expressed as following.

$$C_{L_{quasi\_steady}} = \frac{a_0}{2} + \sum_{i=1}^{n} a_n \cos i\Omega t + b_n \cos i\Omega t \tag{2.22}$$

First harmonic of quasi-steady lift coefficient $C_{L_{quasi\_steady}}$ is $\Omega$ and corresponding reduced frequency is $k_f = \frac{\Omega c}{2V}$. Theodorsen's function corresponding to higher harmonics are computed to calculate unsteady lift coefficient (Eq. 2.23).

$$C_{l_{unsteady}} = \frac{a_0}{2} + \sum_{i=1}^{n} (a_n \cos i\Omega t + b_n \cos i\Omega t) * C(ik_f) \tag{2.23}$$

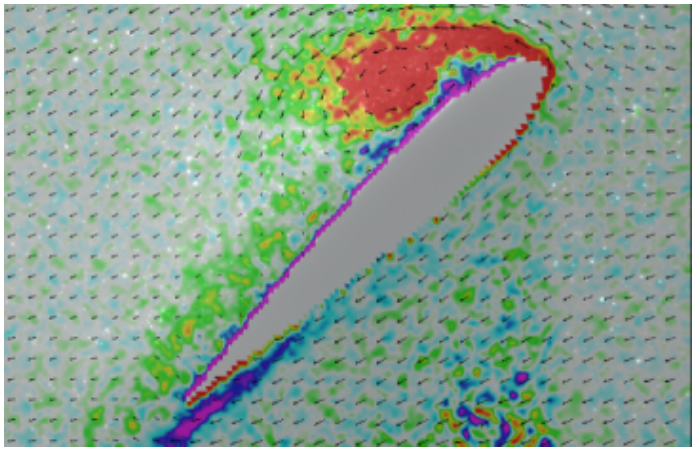

Figure 2.7: Formation of large leading-edge vortex from PIV measurements at pitch amplitude = $45°$ and azimuth = $90°$.

In the above equation, $C(ik_f) = F(ik_f) + jG(ik_f)$ is Theodorsen's function corresponding to reduced frequency $k = ik_f$, where $i$ varies from 1 to $n$.

#### *2.2.1.5 Leading-Edge Vortex*

High amplitude pitching of rotor blade creates strong leading-edge vortex on cycloidal rotor, as shown by some of the on-going in-house experimental studies [103]. Figure 2.7 shows PIV measured flow field showing large leading-edge vortex formation. Leading-edge vortex delays flow separation on rotor blade which significantly improves lift performance of rotor at high pitch angles enabling rotor to operate even at $45°$ pitch amplitudes. Polhamus leading-edge-suction analogy [104, 105] is applied to model leading-edge vortex. Additional lift (vortex lift) due to leading-edge vortex and additional drag due to leading-edge separation are modeled using this suction analogy.

$$C_{L_{LE}} = C_{L_{WLE}}(\cos^2\alpha + \eta \sin^2\alpha) + K_v \cos\alpha \sin^2\alpha \tag{2.24}$$

$$C_{D_{LE}} = C_{L_{WLE}} \sin\alpha \cos\alpha(1 - \eta_{LE}) + K_v \sin^3\alpha \tag{2.25}$$

In the above equations, $C_{L_{LE}}$ and $C_{D_{LE}}$ are lift and drag coefficient with leading edge suction and $C_{L_{WLE}}$ and $C_{D_{WLE}}$ are lift and drag coefficient without leading edge suction. $K_v$ is non-

dimensional coefficient related to additional vortex lift generated by leading edge vortex. $\eta_{LE}$ represents percentage of leading edge suction. $\eta_{LE} = 1$ means no leading edge suction and $\eta_{LE} = 0$ means complete leading edge suction.

#### *2.2.1.6 Force Computation*

Once lift and drag coefficients, $C_L$ and $C_D$, are computed, lift and drag force in blade co-ordinate system is obtained using lift, $L = \frac{1}{2}\rho\ V^2\ S\ C_L$ and drag, $D = \frac{1}{2}\rho\ V^2\ S\ C_D$. Forces in blade co-ordinate are transformed into inertial co-ordinate using proper transformation matrices. To calculate time-averaged rotor thrust, blade force is multiplied with solidity, $\sigma = \frac{N_b\ c}{2\pi R}$ and averaged over one revolution.

#### *2.2.1.7 Hover Inflow Model*

Previously in the analysis of cycloidal rotors and vertical axis wind turbines, Single Streamtube inflow or Double Multiple Streamtube (D-MS) models have been mostly used [98]. For Single Streamtube model, the inflow is considered uniform along the azimuth and inflow at top and bottom halves of the blade is assumed to be same. Therefore, no blade interaction or wake effect is considered after the flow passes through the upper-half. This assumption is not physical. On the other hand, for D-MS model, there is azimuthal variation in inflow magnitude, however, inflow direction is assumed to be radial to blade path in the upper half in the hover state, which is also not physically realistic.

In the present aerodynamic model (schematic shown in Fig. 2.8), the proposed inflow model (modified D-MS model) relaxes these assumptions. In this model, it is assumed that various streamlines interacts with the rotor blade twice, upstream and downstream, with different inflow velocity magnitude and direction. Two adjacent streamlines form a streamtube. Unlike D-MS model, this modified model calculates the inflow direction based on resultant force direction on the blade at that particular azimuthal location (Eq. 2.26). The underlying reasoning behind this approach is that at a local azimuthal location, whatever aerodynamic force the rotor blade experiences, it exerts same force to the nearby fluid in the opposite direction. When the rotor blade

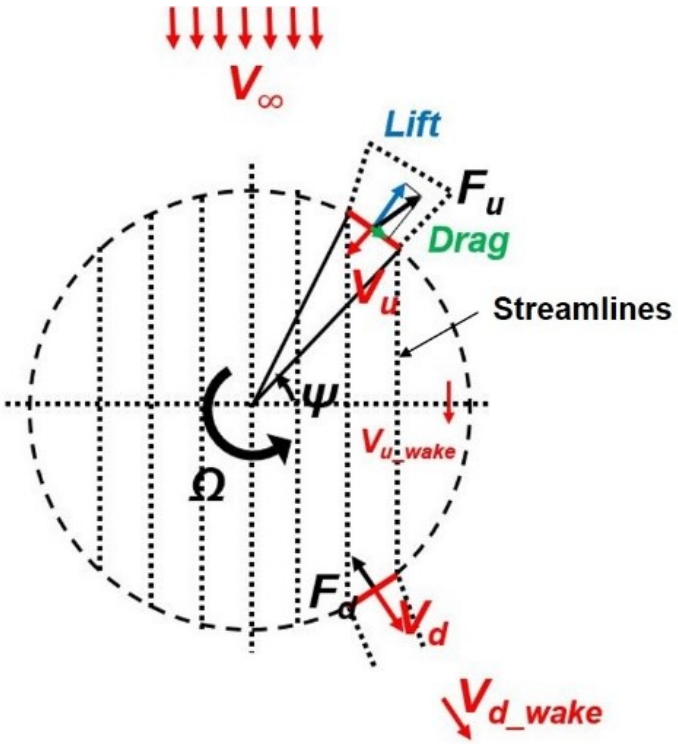


Figure 2.8: Schematic of inflow model.

starts rotating, it would accelerate nearby fluid opposite to the direction of resultant force blade is experiencing (Fig. 2.9).

$$\gamma_u = \pi - \phi - \tan^{-1}\left(\frac{D}{L}\right) \tag{2.26}$$

In Eq. 2.26, $\gamma_u$ is inflow angle at upstream locations, $\phi$ is the angle between local tangent and resultant flow velocity with respect to rotor blade (Fig. 2.9). Once the inflow direction is calculated based on above approach, actuator surface theory and mass and momentum conservation laws were applied to determine magnitude of inflow velocity at upstream ($V_u$) and downstream ($V_d$). The wake velocity of completely expanded flow after interacting with upstream blade is denoted as $V_{u_{wake}}$ and wake velocity after interacting with downstream blade is denoted as $V_{d_{wake}}$ . Using actuator surface theory, inflow velocities can be expressed as Eq. 2.27 and Eq. 2.28.

$$V_u(s) = \frac{1}{2}\left(V_\infty + V_{u_{wake}}(s)\right) \tag{2.27}$$

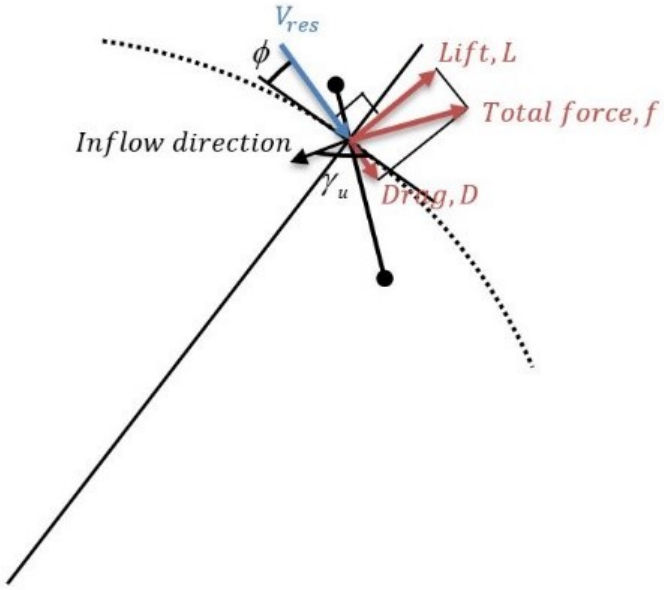


Figure 2.9: Computation of Inflow Direction.

$$V_d(s) = \frac{1}{2}\left(V_w(s) + V_{u_{wake}}(s)\right) \tag{2.28}$$

In the above equation, $s$ denotes position in the rotor disc arc and thus it is basically a function of azimuth. In the present context, subscript '$u$' stands for upstream and subscript '$d$' stands for downstream. Force exerted by fluid on the rotor blade on upstream ($F_u$) and downstream ($F_d$) can be expressed as Eq. 2.29 and Eq. 2.30, respectively.

$$F_u(s) = \dot{m}\left(V_\infty - V_{u_{wake}}(s)\right) \tag{2.29}$$

$$F_d(s) = \dot{m}\left(V_{u_{wake}}(s) - V_w(s)\right) \tag{2.30}$$

Where, $\dot{m}$ is the mass flow rate. Using continuity theory, above equations can be rewritten as Eq. 2.31 and Eq. 2.32.

$$F_u(s) = \rho V_u A \sin\gamma_u \left(V_\infty - V_{u_{wake}}(s)\right) \tag{2.31}$$

$$F_d(s) = \rho V_d A \sin\gamma_d \left(V_{u_{wake}}(s) - V_w(s)\right) \tag{2.32}$$

By comparing Eq. 2.27 and Eq. 2.31, upstream inflow velocity ($V_u$) and upstream wake velocity ($V_{u_{wake}}$) can be obtained (Eq. 2.33 and Eq. 2.34).

$$V_u(s) = \frac{V_\infty}{2} + \sqrt{\frac{V_\infty^2}{4} - \frac{f_u(s)}{2\rho \sin\gamma_u(s)}} \tag{2.33}$$

$$V_{u_{wake}}(s) = V_\infty - \frac{f_u(s)}{\rho V_u(s) \sin\gamma_u(s)} \tag{2.34}$$

In the above equations, $f$ is force per unit area along the direction of flow ($f_u = F_u/A$ and $f_d = F_d/A$). In the similar procedure, downstream inflow velocity ($V_d$) and downstream wake velocity ($V_{u_{wake}}$) can be obtained (Eq. 2.35 and Eq. 2.36) by comparing Eq. 2.28 and Eq. 2.32.

$$V_d(s) = \frac{V_{u_{wake}}(s)}{2} + \sqrt{\frac{V_{u_{wake}}(s)^2}{4} - \frac{f_d(s)}{2\rho \sin\gamma_d(s)}} \tag{2.35}$$

$$V_{d_{wake}}(s) = V_{u_{wake}}(s) - \frac{f_d(s)}{\rho V_d(s) \sin\gamma_d(s)} \tag{2.36}$$

Once, the inflow is updated using above equations (Eq. 2.33-2.36), aerodynamic forces are calculated based on new inflow and circulation. These steps are repeated until both circulation and inflow are converged.

### 2.2.2 Experimental Validation: Hover Aerodynamic Model

Due to the dearth of experimental data in the present literature on time-history of aerodynamic forces on cycloidal rotor blade, in-house experiments were carried out and the present aerodynamic model is validated with the results obtained from these experiments.

#### *2.2.2.1 Experimental Setup*

For model validation, a test setup (Fig. 2.10) is developed where a single bladed cycloidal rotor is tested inside a water tank at a Reynolds number of around 18,000. Forces and moments are measured using a miniature 6-component force balance at the blade root. A 12-channel slip ring is used to transfer the signals from the force balance in the rotating frame to the data acquisition

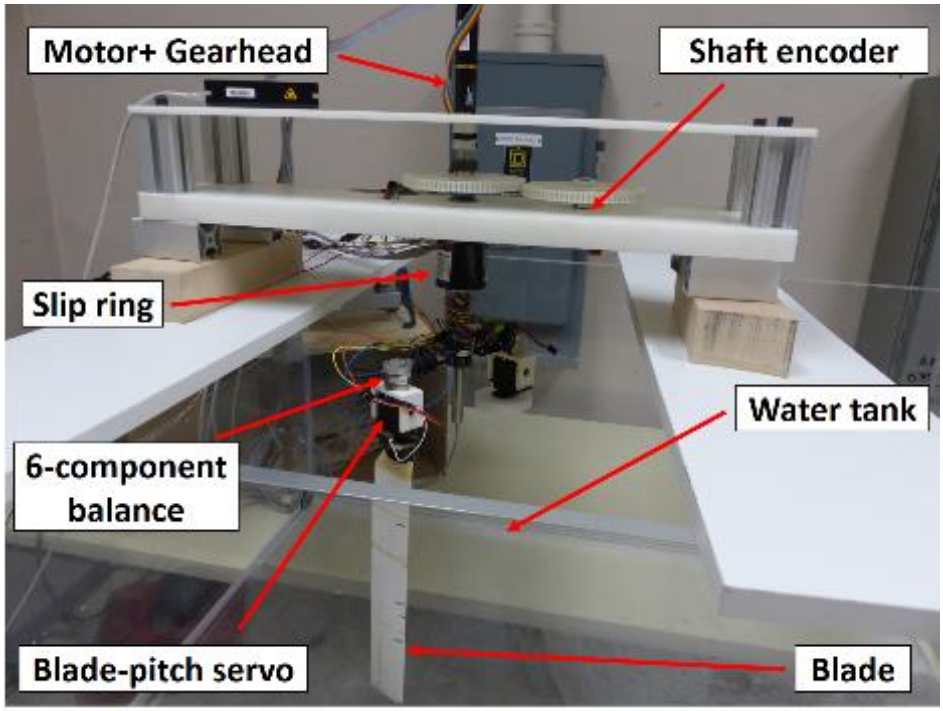


Figure 2.10: Single-bladed cycloidal rotor test rig in water tank.

equipment in the stationary frame. The blade pitching is controlled using an analog servo, which allows us to prescribe specific pitching kinematics for a test. The experiments are first conducted in air which provide the inertial forces; then the same experiments are repeated in water. The pure aerodynamic forces are obtained by subtracting the inertial forces from the force measurements made in water.

#### *2.2.2.2 Hover Validation Results*

Dynamic pitching experiments are conducted with a single bladed cycloidal rotor at $40$ rpm. rotor blade has chord of 2 inches and span of 12 inches and pitched at quarter chord location. Radius of cycloidal rotor is 3.43 inches. Figures 2.11 and 2.12, respectively, show the comparison between measured forces and predictions from the present aerodynamic model. The figures show the variation of radial and tangential force coefficients as a function of blade azimuthal location over a range of pitch amplitudes ($20°$ to $45°$). The results show overall reasonable correlation between the present aerodynamic model prediction and test data. It is also interesting to see both

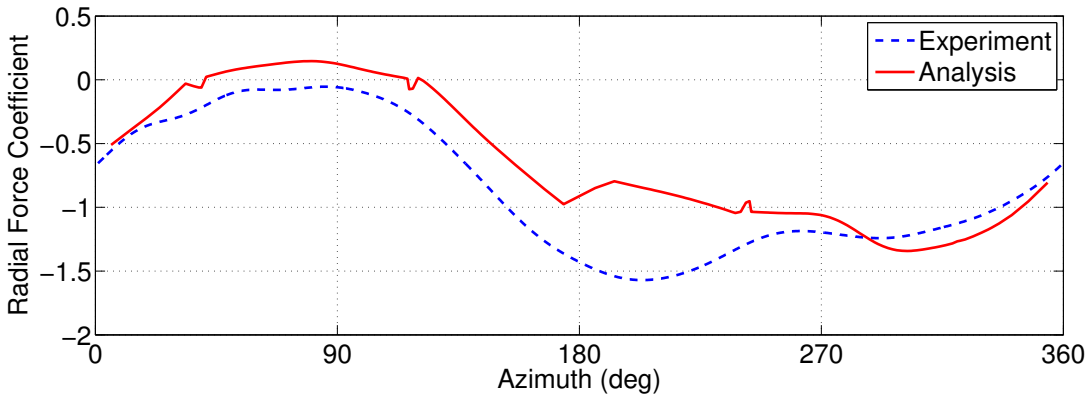


(a) Pitch Amplitude 20°.

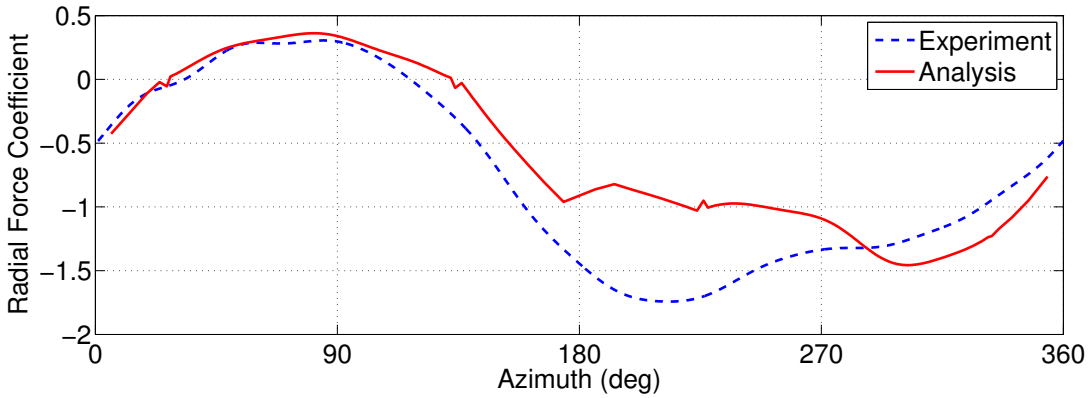


(b) Pitch Amplitude 25°.

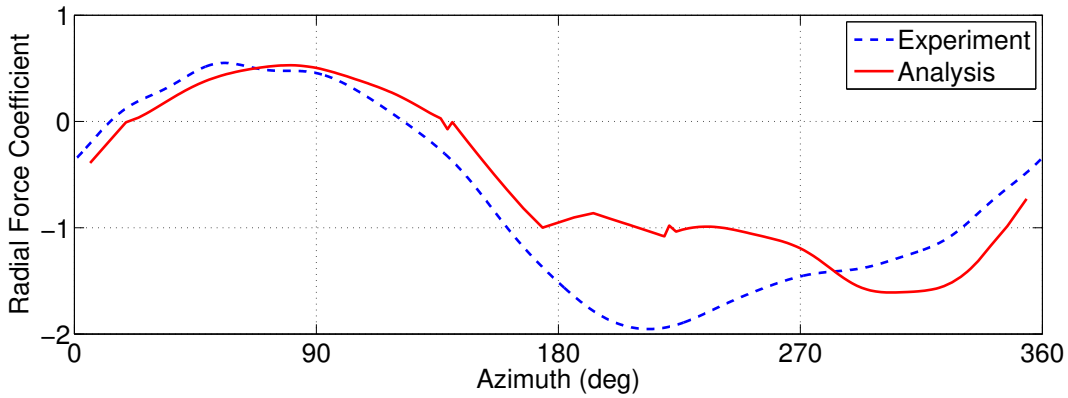


(c) Pitch Amplitude 30°.

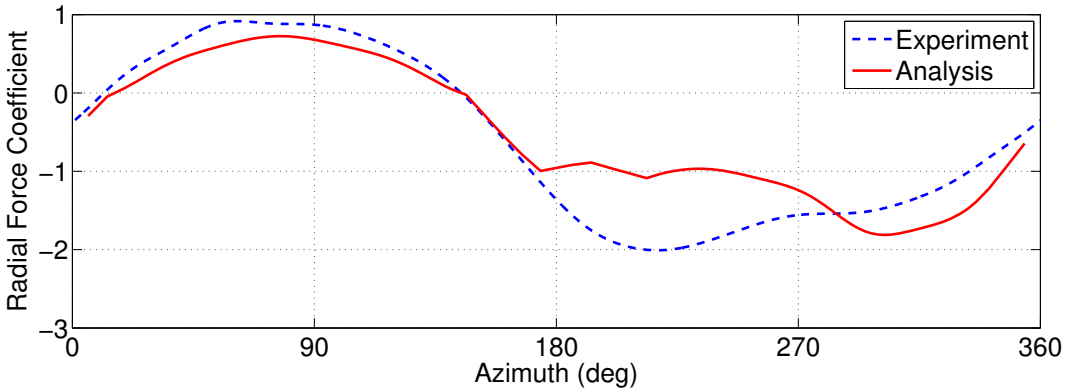


(d) Pitch Amplitude $35°$.

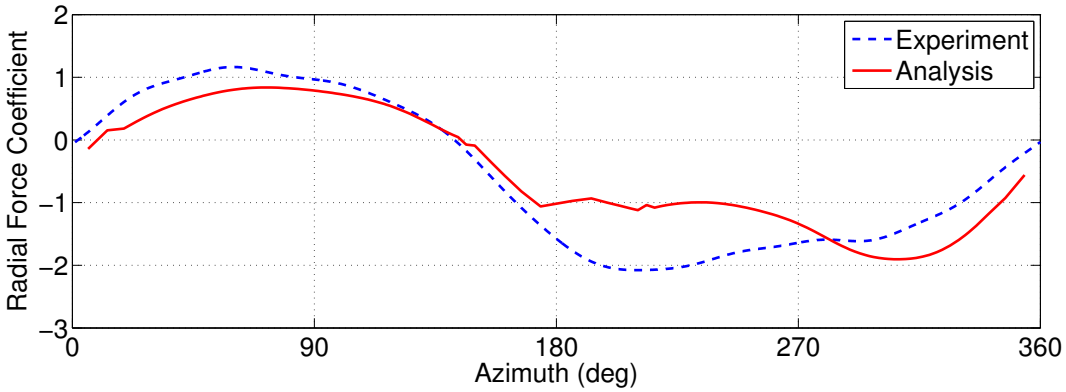


(e) Pitch Amplitude $40°$.

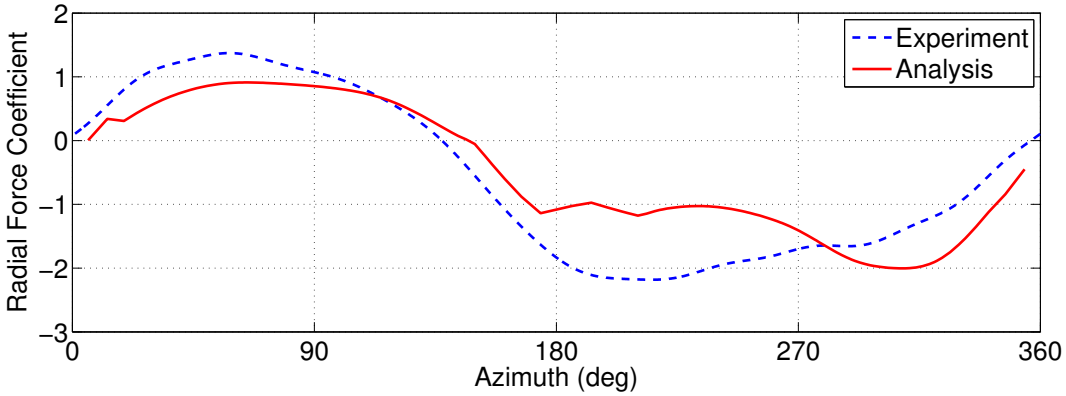


(f) Pitch Amplitude $45°$.

Figure 2.11: Radial force coefficient as a function of azimuth (Experiment vs. Analysis).

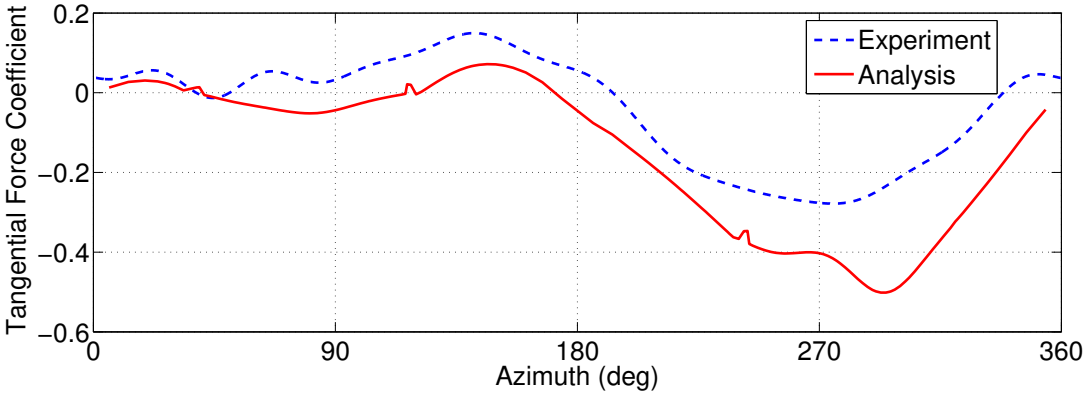


(a) Pitch Amplitude 20°.

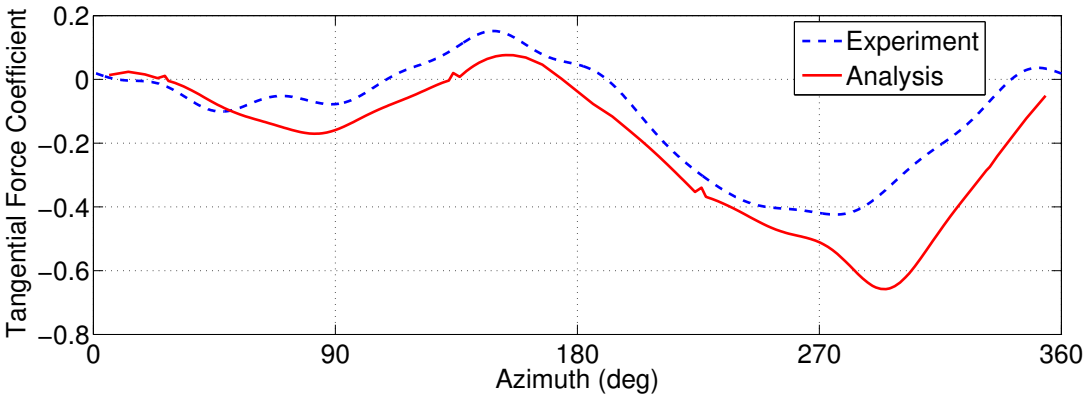


(b) Pitch Amplitude 25°.

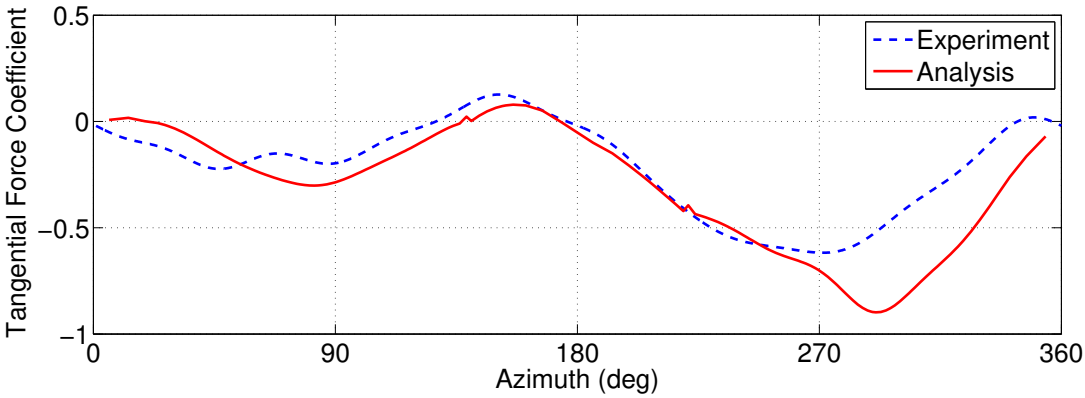


(c) Pitch Amplitude 30°.

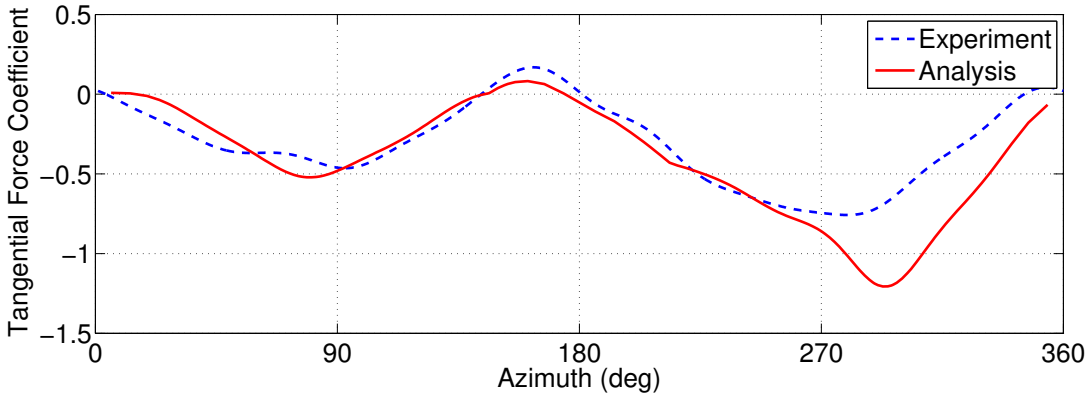


(d) Pitch Amplitude $35°$.

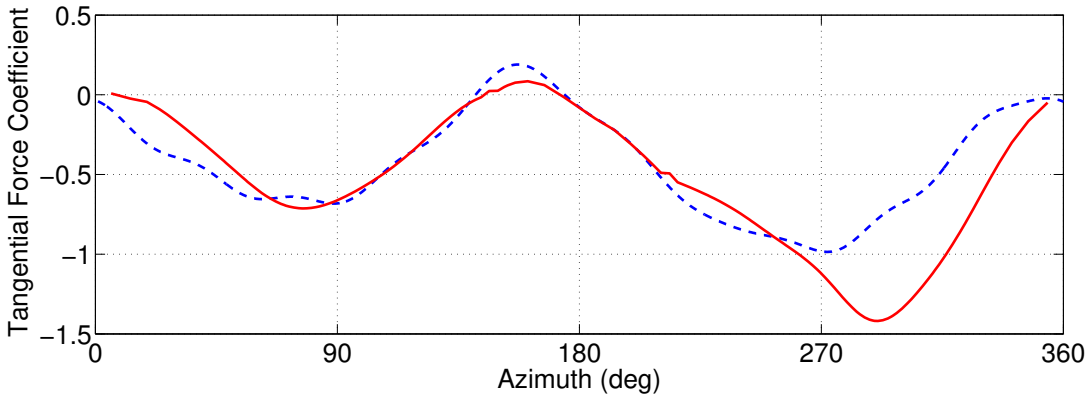


(e) Pitch Amplitude $40°$.

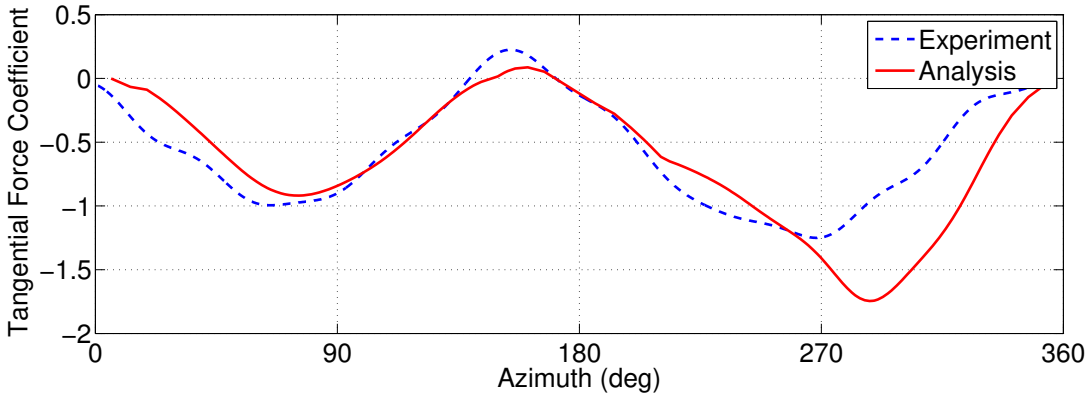


(f) Pitch Amplitude $45°$.

Figure 2.12: Tangential force coefficient as a function of azimuth (Experiment vs. Analysis).

from the experiment and analysis that the blades are producing higher radial and tangential forces at the lower half ($\psi = 180° - 360°$) than the upper half ($\psi = 0° - 180°$). The reason for this will be explained in the discussion section.

### 2.2.3 Discussion: Physics of Force Production in Hover

Once the aerodynamic model is validated with in-house experimental data, it is used to investigate physics behind thrust production of a cycloidal rotor. In the following subsections details of various phenomena are discussed in depth.

#### *2.2.3.1 Cause and Effect of Dynamic Virtual Camber*

As shown by Eq. 2.16, virtual camber manifests as additional lift on the blade. Figure 2.13a shows variation of additional lift coefficient ($C_{L_0}$) due to virtual camber along azimuthal location for a cycloidal rotor blade rotating at $40$ rpm with $35°$ pitch amplitude. Figures 2.13b and 2.13c show corresponding prescribed pitch and pitch rate (measured values), respectively, as blade goes through various azimuthal locations. It shows effects of curvilinear flow, pitch, pitch-rate and inflow on virtual camber and therefore, on additional lift. From Fig. 2.13a it can be observed that virtual camber effect due to only curvilinear geometry (magenta line) is static in nature and it always causes negative virtual camber leading to negative $C_{L_0}$. While pitch, pitch rate and inflow creates time-dependency of virtual camber effect making it a dynamic virtual camber. Figure 2.13a reveals that pitch and especially pitch rate creates a very dominant and characteristic virtual camber effect unlike inflow distribution which is more random in nature.

Figure 2.13a shows that blade pitch decreases negative virtual camber and opposes the effects of curvilinear geometry. The effect of blade pitch is more prominent near $90°$ and $270°$ azimuth since pitch angle reaches at its peak at those locations (Fig. 2.13b). It is also observed that pitch rate creates positive virtual camber effect near $0°$ azimuth, which almost nullifies the effects of curvilinear geometry; while at $180°$, it creates negative virtual camber which together with curvilinear effect produces even larger negative lift. For this reason, as seen from Fig. 2.11, the net radial force coefficient is near zero at $0°$ azimuth, while it is much below zero at $180°$ azimuth,

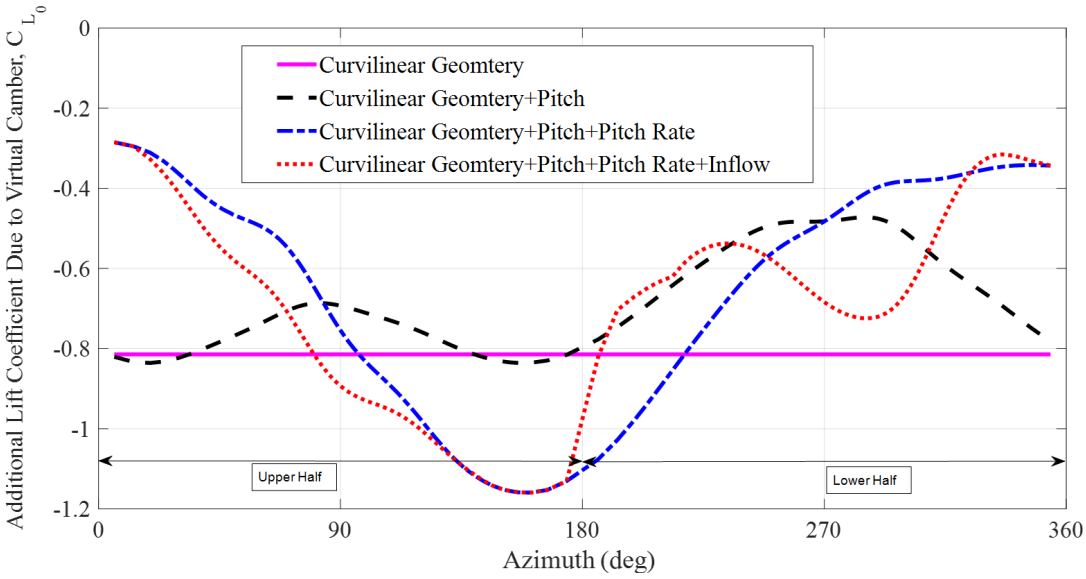


(a) Variation of additional lift coefficient due to virtual camber.

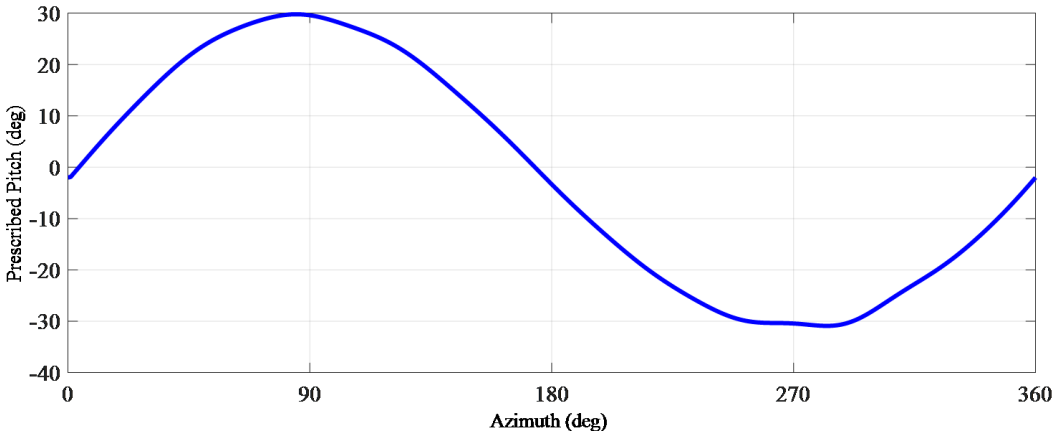


(b) Measured blade pitch along azimuth.

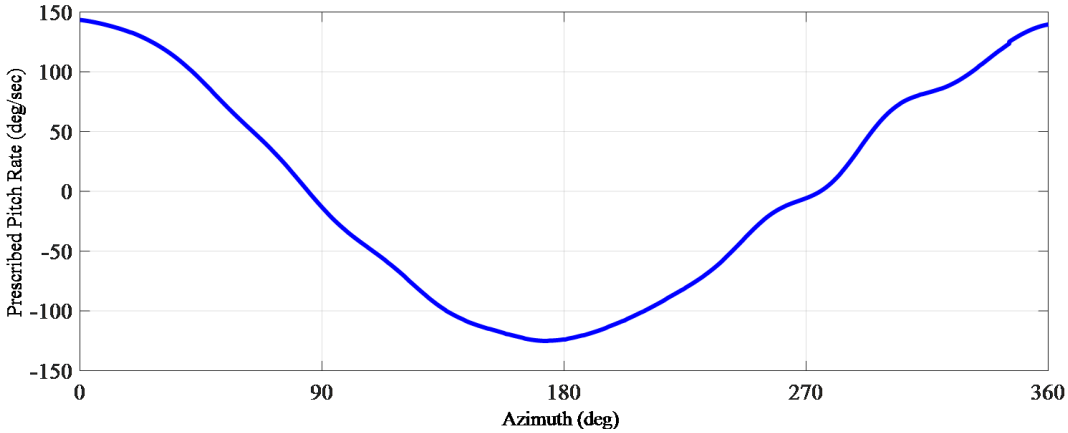


(c) Measured pitch rate along azimuth.

Figure 2.13: Effect of Virtual Camber due to various phenomena.

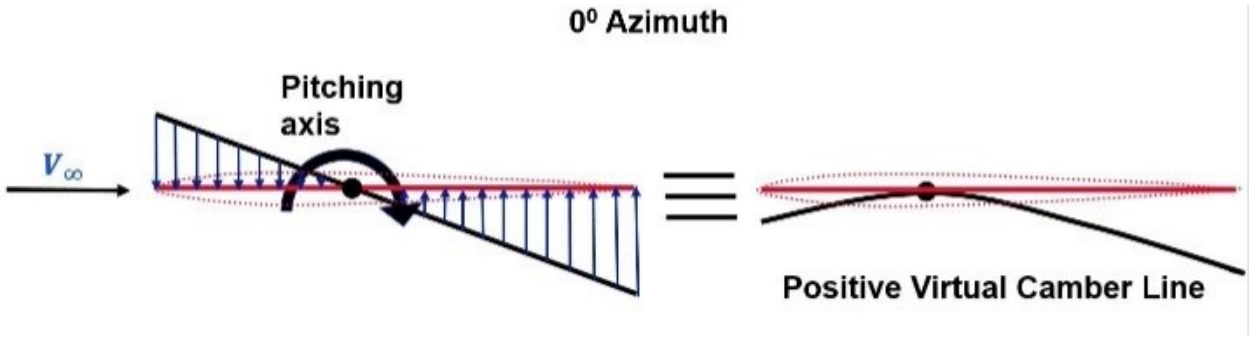


(a) Pitch rate effect at $0°$ azimuth.

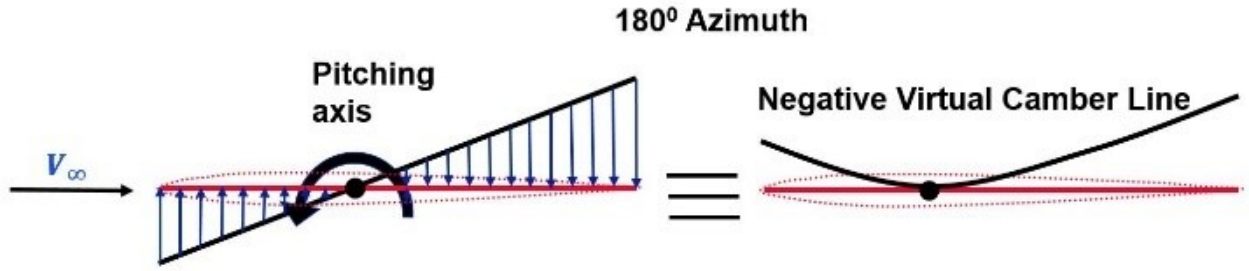


(b) Pitch rate effect at $180°$ azimuth.

Figure 2.14: Effect of Pitch rate on dynamic virtual camber at two extreme azimuthal locations ($0°$ and $180°$).

although pitch angle is near $0°$ at both azimuth locations (Fig. 2.13b). Pitch rate effect on virtual camber is dominant at $0°$ and $180°$ azimuth because pitch rate reaches its peak near these two locations (Fig. 2.13c). Figure 2.14 shows graphically how pitch rate is creating opposite virtual camber effects at different azimuth locations.

This phenomenon is clearly observed in Fig. 2.15. Figure 2.15 shows the actual chord-line of cycloidal rotor blade and virtual chord-line due to virtual camber effect along different azimuth locations. It can be observed again at $0°$ azimuth, virtual camber is minimum producing almost negligible negative lift while at $180°$ azimuth it has huge negative virtual camber producing large negative lift. Moreover, viewing from inertial reference frame, it can be observed from Fig. 2.15 that there is significant negative virtual camber when the blade operates in the upper half, which causes flow to separate very early. While, in the entire lower half, it creates a positive virtual camber, which delays flow separation and blade can attain much higher lift at these locations. More-

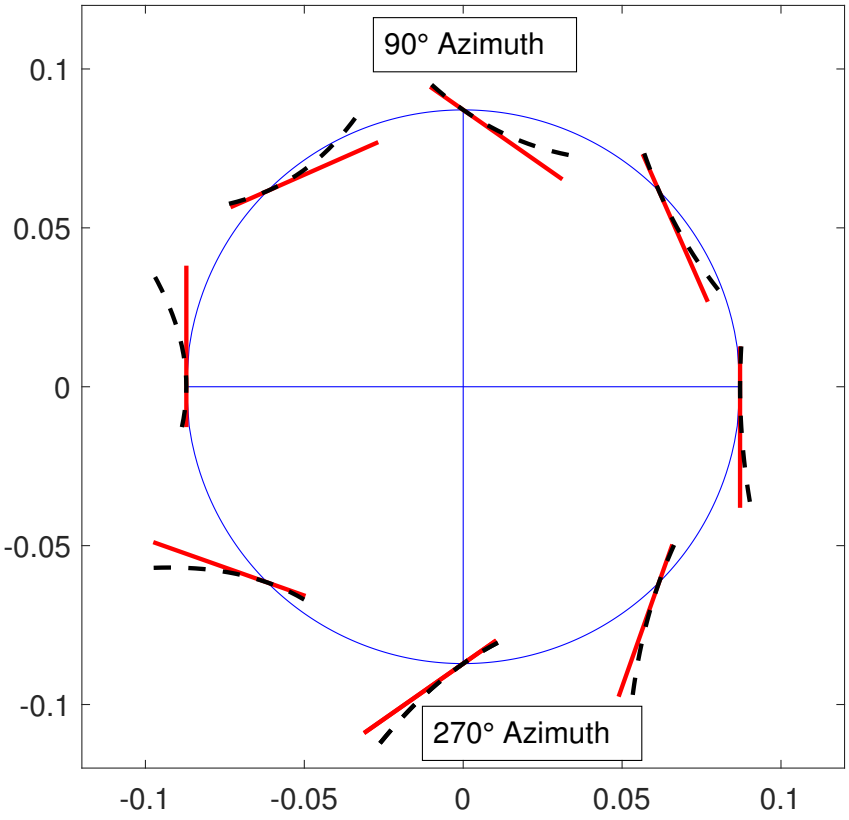


Figure 2.15: Virtual chord-line due to virtual camber effect along azimuth.

over, the virtual incidence decreases the effective angle of attack in the upper half and increases the angle of attack in the lower half. These are the reasons why the magnitude of maximum radial and tangential force coefficients in the downstream half ($\psi = 180° - 360°$) is significantly higher than that at upstream ($\psi = 0° - 180°$)) (Fig. 2.11 and 2.12).

#### *2.2.3.2 Reason for Net Time-Averaged Side Forces*

Another non-intuitive physical phenomenon observed during the operation of cycloidal rotor is asymmetric or non-negative net side force even with a symmetric prescribed pitch without any phase offset ($T_y$ force shown in Fig. 1.3. From the kinematics shown in Fig. 1.3, intuitively, one may expect all the side forces due to drag and lift to cancel each other producing only a net vertical

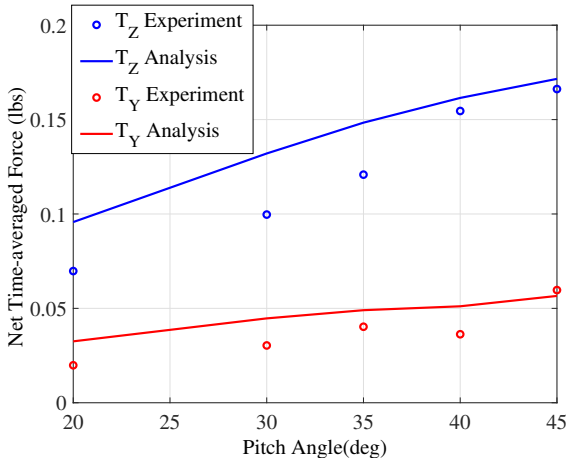


Figure 2.16: Comparison time-averaged forces at different pitch amplitude.

force; however, in reality, experiments have shown the presence of a dominating side force (Figs. 2.16 and 2.17). Figure 2.16 shows experimental comparison of time-averaged forces over a range of pitch amplitude. The results show existence of a non-zero time-averaged side force ($T_y$), even though significantly smaller in magnitude than the vertical force ($T_z$).

To investigate this phenomenon, instantaneous vertical and side forces are plotted and compared in Fig. 2.17. Figures 2.16 and 2.17, show overall reasonable correlation between results obtained from experiments and analysis. Instantaneous vertical and side forces are obtained using following expressions.

$$F_Z = F_R \sin\psi - F_T \cos\psi \tag{2.37}$$

$$F_Y = -F_R \cos\psi - F_T \sin\psi \tag{2.38}$$

In the above equations, $F_R$ is the radial force, $F_T$ is tangential force, $F_Z$ is vertical force and $F_Y$ is side force at azimuth location, $\psi$. This phenomenon can be explained by dynamic virtual camber effect due to pitch rate and flow curvature. It can be observed from Eq. 2.38 that side force comes from two sources, radial and tangential forces. Radial force is mostly dominated by lift while tangential force is mostly dominated by drag. The relation between lift - drag and radial

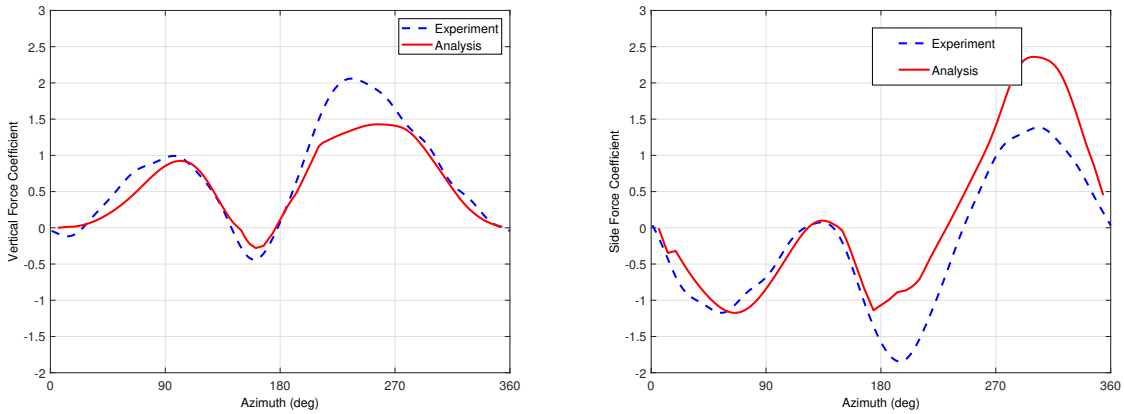


(a) Variation of instantaneous vertical forces along azimuth.

(b) Variation of instantaneous side forces along azimuth.

Figure 2.17: Comparison instantaneous vertical and side forces along azimuth (Pitch Amplitude: $45°$).

- tangential force are given by Eq. 2.39 and 2.40, where $\alpha$ is angle of attack.

$$F_R = L\cos\alpha + D\sin\alpha \tag{2.39}$$

$$F_T = L\sin\alpha - D\cos\alpha \tag{2.40}$$

Therefore, it should be possible to trace back the source of side force to lift and drag on the blade. The validated aerodynamic model is used to investigate underlying reason behind non-zero time-averaged side force. In Fig. 2.18, side force due to lift and drag are plotted separately to distinguish their effects.

Figure 2.18a shows the contribution of instantaneous blade lift to side force. Note that, in this case, the X-axis is plotted differently to separate the left and right halves. It can be observed from Fig. 2.18a that if no virtual camber is considered (dotted blue line), then side force due to lift is perfectly symmetric between left and right halves. Side force from left half of cycloidal rotor cycle ($\psi = 90° - 270°$) cancels side force of right half ($\psi = 270° - 450°$ or $90°$), as seen from Fig. 1.3. The dashed red line in figure 2.18a shows that once the virtual camber due to curvilinear flow geometry and pitch angle is incorporated, the side force is still symmetric between the left

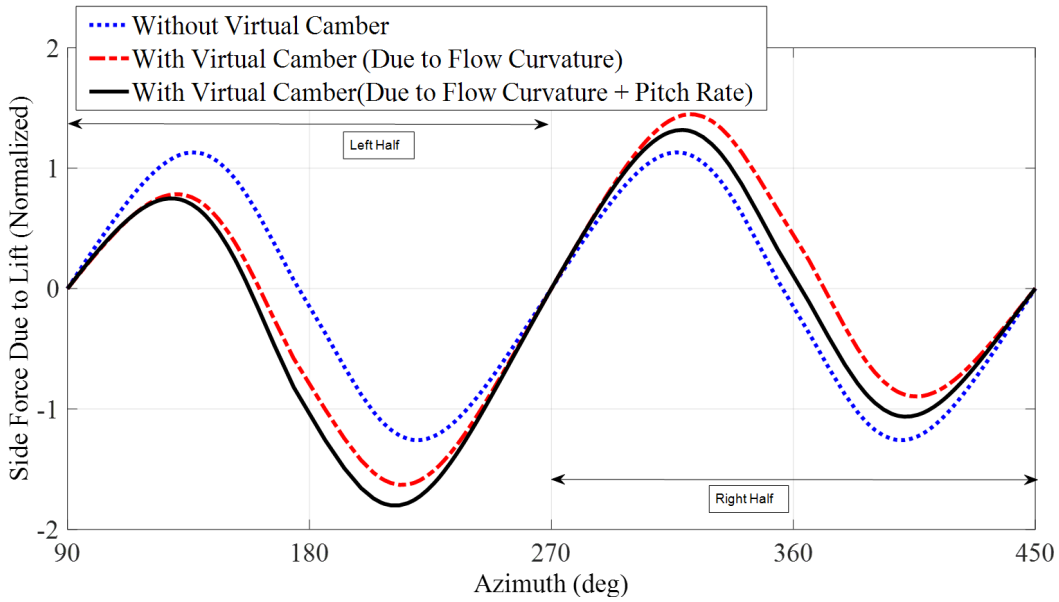


(a) Variation of side force due to lift along azimuth.

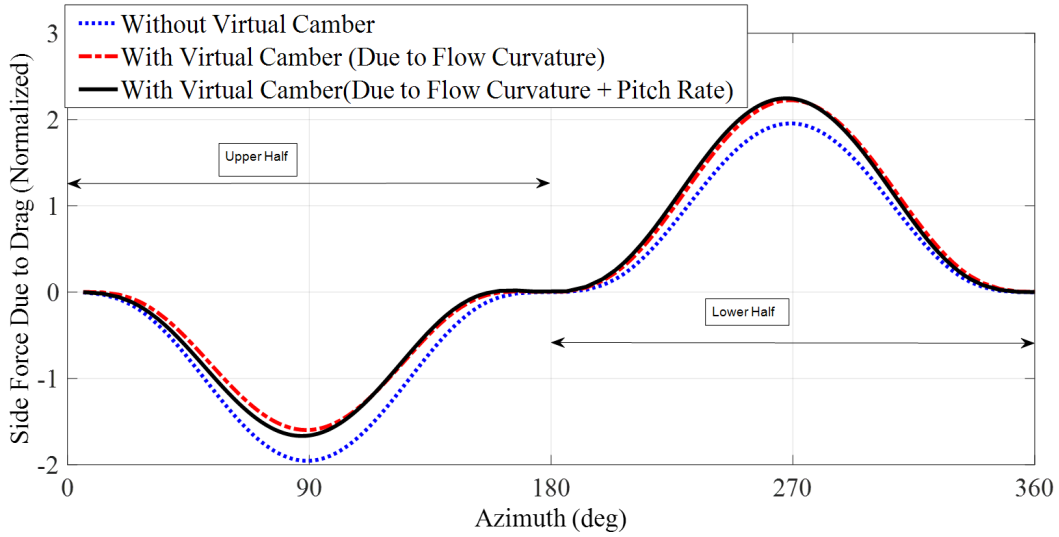


(b) Variation of side force due to drag along azimuth.

Figure 2.18: Effect of virtual camber on asymmetry of side force (Pitch Amplitude: $45°$).

and right halves producing almost zero net side force. This is because virtual camber due to flow curvature introduces asymmetry between top half (upstream) and bottom half (downstream) of the cycle; the symmetry between right and left halves remains intact. But once the virtual camber due to pitch rate is introduced (solid black line in Fig. 2.18a), it causes significant asymmetry in side force between left and right halves causing non-zero net side force. This is because the rotor blade goes through pitch up motion during right half of cycle ($\psi = 270° - 450°$ or $90°$) while it goes through pitch down motion during left side of cycle ($\psi = 90° - 270°$). As explained in the previous section, the pitch up motion causes positive virtual camber effect while pitch down motion creates negative camber effect. Due to this two opposite virtual camber effects in left and right halves, the side force gets unbalanced. This phenomenon becomes evident from Fig. 2.15 where it is observed that cycloidal rotor motion creates mild negative virtual camber on right side while it creates large negative camber on left side.

From Fig. 1.3, one may expect the drag at the top half (upstream) to be canceled by the drag at the bottom half (downstream). Figure 2.18b (contribution of instantaneous blade lift to side force) shows similar results when no virtual camber is included (the dotted blue line is antisymmetric between upper and lower halves). However, once the virtual camber due to flow curvature is included, the dashed red line shows asymmetry in side force due to drag. It shows decrease in magnitude of side force in the upstream half while increase in magnitude of side force in the downstream half. This is because flow curvature creates almost equal negative camber everywhere. In the upstream half, geometric pitch is positive and thus, negative virtual camber decreases effective angle of attack which in turn causes decrease in magnitude of drag and corresponding side force. While in downstream half, the geometric pitch is negative and negative virtual camber creates larger negative effective angle of attack (observed from rotating blade frame) which causes larger magnitude of drag and corresponding side force. This phenomenon causes imbalance in side force due to drag.

## 2.3 Aerodynamic Model in Forward Flight

In this section, the development of a lower order aerodynamic model of cycloidal rotor in forward flight condition, is discussed. The aerodynamics associated with cycloidal rotor is characterized by nonlinear dynamic virtual camber, non-uniform complex inflow characteristics and several unsteady phenomena such as dynamic stall, leading-edge vortices, near and shed wakes. Forward flight velocity changes chord-wise variation of incident flow velocity angle on rotor blade by changing curvilinear flow geometry and it manifests as dynamic nonlinear virtual camber effect very different from what was previously observed in hover and is discussed in detail in later sections. The major effect of forward speed on cycloidal rotor performance is due to changes in inflow speed. During forward flight, a phase shift is introduced in the cyclic blade pitch of cycloidal rotor to tilt the thrust vector forward, resulting in a vertical force and horizontal propulsive force (Fig. 2b). The phasing in cycloidal rotor blade kinematics along with forward velocity direction and magnitude affects the complex non-uniform inflow characteristics associated with cycloidal rotor. To capture that, an inflow model based on double-multiple-streamtube (D-MS) is developed. The developed model is systematically validated with in-house experimental data. Once validated, it is utilized to understand several phenomena behind the force production of cycloidal rotor in forward flight.

### 2.3.1 Modeling Methodology: Forward Flight Model

A flow chart of the proposed aerodynamic model is shown in the Fig. 2.19. The first step in this procedure is to calculate flow velocity. Flow velocity is computed from forward speed and inflow velocity. Blade velocity is obtained from prescribed kinematics. These two information together gives resultant air velocity with respect to blade at each chord-wise and span-wise section. In the next step, chord-wise variation of incident angle of flow velocity, which is manifested as virtual camber, is modeled to obtain virtual shape of the airfoil. In the next-step quasi-steady lift is obtained from airfoil virtual shape while utilizing a modified thin-airfoil theory. A non-linear lifting line model is implemented to capture 3D effects of finite blade. Leading-edge vortex is

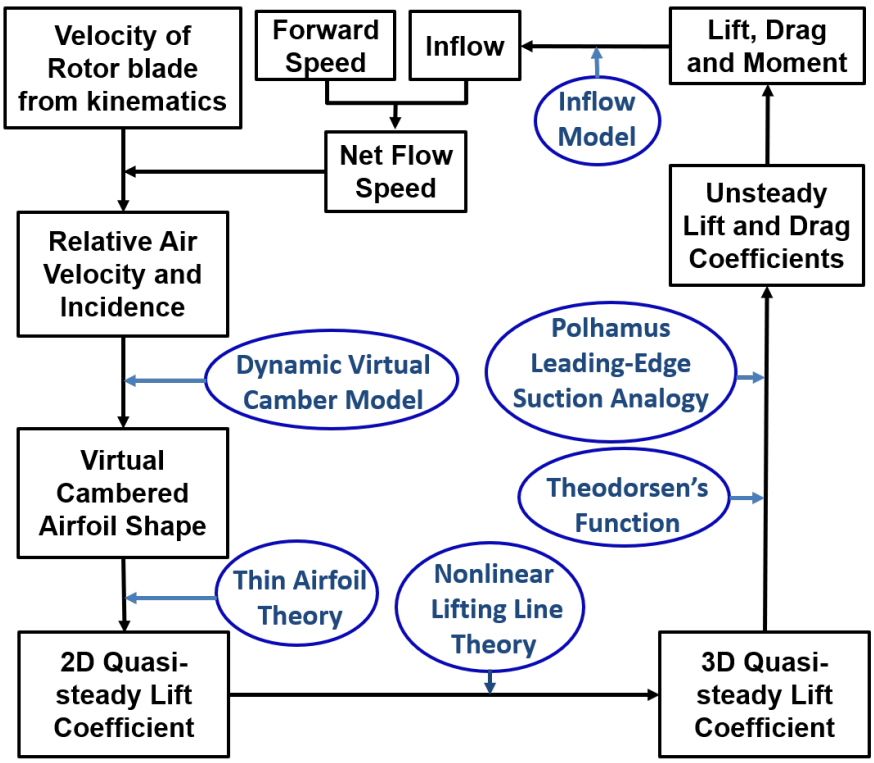


Figure 2.19: Flow chart of Aerodynamic Model in Forward Flight.

modeled using Polhamus leading-edge suction analogy. An unsteady model based on Theodorsen's approach is developed to capture the effects of shed wake. All these models lead to unsteady forces produced by cycloidal rotor blade. In the next step, inflow velocity is updated from aerodynamic forces using a tilting double multiple streamtube model. The above cycle is repeated until both inflow and circulation converges.

#### *2.3.1.1 Virtual Camber*

Flow over a cycloidal rotor is not purely curvilinear in a forward flight motion since the incoming flow due to forward speed changes curvilinear geometry of flow associated with cycloidal rotor. This in turn effects virtual incidence and virtual camber which is very different from what was previously observed in hover. Figure 2.20 shows all the velocity components on cycloidal rotor blade at a local chord position. In case of a forward flight motion, flow velocity ($\vec{V}_\infty$) due to forward flight can be expressed as following.

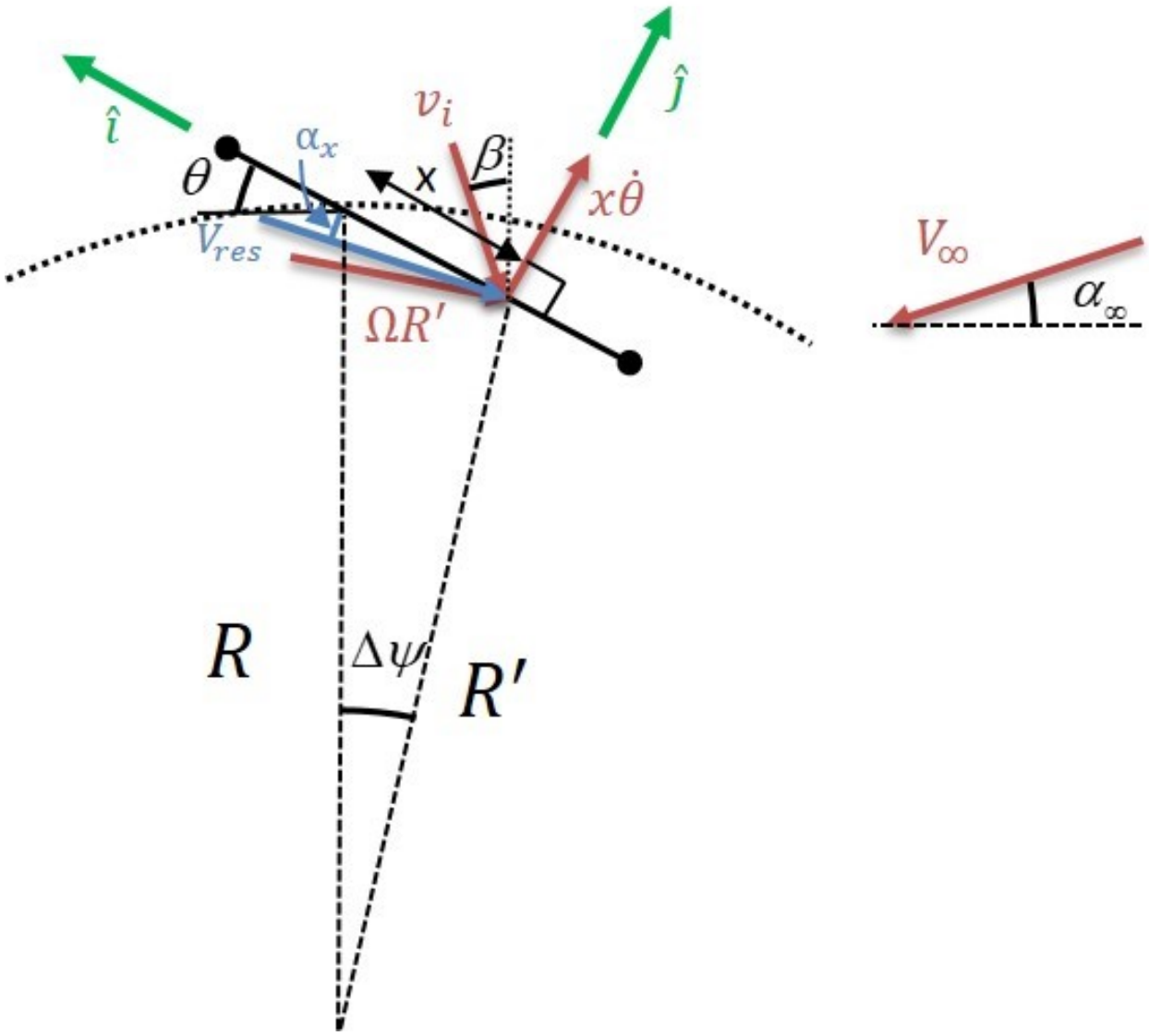


Figure 2.20: Velocity components at a local chord location on cycloidal rotor blade.

$$\vec{V}_\infty = V_\infty \hat{Y} \tag{2.41}$$

In the above equation, $V_\infty$ is forward flight speed of vehicle and $\hat{Y}$ is unit direction in inertial frame as defined in Fig. 2b. For a more general case, where the vehicle is in steady forward flight and steady climbing motion at angle $\alpha_\infty$ (Fig. 2.20), the flow velocity $\vec{V}_\infty$ can be expressed as following.

$$\vec{V}_\infty = V_\infty \cos\alpha_\infty \hat{Y} - V_\infty \sin\alpha_\infty \hat{Z} \tag{2.42}$$

To express $\vec{V}_\infty$ in airfoil co-ordinates a series of co-ordination transformation is required. At first, by transforming co-ordinate from inertial to rotating frame (Fig. 2b), $\vec{V}_\infty$ can be rewritten as Eq. 2.43.

$$\vec{V}_\infty = V_\infty \sin(\psi - \alpha_\infty)\hat{Y}_R - V_\infty \cos(\psi - \alpha_\infty)\hat{Z}_R \tag{2.43}$$

Now, performing co-ordinate transformation from rotating frame to airfoil frame, that is rotating and pitching with airfoil, $\vec{V}_\infty$ is expressed as following.

$$\vec{V}_\infty = V_\infty \sin(\psi - \alpha_\infty - \theta)\hat{i} - V_\infty \cos(\psi - \alpha_\infty - \theta)\hat{j} \tag{2.44}$$

Considering all the velocity components (Fig. 2.20), the net relative flow velocity ($\vec{V}$) with respect to rotor blade can be expressed as following equation.

$$\vec{V}(x) = \vec{V}_p(x) + \vec{V}_i(x) + \vec{V}_\infty - \vec{V}_b(x) \tag{2.45}$$

In the above equation, $\vec{V}_p(x)$ is flow velocity relative to rotor blade due to blade pitching motion, $\vec{V}_i(x)$ is inflow velocity and $\vec{V}_b(x)$ is blade velocity. Expressions of $\vec{V}_b(x)$, $\vec{V}_p(x)$ and $\vec{V}_i(x)$ are obtained from Eq. 2.2, 2.3 and 2.4, respectively. Substituting all the velocity components, the net flow velocity relative to rotor blade is expressed as following.

$$\vec{V}(x) = -U_T\,\hat{i} - U_P\,\hat{j} \tag{2.46}$$

Where,

$$U_T = \Omega R\cos\theta + v_i\sin(\beta+\theta) - V_\infty\sin(\psi-\alpha_\infty-\theta) \tag{2.47}$$

$$U_P = x(\Omega-\dot{\theta}) - \Omega R\sin\theta + v_i\cos(\beta+\theta) + V_\infty\cos(\psi-\alpha_\infty-\theta) \tag{2.48}$$

This information all together gives net flow speed ($V(x)$) and incident angle of attack ($\alpha_x(x)$) at each local chord-wise location of the cycloidal rotor blade.

$$V(x) = \sqrt{U_T^2 + U_P^2} \tag{2.49}$$

$$\alpha_x = -\tan^{-1}\left(\frac{U_P}{U_T}\right) \tag{2.50}$$

In the above expression, $v_i$ is assumed to be zero for the first iteration and updated using inflow model (modified D-MS model, discussed later) for subsequent iterations. For a cambered airfoil in straight flow, the local angle of attack varies along chord according to following equation.

$$\alpha_x(x) = \theta - \frac{dy}{dx}(x) \tag{2.51}$$

By comparing, Eq. 2.50 and Eq. 2.51, expression for virtual camber line of cycloidal rotor blade is computed.

$$\frac{dy}{dx}(x) = \theta + \tan^{-1}\left(\frac{U_P}{U_T}\right) \tag{2.52}$$

#### *2.3.1.2 Force Computation*

From the virtual shape of the airfoil, quasi-steady lift coefficient is obtained using modified thin-airfoil theory. In this step, small angle of attack assumption of thin-airfoil theory is neglected since cycloidal rotor blade experiences large incident angle of attack due to higher operating pitch amplitude ($\sim$40°). To capture the 3D effects of finite wing, a non-linear lifting line model is

incorporated. Leading-edge vortex created by high amplitude pitching motion of cycloidal rotor blade is modeled using Polhamus leading-edge suction analogy. To capture the effects of shed-wake, a model based on Theodorsen's approach is developed. Since quasi-steady lift contains higher harmonic terms, an automated function is developed that would perform Fourier analysis of quasi-steady lift and compute corresponding reduced frequency and Theodorsen's function. Taking all high frequency components into account, unsteady forces are computed. This force computation steps are similar to what was discussed for the hover model.

Once lift and drag coefficients, $C_L$ and $C_D$, are computed, lift and drag force in blade co-ordinate system is obtained using lift, $L = \frac{1}{2}\rho\ V^2\ S\ C_L$ and drag, $D = \frac{1}{2}\rho\ V^2\ S\ C_D$. Forces in blade co-ordinate are transformed into inertial co-ordinate using proper transformation matrices to obtain instantaneous blade force $dT_i$ expressed in inertial frame.

#### *2.3.1.3 Inflow Model*

Previously in the analysis of cycloidal rotors and vertical axis wind turbines, Single Streamtube inflow or Double Multiple Streamtube (D-MS) models have been mostly used [Ref. 32]. For Single Streamtube model, the inflow is considered uniform along the azimuth and inflow at upstream and downstream halves of the blade is assumed to be same. Therefore, no azimuthal variation in inflow, nor blade interaction or wake effect is considered after the flow passes through the upstream half. This assumption is not physical. On the other hand, for D-MS model, there is azimuthal variation in inflow magnitude, however, inflow direction is assumed to be radial to blade path in the upstream half in the hovering state, which is also not physically realistic. In the present aerodynamic model (schematic shown in Fig. 2.21), the proposed inflow model (modified D-MS model) relaxes these assumptions. In this model, it is assumed that various streamlines interacts with the rotor blade twice, upstream and downstream, with different inflow velocity magnitude and direction. Wake velocity is captured by using mass and momentum conservation laws. Also the assumption of radial inflow direction of traditional D-MS model is relaxed by calculating inflow direction based on resultant force, which will be discussed later in detail (Fig. 2.22).

In case of forward flight, the thrust vector of cycloidal rotor is tilted forward by introducing

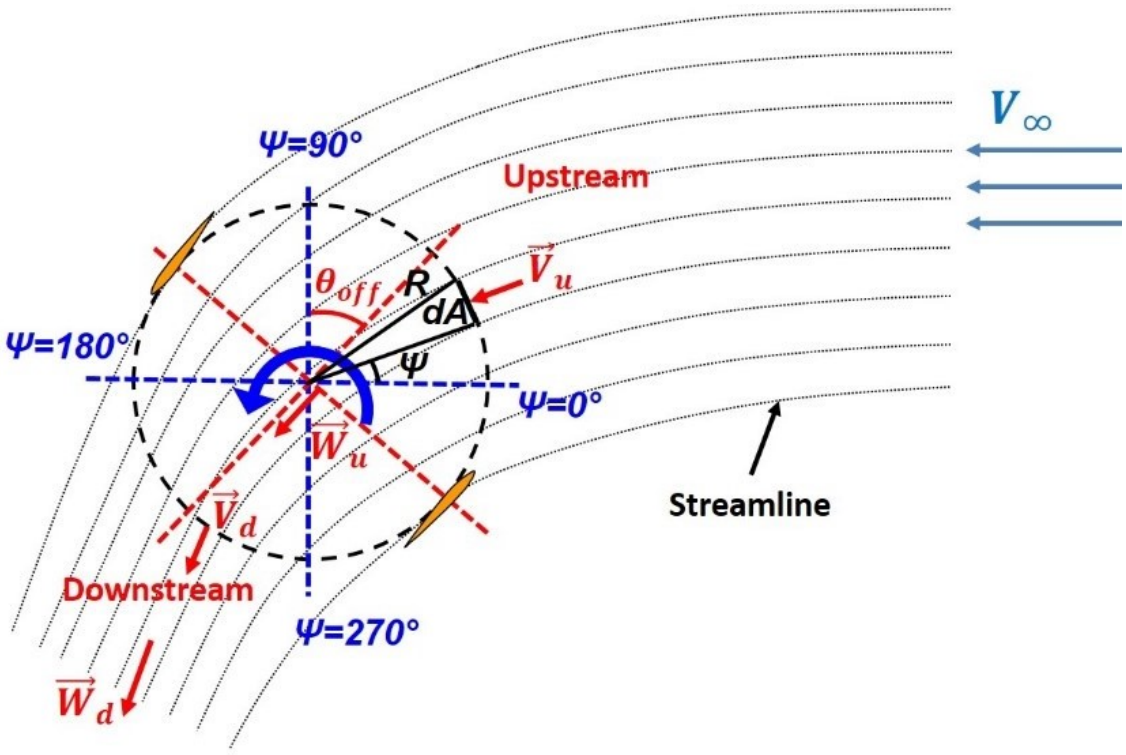


Figure 2.21: Schematic of inflow model.

a phase-shift in the cyclic blade pitching mechanism (Fig. 2b). For this reason, upstream and downstream locations in the cycloidal rotor disk area gets changed. In the proposed inflow model, it is assumed that actuator disk tilts same angle as the phasing and upstream location occurs from $\psi = 0° - \theta_{off}$ to $\psi = 180° - \theta_{off}$ (azimuth locations corresponding to $0°$ pitch angle) as shown in Fig. 2.21.

Now the first step is to calculate time-averaged forces ($dT_a$) from instantaneous forces ($dT_i$) obtained through unsteady aerodynamics modeling. If the time-period of cycloidal rotor blade is $T_P$, and a single blade stays $dt$ time in an infinitesimal area $dA$ (Fig. 2.21) in actuator disk, then time averaged force produced by the that infinitesimal area on actuator disk can be given by Eq. 2.53.

$$dT_a = dT_i \frac{N_b dt}{T_P} \tag{2.53}$$

In the above equation, $N_b$ is total number blades in the rotor. Since, $dt = d\psi/\Omega$ and $T_P = 2\pi/\Omega$, Eq. 2.53 can be rewritten as

$$dT_a = dT_i \frac{N_b d\psi}{2\pi} \tag{2.54}$$

From rotor geometry, $d\psi$ can be expressed as $dA/R$ (Fig. 2.21). Substituting this expression into Eq. 2.54, following equation is obtained.

$$dT_a = dT_i \frac{N_b dA}{2\pi R} \tag{2.55}$$

By performing some mathematical manipulation, above equation can be rewritten as following.

$$\frac{dT_a}{A} = \frac{dT_i}{c}\sigma \tag{2.56}$$

Where, $\sigma = N_b\ c/(2\pi R)$ is solidity of the rotor. Equation 2.56 denotes that time averaged force per unit actuator disk area in a particular azimuth location is equal to instantaneous blade force per unit chord multiplied by solidity. Average force per unit disk area is represented as $f = dT_a/dA$, which is used to calculate inflow velocity.

One major improvement of proposed inflow model over traditional D-MS model is relaxation of the assumption of radial inflow direction. Here, inflow direction is calculated based on resultant force direction on the blade at that particular azimuthal location, where the induced flow due to thrust production is exactly opposite to the direction of net force generated by blade (Fig. 2.22). The underlying reasoning behind this approach is that at a local azimuthal location, whatever aerodynamic force the rotor blade experiences, it exerts same force to the nearby fluid in the exact opposite direction and thereby accelerating the fluid in the same direction. Figure 2.22 shows detail schematic of a streamline. Far from the rotor, streamline has the velocity of forward speed of rotor, $\vec{V}_\infty$. Across the upstream blade path, the rotor induces flow velocity ($\vec{V}_{i_u}$) exactly opposite to the net force generated by rotor and net inflow velocity becomes $\vec{V}_u = \vec{V}_{i_u} + \vec{V}_\infty$. The angle

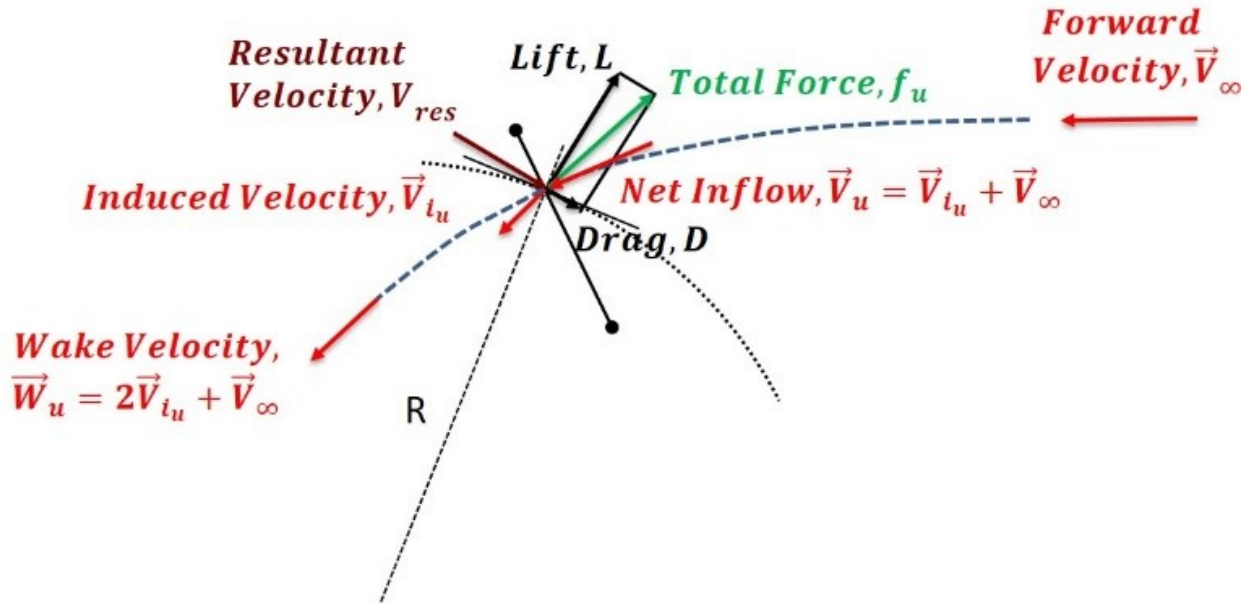


Figure 2.22: Schematic of inflow model in upper half.

between total force, $f$ and forward velocity $\vec{V}_\infty$ is defined as $\gamma_u$. Using conservation of momentum, following expression (Eq. 2.57) can be obtained.

$$f_u = \frac{d\dot{m}_u}{dA_u} w_{i_u} \tag{2.57}$$

In the above equation, subscript $u$ denotes upstream and $w_{i_u}$ is induced wake velocity. Total wake velocity at upstream, $\vec{W}_u$ can be computed as $\vec{W}_u = \vec{W}_{i_u} + \vec{V}_\infty$. Mass flow rate, $d\dot{m}_u$ can be expressed as

$$d\dot{m}_u = \rho dA_u U_u \tag{2.58}$$

In the above equation, $U_u$ is upstream flow velocity along actuator disk given by Eq. 2.59.

$$U_u = \sqrt{(V_\infty \cos\gamma_u + v_{i_u})^2 + (V_\infty \sin\gamma_u)^2} \tag{2.59}$$

Using conservation of energy and comparing with Eq. 2.57 induced wake velocity can be computed

(Eq. 2.60).

$$w_{i_u} = 2v_{i_u} \tag{2.60}$$

Substituting Eq. 2.58, 2.59 and 2.60 into Eq. 2.57, following expression (Eq. 2.61) is obtained.

$$f_u = 2\rho v_{i_u}\sqrt{v_{i_u}^2 + V_\infty^2 + 2v_{i_u}V_\infty \cos\gamma_u} \tag{2.61}$$

Solving the above nonlinear equation induced flow at upstream, $v_{i_u}$ can be obtained. A nonlinear solver based on bisection method is implemented for this purpose. Once the upstream induced inflow and induced wake velocity is obtained from above equations (Eq. 2.57-2.61), downstream inflow and wake velocity is obtained using similar approach by applying mass and momentum conservation laws. Applying conservation of momentum at downstream section of cycloidal rotor, following expression can be calculated (Eq. 2.62).

$$f_d = \frac{d\dot{m}_d}{dA_d} w_{i_d} \tag{2.62}$$

In the above equation, $w_d$ is induced wake velocity at downstream. Subscript *d* in Eq. 2.62 denotes downstream. Mass flow rate, $d\dot{m}_d$ can be expressed as following.

$$d\dot{m}_d = \rho dA_d U_d \tag{2.63}$$

Here, $U_d$ is downstream flow velocity along actuator disk denoted by Eq. 2.64.

$$U_d = \sqrt{(w_u \cos\gamma_d + v_{i_d})^2 + (w_u \sin\gamma_d)^2} \tag{2.64}$$

In above equation, $w_u$ is magnitude of total upstream wake velocity; $\gamma_d$ is angle between force, $f_d$ and upstream wake velocity, $w_u$; $v_{i_d}$ is induced velocity at downstream. Using conservation of energy and comparing with Eq. 2.62 induced wake velocity at downstream can be computed (Eq.

2.65).

$$w_{i_d} = 2v_{i_d} \tag{2.65}$$

Substituting Eq. 2.62, 2.66 and 2.64 into Eq. 2.61, following expression (Eq. 2.66) is obtained.

$$f_d = 2\rho v_{i_d}\sqrt{v_{i_d}^2 + w_u^2 + 2v_{i_d}w_u\cos\gamma_d} \tag{2.66}$$

Solving the above nonlinear equation, induced velocity at downstream, $v_{i_d}$ is obtained. Once. the inflow is updated, aerodynamic forces are calculated based on new inflow and circulation. These steps are repeated until both circulation and inflow are converged.

### 2.3.2 Experimental Validation: Forward Flight Aerodynamic Model

In this context, the proposed aerodynamic model is validated with data obtained from in-house wind tunnel experiments and CFD results published before [Ref. 14]. Figure 2.23 shows comparison of propulsive force, vertical force and total force produced by a 4-bladed cycloidal rotor in forward flight with a forward speed of 3 m/s over a range of rotational speeds. The cycloidal rotor blades have span of 6.25 inches, chord of 0.665 inches and radius of 3 inches. Rotor blades are pitched at mid-chord with 45° pitch amplitude and a 90° phase offset. The analytical results show good correlation with experimental and CFD results.

Figure 2.24 shows experimental validation of time-averaged forces produced by cycloidal rotor in forward flight for 50° phase offset in cyclic blade pitching [88]. In this case, cycloidal rotor rotates at 1000 rpm operating at 9 m/s forward speed (advance ratio = 1.13). The cycloidal rotor has 3 inches radius, 6.25 inches blade span, 1.95 inches blade chord. Figure 2.24 shows good correlation with experimental data.

Since experimental data for time history of forces produced by cycloidal rotor blade in forward flight is not available in literature, analytical model is validated with time-history of forces obtained from CFD studies [Ref. 14]. Figure 2.25 shows comparison of time-history of propulsive force and vertical force produced by a 4-bladed cycloidal rotor at an advance ratio of 0.39. The cycloidal rotor has radius of 3 inches with blades of 2 inches chord and 6.25 inches span. The rotational

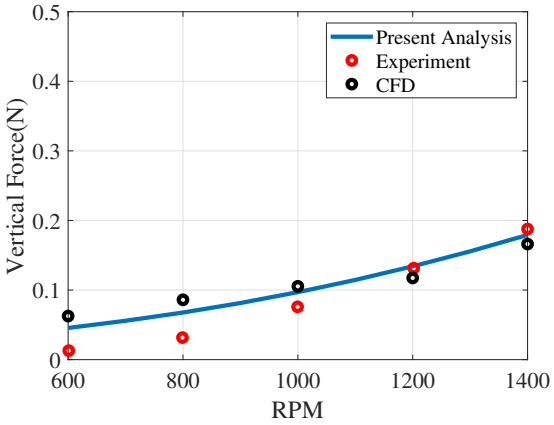


(a) Vertical force validation for different RPM.

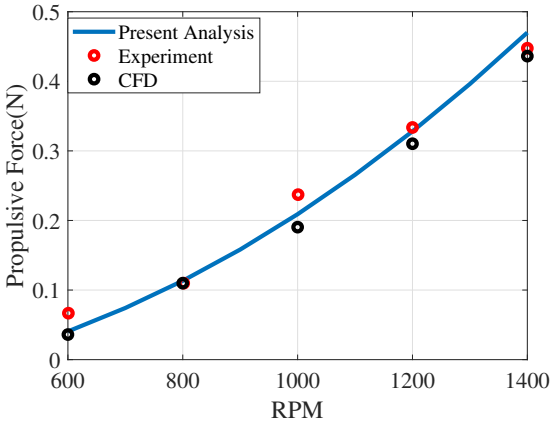


(b) Propulsive force validation for different RPM.

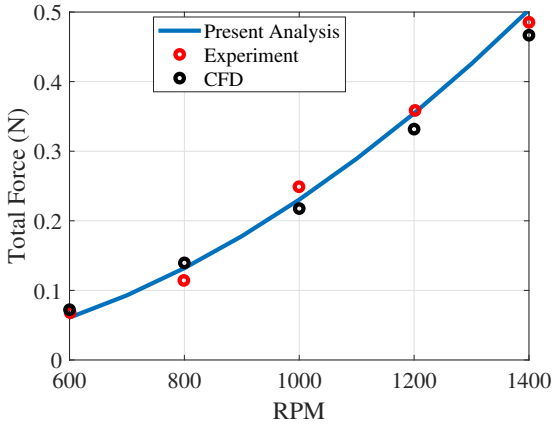


(c) Net force validation for different RPM.

Figure 2.23: Time-averaged force validation of analytical model with data from experiments and CFD.

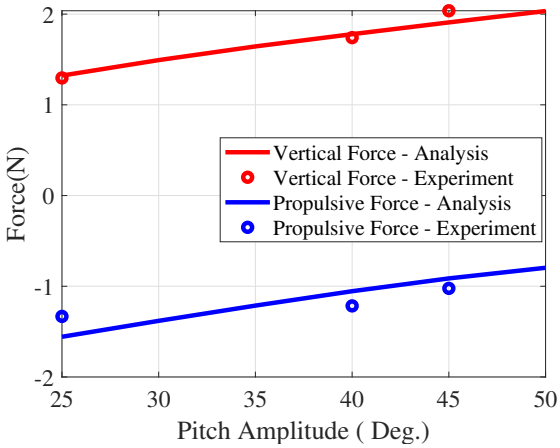


Figure 2.24: Vertical and Propulsive force validation for 50° phase offset at different pitch amplitude (Analysis vs. Experiment).

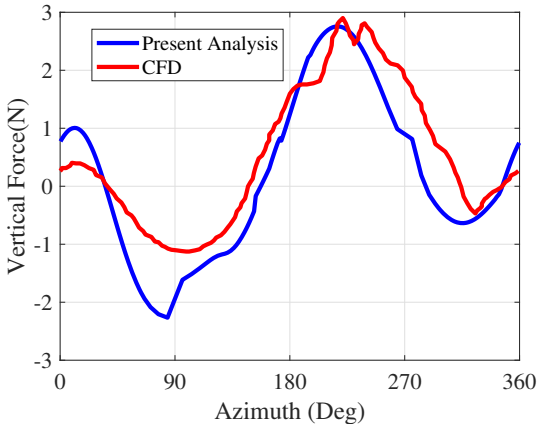


(a) Vertical force validation at different azimuth.

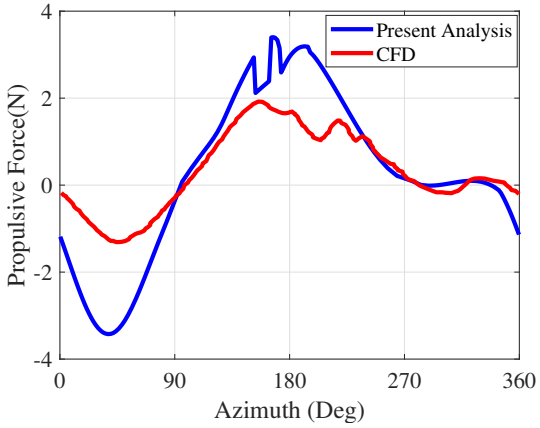


(b) Propulsive Force validation at different azimuth.

Figure 2.25: Validation of time-history of forces (Analysis vs. CFD).

speed of the cycloidal rotor is 1600 rpm at a pitch amplitude of 35° with 90° phase offset operating at 5 m/s flow speed. Figure 2.25 shows reasonable correlation with CFD data. Physics behind the instantaneous propulsive force and vertical force production is discussed in detail in a later section.

### 2.3.3 Discussion: Physics of Force Production in Forward Flight

Once the aerodynamic model is validated with data obtained from in-house experiments and CFD results, it was utilized to understand the vertical and propulsive force production on a cycloidal rotor in forward flight.

#### *2.3.3.1 Effects of Dynamic Virtual Camber*

The results in previous section (Figs. 2.23-2.24) show that cycloidal rotor is capable to producing positive vertical force and propulsive force under a forward flight condition by adjusting the phase offset in cyclic blade pitch kinematics. The analytical model shows that virtual camber and its nonlinear dynamic behavior plays an important role in force production. Figure 2.26 shows virtual cambered airfoil shape (solid black line) and actual airfoil (red line) of a cycloidal rotor blade going through same conditions as of Fig. 2.25 i.e. blade chord of 2 inches, radius of 3 inches, blade

span of 6 inches, rpm of 1600 under 5m/s forward speed (advance ratio = 0.39) and phase offset of 90°. The blue arrows in Fig. 2.26 represents magnitude and direction of relative flow velocity with respect to blade at corresponding azimuth locations. Observing from inertial point of view, that rotor blade shows negative virtual camber near top of the cycle (90° azimuth), while a positive virtual camber near the bottom of the cycle (270° azimuth). For this reason, the blade produces downward force near 90° azimuth while it produces upward force near 270° azimuth. Similar results can be quantitatively observed from Fig. 2.25a. Moreover, while the blade is at the top half of the cycle (retreating side), it experiences smaller magnitude of relative velocity since flow speed due to blade speed ($\Omega R$) is opposed by forward flow speed ($V_\infty$), and therefore, the downward force produced by the blade is smaller in magnitude. At the bottom half (advancing side), rotor blade experiences higher relative flow speed since flow due to blade speed ($\Omega R$) and forward flow speed ($V_\infty$) acts towards same direction. For that reason, rotor blade produces upward force of higher magnitude near bottom portion of cycle. In Fig. 2.25a, it can be seen that the magnitude of negative peak of vertical force near 90° azimuth is much smaller compared to magnitude of positive peak of vertical force near 270° azimuth. These phenomena leads to net positive vertical force over a cycle.

Observing from rotational frame of view, it can be seen from Fig. 2.26 that the forward flow speed decreases effective angle of attack near upstream half (right half) of the cycle (0° azimuth). Although, the rotor blade experiences slight negative camber, it produces small amount of negative lift (force towards left side or negative propulsive force). On the other hand, rotor blade experiences large positive virtual camber as well as positive angle of attack near left side of cycle (270° azimuth), so it creates large lift force towards right side and hence a larger positive propulsive force. Similar trend is also observed from instantaneous propulsive force data of Fig. 2.25b, where the entire positive propulsive force is produced in the downstream half of the cycle (0° - 270°). These phenomena lead to net positive propulsive force over a cycle.

#### *2.3.3.2 Effects of Advance Ratio*

Advance ratio ($\mu$) of cycloidal rotor is the ratio of free-stream velocity ($V_\infty$) and blade speed ($\Omega R$). In this section effects of advance ratio on inflow characteristics, virtual camber and instan-

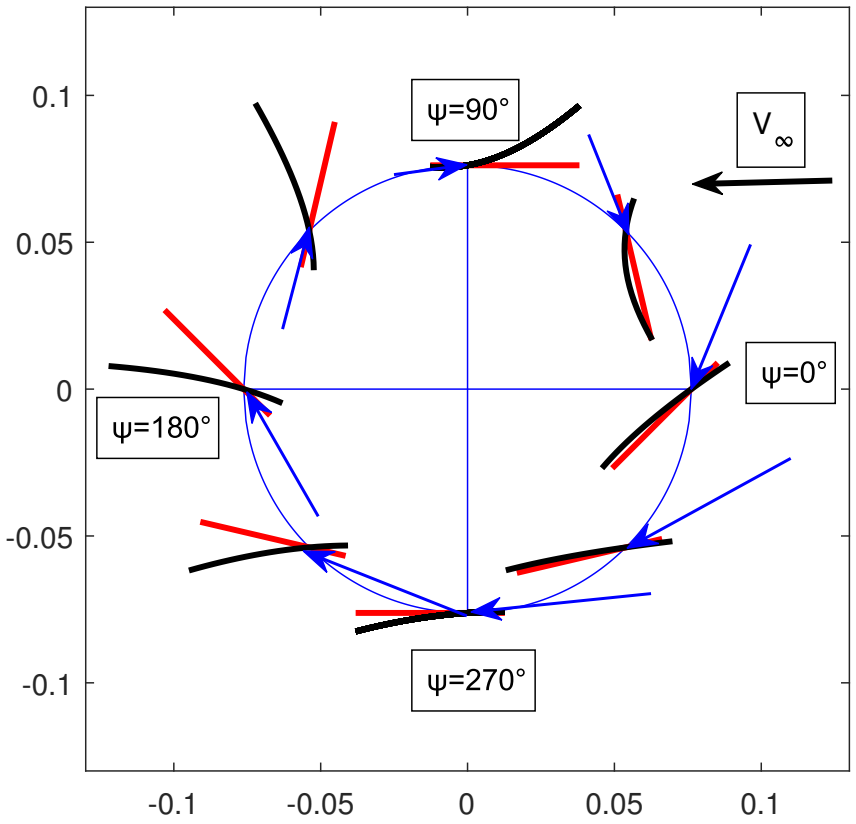


Figure 2.26: Virtual chord-line due to virtual camber effect along azimuth.

taneous blade forces are thoroughly investigated by utilizing the aerodynamic model.

Effects of advance ratio on inflow characteristic are observed in Fig. 2.27 which shows net inflow distribution along azimuth for two different advance ratios of 0.39 and 0.78. For this study, similar configuration of cycloidal rotor discussed in Fig. 2.25 and Fig. 2.26 is used except the advanced ratio is doubled from 0.39 to 0.78 (Fig. 16b) by decreasing rotor rpm from 1600 to 800 at a constant forward speed of 5 m/s. It can be observed from Fig. 2.27a that inflow speed increases from upstream to downstream. This is because induced inflow at upstream is being accelerated and the wake hits the downstream half at higher speed. Fig. 2.27b shows that inflow characteristics become almost uniform. This is because as the advance ratio increases, induced inflow decreases compared to forward speed and effects of induced inflow and induced wake becomes insignificant and the flow speed due to forward motion dominates.

Effects of advance ratio on instantaneous propulsive force, vertical force and virtual camber are investigated in Fig. 2.28. For this study, similar configuration of cycloidal rotor discussed in Fig. 2.25 and Fig. 2.26 is used. Changes in advance ratio is obtained by varying forward speed of cycloidal rotor from 3 m/s to 9 m/s. Figure 2.28a shows that as advance ratio of rotor is increased the additional lift due to virtual camber increases, so higher advance ratio creates more positive cambered effect. Figure 2.28b shows significant decrease in effective angle of attack between 0° to 90° azimuth and 270° to 360° azimuth while there is slight increase between 90° to 270° azimuth. These changes occur due to changes in flow geometry as advance ratio is increased.

As the advance ratio increases, significant variations in vertical force occurs near 0° and 90° azimuth (Fig. 2.28c) and significance variations in propulsive force occurs near 0° and 180° azimuth (Fig. 2.28d). The magnitude of negative peak of vertical force near 90° azimuth decreases (Fig. 2.28c) due to two main reasons:

1. Decrease in the magnitude of flow speed $|\Omega R\text{-}V_\infty|$ around 90° azimuth (retreating side) as advance ratio goes towards 1.

2. Decrease in magnitude of negative peak of additional lift due to virtual camber ($C_{L_0}$) around 90° azimuth.

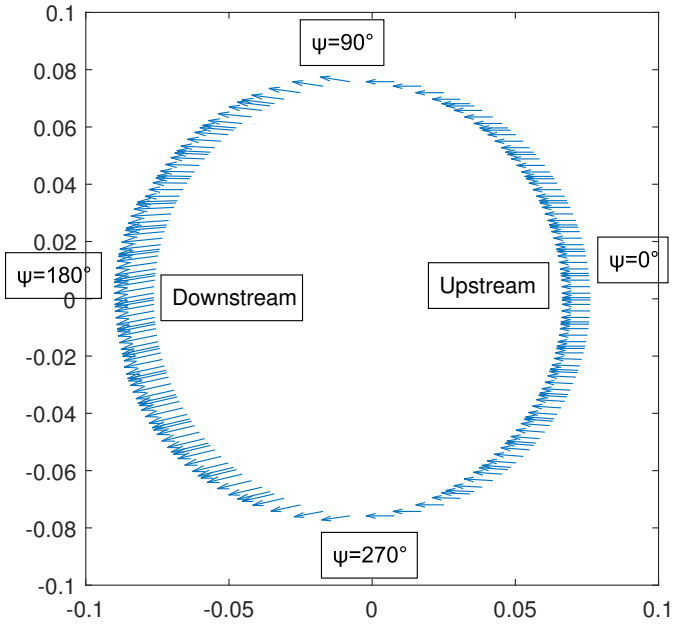


(a) Advance ratio, $\mu = 0.39$.

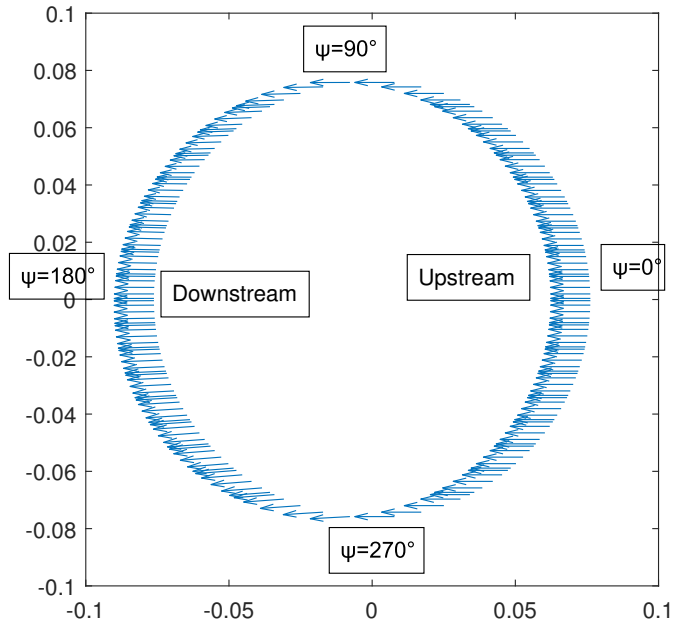


(b) Advance ratio, $\mu = 0.78$.

Figure 2.27: Net inflow distribution along azimuth.

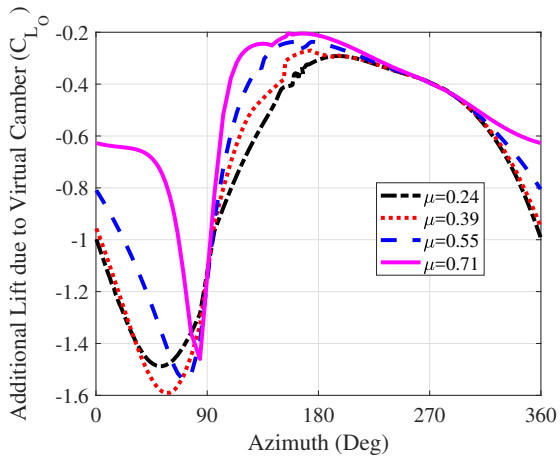


(a) Additional lift due to virtual camber vs. azimuth.

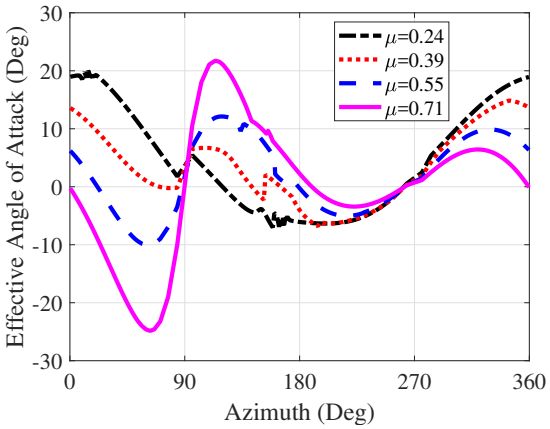


(b) Effective angle of attack vs. azimuth.

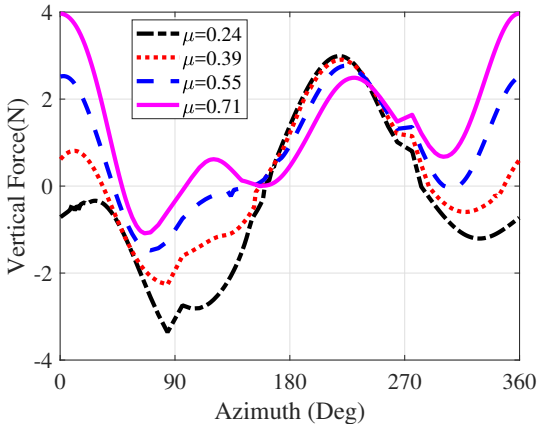


(c) Vertical force vs. azimuth.

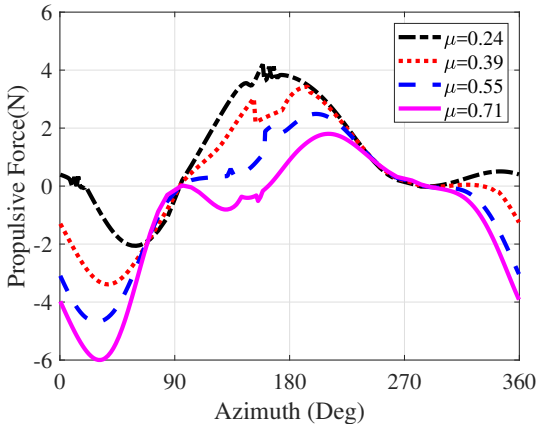


(d) Propulsive force vs. azimuth.

Figure 2.28: Effects of advance ratio on time-history of different parameters.

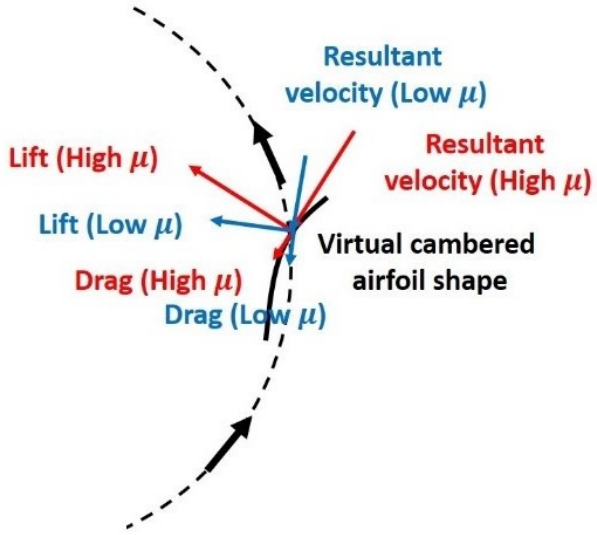


Figure 2.29: Local force generation at 0° azimuth.

Fig. 2.29 shows local lift production near 0° azimuth and it explains why vertical force increases and propulsive force decreases at 0° azimuth as the advance ratio is increased. In Fig. 2.29, red line corresponds to higher advance ratio (High $\mu$) and blue line corresponds to lower advance ratio (Low $\mu$). It can be observed that as the advanced ratio increases, effective angle of attack experienced by rotor blade decreases (observing from rotational frame), and rotor blade produces more negative lift. This increase in magnitude of negative lift causes decrease in propulsive force. Moreover, increase in magnitude of negative lift and its tilting towards upward direction (Fig. 2.29) causes increase in vertical force.

Figure 2.30 shows reason behind decreased propulsive force near 180° azimuth as advanced ratio is increased. Increased forward flow speed increases effective angle of attack and a virtually negatively cambered airfoil produce negative lift in smaller magnitude which causes decrease in propulsive thrust.

#### *2.3.3.3 Effects of Direction of Rotation*

In all the previous cases, cycloidal rotor is rotating in back ward direction with respect to forward speed (blades moving away from the flow or retreating side at top half of the trajectory).

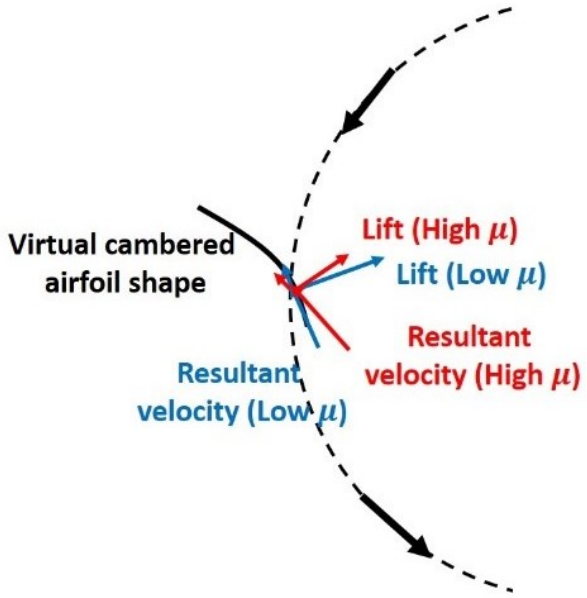


Figure 2.30: Local force generation at $180°$ azimuth.

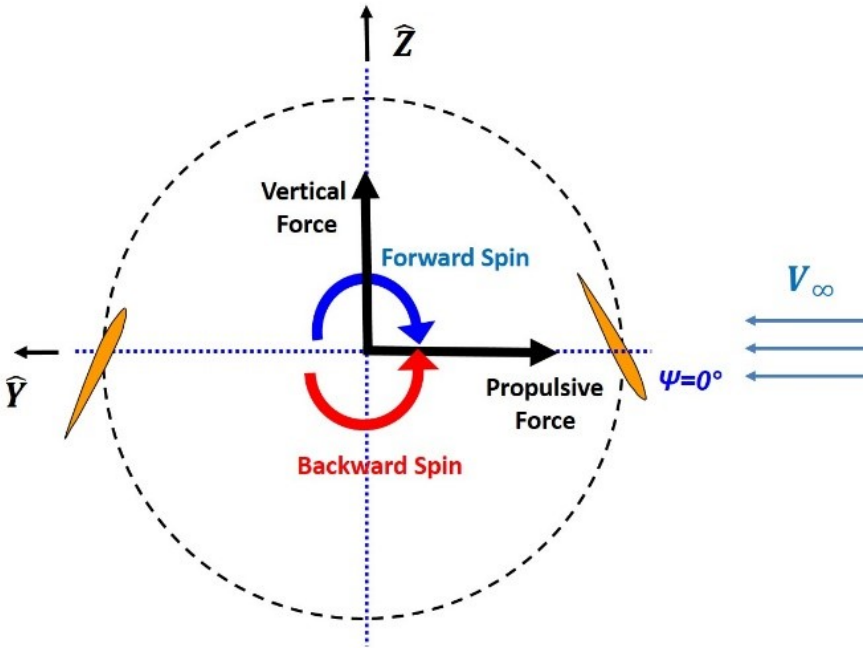


Figure 2.31: Cycloidal rotor kinematics (forward spin vs. back spin, with $90°$ phase offset in forward flight).

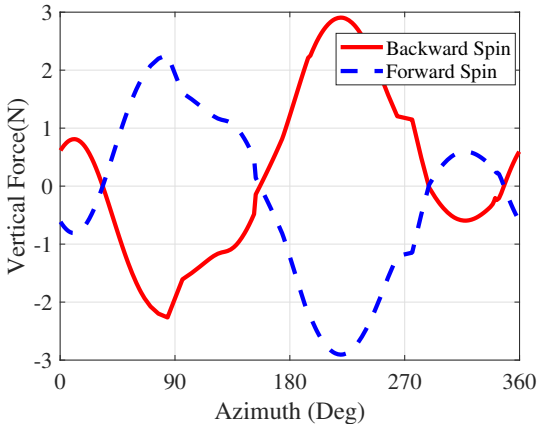


(a) Instantaneous vertical force at different azimuth.

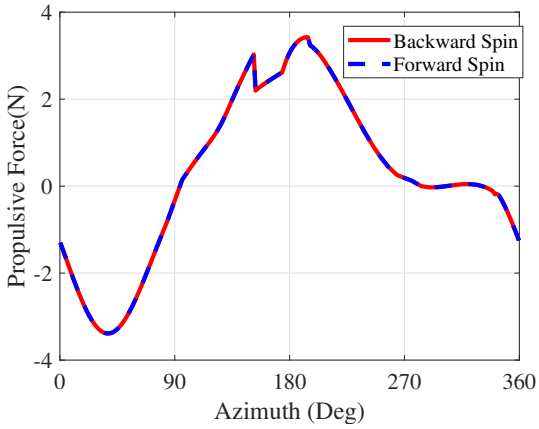


(b) Instantaneous propulsive force at different azimuth.

Figure 2.32: Cycloidal rotor force comparison: forward spin vs. backward spin

Figure 2.31 shows the definition of both forward and backward spin with respect to forward flight direction. Figure 2.32 shows comparison of instantaneous vertical and propulsive force produced by a cycloidal rotor in forward spin vs. backward spin. For this comparison, cycloidal rotor with same configuration as in Fig. 2.25 is considered. Fig. 2.32a shows cycloidal rotor produces exact mirror image of the vertical force in forward spin (blue dashed line) as in back spin (red solid line) which results in a net downward vertical force. For this case, time-averaged vertical force produced by cycloidal rotor is 0.74 N for backward spin and -0.74 N for forward spin. Figure 2.32b shows cycloidal rotor produces exactly same propulsive force in forward spin (blue dashed line) as in backward spin (red solid line). In this case, time-averaged propulsive force by cycloidal rotor for both backward spin and forward spin is 0.95 N. It shows that it is crucial for cycloidal rotor to have a backward spin with respect to forward flight direction in order to generate a net positive vertically upward force to balance the weight of the aircraft.

## 2.4 Free Wake Model

In the previous sections, lower order aerodynamics model of cycloidal rotor is developed. Although the above mentioned lower order model is computationally inexpensive and capable of predicting rotor performance with sufficient accuracy, it cannot capture the complex flow-field of

cycloidal rotor which is characterized by strong leading-edge vortex formation, nonlinear dynamic virtual camber effects, shed wake and blade-wake interactions. Specifically due to complex blade vortex interaction, trajectory of induced flow and trailing vortices becomes highly unpredictable which makes it impossible for a lower order model to capture the wake geometry. For this reason, a high-fidelity model of cycloidal rotor based on free-wake is developed to further investigate aerodynamics of cycloidal rotor in more detail. In this procedure, various trailing vortices from the rotor blade are modeled and these vortices are convected using local inflow velocity induced by all the vortices. Using Biot-Savart law, the instantaneous induced inflow velocity at each blade location is calculated unlike lower order model, where time-averaged inflow velocity is considered. The developed free-wake model is systematically validated with in-house experimental data and compared with the predictions of the lower order model.

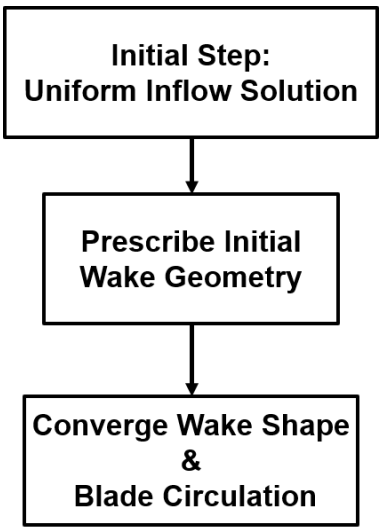


Figure 2.33: Schematic of free-wake model.

### 2.4.1 Modeling Methodology

A schematic of the proposed model is shown in Fig. 2.33. In the first step an uniform inflow solution is obtained. In the next step, wake geometry is prescribed assuming wakes are convected

with uniform inflow velocity. Bound circulation is computed from blade sectional loads obtained from uniform inflow solutions. Strength of individual trailing vortex filaments are computed from bound circulation. In the final step, wake convection is carried out while converging wake geometry and circulations together. Here induced velocity on blade and wake positions are calculated using Biot-Savart Law. Wakes are convected with this induced velocity and at the same time, circulations are updated. This procedure is continued in a iterative manner until convergence is obtained.

#### *2.4.1.1 Uniform Inflow Solution*

Here, similar methodology described in lower order model is implemented except for uniform inflow instead of double multiple streamtube (D-MS), for simplicity. This procedure is mainly due to define prescribed wake model since no other prescribed wake model of cycloidal rotor exists in literature. During this step, initially inflow is assumed to be zero. Based on prescribed kinematics, blade velocity is obtained. Blade velocity and inflow velocity together gives relative air velocity with respect to blade which in-turn provides sectional incident angle of attack on cycloidal rotor blade. Now, the chord-wise variation of incident angle is manifested as virtual camber as discussed before. Virtual shape of airfoil is obtained from virtual camber model. Quasi-steady lift is obtained from virtual airfoil shape. In the next step, lower order models of near wake, shed wake and leading-vortex are implemented to compute unsteady forces. Uniform inflow velocity across the cycloidal rotor is obtained from unsteady forces using following equations.

$$\vec{V}_{ui} = -\left(v_{ui}\sin(\beta_{ui})\hat{Y} + v_{ui}\cos(\beta_{ui})\hat{Z}\right) \tag{2.67}$$

In the above equation, $v_{ui}$ is the uniform velocity which acts exactly opposite to the direction of force ($F$) produced by cycloidal rotor and computed using following formula.

$$v_{ui} = \sqrt{\frac{F}{2\rho A}} \tag{2.68}$$

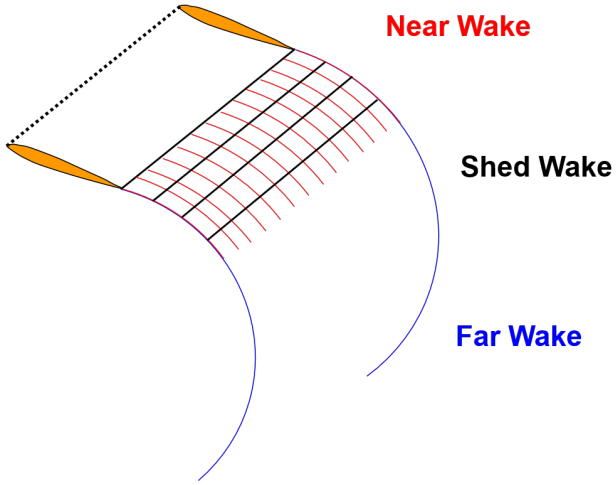


Figure 2.34: Wake structure.

In Eq. 2.67, $\beta_{ui}$ denotes the angle between resultant force and vertical direction and is computed using following formula.

$$\beta_{ui} = \tan^{-1}\left(\frac{F_y}{F_z}\right) \tag{2.69}$$

In the above equation, $F_z$ and $F_y$ are cycle-averaged net aerodynamic forces produced by cycloidal rotor in vertical (along $\hat{Z}$) and horizontal direction (along $\hat{Y}$), respectively. Based on the new inflow, blade loads are updated and the above cycle is repeated until both the inflow and circulation converges.

#### *2.4.1.2 Prescribed Wake Model*

There exists no prescribed wake model of cycloidal rotor in present literature. Due to that reason, uniform inflow solutions are utilized to develop prescribed wake model. The wake model consists of near wake and far wake region (Fig. 2.34). There exists multiple trailing vortices at near wake and only two trailing vortices at far wake which are basically tip vortices. Moreover, there exists shed wake along the span of the blade which is generated and shed due to cyclic pitching of rotor blade. In the initial step, all the wakes are assumed to be convected by the uniform inflow

velocity. The displaced distance ($\vec{s}$) of a wake is computed using following expression.

$$\vec{s} = t\vec{V}_{ui} = \frac{\psi_w}{\Omega}\vec{V}_{ui} \tag{2.70}$$

In the above equation, $\psi_w$ is wake-age and $\Omega$ is angular velocity of cycloidal rotor. The wake gets displaced to exactly the direction of inflow. Next step is to compute circulations. Using Kutta-Joukowski theorem, bound circulation ($\Gamma_b$) of the blade is given as following.

$$\Gamma_b = \frac{L}{\rho V\ dy} \tag{2.71}$$

In the above equation, $L$ is lift produced by a section of cycloidal rotor blade, $V$ is local flow velocity with respect to blade and $dy$ denotes span-wise length of blade section. Here, $L$ and $V$ are obtained from uniform inflow solution. The strength of trailing vortices ($\Gamma_t$) are obtained fro difference in bound circulations in two adjacent blade sections.

$$\Gamma_t(i, \bar{\psi}) = \Gamma_b(i, \bar{\psi}) - \Gamma_b(i-1, \bar{\psi}) \tag{2.72}$$

Where, i=1 to N+1. Here, N is number of blade elemental sections. $\Gamma_b(0, :)$ and $\Gamma_b(N+1, :)$ denotes zero circulation since they correspond to area outside of blade section on both sides of span. In Eq. 2.73, $\bar{\psi}$ denotes the azimuth where trailing vortex started. Now the bound circulation changes continuously due to cyclic pitching of cycloidal rotor blade. Changes in bound circulation creates shed wake across blade span. Strength of this shed wake ($\Gamma_s$) is obtained from temporal changes of bound circulation.

$$\Gamma_s(i, \bar{\psi}) = \Gamma_b(i, \bar{\psi}) - \Gamma_b(i, \bar{\psi} + d\bar{\psi}) \tag{2.73}$$

#### *2.4.1.3 Wake Convection*

Once the prescribed wake model is developed, the wakes are convected in a time-marching manner. At first induced velocity due to all vortex filaments is calculated at blade positions and at each vortex locations using Biot-Savart Law (Eq. 2.75).

$$\vec{V_i} = \frac{\Gamma_v}{4\pi} \frac{d\vec{l} \times \vec{r}}{|\vec{r}|^3} \tag{2.74}$$

In the above equation, $\vec{V_i}$ is induced velocity at a particular point due to a vortex segment of length $d\vec{l}$ and strength $\Gamma_v$. $\vec{r}$ denotes position of the point (where induced velocity is calculated) relative to midpoint of the vortex segment. Important thing to notice here is that a single vortex filament would have multiple segments with different vortex strength. This is because bound circulation is changing continuously and strength of the trailing vortices would also change continuously. Each vortex segment consists of two node on which induced velocities are computed. The vortex nodes are convected using following formula.

$$d\vec{s} = \vec{V_i} \frac{d\psi}{\Omega} \tag{2.75}$$

On the other hand, induced velocity is computed on blade elements at each time step and blade forces are updated. During this step, bound circulation is also updated based on updated blade force. This time-marching scheme is continued until wake shape and circulations converge all together.

### 2.4.2 Experimental Validation

The developed free-wake model is validated with in-house experimental data and compared with the predictions of the lower order model. For the experimental purpose, a cycloidal rotor with with 5.5 inch chord, 11 inch radius and 22 inch span is used. Experiments are carried out over a range of pitch amplitudes and blade numbers. Figure 2.35 shows experimental validation of net thrust predicted by free-wake model and lower-order D-MS model (double multiple streamtube).

Figure 2.36 shows similar experimental validation of time averaged power predicted by free-wake and D-MS model. Figures 2.35 and 2.36 shows that performance predictions of both the free-wake and D-MS model correlate well with experiments. Although, the free-wake model gives slight better prediction compared with D-MS model for most of the cases.

## 2.5 Conclusion

The main objective of this section was to develop an aerodynamic model of cycloidal rotor for different flight conditions (i.e. hover, forward flight) so that it could be utilized for preliminary design and optimization of next generation cycloidal rotors. Towards this, aerodynamics of a cycloidal rotor is investigated thoroughly and various underlying physical phenomena such as dynamic virtual camber, non-uniform inflow, effects of near and shed wake, leading edge vortices are rigorously modeled. All these detail modeling helped the aerodynamic model to systematically validate with not only time averaged forces, but also time-history of aerodynamic forces obtained from in-house experiments. The validated model is utilized for understanding physics behind the force production of cycloidal rotor. Key conclusions from this section is listed below.

### 2.5.1 Concluding Remarks: Hover Study

1. Chord-wise variation of incident velocity angle on cycloidal propeller blade is manifested as virtual camber/incidence effect. Virtual camber and incidence depend on curvilinear flow geometry, pitch angle, pitch-rate and inflow distribution. Considering all these effects, a generalized methodology is developed to model virtual camber.

2. Curvilinear geometry causes a static negative virtual camber at all azimuth locations while pitch, pitch rate and inflow distribution cause cyclic variation of virtual camber with blade azimuthal location making it a dynamic virtual camber. A positive blade pitch-rate (nose-up pitch) creates positive virtual camber, while a negative pitch-rate (nose-down pitch) creates negative virtual camber.

3. Virtual camber caused by pitch rate creates asymmetry in side force due to blade lift between the right and the left halves. However, the virtual camber resulting from flow curvature

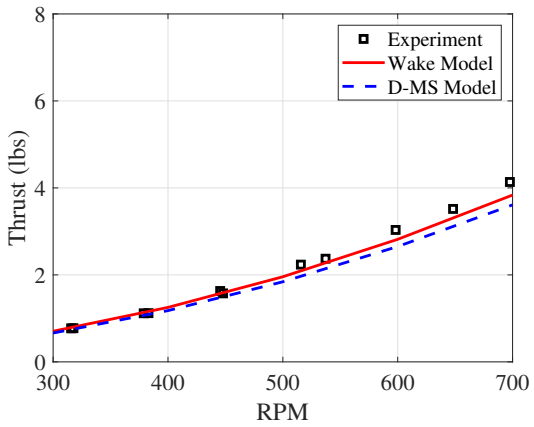


(a) Pitch Amplitude = 25°, Number of blades =2.

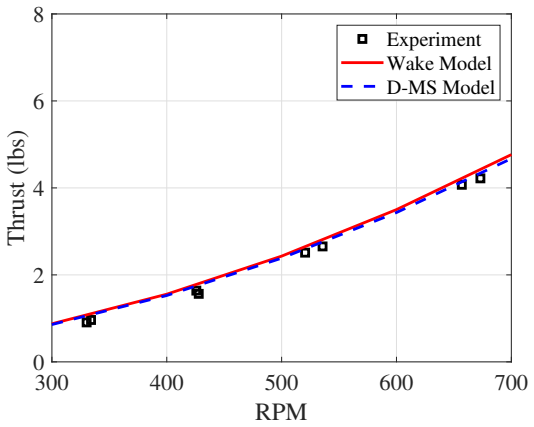


(b) Pitch Amplitude = 25°, Number of blades =3.

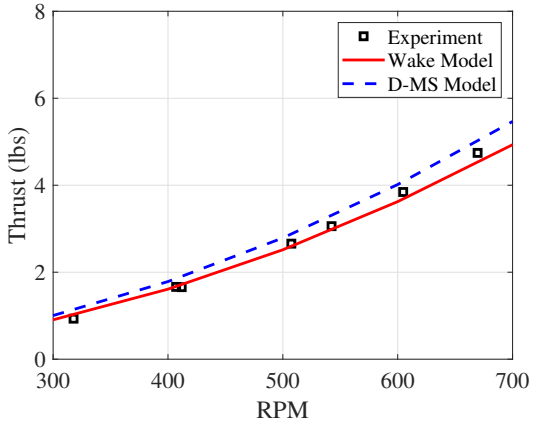


(c) Pitch Amplitude = 25°, Number of blades =4.

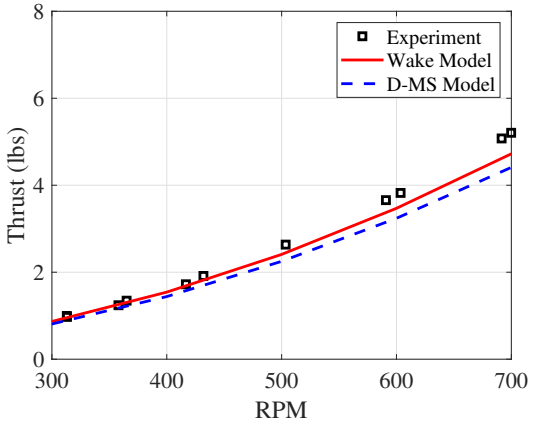


(d) Pitch Amplitude = 30°, Number of blades =2.

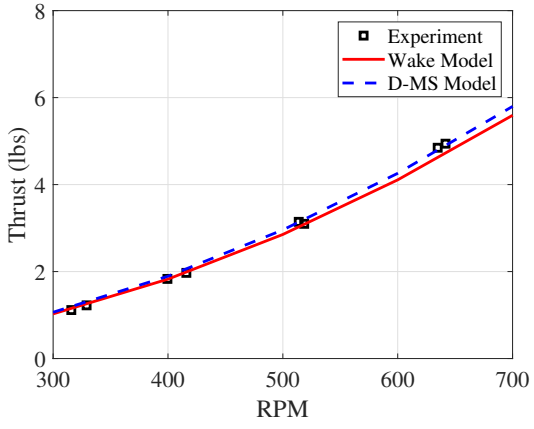


(e) Pitch Amplitude = 30°, Number of blades =3.

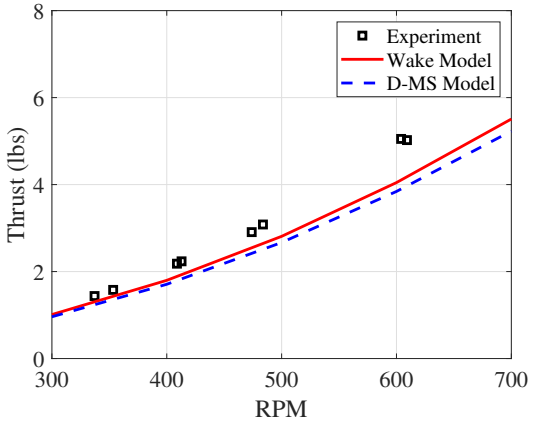


(f) Pitch Amplitude = 35°, Number of blades =2.

Figure 2.35: Validation of time-averaged net force (experiment vs. free-wake vs. D-MS model).

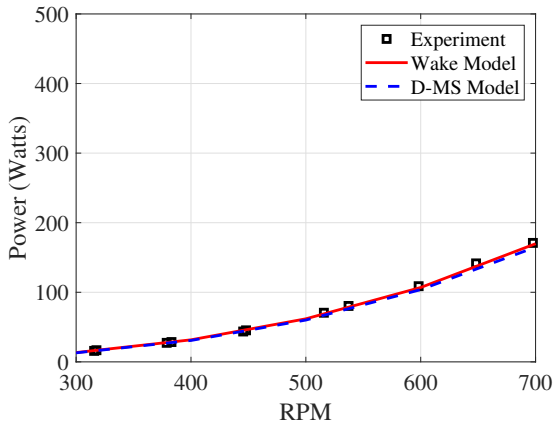


(a) Pitch Amplitude = 25°, Number of blades =2.

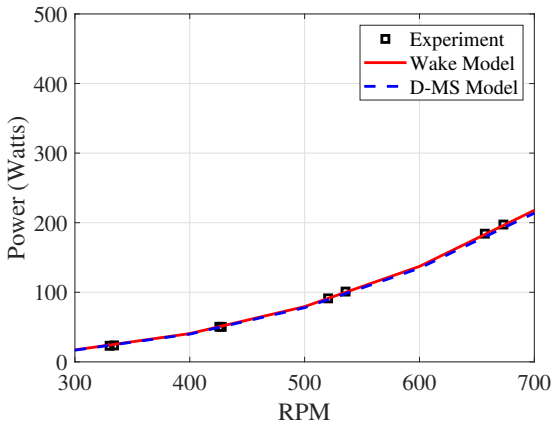


(b) Pitch Amplitude = 25°, Number of blades =3.

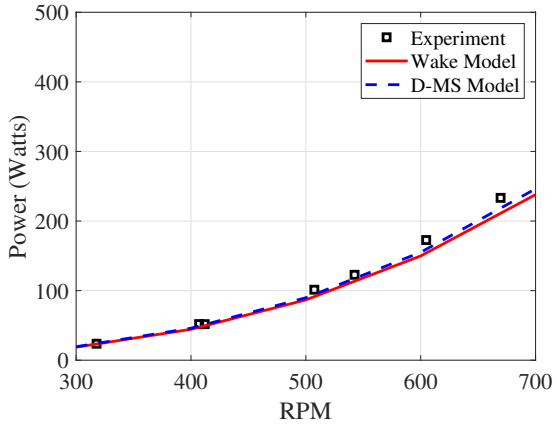


(c) Pitch Amplitude = 25°, Number of blades =4.

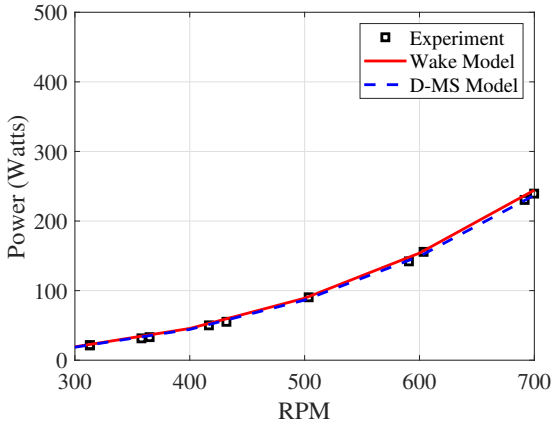


(d) Pitch Amplitude = 30°, Number of blades =2.

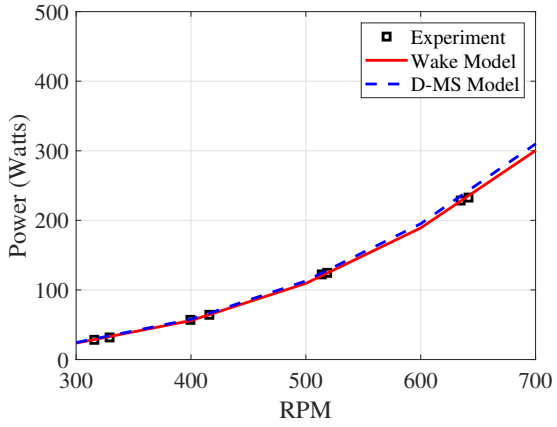


(e) Pitch Amplitude = 30°, Number of blades =3.

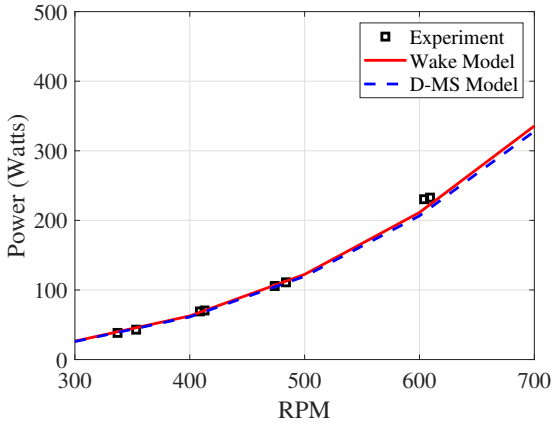


(f) Pitch Amplitude = 35°, Number of blades =2.

Figure 2.36: Validation of time-averaged power (experiment vs. free-wake vs. D-MS model).

creates asymmetry in side force between upper and lower halves due to blade drag. These two types of asymmetries create net time averaged side force on a cycloidal propeller even with zero phase offset.

4. Due to curvilinear flow, the cycloidal propeller blade experiences reverse or negative virtual camber in the upper half (upstream half) of its circular trajectory along with decrease in effective angle of attack due to negative virtual incidence. However, the blade experiences positive virtual camber (observed from inertial frame) and increase in effective angle of attack (due to positive virtual incidence) in the entire lower half (downstream half). For this reason, blades produce larger hydrodynamic forces in the lower or downstream half as observed from both experiments and analysis. Moreover, unsteady phenomena such as dynamic stall keep the flow attached to the cycloidal propeller blade up to very high pitch angles, which results in very high sectional force coefficients.

### 2.5.2 Concluding Remarks: Forward Flight Study

1. It is shown that forward flight velocity changes curvilinear geometry of flow associated with cycloidal rotor and this alters chord-wise variation of incident flow velocity angle on rotor blade. This chord wise variation of incident flow angle is manifested as dynamic nonlinear virtual camber effect, which is very different from what was observed previously for hover.

2. It is shown that dynamic nature of virtual camber plays an important role in the net vertical force production of cycloidal rotor in forward flight. cycloidal rotor blade experiences negative virtual camber near top of the cycle generating a negative vertical force and it experiences a positive virtual camber near bottom of the cycle generating a positive vertical force. Since rotor blade experiences large flow speed at bottom (advancing side) compared to top (retreating side), the positive vertical force produced at the bottom dominates the negative vertical force produced at the top. These phenomena lead to net positive vertical force over a complete cycle.

3. Cycloidal rotor's capability to produce net propulsive thrust heavily depends on dynamic virtual camber as well as local angle of attack and direction of local blade forces. cycloidal rotor blade produces small negative propulsive force in the upstream half of the cycle (near 0° azimuth) due to small negative virtual camber, but it produces large positive propulsive force at the downstream half of cycle (near 180° azimuth) due to combination of large positive virtual camber and positive angle of attack. These phenomena lead to net positive propulsive force over a complete cycle.

4. It is observed that incoming flow impacts downstream of cycloidal rotor at a higher speed compared to upstream due to acceleration of induced wake after upstream. As the advance ratio of the rotor increases, effect of induced flow and induced wake becomes insignificant and flow becomes more uniform and upstream and downstream flow velocity becomes similar.

5. As the advance ratio of cycloidal rotor is increased, net vertical force increases while net propulsive decreases. Also, the additional lift due to virtual camber increases as advance ratio of cycloidal rotor is increased.

6. The study shows that it is very important for the cycloidal rotor to have a backwards rotation with respect to forward speed (blade moving away from the flow in the upper half) in order to generate positive vertically upward force. A forward spin of cycloidal rotor would generate same amount of vertical force in opposite direction. However, the direction of propulsive force is insensitive to the direction of rotation.

Although the above mentioned lower order model is computationally inexpensive and capable of predicting rotor performance with sufficient accuracy, it can not capture the complex flow-field of cycloidal rotor with extreme accuracy. Specifically, it is extremely challenging to the capture the complex inflow distribution, blade vortex interaction and geometry of trailing vortices using a lower order model. For this reason, a high-fidelity model of cycloidal rotor based on free-wake is developed to further investigate aerodynamics of cycloidal rotor in more detail. The

wake model consists of near wake and free wake region which includes trailing vortices and shed wakes. The prediction of the developed free wake model shows even better correlation with in-house experimental data compared to that of a lower model. Although, wake model is much more expensive from computational point of view which limits its application for preliminary design optimization of cycloidal rotor.

# 3. STRUCTURAL MODELING OF CYCLOIDAL ROTOR*

## 3.1 Overview

Key part of any rotor design is to build light-weight blades which would also reduce weight of all load bearing components of rotor hub since they have to withstand less blade inertial forces. On the other hand, considerable blade deflections are inevitable for a light-weight rotor blade. Moreover, in case of cycloidal rotor, the centrifugal force of rotor blade acts radially causing more deflections of rotor blade unlike conventional rotor, where centrifugal force acts axially and causes axial stiffening of the blade. Additionally, the cycloidal rotor blade being constrained in bending at both ends, develops larger bending curvature which in turn causes large nonlinear deflections. It is also observed from in-house experiments that cyclodial rotor blades go through very large bending and torsional deflections which significantly affect rotor performance. In order to accurately obtain rotor performance, it is crucial to predict blade deflections. Towards this, two independent blade structural models are developed. For traditional rotorcraft structural analysis, $2^{nd}$ order nonlinear Hodges-Dowell [106] models are widely used among scientific community. Initially similar $2^{nd}$ order nonlinear model of cycloidal rotor is developed which is capable of predicting blade deflections of moderately flexible cycloidal rotor blades. Although, it is observed that such a $2^{nd}$ order model is unable to capture large deflections of highly flexible cyclodial rotor blades. For this purpose, a fully nonlinear geometrically exact structural model is developed. Detail development of both the models are discussed in the following subsections [30, 107].

To derive governing equations of motion of cycloidal rotor blade , different co-ordinate frames and their transformation matrices are required. Such as position vector is generally defined in mixed co-ordinate and require coordinate transformation. Now, the transformation matrix between

*Part of the data reported in this chapter is reprinted with permission from "Role of Blade Flexibility on Cycloidal Rotor Hover Performance" by Halder, A., and Benedict, M., *Journal of Aircraft*, Vol. 55, No. 5, pp. 1773-1791, 2018 [30] and "Understanding the Effect of Blade flexibility on Cycloidal Rotor Performance in Hover" by Halder, A., and Benedict, M., *Proceedings of the American Helicopter Society Specialists' Meeting on Aeromechanics*, 2016 [107].

deformed blade frame and un-deformed blade frame is very complex. Moreover, computation of kinetic energy requires higher order temporal derivatives of these coordinate transformation matrices and computation of potential energy requires higher order spatial derivatives of these coordinate transformation matrices which become even more complex. To simplify related mathematics and decrease computational expense, a $2^{nd}$ order nonlinear assumption of transformation matrix between deformed and un-deformed blade frame is taken for traditional Hodges-Dowell model where nonlinear terms upto $2^{nd}$ order only are retained while all other higher order nonlinear terms are neglected. These assumptions are not entirely valid for large nonlinear deflections of cycloidal rotor blades. Specifically highly flexible cycloidal rotor blades go through large nonlinear torsional deflections arising due to radial and tangential bending curvature. Unlike conventional rotor blades, which are cantilever in nature, cycloidal rotor blades are fixed in bending at both end which caused even larger bending curvatures and related nonlinear twist. For all these reasons, it is essential to develop a fully nonlinear structural model to accurately capture blade deflections of cycloidal rotor blades. To solve this problem, a geometrically exact beam model is developed where an exact transformation matrix between deformed and un-deformed blade frame is utilized for deriving governing equations of motion and all the higher order non-linear terms are retained in sub-sequence steps.

The governing equations of motion of rotor blades are obtained using generalized Hamilton's principle (Eq. 4.1).

$$\delta\Pi = \int_{t_1}^{t_2} (\delta T - \delta U + \delta W) dt = 0 \tag{3.1}$$

In the above equation, $T$ is kinetic energy,$U$ is potential energy (for cycloidal rotor blades it is basically strain energy) and $W$ is non-potential energy, generally due to aerodynamic forces. For only structural model, aerodynamic forces are neglected. First step in deriving governing differential equation is defining local position vectors of blade element in proper co-ordinate frames. From there, inertial velocity and inertial acceleration vectors are computed using transport theorem. Once the kinematics is derived up to acceleration level, kinetic energy of the system and its variation is computed. On the other, to compute variation of strain energy, strain energy is initially

expressed in terms of stresses and strains. Then, stress-strain relationship used to replace all the stress terms in strain energy. After that, strain-deflection relationships are used to replace all the strain terms in strain energy and finally strain energy is expressed in terms of deflections. And finally substituting kinetic and strain energy in Hamilton's principle (Eq. 4.1), governing equations of motion are formulated. Detail formulations of both 2nd order model and geometrically exact model are given below.

### 3.2 Reference Frames and Coordinate System

Four reference frames and related coordinate systems are used for the purpose of deriving governing equations of motion of cyclodial rotor blades. These reference frames are, 1) Inertial Frame $(X, Y, Z)$, 2) Rotating frame $(X_R, Y_R, Z_R)$ which is rotating with cycloidal rotor blade, 3) Pitching or Un-deformed blade frame $(X_U, Y_U, Z_U)$ which is rotating and pitching with cycloidal rotor blade, and 4) Deformed blade frame $(X_D, Y_D, Z_D)$. Figure 3.1 shows different coordinate frames. $\hat{i}_A$, $\hat{i}_B$ and $\hat{i}_C$ are unit vectors in the inertial coordinate system $(X, Y, Z)$; $\hat{i}_a$, $\hat{i}_b$ and $\hat{i}_c$ are unit vectors in the rotating coordinate system $(X_R, Y_R, Z_R)$; $\hat{i}_x$, $\hat{i}_y$ and $\hat{i}_z$ are unit vectors in the un-deformed blade coordinate system, and $\hat{i}_1$, $\hat{i}_2$ and $\hat{i}_3$ are unit vectors in the deformed blade coordinate system. $\eta$ and $\zeta$ are distance along coordinates parallel and normal to blade chord in deformed blade coordinate $(X_D, Y_D, Z_D)$. These frame of reference were used for formulation of both $2^{nd}$ order model and geometrically exact model. Transformation matrix between rotating frame and inertial frame, $T_{RI}$, is given by following expression

$$[T_{RI}] = \begin{bmatrix} 1 & 0 & 0 \\ 0 & \cos\psi & -\sin\psi \\ 0 & \sin\psi & \cos\psi \end{bmatrix}, \tag{3.2}$$

Where ,

$$\begin{bmatrix} \hat{i}_a \\ \hat{i}_b \\ \hat{i}_c \end{bmatrix} = [T_{RI}] \begin{bmatrix} \hat{i}_A \\ \hat{i}_B \\ \hat{i}_C \end{bmatrix} \tag{3.3}$$

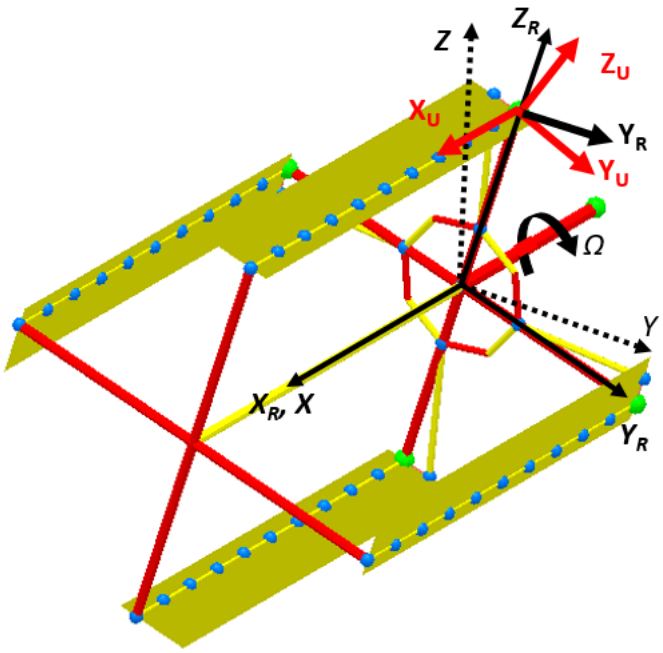


Figure 3.1: Coordinate Frames.

In Eq. 3.2, $\psi$ is azimuth angle. Transformation matrix between un-deformed blade frame and rotating frame, $T_{UR}$, is given by following expression

$$[T_{UR}] = \begin{bmatrix} 1 & 0 & 0 \\ 0 & \cos\theta & \sin\theta \\ 0 & -\sin\theta & \cos\theta \end{bmatrix} \tag{3.4}$$

Where,

$$\begin{bmatrix} \hat{i}_x \\ \hat{i}_y \\ \hat{i}_z \end{bmatrix} = [T_{UR}] \begin{bmatrix} \hat{i}_a \\ \hat{i}_b \\ \hat{i}_c \end{bmatrix} \tag{3.5}$$

In Eq. 3.4, $\theta$ is pitch angle of the cycloidal rotor blade.Transformation matrix between deformed and un-deformed blade frame, $T_{DU}$, is defined as 3.6

$$\begin{bmatrix} \hat{i}_1 \\ \hat{i}_2 \\ \hat{i}_3 \end{bmatrix} = [T_{DU}] \begin{bmatrix} \hat{i}_x \\ \hat{i}_y \\ \hat{i}_z \end{bmatrix} \tag{3.6}$$

$T_{DU}$ matrix depends on blade deflections. Expression of $T_{DU}$ matrix is different in $2^{nd}$ order non-linear model and geometrically exact model. In fact, primary improvement of geometrically exact model over $2^{nd}$ order model is exact computation of this $T_{DU}$ matrix which is a complicated function of deflections and would be discussed in detail later. For $2^{nd}$ order model, all the higher order non-linear terms of $T_{DU}$ matrix is neglected which is not entirely valid for large deflections of cycloidal rotor blade.

## 3.3 $2^{nd}$ Order Nonlinear Model

$2^{nd}$ order nonlinear model is similar to Hodges-Dowell model which is widely used for conventional rotorcraft analysis. In this context, the cycloidal rotor blade is considered as an isotropic beam that can go through four types of deflections: 1) axial elongation ($u$), 2) radial bending (bending deflection in flap direction - $w$), 3) tangential bending (bending deflection in lag direction - $v$), and 4) axial twist ($\phi$). In Fig. 3.2, definition of these four type of deflections are given.

### 3.3.1 Computation of Kinetic Energy

First step towards deriving kinetic energy is to define inertial position vector of a blade element. Generally position vector is defined in mixed coordinate for sake of simplicity and converted to rotating frame using suitable transformation matrices between different frames. Then, inertial velocity vector is calculated from inertial position vector using transport theorem. Once kinematics is computed upto velocity level, variation of kinetic energy is calculated using calculus of variations. Position vector of an arbitrary point on the rotor blade can be expressed in mixed coordinate as

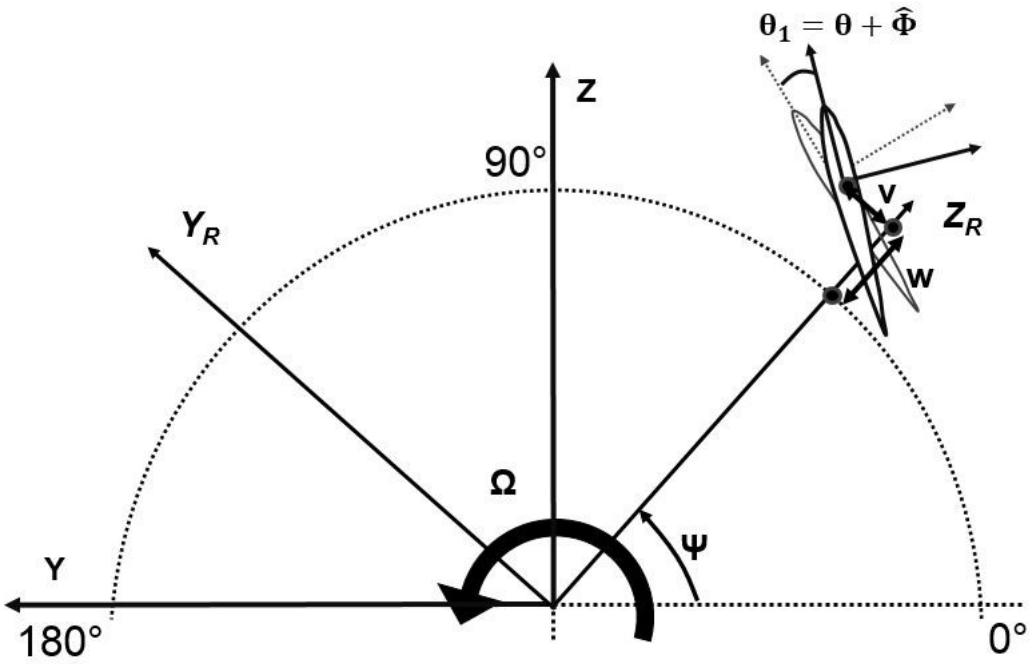


Figure 3.2: Definition of deflections on a cycloidal rotor blade

given in Eq. 3.7.

$$\vec{r} = R\hat{i}_c + (x+u)\hat{i}_a + v\hat{i}_b + w\hat{i}_c + \eta\hat{i}_2 + \zeta\hat{i}_3 \tag{3.7}$$

In the above equation, x is span-wise distance of a blade element in un-deformed blade. Here, the effect of warping is neglected while calculating kinetic energy. Using mathematical manipulation, Eq. 3.7 can be expressed as

$$\vec{r} = [(x+u) \;\; v \;\; (w+R)] \begin{bmatrix} \hat{i}_a \\ \hat{i}_b \\ \hat{i}_c \end{bmatrix} + [0 \;\; \eta \;\; \zeta] \begin{bmatrix} \hat{i}_1 \\ \hat{i}_2 \\ \hat{i}_3 \end{bmatrix} \tag{3.8}$$

$$\vec{r} = [(x+u) \;\; v \;\; (w+R)] \begin{bmatrix} \hat{i}_a \\ \hat{i}_b \\ \hat{i}_c \end{bmatrix} + [0 \;\; \eta \;\; \zeta] \, [T_{DU}] \begin{bmatrix} \hat{i}_x \\ \hat{i}_y \\ \hat{i}_z \end{bmatrix} \tag{3.9}$$

$$\vec{r} = [(x+u) \;\; v \;\; (w+R)] \begin{bmatrix} \hat{i}_a \\ \hat{i}_b \\ \hat{i}_c \end{bmatrix} + [0 \;\; \eta \;\; \zeta] \, [T_{DU}] \, [T_{UR}] \begin{bmatrix} \hat{i}_a \\ \hat{i}_b \\ \hat{i}_c \end{bmatrix} \tag{3.10}$$

$$\vec{r} = \{ \;\; [(x+u) \;\; v \;\; (w+R)] + [0 \;\; \eta \;\; \zeta] \, [T_{DR}] \;\; \} \begin{bmatrix} \hat{i}_a \\ \hat{i}_b \\ \hat{i}_c \end{bmatrix} \tag{3.11}$$

In the above equation, $T_{DR}$ is transformation matrix between deformed blade frame and rotating frame given by following expression

$$[T_{DR}] = [T_{DU}] \, [T_{UR}] \tag{3.12}$$

$$\begin{bmatrix} \hat{i}_1 \\ \hat{i}_2 \\ \hat{i}_3 \end{bmatrix} = [T_{DR}] \begin{bmatrix} \hat{i}_a \\ \hat{i}_b \\ \hat{i}_c \end{bmatrix} \tag{3.13}$$

Let's assume $[\hat{i}_a \;\; \hat{i}_b \;\; \hat{i}_c]$ goes through 3-2-1 Euler rotation by angles $\xi_1$, $-\beta_1$, $\theta_1$ and align with $[\hat{i}_1 \;\; \hat{i}_2 \;\; \hat{i}_3]$. Then $T_{DR}$ matrix can be expressed as

$$[T_{DR}] = \begin{bmatrix} c_{\xi_1} c_{\beta_1} & s_{\xi_1} c_{\beta_1} & s_{\beta_1} \\ -c_{\xi_1} s_{\beta_1} s_{\theta_1} - s_{\xi_1} c_{\theta_1} & -s_{\xi_1} s_{\beta_1} s_{\theta_1} + c_{\xi_1} c_{\theta_1} & c_{\beta_1} s_{\theta_1} \\ -c_{\xi_1} s_{\beta_1} c_{\theta_1} + s_{\xi_1} s_{\theta_1} & -s_{\xi_1} s_{\beta_1} c_{\theta_1} - c_{\xi_1} s_{\theta_1} & c_{\beta_1} c_{\theta_1} \end{bmatrix} \tag{3.14}$$

In the above equation, $c_{()} = \cos()$ and $s_{()} = \sin()$. The objective is to get $T_{DU}$ matrix in terms of deflections. For that reason, $\xi_1$, $\beta_1$ and $\theta_1$ are expressed in terms of deflections. Finally $T_{DU}$ matrix

can be written as [108]

$$[T_{DR}] = \begin{bmatrix} \sqrt{1-v^{+^2}-w^{+^2}} & v^+ & w^+ \\ \frac{-v^+c_{\theta_1}-w^+s_{\theta_1}\sqrt{1-v^{+^2}-w^{+^2}}}{\sqrt{1-w^{+^2}}} & \frac{-v^+w^+s_{\theta_1}+c_{\theta_1}\sqrt{1-v^{+^2}-w^{+^2}}}{\sqrt{1-w^{+^2}}} & s_{\theta_1}\sqrt{1-w^{+^2}} \\ -\frac{v^+s_{\theta_1}-w^+c_{\theta_1}\sqrt{1-v^{+^2}-w^{+^2}}}{\sqrt{1-w^{+^2}}} & \frac{-v^+w^+c_{\theta_1}-s_{\theta_1}\sqrt{1-v^{+^2}-w^{+^2}}}{\sqrt{1-w^{+^2}}} & c_{\theta_1}\sqrt{1-w^{+^2}} \end{bmatrix} \tag{3.15}$$

In the above equation, $()^+ = \frac{\delta}{\delta r}()$. Here $r$ is curvilinear distance coordinate along the span of deformed blade elastic axis. In second order non-linear approximation, $()^+ = ()'$ and $\sqrt{1+d} = 1 + d/2$ when, deflection $d$ is very small. By taking $2^{nd}$ order approximation, Eq. 3.15 can be written as following expression

$$[T_{DR}] = \begin{bmatrix} 1-0.5v'^2-0.5w'^2 & v' & w' \\ -v'c_{\theta_1}-w's_{\theta_1} & -v'w's_{\theta_1}+(1-0.5v'^2)c_{\theta_1} & (1-0.5w'^2)s_{\theta_1} \\ v's_{\theta_1}-w'c_{\theta_1} & -v'w'c_{\theta_1}-(1-0.5v'^2)s_{\theta_1} & (1-0.5w'^2)c_{\theta_1} \end{bmatrix} \tag{3.16}$$

Where,

$$\theta_1 = \theta + \phi - \int_0^x w'v''dx \tag{3.17}$$

In above equation, $\theta$ is pitch angle of the rotor blade. Substituting value of $T_{DR}$ from Eq. 3.16 into Eq. 3.11 and taking $2^{nd}$ order non-linear approximation again, inertial position vector of an arbitrary point on cycloidal rotor blade can be re-written as

$$\vec{r} = x_1\hat{i}_a + y_1\hat{i}_b + (z_1+R)\hat{i}_c \tag{3.18}$$

Where, $x_1, y_1$, and $z_1$ can be expressed as given below.

$$x_1 = x + u - v'(y_1 - v) - w'(z_1 - w) \tag{3.19}$$

$$y_1 = v + \eta\cos(\theta+\phi) - \zeta\sin(\theta+\phi) \tag{3.20}$$

$$z_1 = w + \eta \sin(\theta + \phi) + \zeta \cos(\theta + \phi) \tag{3.21}$$

Inertial velocity vector can be calculated by taking inertial time derivative of inertial position vector. Using transport theorem, inertial velocity can be expressed as

$$\vec{V} = \frac{\partial \vec{r}}{\partial t} + \vec{\Omega} \times \vec{r} \tag{3.22}$$

In above equation, $\vec{\Omega} = -\Omega \hat{i}_a$ is angular velocity of cycloidal rotor. From Eq. 3.22, inertial velocity can be written as

$$\vec{V} = \dot{x}_1 \hat{i}_a + (\dot{y}_1 + \Omega\ (z_1 + R))\hat{i}_b + (\dot{z}_1 - \Omega\ y_1)\hat{i}_c \tag{3.23}$$

Variation of velocity vector is computed as

$$\delta\vec{V} = \delta\dot{x}_1 \hat{i}_a + (\delta\dot{y}_1 + \Omega\ \delta z_1)\hat{i}_b + (\delta\dot{z}_1 - \Omega\ \delta y_1)\hat{i}_c \tag{3.24}$$

$$\vec{V} \cdot \delta\vec{V} = \dot{x}_1\ \delta\dot{x}_1 + (\dot{y}_1 + \Omega\ (z_1 + R))(\delta\dot{y}_1 + \Omega\ \delta z_1) + (\dot{z}_1 - \Omega\ y_1)(\delta\dot{z}_1 - \Omega\ \delta y_1) \tag{3.25}$$

The expression of variation of kinetic energy is given by

$$\delta T = \int_0^L \iint_A \rho \vec{V} \cdot \delta\vec{V}\ \ dA\ \ dx \tag{3.26}$$

According to variational method, above expression of variation of kinetic energy would have to be integrated in time between two arbitrary time-points $t_1$ and $t_2$. By anticipating integration by parts, Eq. 3.25 can be written as:

$$\begin{aligned}
\vec{V} \cdot \delta\vec{V} &= -\ddot{x}_1\ \delta x_1 - (\ddot{y}_1 + \Omega\dot{z}_1)\ \delta y_1 + [\Omega\dot{y}_1 + \Omega^2(z_1 + R)]\ \delta z_1 \\
&\quad + (-\ddot{z}_1 + \Omega\dot{y}_1)\ \delta z_1 - (\Omega\dot{z}_1 - \Omega^2 y_1)\ \delta y_1 \\
&= -\ddot{x}_1\ \delta x_1 - (\ddot{y}_1 + 2\Omega\dot{z}_1 - \Omega^2 y_1)\ \delta y_1 + [-\ddot{z}_1 + 2\Omega\dot{y}_1 + \Omega^2(z_1 + R)]\ \delta z_1
\end{aligned} \tag{3.27}$$

In the above procedure during integration by parts, initial and final values (i.e $\dot{x}_1 \ \delta x_1 \ \Big|_{t1}^{t2}$ ) are taken as zero. Substituting Eq. 3.27 into Eq. 3.26, variation of kinetic energy can be expressed as following equation.

$$\delta T = \int_0^L \iint_A \rho\Big( - \ddot{x}_1 \, \delta x_1 - (\ddot{y}_1 + 2\Omega\dot{z}_1 - \Omega^2 y_1) \, \delta y_1 + [-\ddot{z}_1 + 2\Omega\dot{y}_1 + \Omega^2(z_1 + R)] \, \delta z_1\Big) \ dA \ \ dx \tag{3.28}$$

Now to compute above expression, higher order temporal derivatives of $x_1$, $y_1$ and $z_1$ is required. $\dot{x}_1$ is obtained by taking time derivative of both sides of Eq. 3.19.

$$\begin{aligned}
\dot{x}_1 &= \dot{u} - \dot{v}'[\eta\cos(\theta+\phi) - \zeta\sin(\theta+\phi)] - \dot{w}'[\eta\sin(\theta+\phi) + \zeta\cos(\theta+\phi)] \\
&\quad + \Big(v'[\eta\sin(\theta+\phi) + \zeta\cos(\theta+\phi)] - w'[\eta\cos(\theta+\phi) - \zeta\sin(\theta+\phi)]\Big)(\dot{\theta}+\dot{\phi}) \\
&= \dot{u} - [\eta\cos(\theta+\phi) - \zeta\sin(\theta+\phi)][\dot{v}' + w'(\dot{\theta}+\dot{\phi})] \\
&\quad - [\eta\sin(\theta+\phi) + \zeta\cos(\theta+\phi)][\dot{w}' - v'(\dot{\theta}+\dot{\phi})]
\end{aligned} \tag{3.29}$$

Now, $\ddot{x}_1$ is computed from above equation.

$$\begin{aligned}
\ddot{x}_1 = \ddot{u} &- [\eta\cos(\theta+\phi) - \zeta\sin(\theta+\phi)][\ddot{v}' + w'(\ddot{\theta}+\ddot{\phi}) + \dot{w}'(\dot{\theta}+\dot{\phi})] \\
&- [\eta\sin(\theta+\phi) + \zeta\cos(\theta+\phi)][\ddot{w}' - v'(\ddot{\theta}+\ddot{\phi}) - \dot{v}'(\dot{\theta}+\dot{\phi})] \\
&+ [\eta\sin(\theta+\phi) + \zeta\cos(\theta+\phi)][\dot{v}'(\dot{\theta}+\dot{\phi}) + w'(\dot{\theta}+\dot{\phi})^2] \\
&- [\eta\cos(\theta+\phi) - \zeta\sin(\theta+\phi)][\dot{w}'(\dot{\theta}+\dot{\phi}) - v'(\dot{\theta}+\dot{\phi})^2]
\end{aligned} \tag{3.30}$$

After mathematical manipulation above equation can be re-written as following.

$$\begin{aligned}
\ddot{x}_1 = \ddot{u} &- [\eta\cos(\theta+\phi) - \zeta\sin(\theta+\phi)]a_1 \\
&- [\eta\sin(\theta+\phi) + \zeta\cos(\theta+\phi)]a_2
\end{aligned} \tag{3.31}$$

Where,

$$a_1 = \ddot{v}' + w'(\ddot{\theta} + \ddot{\phi}) + 2\dot{w}'(\dot{\theta} + \dot{\phi}) - v'(\dot{\theta} + \dot{\phi})^2 \tag{3.32}$$

$$a_2 = \ddot{w}' - v'(\ddot{\theta} + \ddot{\phi}) - 2\dot{v}'(\dot{\theta} + \dot{\phi}) - w'(\dot{\theta} + \dot{\phi})^2 \tag{3.33}$$

Now, $\dot{y}_1$ is obtained by taking time derivative of both sides of Eq. 3.20.

$$\dot{y}_1 = \dot{v} - [\eta \sin(\theta + \phi) + \zeta \cos(\theta + \phi)](\dot{\theta} + \dot{\phi}) \tag{3.34}$$

From above equation, $\ddot{y}_1$ is obtained as following.

$$\begin{aligned} \ddot{y}_1 = \ddot{v} &- [\eta \cos(\theta + \phi) - \zeta \sin(\theta + \phi)](\dot{\theta} + \dot{\phi})^2 \\ &- [\eta \sin(\theta + \phi) + \zeta \cos(\theta + \phi)](\ddot{\theta} + \ddot{\phi}) \end{aligned} \tag{3.35}$$

Now, $\dot{z}_1$ is obtained by taking time derivative of both sides of Eq. 3.21.

$$\dot{z}_1 = \dot{w} + [\eta \cos(\theta + \phi) - \zeta \sin(\theta + \phi)](\dot{\theta} + \dot{\phi}) \tag{3.36}$$

From above equation, $\ddot{z}_1$ is obtained as following.

$$\begin{aligned} \ddot{z}_1 = \ddot{w} &- [\eta \sin(\theta + \phi) + \zeta \cos(\theta + \phi)](\dot{\theta} + \dot{\phi})^2 \\ &+ [\eta \cos(\theta + \phi) - \zeta \sin(\theta + \phi)](\ddot{\theta} + \ddot{\phi}) \end{aligned} \tag{3.37}$$

Moreover, to compute variation of kinetic energy, variation of $x_1$, $y_1$ and $z_1$ is required. $\delta x_1$ is obtained from Eq. 3.19.

$$\begin{aligned} \delta x_1 = \delta u &- \delta v'[\eta \cos(\theta + \phi) - \zeta \sin(\theta + \phi)] - \delta w'[\eta \sin(\theta + \phi) + \zeta \cos(\theta + \phi)] \\ &+ \Big(v'[\eta \sin(\theta + \phi) + \zeta \cos(\theta + \phi)] - w'[\eta \cos(\theta + \phi) - \zeta \sin(\theta + \phi)]\Big)\delta\phi \end{aligned} \tag{3.38}$$

From Eq. 3.20, $\delta y_1$ is computed.

$$\delta y_1 = \delta v - [\eta \sin(\theta + \phi) + \zeta \cos(\theta + \phi)]\delta\phi \tag{3.39}$$

From Eq. 3.21, $\delta z_1$ is computed.

$$\delta z_1 = \delta w + [\eta \cos(\theta + \phi) - \zeta \sin(\theta + \phi)]\delta\phi \tag{3.40}$$

Substituting expressions of $x_1$, $y_1$ and $z_1$ from above equations (Eq. 3.38-3.40) into Eq. 3.28, variation of kinetic energy can be expressed as following equation.

$$\begin{aligned}
\delta T = \int_0^L \iint_A \Big( & \delta u(-\rho\ddot{x}_1) + \delta v'\rho\ddot{x}_1[\eta \cos(\theta + \phi) - \zeta \sin(\theta + \phi)] \\
& + \delta w'\rho\ddot{x}_1[\eta \sin(\theta + \phi) + \zeta \cos(\theta + \phi)] \\
& - \delta\phi\rho\ddot{x}_1 v'[\eta \sin(\theta + \phi) + \zeta \cos(\theta + \phi)] \\
& + \delta\phi\rho\ddot{x}_1 w'[\eta \cos(\theta + \phi) - \zeta \sin(\theta + \phi)] \\
& - \rho[\ddot{z}_1 - 2\Omega\dot{y}_1 - \Omega^2(z_1 + R)]\big(\delta w + [\eta \cos(\theta + \phi) - \zeta \sin(\theta + \phi)]\delta\phi\big) \\
& - \rho(\ddot{y}_1 + 2\Omega\dot{z}_1 - \Omega^2 y_1)\big(\delta v - [\eta \sin(\theta + \phi) + \zeta \cos(\theta + \phi)]\delta\phi\big)\Big)\ dA\ dx
\end{aligned} \tag{3.41}$$

Using mathematical manipulation, above equation is re-written as following.

$$\begin{aligned}
\delta T = \int_0^L \iint_A \Big( & \delta u(-\rho\ddot{x}_1) + \delta v\rho(-\ddot{y}_1 - 2\Omega\dot{z}_1 + \Omega^2 y_1) \\
& + \delta w\rho[-\ddot{z}_1 + 2\Omega\dot{y}_1 + \Omega^2(z_1 + R)] \\
& + \delta v'\rho\ddot{x}_1[\eta \cos(\theta + \phi) - \zeta \sin(\theta + \phi)] \\
& + \delta w'\rho\ddot{x}_1[\eta \sin(\theta + \phi) + \zeta \cos(\theta + \phi)] + \delta\phi a_3\Big)\ dA\ dx
\end{aligned} \tag{3.42}$$

Where,

$$a_3 = \rho[\eta \sin(\theta+\phi) + \zeta \cos(\theta+\phi)](-\ddot{x}_1 v' + \ddot{y}_1 + 2\Omega \dot{z}_1 - \Omega^2 y_1) + \rho[\eta \cos(\theta+\phi) - \zeta \sin(\theta+\phi)][\ddot{x}_1 w' - \ddot{z}_1 + 2\Omega \dot{y}_1 + \Omega^2(z_1 + R)] \tag{3.43}$$

Now, variation of kinetic energy can be expressed as following equation.

$$\delta T = \int_0^L (T_u\ \delta u + T_v\ \delta v + T_w\ \delta w + T_{v'}\ \delta v' + T_{w'}\ \delta w' + T_\phi\ \delta\phi)\ dx \tag{3.44}$$

Where,

$$T_u = -\iint_A \rho \ddot{x}_1\ \ dA \tag{3.45}$$

$$T_v = \iint_A \rho(-\ddot{y}_1 - 2\Omega \dot{z}_1 + \Omega^2 y_1)\ \ dA \tag{3.46}$$

$$T_w = \iint_A \rho[-\ddot{z}_1 + 2\Omega \dot{y}_1 + \Omega^2(z_1 + R)]\ \ dA \tag{3.47}$$

$$T_{v'} = \iint_A \rho \ddot{x}_1[\eta \cos(\theta+\phi) - \zeta \sin(\theta+\phi)]\ \ dA \tag{3.48}$$

$$T_{w'} = \iint_A \rho \ddot{x}_1[\eta \sin(\theta+\phi) + \zeta \cos(\theta+\phi)]\ \ dA \tag{3.49}$$

$$T_\phi = \iint_A a_3\ \ dA \tag{3.50}$$

To compute above integrals following sectional properties are introduced.

$$\left.\begin{aligned} \iint_A \rho\ \ dA &= m \\ \iint_A \rho\eta\ \ dA &= m e_g \\ \iint_A \rho\zeta^2\ \ dA &= m k_{m_1}^2 \\ \iint_A \rho\eta^2\ \ dA &= m k_{m_2}^2 \\ \iint_A \rho(\eta^2+\zeta^2)\ \ dA &= m k_{m_1}^2 + m k_{m_2}^2 = m k_m^2 \end{aligned}\right\} \tag{3.51}$$

In the above equation, $m$ is blade mass per unit length and $e_g$ is position of blade center of gravity ahead from from blade elastic axis. $k_{m_1}^2$ and $k_{m_2}^2$ are mass moments of inertia per unit blade along flap and lag directions respectively.These moments of inertia are about elastic axis. The rotor blade cross-section is assumed to be symmetric about the $\hat{i}_2$ axis. For that reason, following integrals become zeros.

$$\left.\begin{aligned} \iint_A \rho\zeta \ \ dA = 0 \\ \iint_A \rho\zeta\eta \ \ dA = 0 \end{aligned}\right\} \tag{3.52}$$

Using the above mentioned sectional properties, the coefficients ($T_u$, $T_v$, $T_w$, $T_{v'}$, $T_{w'}$ and $T_\phi$) of variation of deflections are computed using following approach.

Substituting expression of $\ddot{x}_1$ from Eq. 3.31 into Eq. 3.45, $T_u$ can be expressed as

$$\begin{aligned} T_u = &- \iint_A \rho\Big(\ddot{u} - [\eta\cos(\theta+\phi) - \zeta\sin(\theta+\phi)]a_1 \\ &\quad - [\eta\sin(\theta+\phi) + \zeta\cos(\theta+\phi)]a_2\Big) \ \ dA \\ &= -m\ddot{u} + a_1 I_{a1} + a_2 I_{a2} \end{aligned} \tag{3.53}$$

Where,

$$\begin{aligned} I_{a1} &= \iint_A \rho[\eta\cos(\theta+\phi) - \zeta\sin(\theta+\phi)] \ \ dA \\ &= me_g\cos(\theta+\phi) \end{aligned} \tag{3.54}$$

$$\begin{aligned} I_{a2} &= \iint_A \rho[\eta\sin(\theta+\phi) + \zeta\cos(\theta+\phi)] \ \ dA \\ &= me_g\sin(\theta+\phi) \end{aligned} \tag{3.55}$$

Substituting values of $I_{a1}$, $I_{a2}$, $a_1$ and $a_2$ into Eq. 3.53, $T_u$ can expressed as following equation.

$$\begin{aligned} T_u = &-m\ddot{u} + [\ddot{v}' + w'(\ddot{\theta} + \ddot{\phi}) + 2\dot{w}'(\dot{\theta} + \dot{\phi}) - v'(\dot{\theta} + \dot{\phi})^2]me_g \cos(\theta + \phi) \\ &+ [\ddot{w}' - v'(\ddot{\theta} + \ddot{\phi}) - 2\dot{v}'(\dot{\theta} + \dot{\phi}) - w'(\dot{\theta} + \dot{\phi})^2]me_g \sin(\theta + \phi) \end{aligned} \tag{3.56}$$

Substituting expression of $\ddot{y}_1$ (from Eq. 3.35), $\dot{z}_1$ (from Eq. 3.36) and $y_1$ (from Eq. 3.20) into Eq. 3.46, $T_v$ can be computed.

$$\begin{aligned} T_v = \iint_A \Big(\rho\big( &- \ddot{v} + [\eta\cos(\theta + \phi) - \zeta\sin(\theta + \phi)](\dot{\theta} + \dot{\phi})^2 \\ &+ [\eta\sin(\theta + \phi) + \zeta\cos(\theta + \phi)](\ddot{\theta} + \ddot{\phi})\big) \\ &- 2\Omega\rho\big(\dot{w} + [\eta\cos(\theta + \phi) - \zeta\sin(\theta + \phi)](\dot{\theta} + \dot{\phi})\big) \\ &+ \Omega^2\rho\big(v + [\eta\cos(\theta + \phi) - \zeta\sin(\theta + \phi)]\big)\Big)\ dA \end{aligned} \tag{3.57}$$

Using mathematical manipulation, $T_v$ can be re-writtens as

$$\begin{aligned} T_v = &-m\ddot{v} + me_g\cos(\theta + \phi)(\dot{\theta} + \dot{\phi})^2 + me_g\sin(\theta + \phi)(\ddot{\theta} + \ddot{\phi}) \\ &- 2\Omega m[\dot{w} + e_g\cos(\theta + \phi)(\dot{\theta} + \dot{\phi})] + m\Omega^2[v + e_g\cos(\theta + \phi)] \end{aligned} \tag{3.58}$$

Substituting expression of $\ddot{z}_1$ (from Eq. 3.37), $\dot{y}_1$ (from Eq. 3.34) and $z_1$ (from Eq. 3.21) into Eq. 3.47, $T_w$ can be computed.

$$\begin{aligned} T_w = \iint_A \Big(\rho\big( &- \ddot{z} + [\eta\sin(\theta + \phi) + \zeta\cos(\theta + \phi)](\dot{\theta} + \dot{\phi})^2 \\ &- [\eta\cos(\theta + \phi) - \zeta\sin(\theta + \phi)](\ddot{\theta} + \ddot{\phi})\big) \\ &+ 2\Omega\rho\big(\dot{v} - [\eta\sin(\theta + \phi) + \zeta\cos(\theta + \phi)]](\dot{\theta} + \dot{\phi})\big) \\ &+ \Omega^2\rho\big(w + R + [\eta\sin(\theta + \phi) + \zeta\cos(\theta + \phi)]\big)\Big)\ dA \end{aligned} \tag{3.59}$$

Using mathematical manipulation, $T_w$ can be re-writtens as

$$T_w = -m\ddot{w} + me_g \sin(\theta+\phi)(\dot{\theta}+\dot{\phi})^2 - me_g \cos(\theta+\phi)(\ddot{\theta}+\ddot{\phi}) + 2\Omega m[\dot{v} - e_g \sin(\theta+\phi)(\dot{\theta}+\dot{\phi})] + m\Omega^2[w + R + e_g \sin(\theta+\phi)] \tag{3.60}$$

Substituting expression of $\ddot{x}_1$ from Eq. 3.31 into Eq. 3.48, $T_{v'}$ can be expressed as

$$\begin{aligned} T_{v'} &= \iint_A \rho\Big(\ddot{u}[\eta\cos(\theta+\phi) - \zeta\sin(\theta+\phi)] - [\eta\cos(\theta+\phi) - \zeta\sin(\theta+\phi)]^2 a_1 \\ &\qquad - [\eta\cos(\theta+\phi) - \zeta\sin(\theta+\phi)][\eta\sin(\theta+\phi) + \zeta\cos(\theta+\phi)]a_2\Big)\ dA \\ &= m\ddot{u}e_g\cos(\theta+\phi) + a_1 I_{a3} + a_2 I_{a4} \end{aligned} \tag{3.61}$$

Where,

$$\begin{aligned} I_{a3} &= \iint_A \rho[\eta\cos(\theta+\phi) - \zeta\sin(\theta+\phi)]^2\ dA \\ &= \iint_A \rho[\eta^2\cos^2(\theta+\phi) + \zeta^2\sin^2(\theta+\phi) - 2\eta\zeta\sin\theta+\phi\cos\theta+\phi]\ dA \\ &= mk_{m_2}^2\cos^2(\theta+\phi) + mk_{m_1}^2\sin^2(\theta+\phi) \end{aligned} \tag{3.62}$$

$$\begin{aligned} I_{a4} &= \iint_A \rho[\eta\cos(\theta+\phi) - \zeta\sin(\theta+\phi)][\eta\sin(\theta+\phi) + \zeta\cos(\theta+\phi)]\ dA \\ &= \iint_A \rho[\eta^2\sin(\theta+\phi)\cos(\theta+\phi) + \eta\zeta\cos^2(\theta+\phi) - \eta\zeta\sin^2(\theta+\phi) \\ &\qquad - \zeta^2\sin(\theta+\phi)\cos(\theta+\phi)]\ dA \\ &= m(k_{m_2}^2 - k_{m_1}^2)\sin(\theta+\phi)\cos(\theta+\phi) \end{aligned} \tag{3.63}$$

Substituting values of $I_{a3}$, $I_{a4}$, $a_1$ and $a_2$ into Eq. 3.61, $T_{v'}$ can expressed as following equation.

$$\begin{aligned} T_{v'} = & m\ddot{u}e_g \sin(\theta+\phi) + [\ddot{v}' + w'(\ddot{\theta}+\ddot{\phi}) + 2\dot{w}'(\dot{\theta}+\dot{\phi}) - v'(\dot{\theta}+\dot{\phi})^2] \\ & [mk_{m_1}^2 \sin^2(\theta+\phi) + mk_{m_2}^2 \cos^2(\theta+\phi)] \\ & + [\ddot{w}' - v'(\ddot{\theta}+\ddot{\phi}) - 2\dot{v}'(\dot{\theta}+\dot{\phi}) - w'(\dot{\theta}+\dot{\phi})^2] \\ & [m(k_{m_2}^2 - k_{m_1}^2)\sin(\theta+\phi)\cos(\theta+\phi)] \end{aligned} \tag{3.64}$$

Substituting expression of $\ddot{x}_1$ from Eq. 3.31 into Eq. 3.49, $T_{w'}$ can be expressed as

$$\begin{aligned} T_{w'} = & \iint_A \rho\Big(\ddot{u}[\eta\sin(\theta+\phi) + \zeta\cos(\theta+\phi)] - [\eta\sin(\theta+\phi) + \zeta\cos(\theta+\phi)]^2 a_2 \\ & - [\eta\cos(\theta+\phi) - \zeta\sin(\theta+\phi)][\eta\sin(\theta+\phi) + \zeta\cos(\theta+\phi)]a_1\Big)\ dA \\ = & m\ddot{u}e_g\sin(\theta+\phi) - a_1 m(k_{m_2}^2 - k_{m_1}^2)\sin(\theta+\phi)\cos(\theta+\phi) - a_2 I_{a5} \end{aligned} \tag{3.65}$$

Where,

$$\begin{aligned} I_{a5} = & \iint_A \rho[\eta\sin(\theta+\phi) + \zeta\cos(\theta+\phi)]^2\ dA \\ = & \iint_A \rho[\eta^2\sin^2(\theta+\phi) + \zeta^2\cos^2(\theta+\phi) + 2\eta\zeta\sin\theta+\phi\cos\theta+\phi]\ dA \\ = & mk_{m_2}^2\sin^2(\theta+\phi) + mk_{m_1}^2\cos^2(\theta+\phi) \end{aligned} \tag{3.66}$$

Substituting values of $I_{a3}$, $I_{a4}$, $a_1$ and $a_2$ into Eq. 3.65, $T_{w'}$ can be re-written as following equation.

$$\begin{aligned} T_{w'} = & m\ddot{u}e_g\sin(\theta+\phi) - [\ddot{v}' + w'(\ddot{\theta}+\ddot{\phi}) + 2\dot{w}'(\dot{\theta}+\dot{\phi}) - v'(\dot{\theta}+\dot{\phi})^2] \\ & [m(k_{m_2}^2 - k_{m_1}^2)\sin(\theta+\phi)\cos(\theta+\phi)] \\ & - [\ddot{w}' - v'(\ddot{\theta}+\ddot{\phi}) - 2\dot{v}'(\dot{\theta}+\dot{\phi}) - w'(\dot{\theta}+\dot{\phi})^2] \\ & [mk_{m_1}^2\cos^2(\theta+\phi) + mk_{m_2}^2\sin^2(\theta+\phi)] \end{aligned} \tag{3.67}$$

Utlizing Eq. 3.50 and 3.43, $T_\phi$ can be computed as following procedure.

$$T_\phi = \iint_A \Big(\rho[\eta\sin(\theta+\phi)+\zeta\cos(\theta+\phi)](-\ddot{x}_1 v' + \ddot{y}_1 + 2\Omega\dot{z}_1 - \Omega^2 y_1) + \rho[\eta\cos(\theta+\phi)-\zeta\sin(\theta+\phi)][\ddot{x}_1 w' - \ddot{z}_1 + 2\Omega\dot{y}_1 + \Omega^2(z_1+R)]\Big)\ dA \tag{3.68}$$

Using mathematical manipulation, above equation can be re-written as

$$T_\phi = -v'T_{w'} + w'T_{v'} + \iint_A \Big(\rho[\eta\sin(\theta+\phi)+\zeta\cos(\theta+\phi)]a_4 + \rho[\eta\cos(\theta+\phi)-\zeta\sin(\theta+\phi)]a_5\Big)\ dA \tag{3.69}$$

Where,

$$a_4 = \ddot{y}_1 + 2\Omega\dot{z}_1 - \Omega^2 y_1 \tag{3.70}$$

$$a_5 = -\ddot{z}_1 + 2\Omega\dot{y}_1 + \Omega^2(z_1+R) \tag{3.71}$$

Let's define two more integrals.

$$I_{a6} = \iint_A \rho a_4[\eta\sin(\theta+\phi)+\zeta\cos(\theta+\phi)]\ dA \tag{3.72}$$

$$I_{a7} = \iint_A \rho a_5[\eta\cos(\theta+\phi)-\zeta\sin(\theta+\phi)]\ dA \tag{3.73}$$

So, $T_\phi$ can be expressed as

$$T_\phi = -v'T_{w'} + w'T_{v'} + I_{a6} + I_{a7} \tag{3.74}$$

Substituting expression of $\ddot{y}_1$ (from Eq. 3.35), $\dot{z}_1$ (from Eq. 3.36) and $y_1$ (from Eq. 3.20) into Eq.

3.70, $a_4$ can be computed.

$$\begin{aligned} a_4 = \ddot{v} &- [\eta\cos(\theta+\phi) - \zeta\sin(\theta+\phi)](\dot{\theta}+\dot{\phi})^2 \\ &- [\eta\sin(\theta+\phi) + \zeta\cos(\theta+\phi)](\ddot{\theta}+\ddot{\phi}) \\ &+ 2\Omega\big(\dot{w} + [\eta\cos(\theta+\phi) - \zeta\sin(\theta+\phi)](\dot{\theta}+\dot{\phi})\big) \\ &- \Omega^2\big(v + [\eta\cos(\theta+\phi) - \zeta\sin(\theta+\phi)]\big) \end{aligned} \tag{3.75}$$

Using mathematical manipulation, $a_4$ can be re-written as

$$\begin{aligned} a_4 = a_{4a} &- a_{4b}[\eta\cos(\theta+\phi) - \zeta\sin(\theta+\phi)] \\ &- [\eta\sin(\theta+\phi) + \zeta\cos(\theta+\phi)](\ddot{\theta}+\ddot{\phi}) \end{aligned} \tag{3.76}$$

Where,

$$a_{4a} = \ddot{v} + 2\Omega\dot{w} - \Omega^2 v \tag{3.77}$$

$$a_{4b} = (\dot{\theta}+\dot{\phi})^2 - 2\Omega(\dot{\theta}+\dot{\phi}) + \Omega^2 \tag{3.78}$$

Substituting expression of $\ddot{z}_1$ (from Eq. 3.37), $\dot{y}_1$ (from Eq. 3.34) and $z_1$ (from Eq. 3.21) into Eq. 3.71, $a_5$ can be computed.

$$\begin{aligned} a_5 = -\ddot{w} &+ [\eta\sin(\theta+\phi) + \zeta\cos(\theta+\phi)](\dot{\theta}+\dot{\phi})^2 \\ &- [\eta\cos(\theta+\phi) - \zeta\sin(\theta+\phi)](\ddot{\theta}+\ddot{\phi}) \\ &+ 2\Omega\big(\dot{v} - [\eta\sin(\theta+\phi) + \zeta\cos(\theta+\phi)](\dot{\theta}+\dot{\phi})\big) \\ &+ \Omega^2\big(w + R + [\eta\sin(\theta+\phi) + \zeta\cos(\theta+\phi)]\big) \end{aligned} \tag{3.79}$$

Using mathematical manipulation, $a_5$ can be re-written as

$$\begin{aligned} a_5 = a_{5a} + a_{4b}[\eta \sin(\theta+\phi) + \zeta \cos(\theta+\phi)] \\ - [\eta \cos(\theta+\phi) - \zeta \sin(\theta+\phi)](\ddot{\theta} + \ddot{\phi}) \end{aligned} \tag{3.80}$$

Where,

$$a_{5a} = -\ddot{w} + 2\Omega\dot{v} + \Omega^2(w+R) \tag{3.81}$$

Substituting values of $a_4$ (from Eq. 3.76) and $a_5$ (from Eq. 3.80) into Eq. 3.72, $I_{a6}$ can be computed.

$$\begin{aligned} I_{a6} &= \iint_A \rho\Big(a_{4a}[\eta \sin(\theta+\phi) + \zeta \cos(\theta+\phi)] - (\ddot{\theta}+\ddot{\phi})[\eta \sin(\theta+\phi) + \zeta \cos(\theta+\phi)]^2 \\ &\quad - a_{4b}[\eta \sin(\theta+\phi) + \zeta \cos(\theta+\phi)][\eta \cos(\theta+\phi) - \zeta \sin(\theta+\phi)]\Big)\ dA \\ &= a_{4a} I_{a2} - a_{4b} I_{a4} - (\ddot{\theta}+\ddot{\phi}) I_{a5} \\ &= a_{4a} m e_g \sin(\theta+\phi) - a_{4b} m (k_{m_2}^2 - k_{m_1}^2) \sin(\theta+\phi)\cos(\theta+\phi) \\ &\quad - (\ddot{\theta}+\ddot{\phi})[k_{m_1}^2 \cos^2(\theta+\phi) + k_{m_2}^2 \sin^2(\theta+\phi)] \end{aligned} \tag{3.82}$$

Substituting values of $a_4$ (from Eq. 3.76) and $a_5$ (from Eq. 3.80) into Eq. 3.73, $I_{a6}$ can be computed.

$$\begin{aligned} I_{a7} &= \iint_A \rho\Big(a_{5a}[\eta \cos(\theta+\phi) - \zeta \sin(\theta+\phi)] - (\ddot{\theta}+\ddot{\phi})[\eta \cos(\theta+\phi) - \zeta \sin(\theta+\phi)]^2 \\ &\quad + a_{4b}[\eta \sin(\theta+\phi) + \zeta \cos(\theta+\phi)][\eta \cos(\theta+\phi) - \zeta \sin(\theta+\phi)]\Big)\ dA \\ &= a_{5a} I_{a1} + a_{4b} I_{a4} - (\ddot{\theta}+\ddot{\phi}) I_{a3} \\ &= a_{5a} m e_g \cos(\theta+\phi) + a_{4b} m (k_{m_2}^2 - k_{m_1}^2) \sin(\theta+\phi)\cos(\theta+\phi) \\ &\quad - (\ddot{\theta}+\ddot{\phi})[k_{m_1}^2 \sin^2(\theta+\phi) + k_{m_2}^2 \cos^2(\theta+\phi)] \end{aligned} \tag{3.83}$$

Substituting values of $I_{a6}$ (from Eq. 3.82) and $I_{a7}$ (from Eq. 3.83) into Eq. 3.74, $T_\phi$ can be

computed.

$$T_\phi = -v'T_{w'} + w'T_{v'} + a_{4a}me_g \sin(\theta+\phi) + a_{5a}me_g \cos(\theta+\phi) - (\ddot{\theta}+\ddot{\phi})mk_m^2 \tag{3.84}$$

Again, substituting values of $a_{4a}$ (from Eq. 3.77) and $a_{5a}$ (from Eq. 3.81) into above equation, $T_\phi$ is computed.

$$\begin{aligned} T_\phi = &-v'T_{w'} + w'T_{v'} + (\ddot{v} + 2\Omega\dot{w} - \Omega^2 v)me_g \sin(\theta+\phi) \\ &+ [-\ddot{w} + 2\Omega\dot{v} + \Omega^2(w+R)]me_g \cos(\theta+\phi) - (\ddot{\theta}+\ddot{\phi})mk_m^2 \end{aligned} \tag{3.85}$$

### 3.3.2 Computation of Strain Energy

For purpose of deriving strain energy, cyclodial rotor blade is assumed to be long slender isotropic beam. Strain energy can be expressed in terms of stresses and strains. Using stress-strain relationship, stresses are written in terms of strains. Then, using strain-displacement relationships, strains can be written in terms of displacements. Finally substituting all these relationships, variation of strain energy can be expressed in terms of deflections.

Variation of strain energy is computed using following formula (Eq. 3.86).

$$\delta U = \int_0^L \iint_A \sigma_{ij}\delta\epsilon_{ij} \; dA \; dx \tag{3.86}$$

Using uni-axial stress assumption, following stress components become zero.

$$\sigma_{22} = \sigma_{33} = \sigma_{23} = 0 \tag{3.87}$$

Moreover, due to symmetry of stress and strain tensor, following expressions can be written.

$$\sigma_{ij} = \sigma_{ji} \tag{3.88}$$

$$\epsilon_{ij} = \epsilon_{ji} \tag{3.89}$$

Substituting Eqs. 3.87 - 3.89 into Eq. 3.86, variation of strain energy can be expressed as following equation.

$$\delta U = \int_0^L \iint_A (\sigma_{11}\delta\epsilon_{11} + 2\sigma_{12}\delta\epsilon_{12} + 2\sigma_{13}\delta\epsilon_{13}) \ dA \ dx \tag{3.90}$$

Now engineering strains are used to compute strain energy. Here, engineering strains can be written in terms of classical strains.

$$\epsilon_{xx} = \epsilon_{11} \tag{3.91}$$

$$\epsilon_{x\eta} = 2\epsilon_{12} \tag{3.92}$$

$$\epsilon_{x\zeta} = 2\epsilon_{13} \tag{3.93}$$

Based on engineering strains and stresses, variation of strain energy can be expressed as following equation.

$$\delta U = \int_0^L \iint_A (\sigma_{xx}\delta\epsilon_{xx} + \sigma_{x\eta}\delta\epsilon_{x\eta} + \sigma_{x\zeta}\delta\epsilon_{x\zeta}) \ dA \ dx \tag{3.94}$$

The stresses can be expressed in terms of engineering strains as

$$\sigma_{xx} = E\epsilon_{xx} \tag{3.95}$$

$$\sigma_{x\eta} = G\epsilon_{x\eta} \tag{3.96}$$

$$\sigma_{x\zeta} = G\epsilon_{x\zeta} \tag{3.97}$$

Substituting expression of stresses from Eq. 3.95 - Eq. 3.97, variation of strain energy (Eq. 3.94) can be re-written as

$$\delta U = \int_0^L \iint_A (E\epsilon_{xx}\delta\epsilon_{xx} + G\epsilon_{x\eta}\delta\epsilon_{x\eta} + G\epsilon_{x\zeta}\delta\epsilon_{x\zeta}) \ dA \ dx \tag{3.98}$$

Now, strain-displacement relationships are used to get strain energy in terms of displacements.

$$\begin{aligned}\epsilon_{xx} = u' + \frac{v'^2}{2} + \frac{w'^2}{2} - \lambda_T\phi'' + (\eta^2+\zeta^2)(\theta'\phi' + \frac{\phi'^2}{2}) \\ - v''[\eta\cos(\theta+\phi) - \zeta\sin(\theta+\phi)] \\ - w''[\eta\sin(\theta+\phi) + \zeta\cos(\theta+\phi)]\end{aligned} \tag{3.99}$$

$$\epsilon_{x\eta} = -(\zeta + \frac{\partial\lambda_T}{\delta\eta})\phi' \tag{3.100}$$

$$\epsilon_{x\zeta} = -(\eta - \frac{\partial\lambda_T}{\delta\zeta})\phi' \tag{3.101}$$

In the above equations, $\lambda_T$ is cross-sectional warping function. Variation of strains can be expressed as following equations.

$$\begin{aligned}\delta\epsilon_{xx} = \delta u' + v'\delta v' + w'\delta w' - \lambda_T\delta\phi'' + (\eta^2+\zeta^2)(\theta+\phi)'\delta\phi' \\ - \delta v''[\eta\cos(\theta+\phi) - \zeta\sin(\theta+\phi)] \\ - \delta w''[\eta\sin(\theta+\phi) + \zeta\cos(\theta+\phi)] \\ - v''[-\eta\sin(\theta+\phi)\delta\phi - \zeta\cos(\theta+\phi)\delta\phi] \\ - w''[\eta\cos(\theta+\phi)\delta\phi - \zeta\sin(\theta+\phi)\delta\phi]\end{aligned} \tag{3.102}$$

$$\delta\epsilon_{x\eta} = -(\zeta + \frac{\partial\lambda_T}{\delta\eta})\delta\phi' \tag{3.103}$$

$$\delta\epsilon_{x\zeta} = -(\eta - \frac{\partial\lambda_T}{\delta\zeta})\delta\phi' \tag{3.104}$$

Substituting expression of variation of strains (Eq. 3.102-3.104) into Eq. 3.98, variation of strain

energy can be expressed as following equation.

$$\delta U = \int_0^L \iint_A \Big( \delta u'(E\epsilon_{xx}) + \delta v'(v' E\epsilon_{xx}) + \delta w'(w' E\epsilon_{xx}) - \delta\phi''(\lambda_T E\epsilon_{xx}) \\ - \delta v''[\eta\cos(\theta+\phi) - \zeta\sin(\theta+\phi)]E\epsilon_{xx} - \delta w''[\eta\sin(\theta+\phi) + \zeta\cos(\theta+\phi)]E\epsilon_{xx} \\ + \delta\phi\ E\epsilon_{xx}\big(v''[\eta\sin(\theta+\phi) + \zeta\cos(\theta+\phi)] - w''[\eta\cos(\theta+\phi) - \zeta\sin(\theta+\phi)]\ \big) \\ + \delta\phi'[(\eta^2+\zeta^2)(\theta+\phi)' E\epsilon_{xx} - (\zeta + \frac{\partial\lambda_T}{\delta\eta})G\epsilon_{x\eta} - (\eta - \frac{\partial\lambda_T}{\delta\zeta})G\epsilon_{x\zeta}]\Big)\ dA\ \ dx \tag{3.105}$$

The above expression can be re-written as following equation.

$$\delta U = \int_0^L \big( U_{u'}\ \delta u' + U_{v'}\ \delta v' + U_{v''}\ \delta v'' + U_{w'}\ \delta w' + U_{w''}\ \delta w'' + U_{\phi}\ \delta\phi + U_{\phi'}\ \delta\phi' + U_{\phi''}\ \delta\phi''\big)\ \ dx \tag{3.106}$$

The coefficients of variation of displacements can be computed as following.

$$U_{u'} = \iint_A E\epsilon_{xx}\ \ dA = EI_{b1} \tag{3.107}$$

Where,

$$I_{b1} = \iint_A \epsilon_{xx}\ \ dA \tag{3.108}$$

$$U_{v'} = \iint_A v' E\epsilon_{xx}\ \ dA = v' EI_{b1} = v' U_{u'} \tag{3.109}$$

$$U_{w'} = \iint_A w' E\epsilon_{xx}\ \ dA = w' EI_{b1} = w' U_{u'} \tag{3.110}$$

$$\begin{aligned} U_{v''} &= -\iint_A [\eta\cos(\theta+\phi) - \zeta\sin(\theta+\phi)]E\epsilon_{xx}\ \ dA \\ &= -E\cos(\theta+\phi)\iint_A \eta\epsilon_{xx}\ \ dA + E\sin(\theta+\phi)\iint_A \zeta\epsilon_{xx}\ \ dA \\ &= -E\cos(\theta+\phi)\ I_{b2} + E\sin(\theta+\phi)\ I_{b3} \end{aligned} \tag{3.111}$$

Where,

$$I_{b2} = \iint_A \eta \epsilon_{xx} \ dA \tag{3.112}$$

Where,

$$I_{b3} = \iint_A \zeta \epsilon_{xx} \ dA \tag{3.113}$$

$$\begin{aligned} U_{w''} &= -\iint_A [\eta \sin(\theta+\phi) + \zeta \cos(\theta+\phi)] E \epsilon_{xx} \ dA \\ &= -E \sin(\theta+\phi) \iint_A \eta \epsilon_{xx} \ dA - E \cos(\theta+\phi) \iint_A \zeta \epsilon_{xx} \ dA \\ &= -E \sin(\theta+\phi) \ I_{b2} - E \cos(\theta+\phi) \ I_{b3} \end{aligned} \tag{3.114}$$

$$\begin{aligned} U_{\phi} = \iint_A \big( & \ v''[\eta \sin(\theta+\phi) + \zeta \cos(\theta+\phi)] \\ & - w''[\eta \cos(\theta+\phi) - \zeta \sin(\theta+\phi)] \ \big) E \epsilon_{xx} \ dA \\ = \iint_A \big( & \ \eta[v'' \sin(\theta+\phi) - w'' \cos(\theta+\phi)] \\ & + \zeta[v'' \cos(\theta+\phi) + w'' \sin(\theta+\phi)] \ \big) E \epsilon_{xx} \ dA \\ = & \quad E[v'' \sin(\theta+\phi) - w'' \cos(\theta+\phi)] \iint_A \eta \epsilon_{xx} \ dA \\ & + E[v'' \cos(\theta+\phi) + w'' \sin(\theta+\phi)] \iint_A \zeta \epsilon_{xx} \ dA \\ = & \quad E[v'' \sin(\theta+\phi) - w'' \cos(\theta+\phi)] \ I_{b2} \\ & + E[v'' \cos(\theta+\phi) + w'' \sin(\theta+\phi)] \ I_{b3} \end{aligned} \tag{3.115}$$

$$\begin{aligned} U_{\phi'} &= \iint_A [(\eta^2+\zeta^2)(\theta+\phi)' E \epsilon_{xx} - (\zeta + \frac{\partial \lambda_T}{\delta \eta}) G \epsilon_{x\eta} - (\eta - \frac{\partial \lambda_T}{\delta \zeta}) G \epsilon_{x\zeta}] \ dA \\ &= (\theta+\phi)' E \iint_A (\eta^2+\zeta^2) \epsilon_{xx} \ dA - G \iint_A [(\zeta + \frac{\partial \lambda_T}{\delta \eta}) \epsilon_{x\eta} + (\eta - \frac{\partial \lambda_T}{\delta \zeta}) \epsilon_{x\zeta}] \ dA \\ &= (\theta+\phi)' E \ I_{b4} - G \ I_{b5} \end{aligned} \tag{3.116}$$

Where,

$$I_{b4} = \iint_A (\eta^2 + \zeta^2)\epsilon_{xx} \ dA \tag{3.117}$$

$$I_{b5} = \iint_A [(\zeta + \frac{\partial \lambda_T}{\delta \eta})\epsilon_{x\eta} + (\eta - \frac{\partial \lambda_T}{\delta \zeta})\epsilon_{x\zeta}] \ dA \tag{3.118}$$

$$U_{\phi''} = -\iint_A \lambda_T E \epsilon_{xx} \ dA = -EI_{b6} \tag{3.119}$$

Where,

$$I_{b6} = \iint_A \lambda_T \epsilon_{xx} \ dA \tag{3.120}$$

To compute the integrals $I_{b1}$, $I_{b2}$, $I_{b3}$, $I_{b4}$, $I_{b5}$ and $I_{b6}$ following sectional properties are introduced.

$$\left.\begin{aligned}
\iint_A dA &= A \\
\iint_A \eta \ dA &= Ae_A \\
\iint_A \zeta^2 \ dA &= I_y \\
\iint_A \eta^2 \ dA &= I_z \\
\iint_A (\eta^2 + \zeta^2) \ dA &= Ak_A^2 \\
\iint_A \left((\zeta + \frac{\partial \lambda_T}{\delta \eta})^2 + (\eta - \frac{\partial \lambda_T}{\delta \zeta})^2\right) \ dA &= J \\
\iint_A (\eta^2 + \zeta^2)^2 \ dA &= B_1 \\
\iint_A \eta(\eta^2 + \zeta^2) \ dA &= B_2 \\
\iint_A \lambda_T^2 \ dA &= C_1 \\
\iint_A \zeta \lambda_T \ dA &= C_2
\end{aligned}\right\} \tag{3.121}$$

In the above equation, $A$ is blade cross-sectional area, $e_A$ is tensile axis offset ffrom the blade elastic axis, $I_y$ is area moment of inertia along flap direction, $I_z$ is area moment of inertia along lag direction, $k_A$ is radius of gyration of blade cross section and $J$ is torsion constant. $B_1$ and $B_2$ are sectional constants that appear due to blade pitch. $C_1$ and $C_2$ are constants related to warping

of beam section. Moreover, $EC_1$ is known as warping rigidity. The rotor blade cross-section is assumed to be symmetric about the $\hat{i}_2$ axis. Moreover the warping function $\lambda_T$ also has anti-symmetric characteristic. For these two reasons, following integrals become zeros.

$$\left.\begin{aligned} \iint_A \lambda_T \ dA &= 0 \\ \iint_A \zeta \ dA &= 0 \\ \iint_A \lambda_T(\eta^2+\zeta^2) \ dA &= 0 \\ \iint_A \zeta(\eta^2+\zeta^2) \ dA &= 0 \\ \iint_A \lambda_T \eta \ dA &= 0 \\ \iint_A \zeta\eta \ dA &= 0 \end{aligned}\right\} \tag{3.122}$$

Based on above assumptions and substituting expressions of strains (Eq. 3.99-3.101), following integrals are computed.

$$\begin{aligned} I_{b1} &= \iint_A \epsilon_{xx} \ dA \\ &= A(u' + \frac{v'^2}{2}) + \frac{w'^2}{2}) + AK_A^2(\theta'\phi' + \frac{\phi'^2}{2}) \\ &\quad - Ae_A[v''\cos(\theta+\phi) + w''\sin(\theta+\phi)] \end{aligned} \tag{3.123}$$

$$\begin{aligned} I_{b2} &= \iint_A \eta\epsilon_{xx} \ dA \\ &= \iint_A \Big(\eta(u' + \frac{v'^2}{2}) + \frac{w'^2}{2}) - \eta\lambda_T\phi'' + \eta(\eta^2+\zeta^2)(\theta'\phi' + \frac{\phi'^2}{2}) \\ &\qquad - \eta^2[v''\cos(\theta+\phi) + w''\sin(\theta+\phi)] \\ &\qquad + \zeta\eta[v''\sin(\theta+\phi) - w''\cos(\theta+\phi)]\Big) dA \\ &= Ae_A(u' + \frac{v'^2}{2}) + B_2(\theta'\phi' + \frac{\phi'^2}{2}) - I_z[v''\cos(\theta+\phi) + w''\sin(\theta+\phi)] \end{aligned} \tag{3.124}$$

$$
\begin{aligned}
I_{b3} &= \iint_A \zeta \epsilon_{xx} \ dA \\
&= \iint_A \Big( \zeta(u' + \frac{v'^2}{2}) + \frac{w'^2}{2}) - \zeta \lambda_T \phi'' + \zeta(\eta^2 + \zeta^2)(\theta'\phi' + \frac{\phi'^2}{2}) \\
&\qquad - \zeta\eta[v'' \cos(\theta + \phi) + w'' \sin(\theta + \phi)] \\
&\qquad + \zeta^2[v'' \sin(\theta + \phi) - w'' \cos(\theta + \phi)] \Big) dA \\
&= -C_2\phi'' + I_y[v'' \sin(\theta + \phi) - w'' \cos(\theta + \phi)]
\end{aligned} \tag{3.125}
$$

$$
\begin{aligned}
I_{b4} &= \iint_A (\eta^2 + \zeta^2)\epsilon_{xx} \ dA \\
&= \iint_A \Big( (\eta^2 + \zeta^2)(u' + \frac{v'^2}{2}) + \frac{w'^2}{2}) - (\eta^2 + \zeta^2)\lambda_T \phi'' + (\eta^2 + \zeta^2)^2(\theta'\phi' + \frac{\phi'^2}{2}) \\
&\qquad - \eta(\eta^2 + \zeta^2)[v'' \cos(\theta + \phi) + w'' \sin(\theta + \phi)] \\
&\qquad + \zeta(\eta^2 + \zeta^2)[v'' \sin(\theta + \phi) - w'' \cos(\theta + \phi)] \Big) dA \\
&= Ak_A^2(u' + \frac{v'^2}{2}) + B_1(\theta'\phi' + \frac{\phi'^2}{2}) - B_2[v'' \cos(\theta + \phi) + w'' \sin(\theta + \phi)]
\end{aligned} \tag{3.126}
$$

$$
\begin{aligned}
I_{b5} &= \iint_A [(\zeta + \frac{\partial \lambda_T}{\partial \eta})\epsilon_{x\eta} + (\eta - \frac{\partial \lambda_T}{\partial \zeta})\epsilon_{x\zeta}] \ dA \\
&= \iint_A -[(\zeta + \frac{\partial \lambda_T}{\partial \eta})^2 \phi' + (\eta - \frac{\partial \lambda_T}{\partial \zeta})^2 \phi'] \ dA \\
&= -J\phi'
\end{aligned} \tag{3.127}
$$

$$
\begin{aligned}
I_{b6} &= \iint_A \lambda_T \epsilon_{xx} \ dA \\
&= \iint_A \Big( \lambda_T(u' + \frac{v'^2}{2}) + \frac{w'^2}{2}) - \lambda_T^2 \phi'' + \lambda_T(\eta^2 + \zeta^2)(\theta'\phi' + \frac{\phi'^2}{2}) \\
&\qquad - \lambda_T\eta[v'' \cos(\theta + \phi) + w'' \sin(\theta + \phi)] \\
&\qquad + \lambda_T\zeta[v'' \sin(\theta + \phi) - w'' \cos(\theta + \phi)] \Big) dA \\
&= -C_1\phi'' + C_2[v'' \sin(\theta + \phi) - w'' \cos(\theta + \phi)]
\end{aligned} \tag{3.128}
$$

Now, substituting above expressions of $I_{b1}$, $I_{b1}$, $I_{b1}$, $I_{b1}$ and $I_{b1}$, the coefficients of variation of displacements can be computed as follow.

$$\begin{aligned} U_{u'} &= EI_{b1} \\ &= EA(u' + \frac{v'^2}{2}) + \frac{w'^2}{2}) + EAK_A^2(\theta'\phi' + \frac{\phi'^2}{2}) \\ &\quad - EAe_A[v''\cos(\theta+\phi) + w''\sin(\theta+\phi)] \end{aligned} \tag{3.129}$$

$$\begin{aligned} U_{v'} &= v'EI_{b1} \\ &= EAv'(u' + \frac{v'^2}{2}) + \frac{w'^2}{2}) + EAK_A^2v'(\theta'\phi' + \frac{\phi'^2}{2}) \\ &\quad - EAe_Av'[v''\cos(\theta+\phi) + w''\sin(\theta+\phi)] \end{aligned} \tag{3.130}$$

$$\begin{aligned} U_{w'} &= w'EI_{b1} \\ &= EAw'(u' + \frac{v'^2}{2}) + \frac{w'^2}{2}) + EAK_A^2w'(\theta'\phi' + \frac{\phi'^2}{2}) \\ &\quad - EAe_Aw'[v''\cos(\theta+\phi) + w''\sin(\theta+\phi)] \end{aligned} \tag{3.131}$$

$$\begin{aligned} U_{v''} &= -E\cos(\theta+\phi)I_{b2} + E\sin(\theta+\phi)I_{b3} \\ &= -E\cos(\theta+\phi)\Big(Ae_A(u' + \frac{v'^2}{2}) + B_2(\theta'\phi' + \frac{\phi'^2}{2}) \\ &\qquad\qquad - I_z[v''\cos(\theta+\phi) + w''\sin(\theta+\phi)]\Big) \\ &\quad + E\sin(\theta+\phi)\Big(-C_2\phi'' + I_y[v''\sin(\theta+\phi) - w''\cos(\theta+\phi)]\Big) \\ &= v''(EI_z\cos^2(\theta+\phi) + EI_y\sin^2(\theta+\phi)) \\ &\quad + w''(EI_z - EI_y)\sin(\theta+\phi)\cos(\theta+\phi) \\ &\quad - \cos(\theta+\phi)[EAe_A(u' + \frac{v'^2}{2}) + EB_2(\theta'\phi' + \frac{\phi'^2}{2})] - EC_2\sin(\theta+\phi)\phi'' \end{aligned} \tag{3.132}$$

$$
\begin{aligned}
U_{w''} &= -E\sin(\theta+\phi)I_{b2} - E\cos(\theta+\phi)I_{b3} \\
&= -E\sin(\theta+\phi)\Big(Ae_A(u' + \frac{v'^2}{2}) + B_2(\theta'\phi' + \frac{\phi'^2}{2}) \\
&\qquad\qquad - I_z[v''\cos(\theta+\phi) + w''\sin(\theta+\phi)]\Big) \\
&\quad - E\cos(\theta+\phi)\Big( - C_2\phi'' + I_y[v''\sin(\theta+\phi) - w''\cos(\theta+\phi)]\Big) \\
&= w''(EI_z\sin^2(\theta+\phi) + EI_y\cos^2(\theta+\phi)) \\
&\quad + v''(EI_z - EI_y)\sin(\theta+\phi)\cos(\theta+\phi) \\
&\quad - \sin(\theta+\phi)[EAe_A(u' + \frac{v'^2}{2}) + EB_2(\theta'\phi' + \frac{\phi'^2}{2}) + EC_2\cos(\theta+\phi)\phi'' \qquad (3.133)
\end{aligned}
$$

$$
\begin{aligned}
U_\phi &= [v''\sin(\theta+\phi) - w''\cos(\theta+\phi)]I_{b2} + [v''\cos(\theta+\phi) + w''\sin(\theta+\phi)]I_{b3} \\
&= [v''\sin(\theta+\phi) - w''\cos(\theta+\phi)]\Big(Ae_A(u' + \frac{v'^2}{2}) + B_2(\theta'\phi' + \frac{\phi'^2}{2}) \\
&\qquad\qquad - I_z[v''\cos(\theta+\phi) + w''\sin(\theta+\phi)]\Big) \\
&\quad + E[v''\cos(\theta+\phi) + w''\sin(\theta+\phi)]\Big( - C_2\phi'' \\
&\qquad\qquad + I_y[v''\sin(\theta+\phi) - w''\cos(\theta+\phi)]\Big) \\
&= \quad EI_z[w''^2\sin(\theta+\phi)\cos(\theta+\phi) - v''w''\sin^2(\theta+\phi) + v''w''\cos^2(\theta+\phi) \\
&\qquad\qquad - v''^2\sin(\theta+\phi)\cos(\theta+\phi)] \\
&\quad + EI_y[\, v''^2\sin(\theta+\phi)\cos(\theta+\phi) + v''w''\sin^2(\theta+\phi) - v''w''\cos^2(\theta+\phi) \\
&\qquad\qquad - w''^2\sin(\theta+\phi)\cos(\theta+\phi)] \\
&\quad + EB_2\theta'\phi'[v''\sin(\theta+\phi) - w''\cos(\theta+\phi)] \\
&\quad - EC_2\phi''[v''\cos(\theta+\phi) + w''\sin(\theta+\phi)] \\
&= (w''^2 - v''^2)(EI_z - EI_y)\sin(\theta+\phi)\cos(\theta+\phi) \\
&\quad - v''w''(EI_z - EI_y)\cos 2(\theta+\phi) \\
&\quad + EB_2\theta'\phi'[v''\sin(\theta+\phi) - w''\cos(\theta+\phi)] \\
&\quad - EC_2\phi''[v''\cos(\theta+\phi) + w''\sin(\theta+\phi)] \qquad (3.134)
\end{aligned}
$$

$$
\begin{aligned}
U_{\phi'} &= (\theta+\phi)' EI_{b4} - GI_{b5} \\
&= GJ\phi' + (\theta+\phi)' E\Big( Ak_A^2 (u' + \frac{v'^2}{2}) + B_1(\theta'\phi' + \frac{\phi'^2}{2}) \\
&\qquad - B_2[v''\cos(\theta+\phi) + w''\sin(\theta+\phi)]\Big)
\end{aligned} \tag{3.135}
$$

$$
\begin{aligned}
U_{\phi''} &= -EI_{b6} \\
&= EC_1\phi'' - EC_2(v''\sin(\theta+\phi) - w''\cos(\theta+\phi))
\end{aligned} \tag{3.136}
$$

In the above expressions, $EI_y$ is bending stiffness along flap direction, $EI_z$ is bending stiffness along lag direction, $GJ$ is torsional stiffness and $EA$ is axial stiffness of the rotor blade.

## 3.4 Geometrically-exact Beam Model

$2^{nd}$ order approximation of Hodges-Dowell ($2^{nd}$ order nonlinear) type model is valid for only stiff blades going through moderate deflections. Cyclodial rotor blades go through large centrifugal force which acts radially creating large bending and torsional deflections unlike conventional rotor, where centrifugal force acts axially providing axial stiffness. Moreover, nonlinear behaviours are significant in cycloidal rotor blades due to more constrained geometry (fixed-fixed boundary condition for bending at both end) which will be discussed later. For this purpose, a fully nonlinear geometrically exact structural model of cycloidal rotor is developed. In this case also, cycloidal rotor blade is modeled as an isotropic beam that can go through four types of deflections: 1) axial elongation ($u$), 2) normal bending (bending normal to rotor blade - $\bar{w}$), 3) side bending ($\bar{v}$), and 4) axial twist ($\phi$). In Fig. 3.3, definition of these four type of deflections are given.

### 3.4.1 Computation of Kinetic Energy

First step towards deriving kinetic energy is to define inertial position vector of a blade element. Here, position vector is defined in mixed coordinate. Then, inertial velocity vector is calculated from inertial position vector and inertial acceleration vector is calculated from inertial velocity vector using transport theorem. Kinematics upto acceleration level is computed in mixed coordi-

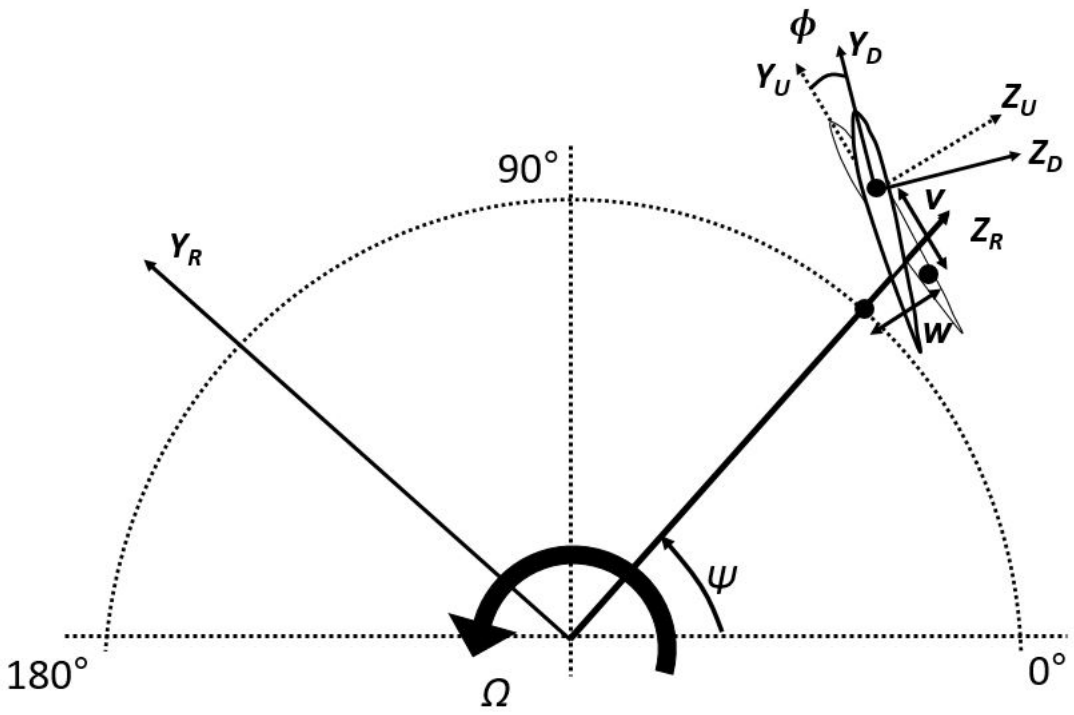


Figure 3.3: Definition of deflections on a cycloidal rotor blade

nate frames. Once kinematics is computed upto acceleration level, variation of kinetic energy is calculated using calculus of variations.

Position vector of an arbitrary point on the rotor blade can be expressed as Eq. 3.137.

$$\vec{r} = R\hat{i}_c + (x+u)\hat{i}_x + \bar{v}\hat{i}_y + \bar{w}\hat{i}_z + \eta\hat{i}_2 + \zeta\hat{i}_3 \tag{3.137}$$

$$\vec{r} = [0 \;\; 0 \;\; R] \begin{bmatrix} \hat{i}_a \\ \hat{i}_b \\ \hat{i}_c \end{bmatrix} + [(x+u) \;\; \bar{v} \;\; \bar{w}] \begin{bmatrix} \hat{i}_x \\ \hat{i}_y \\ \hat{i}_z \end{bmatrix} + [0 \;\; \eta \;\; \zeta] \begin{bmatrix} \hat{i}_1 \\ \hat{i}_2 \\ \hat{i}_3 \end{bmatrix} \tag{3.138}$$

Inertial velocity (Eq. 3.139) vector is computed from inertial position vector (Eq. 3.138).

$$\dot{\vec{r}} = [0 \;\; 0 \;\; R] \begin{bmatrix} \dot{\hat{i}}_a \\ \dot{\hat{i}}_b \\ \dot{\hat{i}}_c \end{bmatrix} + [(x+u) \;\; \bar{v} \;\; \bar{w}] \begin{bmatrix} \dot{\hat{i}}_x \\ \dot{\hat{i}}_y \\ \dot{\hat{i}}_z \end{bmatrix} + [\dot{u} \;\; \dot{\bar{v}} \;\; \dot{\bar{w}}] \begin{bmatrix} \hat{i}_x \\ \hat{i}_y \\ \hat{i}_z \end{bmatrix} + [0 \;\; \eta \;\; \zeta] \begin{bmatrix} \dot{\hat{i}}_1 \\ \dot{\hat{i}}_2 \\ \dot{\hat{i}}_3 \end{bmatrix} \tag{3.139}$$

Inertial acceleration vector (Eq. 3.140) can be computed from inertial velocity vector (Eq. 3.139).

$$\ddot{\vec{r}} = [0 \;\; 0 \;\; R] \begin{bmatrix} \ddot{\hat{i}}_a \\ \ddot{\hat{i}}_b \\ \ddot{\hat{i}}_c \end{bmatrix} + [(x+u) \;\; \bar{v} \;\; \bar{w}] \begin{bmatrix} \ddot{\hat{i}}_x \\ \ddot{\hat{i}}_y \\ \ddot{\hat{i}}_z \end{bmatrix} + 2[\dot{u} \;\; \dot{\bar{v}} \;\; \dot{\bar{w}}] \begin{bmatrix} \dot{\hat{i}}_x \\ \dot{\hat{i}}_y \\ \dot{\hat{i}}_z \end{bmatrix} + [\ddot{u} \;\; \ddot{\bar{v}} \;\; \ddot{\bar{w}}] \begin{bmatrix} \hat{i}_x \\ \hat{i}_y \\ \hat{i}_z \end{bmatrix} + [0 \;\; \eta \;\; \zeta] \begin{bmatrix} \ddot{\hat{i}}_1 \\ \ddot{\hat{i}}_2 \\ \ddot{\hat{i}}_3 \end{bmatrix} \tag{3.140}$$

The temporal derivatives of $[\hat{i}_a, \;\; \hat{i}_b, \;\; \hat{i}_c]^T$ are computed using transport theorem (Eq. 3.141)

$$\begin{bmatrix} \dot{\hat{i}}_a \\ \dot{\hat{i}}_b \\ \dot{\hat{i}}_c \end{bmatrix} = \vec{\omega}^r \times \begin{bmatrix} \hat{i}_a \\ \hat{i}_b \\ \hat{i}_c \end{bmatrix} \tag{3.141}$$

In the above equations, $\vec{\omega}^r = -\Omega \hat{i}_a$ is angular velocity of rotating frame with respect to inertial frame. Moreover, above equation (Eq. 3.141) can be re-written in the vector form as following equations (Eq. 3.142-3.144).

$$[\dot{\hat{i}}_a]_{abc} = [P(\; [\vec{\omega}^r]_{abc}) \;][\hat{i}_a]_{abc} \tag{3.142}$$

$$[\dot{\hat{i}}_b]_{abc} = [P(\; [\vec{\omega}^r]_{abc}) \;][\hat{i}_b]_{abc} \tag{3.143}$$

$$[\dot{\hat{i}}_c]_{abc} = [P(\; [\vec{\omega}^r]_{abc}) \;][\hat{i}_c]_{abc} \tag{3.144}$$

In the above equations (Eq. 3.142-3.144), for any arbitrary vector $\vec{X}$, $[\vec{X}]_{abc}$ denotes components of $\vec{X}$ in the rotating coordinate system $(X_R, Y_R, Z_R)$ along $[\hat{i}_a, \hat{i}_b$ and $\hat{i}_c]$ coordinate axes. Accord-

ingly,

$$[\hat{i}_a]_{abc} = \begin{bmatrix} 1 \\ 0 \\ 0 \end{bmatrix}, \qquad [\hat{i}_b]_{abc} = \begin{bmatrix} 0 \\ 1 \\ 0 \end{bmatrix}, \qquad [\hat{i}_c]_{abc} = \begin{bmatrix} 0 \\ 0 \\ 1 \end{bmatrix} \tag{3.145}$$

In equations (Eq. 3.142-3.144), function $P$ is defined such that if any arbitrary vector $\vec{X}$ having components $X_1, X_2$, and $X_3$ along any coordinate frame (let's say in coordinate frame $[\hat{i}_a$, $\hat{i}_b$ and $\hat{i}_c]$), then

$$[P(\ [\vec{X}]_{abc})\ ] \equiv [P(X_1, X_2, X_3)] \equiv \begin{bmatrix} 0 & X_3 & -X_2 \\ -X_3 & 0 & X_1 \\ X_2 & -X_1 & 0 \end{bmatrix} = -[P(\ [\vec{X}]_{abc})\ ]^T \tag{3.146}$$

Moreover, it can be noticed that if there exist two vectors $\vec{X} = X_1\hat{i}_a + X_2\hat{i}_b + X_3\hat{i}_c$ and $\vec{Y} = Y_1\hat{i}_a + Y_2\hat{i}_b + Y_3\hat{i}_c$, then

$$\begin{aligned} \vec{X} \times \vec{Y} &= -[\vec{X}]^T_{abc}[P(\ [\vec{Y}]_{abc})\ ] \begin{bmatrix} \hat{i}_a \\ \hat{i}_b \\ \hat{i}_c \end{bmatrix} \\ &= [\vec{Y}]^T_{abc}[P(\ [\vec{X}]_{abc})\ ] \begin{bmatrix} \hat{i}_a \\ \hat{i}_b \\ \hat{i}_c \end{bmatrix} \end{aligned} \tag{3.147}$$

So,

$$[\vec{X}]^T_{abc}[P(\ [\vec{Y}]_{abc})\ ] = -[\vec{Y}]^T_{abc}[P(\ [\vec{X}]_{abc})\ ] \tag{3.148}$$

Together, Eq. 3.142-3.144 can be re-written as following Eq. 3.149

$$\begin{bmatrix} \dot{\hat{i}}_a \\ \dot{\hat{i}}_b \\ \dot{\hat{i}}_c \end{bmatrix} = [P(\ [\vec{\omega}^r]_{abc})\ ] \begin{bmatrix} \hat{i}_a \\ \hat{i}_b \\ \hat{i}_c \end{bmatrix} \tag{3.149}$$

Similarly, $[\ddot{\hat{i}}_a,\ \ \ddot{\hat{i}}_b,\ \ \ddot{\hat{i}}_c]^T$ can be computed by taking time derivative of both side of Eq. 3.141.

$$\begin{bmatrix} \ddot{\hat{i}}_a \\ \ddot{\hat{i}}_b \\ \ddot{\hat{i}}_c \end{bmatrix} = \dot{\vec{\omega}}^r \times \begin{bmatrix} \hat{i}_a \\ \hat{i}_b \\ \hat{i}_c \end{bmatrix} + \vec{\omega}^r \times \begin{bmatrix} \dot{\hat{i}}_a \\ \dot{\hat{i}}_b \\ \dot{\hat{i}}_c \end{bmatrix} \tag{3.150}$$

Using transport theorem, Eq. 3.150 can be re-written as

$$\begin{bmatrix} \ddot{\hat{i}}_a \\ \ddot{\hat{i}}_b \\ \ddot{\hat{i}}_c \end{bmatrix} = \dot{\vec{\omega}}^r \times \begin{bmatrix} \hat{i}_a \\ \hat{i}_b \\ \hat{i}_c \end{bmatrix} + \vec{\omega}^r \times \vec{\omega}^r \times \begin{bmatrix} \hat{i}_a \\ \hat{i}_b \\ \hat{i}_c \end{bmatrix} \tag{3.151}$$

$$\begin{bmatrix} \ddot{\hat{i}}_a \\ \ddot{\hat{i}}_b \\ \ddot{\hat{i}}_c \end{bmatrix} = [P(\ [\dot{\vec{\omega}}^r]_{abc})\ ] \begin{bmatrix} \hat{i}_a \\ \hat{i}_b \\ \hat{i}_c \end{bmatrix} + [P(\ [\vec{\omega}^r]_{abc})\ ][P(\ [\vec{\omega}^r]_{abc})\ ] \begin{bmatrix} \hat{i}_a \\ \hat{i}_b \\ \hat{i}_c \end{bmatrix} \tag{3.152}$$

On the other hand, temporal derivatives of $[\dot{\hat{i}}_a,\ \ \dot{\hat{i}}_b,\ \ \dot{\hat{i}}_c]^T$ can be computed using transformation matrix $T_{RI}$ between inertial frame and rotational frame.By taking temporal derivative of both sides of Eq. 3.3, following expression (Eq. 3.153) is obtained.

$$\begin{bmatrix} \dot{\hat{i}}_a \\ \dot{\hat{i}}_b \\ \dot{\hat{i}}_c \end{bmatrix} = [\dot{T}_{RI}] \begin{bmatrix} \hat{i}_A \\ \hat{i}_B \\ \hat{i}_C \end{bmatrix} \tag{3.153}$$

Substituting Eq. 3.3 into Eq. 3.153, following expression is derived.

$$\begin{bmatrix} \dot{\hat{i}}_a \\ \dot{\hat{i}}_b \\ \dot{\hat{i}}_c \end{bmatrix} = [\dot{T}_{RI}]\ [T_{RI}]^T \begin{bmatrix} \hat{i}_a \\ \hat{i}_b \\ \hat{i}_c \end{bmatrix} \tag{3.154}$$

By taking time-derivative of Eq. 3.153, following expression (Eq. 3.155) is obtained.

$$\begin{bmatrix} \ddot{\hat{i}}_a \\ \ddot{\hat{i}}_b \\ \ddot{\hat{i}}_c \end{bmatrix} = [\ddot{T}_{RI}] \begin{bmatrix} \hat{i}_A \\ \hat{i}_B \\ \hat{i}_C \end{bmatrix} \tag{3.155}$$

Substituting Eq. 3.3 into above equation (Eq. 3.155), following expression is derived.

$$\begin{bmatrix} \ddot{\hat{i}}_a \\ \ddot{\hat{i}}_b \\ \ddot{\hat{i}}_c \end{bmatrix} = [\ddot{T}_{RI}]\ [T_{RI}]^T \begin{bmatrix} \hat{i}_a \\ \hat{i}_b \\ \hat{i}_c \end{bmatrix} \tag{3.156}$$

Using similar approach, temporal derivatives of $[\hat{i}_x,\ \ \hat{i}_y,\ \ \hat{i}_z]^T$ can be computed.

$$\begin{bmatrix} \dot{\hat{i}}_x \\ \dot{\hat{i}}_y \\ \dot{\hat{i}}_z \end{bmatrix} = \vec{\omega}^u \times \begin{bmatrix} \hat{i}_x \\ \hat{i}_y \\ \hat{i}_z \end{bmatrix} = [P(\ [\vec{\omega}^u]_{xyz})\ ] \begin{bmatrix} \hat{i}_x \\ \hat{i}_y \\ \hat{i}_z \end{bmatrix} = [\dot{T}_{UI}]\ [T_{UI}]^T \begin{bmatrix} \hat{i}_x \\ \hat{i}_y \\ \hat{i}_z \end{bmatrix} \tag{3.157}$$

$$
\begin{aligned}
\begin{bmatrix} \ddot{\hat{i}}_x \\ \ddot{\hat{i}}_y \\ \ddot{\hat{i}}_z \end{bmatrix} &= \dot{\vec{\omega}}^u \times \begin{bmatrix} \hat{i}_x \\ \hat{i}_y \\ \hat{i}_z \end{bmatrix} + \vec{\omega}^u \times \vec{\omega}^u \times \begin{bmatrix} \hat{i}_x \\ \hat{i}_y \\ \hat{i}_z \end{bmatrix} \\
&= [P(\ [\dot{\vec{\omega}}^u]_{xyz})\ ] \begin{bmatrix} \hat{i}_x \\ \hat{i}_y \\ \hat{i}_z \end{bmatrix} + [P(\ [\vec{\omega}^r]_{xyz})\ ][P(\ [\vec{\omega}^r]_{xyz})\ ] \begin{bmatrix} \hat{i}_x \\ \hat{i}_y \\ \hat{i}_z \end{bmatrix} \\
&= [\ddot{T}_{UI}]\ [T_{UI}]^T \begin{bmatrix} \hat{i}_x \\ \hat{i}_y \\ \hat{i}_z \end{bmatrix}
\end{aligned} \tag{3.158}
$$

In Eqs. 3.157 and 3.158, $\vec{\omega}^u = (\dot{\theta} - \Omega)\hat{i}_x$ is angular velocity of un-deformed pitching blade frame with respect to inertial frame. $T_{UI}$ is transformation matrix between un-deformed pitching frame and inertial frame, defined by following equation (Eq. 3.159).

$$
\begin{bmatrix} \hat{i}_x \\ \hat{i}_y \\ \hat{i}_z \end{bmatrix} = [T_{UI}] \begin{bmatrix} \hat{i}_A \\ \hat{i}_B \\ \hat{i}_C \end{bmatrix} \tag{3.159}
$$

$T_{UI}$ can be expressed in terms of azimuth angle ($\psi = \Omega\, t$) and pitch angle ($\theta$) as Eq. 3.160.

$$
[T_{UI}] = [T_{UR}][T_{RI}] = \begin{bmatrix} 1 & 0 & 0 \\ 0 & \cos(\psi - \theta) & -\sin(\psi - \theta) \\ 0 & \sin(\psi - \theta) & \cos(\psi - \theta) \end{bmatrix} \tag{3.160}
$$

Using similar approach, temporal derivatives of $[\hat{i}_1,\ \hat{i}_2,\ \hat{i}_3]^T$ can be computed.

$$
\begin{bmatrix} \dot{\hat{i}}_1 \\ \dot{\hat{i}}_2 \\ \dot{\hat{i}}_3 \end{bmatrix} = \vec{\omega}^d \times \begin{bmatrix} \hat{i}_1 \\ \hat{i}_2 \\ \hat{i}_3 \end{bmatrix} = [P(\ [\vec{\omega}^d]_{123})\ ] \begin{bmatrix} \hat{i}_1 \\ \hat{i}_2 \\ \hat{i}_3 \end{bmatrix} = [\dot{T}_{DI}]\ [T_{DI}]^T \begin{bmatrix} \hat{i}_1 \\ \hat{i}_2 \\ \hat{i}_3 \end{bmatrix} \tag{3.161}
$$

$$\begin{bmatrix} \ddot{\hat{i}}_1 \\ \ddot{\hat{i}}_2 \\ \ddot{\hat{i}}_3 \end{bmatrix} = \dot{\vec{\omega}}^d \times \begin{bmatrix} \hat{i}_1 \\ \hat{i}_2 \\ \hat{i}_3 \end{bmatrix} + \vec{\omega}^d \times \vec{\omega}^d \times \begin{bmatrix} \hat{i}_1 \\ \hat{i}_2 \\ \hat{i}_3 \end{bmatrix}$$

$$= [P(\ [\dot{\vec{\omega}}^d]_{123})\ ] \begin{bmatrix} \hat{i}_1 \\ \hat{i}_2 \\ \hat{i}_3 \end{bmatrix} + [P(\ [\vec{\omega}^d]_{123})\ ][P(\ [\vec{\omega}^d]_{123})\ ] \begin{bmatrix} \hat{i}_1 \\ \hat{i}_2 \\ \hat{i}_3 \end{bmatrix}$$

$$= [\ddot{T}_{DI}]\ [T_{DI}]^T \begin{bmatrix} \hat{i}_1 \\ \hat{i}_2 \\ \hat{i}_3 \end{bmatrix} \tag{3.162}$$

In Eqs. 3.161 and 3.162, $\vec{\omega}^d$ is angular velocity of un-deformed pitching blade frame with respect to inertial frame. $T_{DI}$ is transformation matrix between deformed blade frame and inertial frame, defined by following equation (Eq. 3.159).

$$\begin{bmatrix} \hat{i}_1 \\ \hat{i}_2 \\ \hat{i}_3 \end{bmatrix} = [T_{DI}] \begin{bmatrix} \hat{i}_A \\ \hat{i}_B \\ \hat{i}_C \end{bmatrix} \tag{3.163}$$

$$[T_{UI}] = [T_{DU}][T_{UR}][T_{RI}] \tag{3.164}$$

$T_{DU}$ is transformation between deformed and un-deformed matrix and is a non-linear function of deflections. The main improvement of the geometrically exact model is exact computation of $T_{DU}$ matrix which is given below (Eq. 3.165-3.173). $T_{DU}$ depends upon deflections $u, v, w, \phi$ and their spatial derivatives. To formulate $T_{DU}$, Euler angle approach is taken where each Euler angle rotation is defined in terms of deflections. Detail computation of $T_{DU}$ and its spatial derivative is carried out by Pai [108]. Using similar approach, temporal derivatives of $T_{DU}$ is being calculated.

$$T_{DU}(1,1) = \frac{1 + u' - \bar{v}k_3 + \bar{w}k_2}{1 + e} \tag{3.165}$$

$$T_{DU}(1,2) = \frac{\bar{v}' + uk_3 - \bar{w}k_1}{1+e} \tag{3.166}$$

$$T_{DU}(1,3) = \frac{\bar{w}' - uk_2 + \bar{v}k_1}{1+e} \tag{3.167}$$

$$T_{DU}(2,1) = -\cos\phi\, T_{DU}(1,2) - \sin\phi\, T_{DU}(1,3) \tag{3.168}$$

$$T_{DU}(2,2) = \cos\phi\left(T_{DU}(1,1) + \frac{T_{DU}(1,3)^2}{1+T_{DU}(1,1)}\right) - \sin\phi\,\frac{T_{DU}(1,2)\,T_{DU}(1,3)}{1+T_{DU}(1,1)} \tag{3.169}$$

$$T_{DU}(2,3) = \sin\phi\left(T_{DU}(1,1) + \frac{T_{DU}(1,2)^2}{1+T_{DU}(1,1)}\right) - \cos\phi\,\frac{T_{DU}(1,2)\,T_{DU}(1,3)}{1+T_{DU}(1,1)} \tag{3.170}$$

$$T_{DU}(3,1) = \sin\phi\, T_{DU}(1,2) - \cos\phi\, T_{DU}(1,3) \tag{3.171}$$

$$T_{DU}(3,2) = -\sin\phi\left(T_{DU}(1,1) + \frac{T_{DU}(1,3)^2}{1+T_{DU}(1,1)}\right) - \cos\phi\,\frac{T_{DU}(1,2)\,T_{DU}(1,3)}{1+T_{DU}(1,1)} \tag{3.172}$$

$$T_{DU}(3,3) = \cos\phi\left(T_{DU}(1,1) + \frac{T_{DU}(1,2)^2}{1+T_{DU}(1,1)}\right) + \sin\phi\,\frac{T_{DU}(1,2)\,T_{DU}(1,3)}{1+T_{DU}(1,1)} \tag{3.173}$$

In the above equations, $e$ represents axial strain given by following equation.

$$e = \sqrt{(1+u'-vk_3+wk_2)^2 + (v'+uk_3-wk_1)^2 + (w'-uk_2+vk_1)^2} - 1 \tag{3.174}$$

Now, substituting expression of $[\ddot{\hat{i}}_a, \ddot{\hat{i}}_b, \ddot{\hat{i}}_c]^T$ (from Eq. 3.152), $[\dot{\hat{i}}_x, \dot{\hat{i}}_y, \dot{\hat{i}}_z]^T$ (from Eq. 3.157), $[\ddot{\hat{i}}_x, \ddot{\hat{i}}_y, \ddot{\hat{i}}_z]^T$ (from Eq. 3.158) and $[\ddot{\hat{i}}_1, \ddot{\hat{i}}_2, \ddot{\hat{i}}_3]^T$ (from Eq. 3.162) into Eq. 3.140, inertial acceleration of rotor

blade can be computed.

$$\ddot{\vec{r}} = [0 \;\; 0 \;\; R]\Big([P(\,[\dot{\vec{\omega}}^r]_{abc})\,] + [P(\,[\vec{\omega}^r]_{abc})\,][P(\,[\vec{\omega}^r]_{abc})\,]\Big)\begin{bmatrix}\hat{i}_a\\ \hat{i}_b\\ \hat{i}_c\end{bmatrix}$$

$$+ [(x+u) \;\; \bar{v} \;\; \bar{w}]\Big([P(\,[\dot{\vec{\omega}}^u]_{xyz})\,] + [P(\,[\vec{\omega}^u]_{xyz})\,][P(\,[\vec{\omega}^u]_{xyz})\,]\Big)\begin{bmatrix}\hat{i}_x\\ \hat{i}_y\\ \hat{i}_z\end{bmatrix}$$

$$+ 2[\dot{u} \;\; \dot{\bar{v}} \;\; \dot{\bar{w}}][P(\,[\vec{\omega}^u]_{xyz})\,]\begin{bmatrix}\hat{i}_x\\ \hat{i}_y\\ \hat{i}_z\end{bmatrix} + [\ddot{u} \;\; \ddot{\bar{v}} \;\; \ddot{\bar{w}}]\begin{bmatrix}\hat{i}_x\\ \hat{i}_y\\ \hat{i}_z\end{bmatrix}$$

$$+ [0 \;\; \eta \;\; \zeta]\Big([P(\,[\dot{\vec{\omega}}^d]_{123})\,] + [P(\,[\vec{\omega}^d]_{123})\,][P(\,[\vec{\omega}^d]_{123})\,]\Big)\begin{bmatrix}\hat{i}_1\\ \hat{i}_2\\ \hat{i}_3\end{bmatrix} \tag{3.175}$$

Using mathematical manipulation, inertial acceleration vector can be re-wrtieen as following equation.

$$\ddot{\vec{r}} = [Q_1]\begin{bmatrix}\hat{i}_a\\ \hat{i}_b\\ \hat{i}_c\end{bmatrix} + [Q_2]\begin{bmatrix}\hat{i}_x\\ \hat{i}_y\\ \hat{i}_z\end{bmatrix} + [Q_3]\begin{bmatrix}\hat{i}_1\\ \hat{i}_2\\ \hat{i}_3\end{bmatrix} \tag{3.176}$$

Where,

$$[Q_1] = [0 \;\; 0 \;\; R]\Big([P(\,[\dot{\vec{\omega}}^r]_{abc})\,] + [P(\,[\vec{\omega}^r]_{abc})\,][P(\,[\vec{\omega}^r]_{abc})\,]\Big) \tag{3.177}$$

$$[Q_2] = [\ddot{u} \;\; \ddot{\bar{v}} \;\; \ddot{\bar{w}}] + 2[\dot{u} \;\; \dot{\bar{v}} \;\; \dot{\bar{w}}][P(\,[\vec{\omega}^u]_{xyz})\,] + [(x+u) \;\; \bar{v} \;\; \bar{w}]\Big([P(\,[\dot{\vec{\omega}}^u]_{xyz})\,] + [P(\,[\vec{\omega}^u]_{xyz})\,][P(\,[\vec{\omega}^u]_{xyz})\,]\Big) \tag{3.178}$$

$$[Q_3] = [0 \;\; \eta \;\; \zeta]\Big([P(\,[\dot{\vec{\omega}}^d]_{123})\,] + [P(\,[\vec{\omega}^d]_{123})\,][P(\,[\vec{\omega}^d]_{123})\,]\Big) \tag{3.179}$$

Now, variation of inertial position vector $\delta\vec{r}$ is computed from Eq. 3.138.

$$\delta\vec{r} = [\delta u \;\; \delta\bar{v} \;\; \delta\bar{w}] \begin{bmatrix} \hat{i}_x \\ \hat{i}_y \\ \hat{i}_z \end{bmatrix} + [0 \;\; \eta \;\; \zeta] \begin{bmatrix} \delta\hat{i}_1 \\ \delta\hat{i}_2 \\ \delta\hat{i}_3 \end{bmatrix} = \delta\vec{r}_1 + \delta\vec{r}_2 \tag{3.180}$$

Where,

$$\delta\vec{r}_1 = [\delta u \;\; \delta\bar{v} \;\; \delta\bar{w}] \begin{bmatrix} \hat{i}_x \\ \hat{i}_y \\ \hat{i}_z \end{bmatrix} = [\hat{i}_x \;\; \hat{i}_y \;\; \hat{i}_z] \begin{bmatrix} \delta u \\ \delta\bar{v} \\ \delta\bar{w} \end{bmatrix} \tag{3.181}$$

$$\delta\vec{r}_2 = [0 \;\; \eta \;\; \zeta] \begin{bmatrix} \delta\hat{i}_1 \\ \delta\hat{i}_2 \\ \delta\hat{i}_3 \end{bmatrix} \tag{3.182}$$

Variation of the unit vectors $\hat{i}_1$, $\hat{i}_2$ and $\hat{i}_3$ are caused by virtual rotations of the deformed blade coordinate system $(X_D, Y_D, Z_D)$. If $\delta\theta_1$, $\delta\theta_2$ and $\delta\theta_3$ are virtual rotation angles with respect to the axes $X_D$, $Y_D$ and $Z_D$, respectively, then following equation can be written.

$$\begin{bmatrix} \delta\hat{i}_1 \\ \delta\hat{i}_2 \\ \delta\hat{i}_3 \end{bmatrix} = \begin{bmatrix} 0 & \delta\theta_3 & -\delta\theta_2 \\ -\delta\theta_3 & 0 & \delta\theta_1 \\ \delta\theta_2 & -\delta\theta_1 & 0 \end{bmatrix} \begin{bmatrix} \hat{i}_1 \\ \hat{i}_2 \\ \hat{i}_3 \end{bmatrix} = [P(\delta\theta_1, \delta\theta_2, \delta\theta_3)] \begin{bmatrix} \hat{i}_1 \\ \hat{i}_2 \\ \hat{i}_3 \end{bmatrix} \tag{3.183}$$

Substituting above expression into Eq. 3.182, $\delta\vec{r}_2$ can be computed as following.

$$\delta\vec{r}_2 = [0 \;\; \eta \;\; \zeta][P(\delta\theta_1, \delta\theta_2, \delta\theta_3)] \begin{bmatrix} \hat{i}_1 \\ \hat{i}_2 \\ \hat{i}_3 \end{bmatrix} \tag{3.184}$$

Using properties of function $P$ from Eq. 3.148, $\delta\vec{r}_2$ can be re-written as following.

$$\begin{aligned}\delta\vec{r}_2 &= -[0 \;\; \eta \;\; \zeta][P(\hat{i}_1, \hat{i}_2, \hat{i}_3)] \begin{bmatrix}\delta\theta_1 \\ \delta\theta_2 \\ \delta\theta_3\end{bmatrix} \\ &= [\hat{i}_1 \;\; \hat{i}_2 \;\; \hat{i}_3][P(0, \eta, \zeta)] \begin{bmatrix}\delta\theta_1 \\ \delta\theta_2 \\ \delta\theta_3\end{bmatrix}\end{aligned} \tag{3.185}$$

The expression of variation of kinetic energy is given by following expression.

$$\delta T = \int_0^L \iint_A \rho\dot{\vec{r}} \cdot \delta\dot{\vec{r}} \;\; dA \;\; ds \tag{3.186}$$

In the above equation, $\rho$ is density and $A$ is cross-sectional area of the rotor blade. According to variational method, above expression of variation of kinetic energy would have to be integrated in time between two arbitrary time-points $t_1$ and $t_2$. By anticipating integration by parts, Eq. 3.137 can be re-written as:

$$\delta T = -\int_0^L \iint_A \rho\ddot{\vec{r}} \cdot \delta\vec{r} \;\; dA \;\; ds \tag{3.187}$$

In the above procedure during integration by parts, initial and final values (i.e $[\dot{\vec{r}} \cdot \delta r]_{t1}^{t2}$ ) are taken as zero. Substituting value of $\delta\vec{r}$ from Eq. 3.180, above equation can be re-written as following.

$$\delta T = -\int_0^L \iint_A \rho(\ddot{\vec{r}} \cdot \delta\vec{r}_1 + \ddot{\vec{r}} \cdot \delta\vec{r}_2) \;\; dA \;\; ds \tag{3.188}$$

To compute $\ddot{\vec{r}} \cdot \delta\vec{r}_1$, $\ddot{\vec{r}}$ is expressed in un-deformed blade pitching coordinate frame $(X_U, Y_U, Z_U)$ since $\delta\vec{r}_1$ is also expressed in same coordinate frame. Utilizing Eq. 3.5 and 3.6, inertial acceleration

vector can be computed from Eq. 3.176 using following procedure.

$$\begin{aligned}\ddot{\vec{r}} &= [Q_1][T_{UR}]^T \begin{bmatrix}\hat{i}_x\\ \hat{i}_y\\ \hat{i}_z\end{bmatrix} + [Q_2] \begin{bmatrix}\hat{i}_x\\ \hat{i}_y\\ \hat{i}_z\end{bmatrix} + [Q_3][T_{DU}] \begin{bmatrix}\hat{i}_x\\ \hat{i}_y\\ \hat{i}_z\end{bmatrix} \\ &= \Big([Q_1][T_{UR}]^T + [Q_2] + [Q_3][T_{DU}]\Big) \begin{bmatrix}\hat{i}_x\\ \hat{i}_y\\ \hat{i}_z\end{bmatrix} \end{aligned} \tag{3.189}$$

In the above formula, orthogonality of transformation matrix, $T_{UR}$, ($[T_{UR}]^{-1} = [T_{UR}]^T$) is utilized. Utilizing Eq. 3.189 and 3.181, $\ddot{\vec{r}} \cdot \delta\vec{r}_1$ is computed.

$$\begin{aligned}\ddot{\vec{r}} \cdot \delta\vec{r}_1 &= \Big([Q_1][T_{UR}]^T + [Q_2] + [Q_3][T_{DU}]\Big) \begin{bmatrix}\hat{i}_x\\ \hat{i}_y\\ \hat{i}_z\end{bmatrix} \cdot [\hat{i}_x \;\; \hat{i}_y \;\; \hat{i}_z] \begin{bmatrix}\delta u\\ \delta\bar{v}\\ \delta\bar{w}\end{bmatrix} \\ &= \Big([Q_1][T_{UR}]^T + [Q_2] + [Q_3][T_{DU}]\Big) \begin{bmatrix}\delta u\\ \delta\bar{v}\\ \delta\bar{w}\end{bmatrix} \end{aligned} \tag{3.190}$$

To compute $\ddot{\vec{r}} \cdot \delta\vec{r}_2$, $\ddot{\vec{r}}$ is expressed in deformed blade coordinate frame $(X_D, Y_D, Z_D)$ since $\delta\vec{r}_2$ is also expressed in same coordinate frame. For this purpose, unit vectors in rotating frame, $[\hat{i}_a, \hat{i}_b, \hat{i}_c]^T$, are converted into unit vectors in deformed blade frame, $[\hat{i}_1, \hat{i}_2, \hat{i}_3]^T$, using suitable transformation matrices (Eq. 3.5 and 3.6) as discussed below.

$$\begin{bmatrix}\hat{i}_1\\ \hat{i}_2\\ \hat{i}_3\end{bmatrix} = [T_{DU}] \begin{bmatrix}\hat{i}_x\\ \hat{i}_y\\ \hat{i}_z\end{bmatrix} = [T_{DU}][T_{UR}] \begin{bmatrix}\hat{i}_a\\ \hat{i}_b\\ \hat{i}_c\end{bmatrix} = [T_{DR}] \begin{bmatrix}\hat{i}_a\\ \hat{i}_b\\ \hat{i}_c\end{bmatrix} \tag{3.191}$$

Where,

$$[T_{DR}] = [T_{DU}][T_{UR}] \tag{3.192}$$

Utilizing Eq. 3.6 and 3.191, inertial acceleration vector, $\ddot{\vec{r}}$, can be computed in deformed blade coordinate frame $(X_D, Y_D, Z_D)$ from Eq. 3.176 using following procedure.

$$\begin{aligned}\ddot{\vec{r}} &= [Q_1][T_{DR}]^T \begin{bmatrix}\hat{i}_1\\ \hat{i}_2\\ \hat{i}_3\end{bmatrix} + [Q_2][T_{DU}]^T \begin{bmatrix}\hat{i}_1\\ \hat{i}_2\\ \hat{i}_3\end{bmatrix} + [Q_3] \begin{bmatrix}\hat{i}_1\\ \hat{i}_2\\ \hat{i}_3\end{bmatrix} \\ &= \Big([Q_1][T_{DR}]^T + [Q_2][T_{DU}]^T + [Q_3]\Big) \begin{bmatrix}\hat{i}_1\\ \hat{i}_2\\ \hat{i}_3\end{bmatrix}\end{aligned} \tag{3.193}$$

In the above formula, orthogonality of transformation matrices, $T_{DR}$ and $T_{DU}$, ($[T_{DR}]^{-1} = [T_{DR}]^T,\ [T_{DU}]^{-1} = [T_{DU}]^T$) is utilized. Utilizing Eq. 3.193 and 3.181, $\ddot{\vec{r}} \cdot \delta\vec{r}_2$ is computed.

$$\begin{aligned}\ddot{\vec{r}} \cdot \delta\vec{r}_2 &= \Big([Q_1][T_{DR}]^T + [Q_2][T_{DU}]^T + [Q_3]\Big) \begin{bmatrix}\hat{i}_1\\ \hat{i}_2\\ \hat{i}_3\end{bmatrix} \cdot [\hat{i}_1\ \ \hat{i}_2\ \ \hat{i}_3][P(0,\eta,\zeta)] \begin{bmatrix}\delta\theta_1\\ \delta\theta_2\\ \delta\theta_3\end{bmatrix} \\ &= \Big([Q_1][T_{DR}]^T + [Q_2][T_{DU}]^T + [Q_3]\Big)[P(0,\eta,\zeta)] \begin{bmatrix}\delta\theta_1\\ \delta\theta_2\\ \delta\theta_3\end{bmatrix}\end{aligned} \tag{3.194}$$

Substituting expression of $\ddot{\vec{r}} \cdot \delta\vec{r}_1$ (from Eq. 3.190) and $\ddot{\vec{r}} \cdot \delta\vec{r}_2$ (from Eq. 3.194) into Eq. 3.188,

variation of kinetic energy is computed.

$$\delta T = -\int_0^L \iint_A \rho \Bigg( \Big( [Q_1][T_{UR}]^T + [Q_2] + [Q_3][T_{DU}] \Big) \begin{bmatrix} \delta u \\ \delta \bar{v} \\ \delta \bar{w} \end{bmatrix} + \Big( [Q_1][T_{DR}]^T + [Q_2][T_{DU}]^T + [Q_3] \Big) [P(0,\eta,\zeta)] \begin{bmatrix} \delta\theta_1 \\ \delta\theta_2 \\ \delta\theta_3 \end{bmatrix} \Bigg) \; dA \; ds \tag{3.195}$$

Using mathematical manipulation, above expression can be re-written as following equation.

$$\delta T = -\int_0^L \left( \Big( [I_{c1}] + [I_{c2}] \Big) \begin{bmatrix} \delta u \\ \delta \bar{v} \\ \delta \bar{w} \end{bmatrix} + \Big( [I_{c3}] + [I_{c4}] \Big) \begin{bmatrix} \delta\theta_1 \\ \delta\theta_2 \\ \delta\theta_3 \end{bmatrix} \right) \; ds \tag{3.196}$$

Where,

$$[I_{c1}] = \iint_A \rho \Big( [Q_1][T_{UR}]^T + [Q_2] \Big) \; dA \tag{3.197}$$

$$[I_{c2}] = \iint_A \rho [Q_3][T_{DU}] \; dA \tag{3.198}$$

$$[I_{c3}] = \iint_A \rho \Big( [Q_1][T_{DR}]^T + [Q_2][T_{DU}]^T \Big) [P(0,\eta,\zeta)] \; dA \tag{3.199}$$

$$[I_{c4}] = \iint_A \rho [Q_3][P(0,\eta,\zeta)] \; dA \tag{3.200}$$

To compute above integrals, sectional properties from Eq. 3.51 and 3.52 are utilized. Based on these sectional properties, following integrals are introduced.

$$[J_1] = \iint_A \rho [P(0,\eta,\zeta)] \; dA = m[P(0,e_g,0)] \tag{3.201}$$

$$
\begin{aligned}
[J_2] &= \iint_A \rho[P(0,\eta,\zeta)]^T[P(0,\eta,\zeta)]\ dA \\
&= \iint_A \rho\left( \begin{bmatrix} (\eta^2+\zeta^2) & 0 & 0 \\ 0 & \zeta^2 & 0 \\ 0 & 0 & \eta^2 \end{bmatrix} \right)\ dA \\
&= m \begin{bmatrix} k_m^2 & 0 & 0 \\ 0 & k_{m_1}^2 & 0 \\ 0 & 0 & k_{m_2}^2 \end{bmatrix}
\end{aligned} \tag{3.202}
$$

Now, $[I_{c1}]$ is computed from Eq. 3.197.

$$
[I_{c1}] = m\Big([Q_1][T_{UR}]^T + [Q_2]\Big) \tag{3.203}
$$

To compute $[I_{c2}]$, expression $[Q_3]$ from Eq. 3.179 is modified using properties of function P (Eq. 3.148).

$$
[Q_3] = -[\dot{\vec{\omega}}^d]_{123}^T[P(0,\eta,\zeta)] - [\vec{\omega}^d]_{123}^T[P(0,\eta,\zeta)][P(\ [\vec{\omega}^d]_{123})\ ] \tag{3.204}
$$

Utilizing eq. 3.198 and 3.204,$[I_{c2}]$ is computed.

$$
\begin{aligned}
[I_{c2}] &= -\iint_A \rho\Big([\dot{\vec{\omega}}^d]_{123}^T[P(0,\eta,\zeta)] + [\vec{\omega}^d]_{123}^T[P(0,\eta,\zeta)][P(\ [\vec{\omega}^d]_{123})\ ]\Big)[T_{DU}]\ \ dA \\
&= -\Big([\dot{\vec{\omega}}^d]_{123}^T[J_1] + [\vec{\omega}^d]_{123}^T[J_1][P(\ [\vec{\omega}^d]_{123})\ ]\Big)[T_{DU}]
\end{aligned} \tag{3.205}
$$

From Eq. 3.199, $[I_{c3}]$ is computed.

$$
\begin{aligned}
[I_{c3}] &= \Big([Q_1][T_{DR}]^T + [Q_2][T_{DU}]^T\Big) \iint_A \rho[P(0,\eta,\zeta)]\ \ dA \\
&= \Big([Q_1][T_{DR}]^T + [Q_2][T_{DU}]^T\Big)[J_1]
\end{aligned} \tag{3.206}
$$

Utilizing eq. 3.200 and 3.204,$[I_{c4}]$ is computed.

$$[I_{c4}] = \iint_A \rho\Big( - [\dot{\vec{\omega}}^d]^T_{123}[P(0,\eta,\zeta)] - [\vec{\omega}^d]^T_{123}[P(0,\eta,\zeta)][P(\ [\vec{\omega}^d]_{123})\ ]\Big)[P(0,\eta,\zeta)]\ \ dA \quad (3.207)$$

By simple matrix expansion, it can be shown that

$$[P(\ [\vec{\omega}^d]_{123}[P(0,\eta,\zeta)] = [P(0,\eta,\zeta)][P(\ [\vec{\omega}^d]_{123} \quad (3.208)$$

Utilizing above equation (Eq. 3.208) and property of function P (Eq. 3.146), $I_{c4}$ is computed from Eq. 3.207.

$$\begin{aligned}[I_{c4}] &= \iint_A \rho\Big([\dot{\vec{\omega}}^d]^T_{123}[P(0,\eta,\zeta)]^T[P(0,\eta,\zeta)] \\ &\qquad + [\vec{\omega}^d]^T_{123}[P(0,\eta,\zeta)]^T[P(0,\eta,\zeta)][P(\ [\vec{\omega}^d]_{123})\ ]\Big)\ \ dA \\ &= [\dot{\vec{\omega}}^d]^T_{123}[J_2] + [\vec{\omega}^d]^T_{123}[J_2][P(\ [\vec{\omega}^d]_{123})\ ] \end{aligned} \quad (3.209)$$

### 3.4.2 Computation of Strain Energy

For purpose of deriving strain energy, cyclodial rotor blade is assumed to be long slender isotropic beam. Strain energy can be expressed in terms of stresses and strains. For this purpose nonlinear Jaumann strain is used instead of linear Cauchy strains used in $2^{nd}$ order nonlinear model. This is because Jaumann strains are fully non-linear, objective and the geometric strain measures and their directions are defined with respect to deformed coordinate system $(X_D, Y_D, Z_D)$. Inclusion of nonlinear Jaumann stress-strain over linear stress strain is another major improvement of geometrically exact model over $2^{nd}$ order nonlinear model. The objective here is to express strain energy in terms of deflections. Using stress-strain relationship, stresses in the strain energy expression are written in terms of strains. Then, using strain-deflection relationships, strains can be written in terms of deflections.

Elastic strain energy can be expressed as following equation.

$$\delta U = \int_0^L \iint_A J_{ij}\ \delta B_{ij}\ \ dA\ \ ds \tag{3.210}$$

In the above equation, $J$ is Jaumann stress tensor and $B$ is Jaumann strain tensor. Using uni-axial stress assumptions, following stress components are considered zero.

$$J_{22} = J_{33} = J_{23} = 0 \tag{3.211}$$

Moreover,

$$J_{ij} = J_{ji} \tag{3.212}$$

$$B_{ij} = B_{ji} \tag{3.213}$$

Substituting Eqs. 3.211 - 3.213 into Eq. 3.210, variation of strain energy can be expressed as following equation.

$$\delta U = \int_0^L \iint_A (J_{11}\ \delta B_{11} + 2J_{12}\ \delta B_{12} + 2J_{13}\ \delta B_{13})\ \ dA\ \ ds \tag{3.214}$$

Relationship between Jaumann stress and Jaumann strain for an isotropic beam is given by following expression.

$$\begin{bmatrix} J_{11} \\ J_{12} \\ J_{13} \end{bmatrix} = \begin{bmatrix} E & 0 & 0 \\ 0 & G & 0 \\ 0 & 0 & G \end{bmatrix} \begin{bmatrix} B_{11} \\ 2B_{12} \\ 2B_{13} \end{bmatrix} \tag{3.215}$$

Substituting expression of Jauman stress (Eq. 3.215) into expression of strain energy (Eq. 3.214), following equation is obtained.

$$\delta U = \iint_0^L \iint_A (EB_{11}\ \delta B_{11} + 4GB_{12}\ \delta B_{12} + 4GB_{13}\ \delta B_{13})\ \ dA\ \ dS \tag{3.216}$$

The next objective is to express strain in terms of blade deflections. For that reason, Jaumann

strains are expressed in terms of deflections as following.

$$B_{11} = \frac{\partial \vec{U}}{\partial s}.\hat{i}_1 \tag{3.217}$$

$$2B_{12} = \frac{\partial \vec{U}}{\partial s}.\hat{i}_2 + \frac{\partial \vec{U}}{\partial \eta}.\hat{i}_1 \tag{3.218}$$

$$2B_{13} = \frac{\partial \vec{U}}{\partial s}.\hat{i}_3 + \frac{\partial \vec{U}}{\partial \zeta}.\hat{i}_1 \tag{3.219}$$

In the above equations $\vec{U}$ is the local displacement field. $\vec{U}$ can be expressed as following.

$$\vec{U} = u_1\hat{i}_1 + u_2\hat{i}_2 + u_3\hat{i}_3 \tag{3.220}$$

Where, $u_1$, $u_2$ and $u_3$ are local strainable displacements with respect to deformed blade coordinate axes $X_D$, $Y_D$ and $Z_D$ respectively. $u_1$, $u_2$ and $u_3$ can be expressed as following [108].

$$u_1 = u_1^0 + \zeta\bar{\theta}_2 - \eta\bar{\theta}_3 \tag{3.221}$$

$$u_2 = u_2^0 - \zeta\bar{\theta}_1 \tag{3.222}$$

$$u_3 = u_3^0 + \eta\bar{\theta}_1 \tag{3.223}$$

In the above equations, $\bar{\theta}_i = \theta_i - \theta_{i0}$ for $i = 1, 2, 3$. $\theta_1$, $\theta_1$ and $\theta_1$ are rotation angles of the blade cross section with respect to deformed blade coordinate axes $X_D$, $Y_D$ and $Z_D$ respectively. $\theta_{10}$, $\theta_{20}$ and $\theta_{30}$ are initial rotation angles of the blade cross section with respect to deformed blade coordinate axes $X_D$, $Y_D$ and $Z_D$ respectively. Since, $X_D$, $Y_D$ and $Z_D$ are the co-ordinate system attached to deformed blade frame, following terms are zero by definition.

$$u_1^0 = u_2^0 = u_3^0 = 0 \tag{3.224}$$

$$\theta_1 = \theta_2 = \theta_3 = 0 \tag{3.225}$$

$$\theta_{10} = \theta_{20} = \theta_{30} = 0 \tag{3.226}$$

Although, the variations of all the above variables ($u_i^0$, $\theta_i$ and $\theta_{i0}$) are not zero. This is due to the face that $X_D$, $Y_D$ and $Z_D$ axes are not straight lines because of blade deformation. Axial derivative of $u_i^0$ can be expressed as following.

$$\frac{\partial u_1^0}{\partial s} = e \tag{3.227}$$

$$\frac{\partial u_2^0}{\partial s} = 0 \tag{3.228}$$

$$\frac{\partial u_3^0}{\partial s} = 0 \tag{3.229}$$

In Eq. 3.229, $e$ is axial elongation. Axial derivative of rotation angles ($\theta_i$) can be expressed as following.

$$\frac{\partial \theta_i}{\partial s} = \rho_i \tag{3.230}$$

In the above equation, $\rho_1$, $\rho_2$ and $\rho_3$ are deformed curvatures of rotor blade with respect to deformed blade coordinate axes $X_D$, $Y_D$ and $Z_D$ respectively. Axial derivative of initial rotation angles ($\theta_i$) can be expressed as following.

$$\frac{\partial \theta_{i0}}{\partial s} = k_i \tag{3.231}$$

In the above equation, $k_{10}$, $k_{20}$ and $k_{30}$ are deformed curvatures of rotor blade with respect to deformed blade coordinate axes $X_D$, $Y_D$ and $Z_D$ respectively. Using above formulas, strains can be expressed in terms of deflections. From Eq. 3.220, axial derivative of local displacement field can be obtained in the following manner.

$$\frac{\partial \vec{U}}{\partial s} = \frac{\partial u_1}{\partial s}\hat{i}_1 + \frac{\partial u_2}{\partial s}\hat{i}_2 + \frac{\partial u_3}{\partial s}\hat{i}_3 \tag{3.232}$$

Substituting values of $u_1$, $u_2$ and $u_3$, above equation can be re-written as following.

$$\begin{aligned}\frac{\partial \vec{U}}{\partial s} &= \left(\frac{\partial u_1^0}{\partial s} + \zeta\frac{\partial \bar{\theta}_2}{\partial s} - \eta\frac{\partial \bar{\theta}_3}{\partial s}\right)\hat{i}_1 + \left(\frac{\partial u_2^0}{\partial s} - \zeta\frac{\partial \bar{\theta}_1}{\partial s}\right)\hat{i}_2 + \left(\frac{\partial u_3^0}{\partial s} + \eta\frac{\partial \bar{\theta}_1}{\partial s}\right)\hat{i}_3 \\ &= (e + \zeta\bar{\rho}_2 - \eta\bar{\rho}_3)\hat{i}_1 - \zeta\bar{\rho}_1\hat{i}_2 + \eta\bar{\rho}_1\hat{i}_3 \end{aligned} \tag{3.233}$$

In the above equations,

$$\bar{\rho}_i = \rho_i - k_i \tag{3.234}$$

Now, $y$ and $z$ derivative of local displacement field is computed using following procedure.

$$\begin{aligned}\frac{\partial \vec{U}}{\partial \eta} &= \frac{\partial u_1}{\partial \eta}\hat{i}_1 + \frac{\partial u_2}{\partial \eta}\hat{i}_2 + \frac{\partial u_3}{\partial \eta}\hat{i}_3 \\ &= -\bar{\theta}_3\hat{i}_1 + \bar{\theta}_1\hat{i}_3 \\ &= 0 \end{aligned} \tag{3.235}$$

$$\begin{aligned}\frac{\partial \vec{U}}{\partial \zeta} &= \frac{\partial u_1}{\partial \zeta}\hat{i}_1 + \frac{\partial u_2}{\partial \zeta}\hat{i}_2 + \frac{\partial u_3}{\partial \zeta}\hat{i}_3 \\ &= \bar{\theta}_2\hat{i}_1 - \bar{\theta}_1\hat{i}_2 \\ &= 0 \end{aligned} \tag{3.236}$$

Utilizing derivatives of local displacement field in the above expressions, Jaumann strains are computed.

$$B_{11} = \frac{\partial \vec{U}}{\partial s}.\hat{i}_1 = e + \zeta\bar{\rho}_2 - \eta\bar{\rho}_3 \tag{3.237}$$

$$2B_{12} = \frac{\partial \vec{U}}{\partial s}.\hat{i}_2 + \frac{\partial \vec{U}}{\partial \eta}.\hat{i}_1 = -\zeta\bar{\rho}_1 \tag{3.238}$$

$$2B_{13} = \frac{\partial \vec{U}}{\partial s}.\hat{i}_3 + \frac{\partial \vec{U}}{\partial \zeta}.\hat{i}_1 = \eta\bar{\rho}_1 \tag{3.239}$$

Now variation of Jaumann strains are computed from above equations.

$$\delta B_{11} = \delta e + \zeta \delta \bar{\rho}_2 - \eta \delta \bar{\rho}_3 \tag{3.240}$$

$$2\delta B_{12} = -\zeta \delta \bar{\rho}_1 \tag{3.241}$$

$$2\delta B_{13} = \eta \delta \bar{\rho}_1 \tag{3.242}$$

Now, $k_1$, $k_2$ and $k_3$ are inital curvatures. So, its variations are zero ($\delta k_i = 0$). Which leads to $\delta \bar{\rho}_i = \delta \rho_i$ for $i = 1$, 2 and 3. Substituting expressions of $\delta B_{11}$, $\delta B_{12}$ and $\delta B_{13}$ from above equations into Eq. 3.216, variation of strain energy can be computed.

$$\begin{aligned}
\delta U &= \int_0^L \iint_A [(EB_{11}\ (\delta e + \zeta \delta \bar{\rho}_2 - \eta \delta \bar{\rho}_3) + 2GB_{12}(-\zeta \delta \bar{\rho}_1) + 2GB_{13}(\eta \delta \bar{\rho}_1)]\ \ dA\ \ dS \\
&= \int_0^L \iint_A [(EB_{11})\delta e + 2G(\eta B_{13} - \zeta B_{12})\delta \rho_1 + \zeta EB_{11}\delta \rho_2 - \eta EB_{11}\delta \rho_2]]\ \ dA\ \ dS \\
&= \int_0^L (F_1 \delta e + M_1 \delta \rho_1 + M_2 \delta \rho_2 + M_3 \delta \rho_3)\ \ dS
\end{aligned} \tag{3.243}$$

Where,

$$F_1 = \iint_A EB_{11}\ \ dA \tag{3.244}$$

$$M_1 = \iint_A 2G(\eta B_{13} - \zeta B_{12})\ \ dA \tag{3.245}$$

$$M_2 = \iint_A \zeta EB_{11}\ \ dA \tag{3.246}$$

$$M_3 = \iint_A -\eta EB_{11}\ \ dA \tag{3.247}$$

To compute above integrals, following sectional properties are introduced

$$\left.\begin{aligned} \iint_A dA &= A \\ \iint_A \eta \ dA &= Ae_A \\ \iint_A \zeta^2 \ dA &= I_y \\ \iint_A \eta^2 \ dA &= I_z \\ \iint_A (\eta^2 + \zeta^2) \ dA &= Ak_A^2 \end{aligned}\right\} \tag{3.248}$$

In the above equation, $A$ is blade cross-sectional area, $e_A$ is tensile axis offset from the blade elastic axis and $k_A$ is radius of gyration of blade cross section. $I_y$ and $I_z$ are area moment of inertia along flap and lag directions respectively. The rotor blade cross-section is assumed to be symmetric about the $\hat{i}_2$ axis. For this reason, following integrals become zeros.

$$\left.\begin{aligned} \iint_A \zeta \ dA &= 0 \\ \iint_A \zeta\eta \ dA &= 0 \end{aligned}\right\} \tag{3.249}$$

Using above sectional properties, following integrals are computed.

$$\begin{aligned} F_1 &= \iint_A EB_{11} \ dA \\ &= \iint_A E(e + \zeta\bar{\rho}_2 - \eta\bar{\rho}_3) \ dA \\ &= Ee \iint_A dA + E\bar{\rho}_2 \iint_A \zeta \ dA - E\bar{\rho}_3 \iint_A \eta \ dA \\ &= EAe - EAe_A\bar{\rho}_3 \end{aligned} \tag{3.250}$$

$$
\begin{aligned}
M_1 &= \iint_A 2G(\eta B_{13} - \zeta B_{12}) \ dA \\
&= \iint_A G[\eta.\eta\bar{\rho}_1 - \zeta(-\zeta\bar{\rho}_1)] \ dA \\
&= G\bar{\rho}_1 \iint_A (\eta^2 + \zeta^2) \ dA \\
&= GAk_A^2\bar{\rho}_1
\end{aligned} \tag{3.251}
$$

$$
\begin{aligned}
M_2 &= \iint_A \zeta E B_{11} \ dA \\
&= \iint_A \zeta E(e + \zeta\bar{\rho}_2 - \eta\bar{\rho}_3) \ dA \\
&= Ee \iint_A \zeta \ dA + E\bar{\rho}_2 \iint_A \zeta^2 \ dA - E\bar{\rho}_3 \iint_A \eta\zeta \ dA \\
&= EI_y\bar{\rho}_2
\end{aligned} \tag{3.252}
$$

$$
\begin{aligned}
M_3 &= -\iint_A \eta E B_{11} \ dA \\
&= \iint_A \eta E(-e - \zeta\bar{\rho}_2 + \eta\bar{\rho}_3) \ dA \\
&= -Ee \iint_A \eta \ dA - E\bar{\rho}_2 \iint_A \eta\zeta \ dA + E\bar{\rho}_3 \iint_A \eta^2 \ dA \\
&= -EAe_Ae + EI_z\bar{\rho}_3
\end{aligned} \tag{3.253}
$$

It can be shown (ref: PI's book) that if $H$ is a function of $s$, then

$$
\int_0^L H\delta\rho_1 \ ds = \int_0^L (-H'\delta\theta_1 - H\rho_3\delta\theta_2 + H\rho_2\delta\theta_3)ds + H\delta\theta_1\Big|_0^L \tag{3.254}
$$

$$
\int_0^L H\delta\rho_2 \ ds = \int_0^L (-H'\delta\theta_2 - H\rho_1\delta\theta_3 + H\rho_3\delta\theta_1)ds + H\delta\theta_2\Big|_0^L \tag{3.255}
$$

$$
\int_0^L H\delta\rho_3 \ ds = \int_0^L (-H'\delta\theta_3 - H\rho_2\delta\theta_1 + H\rho_1\delta\theta_2)ds + H\delta\theta_3\Big|_0^L \tag{3.256}
$$

In the above equations, $\delta\theta_1$, $\delta\theta_2$ and $\delta\theta_3$ are virtual rotation angles with respect to the axes $X_D$,

$Y_D$ and $Z_D$, respectively. Utilizing above set of equations, variation of strain energy can computed from Eq. 3.243.

$$\delta U = \int_0^L (F_1 \delta e + B_{\theta_1} \delta\theta_1 + B_{\theta_2} \delta\theta_2 + B_{\theta_3} \delta\theta_3) \ dS + [M_1 \delta\theta_1 + M_2 \delta\theta_2 + M_3 \delta\theta_3]_0^L \tag{3.257}$$

Where,

$$B_{\theta_1} = (-M_1' + M_2\rho_3 - M_3\rho_2) \tag{3.258}$$

$$B_{\theta_2} = (-M_2' + M_3\rho_1 - M_1\rho_3) \tag{3.259}$$

$$B_{\theta_3} = (-M_3' + M_1\rho_2 - M_2\rho_1) \tag{3.260}$$

The next job is to express $e$ in terms of deflections. it can be shown (ref:PI's book) that

$$\begin{bmatrix} \delta e \\ (1+e)\delta\theta_3 \\ -(1+e)\delta\theta_2 \end{bmatrix} = [T_{DU}] \begin{bmatrix} \delta u' \\ \delta v' \\ \delta w' \end{bmatrix} - [T_{DU}][P(k_1, k_2, k_3)] \begin{bmatrix} \delta u \\ \delta v \\ \delta w \end{bmatrix} \tag{3.261}$$

In the above equation, $k_1$, $k_2$ and $k_3$ are initial curvatures with respect to $X_D$, $Y_D$ and $Z_D$ axes, respectively. Utilizing Eq. 3.261, variation of strain energy can be re-written from Eq. 3.262

$$\begin{aligned} \delta U = \int_0^L \Bigg( & [F_1 \ \ 0 \ \ 0][T_{DU}] \begin{bmatrix} \delta u' \\ \delta v' \\ \delta w' \end{bmatrix} - [F_1 \ \ 0 \ \ 0][T_{DU}][P(k_1, k_2, k_3)] \begin{bmatrix} \delta u \\ \delta v \\ \delta w \end{bmatrix} \\ & + [B_{\theta_1} \ \ B_{\theta_2} \ \ B_{\theta_3}] \begin{bmatrix} \delta\theta_1 \\ \delta\theta_2 \\ \delta\theta_3 \end{bmatrix} \Bigg) \ dS + [M_1 \delta\theta_1 + M_2 \delta\theta_2 + M_3 \delta\theta_3]_0^L \end{aligned} \tag{3.262}$$

#### *3.4.2.1 Solution Methodology*

For purely structural problem, virtual work done by external forces ($\delta W$) are zero. Substituting expressions of variation of kinetic energy (Eq. 3.44 for $2^{nd}$ order model or Eq. 3.196 for geometrically exact model ) and variation of elastic strain energy (Eq. 3.106 for $2^{nd}$ order model or Eq. 3.211 for geometrically exact model) and variation of virtual work done by external forces (Eq. **??**) into Hamilton's principle (Eq. 4.1), governing differential equations are obtained (Eq. 3.263).

$$\underline{f}(\underline{y}, \underline{\dot{y}}, \underline{\ddot{y}}) = 0 \tag{3.263}$$

In Eq. 3.263, $\underline{y} = [u, u', u'', v, v', v'', w, w', w'', \phi, \phi']^T$ are bending and torsional deflections and their spatial derivatives. To solve the above PDE, proper discretization scheme is being applied to convert differential equation into algebraic equations. To convert spatial derivative into algebraic forms, PDE in Eq. 3.263 is discretized in space using Finite Element Method (FEM) and the following equation is obtained (Eq. 3.264).

$$M\underline{\ddot{x}} + C\underline{\dot{x}} + K\underline{x} = 0 \tag{3.264}$$

For this purpose, mixed higher order interpolation functions are used to avoid shear locking. Hermite interpolation function is used to discretize $u, v$ and $w$ while Lagrange interpolation function is used to discretize $\phi$. To obtain steady state blade response, above equation (Eq. 3.264) is discretized in time using Newmark-$\beta$ method which gives an algebraic equation (Eq. 3.265).

$$A\underline{z} = \underline{Q} \tag{3.265}$$

The nonlinear systems of equations (Eq. 3.265) is solved numerically to obtain steady state blade response $\underline{z}$. A solution scheme based on Newton-Raphson method is developed in this purpose to solve nonlinear systems of equations given in Eq. 3.265. Present structural model and the computational framework has the flexibility to incorporate any necessary boundary conditions at

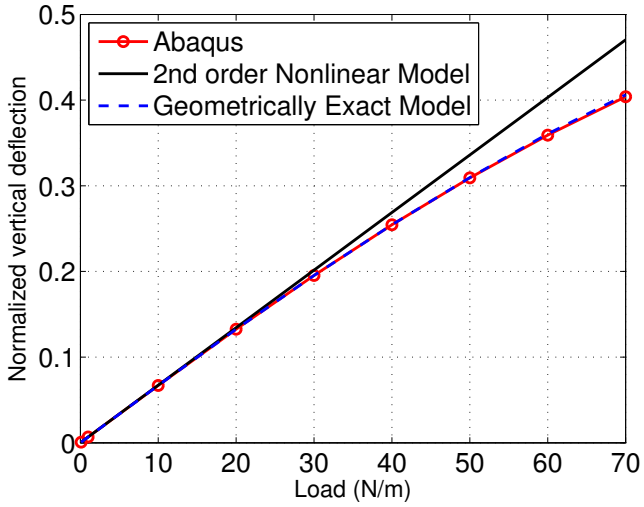


Figure 3.4: Comparison of tip normal deflection for a cantilever beam under uniformly distributed load at Neutral Axis.

both ends. For analysis presented in this paper, the beam is assumed to be fixed in bending at both end, while torsion boundary condition is assumed to be fixed only at root end and free at other end. This is because of the pitch link at root end which is assumed to be rigid.

### 3.5 Validation of Structural Model

Both the developed models, second-order nonlinear beam model and geometrically exact beam model, have been validated by comparing them with the deflections predicted by Abaqus (a commercial structural analysis software) over a range of cases.

Figure 3.4 shows static validation of a cantilever beam for very high deflections. A distributed load has been applied at neutral axis of a rectangular Aluminum beam of 20 inch length having cross section 0.5 inch x 0.125 inch. In Fig. 3.4, Y- axis shows vertical (normal) deflection of beam tip normalized by the beam span which is plotted against distributed load per unit span in X- axis. It is clearly observed from the figure that $2^{nd}$ order nonlinear model starts over-predicting deflection after $15-20\%$, although geometrically exact beam model can accurately predict very high deflection. This is due to the reason that nonlinearities in bending are of third order which is not captured by $2^{nd}$ order nonlinear model. Figure 3.5 shows static deflections of a similar cantilever

beam (0.125 inch x 0.5 inch cross section and 20 inch lenght) due to application of distributed load along the elastic axis. In this case the beam is at an angle of $15^0$ from vertical so that load would create both radial and tangential bending. Figures 3.5a, 3.5b and 3.5c show comparison of tip radial bending, tip tangential bending and tip twist, respectively, with increasing distributed vertical load (along X-axis) on the beam. Although no external moment is applied, bending curvature produces nonlinear moment (Eq. 27) and thus beam undergoes torsional deflection. Prediction of this nonlinear twist is only as good as the estimation of bending deflections and bending curvature. Second-order nonlinear model can capture this nonlinear twist till bending deflections are not large. Figure 3.5 shows that radial bending is over-predicted by $2^{nd}$ order model after 15% (Fig. 3.5a)and tangential bending is over-predicted after 10-12% (Fig. 3.5b) and around the same level of bending deflection this model starts over-predicting the tip twist (Fig. 3.5c). However, geometrically exact model can accurately predict very high radial and tangential bending deflections (Fig. 3.5a). For that reason, geometrically exact model is capable of accurately predicting nonlinear twist arising from bending curvatures (Fig. 3.5c). Figures 3.6 and 3.7 show similar comparison as in the case of Fig. 3.4, with only different boundary conditions. Figure 3.6 shows mid-beam vertical deflection (Y-axis) of a simply supported beam [same rectangular beam discussed before under uniformly distributed load (X-axis)]. In this case, mid-beam deflection is over-predicted by $2^{nd}$ order nonlinear model after the deflection is 6%-7% of beam span. The effect of higher order nonlinearities become significant at much lower deflections compared to cantilever cases. This is because of additional constraints at both ends of a cantilever beam which creates larger bending curvatures leading to nonlinear behavior starting much earlier. Figure 3.7 shows mid-beam vertical deflection (Y-axis) of a beam fixed/clamped at both ends under the action of uniformly distributed load (X-axis) at neutral axis. In this case, over-prediction of deflection by $2^{nd}$ order nonlinear model starts even earlier, at 0.2% mid-beam vertical deflection. This is because of more constraints imposed at both ends, which creates more bending curvature. In both Figs. 3.6 and 3.7, geometrically exact beam model accurately predicts the deflections. To calculate even smaller deflections of beam under these types of boundary conditions, a fully nonlinear model is neces-

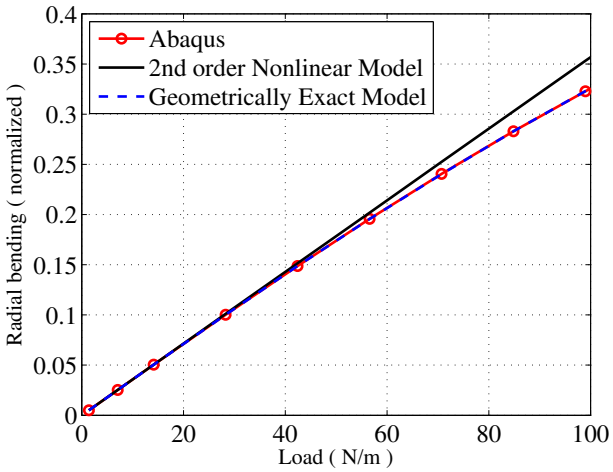


(a) a) Comparison of Tip Radial bending

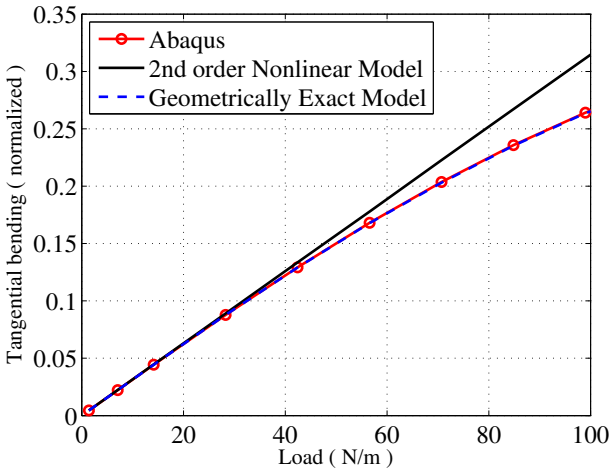


(b) b) Comparison of Tip Tangential bending

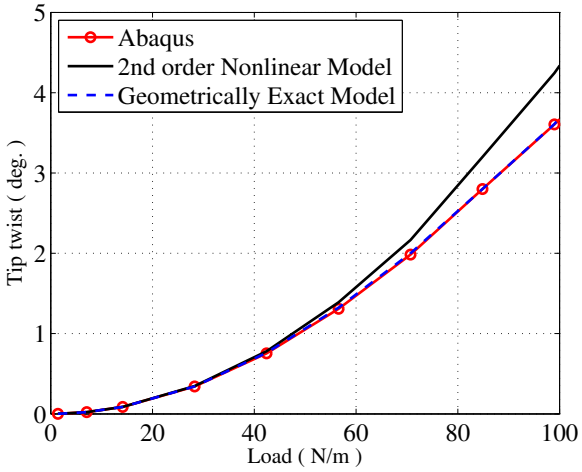


(c) c) Comparison of Tip twist

Figure 3.5: Comparison of tip deflection for a cantilever beam with uniform load applied at elastic axis at $15^0$ angle and with no external moment.

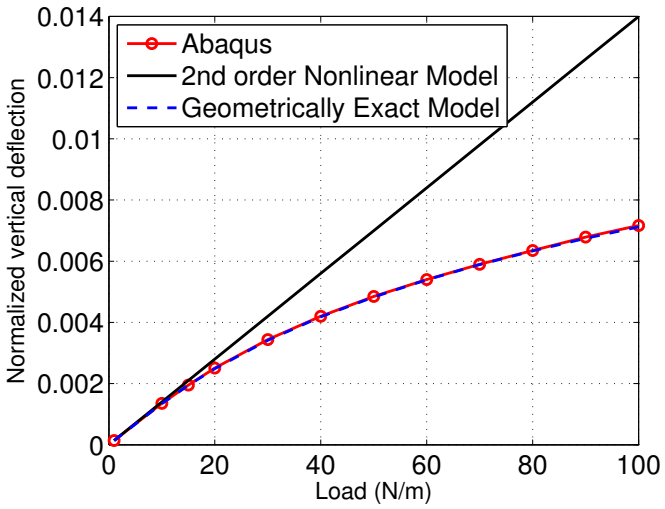


Figure 3.6: Comparison of Mid-beam normal deflection for a simply supported beam.

sary. Since conventional rotor blades are cantilever in nature, the nonlinearities in those blades starts dominating at high deflections over 10-15% of blade span. For that reason, a $2^{nd}$ order model (Hodges-Dowell model) is good enough for structural analysis for these types of blades of conventional rotor. On the other hand, cycloidal rotor blades are fixed-fixed in bending at both ends which creates much more bending curvature due to constraints. These bending curvatures create more nonlinearity in both bending and twist even at small deflections. For that reason, it is extremely necessary to develop and utilize a fully nonlinear model to analyze blades of cycloidal rotor.

## 3.6 Conclusion

In this chapter, development of structural model of cycloidal rotor is discussed in detail. Towards this, two independent blade structural models are developed. For traditional rotorcraft structural analysis, $2^{nd}$ order nonlinear Hodges-Dowell [106] models are widely used among scientific community. Initially similar $2^{nd}$ order nonlinear model of cycloidal rotor is developed which is capable of predicting moderate bending and torsional deflections of cycloidal rotor blades. In case of cycloidal rotor, the blades go through large centrifugal force which causes large nonlinear deflections. $2^{nd}$ order non-linear model can not capture this large bending and torsional deflections

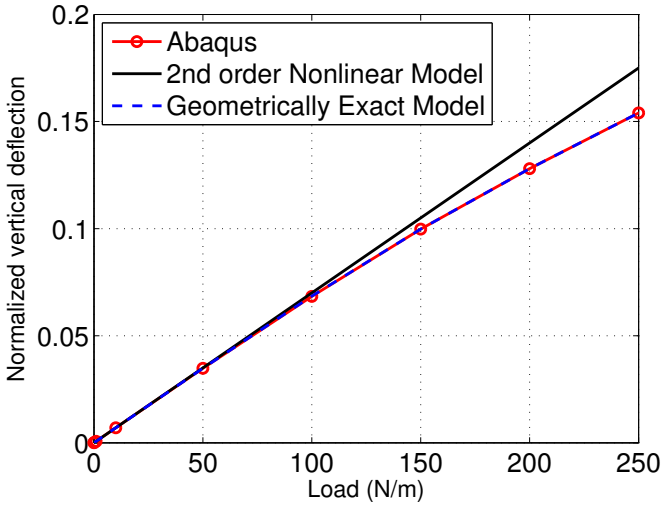


Figure 3.7: Comparison of Mid-beam normal deflection for a beam with fixed/clamped boundary condition at both ends.

of rotor blade properly. For this reason, a fully nonlinear geometrically exact beam based structural model is developed. Both the models are systematically validated with results obtained from Abaqus, a commonly used software in scientific community. Key conclusions from the structural analysis are listed below.

1. The $2^{nd}$ order nonlinear model over-predicts bending deflections. This is because nonlinearities in bending are of third order which is not accurately captured by this $2^{nd}$ order nonlinear model. The geometrically exact model can capture large bending deflections accurately.

2. On of the major source of twist of cycloidal rotor blade is nonlinear torsional moment generated due to bending curvatures. Over-prediction of bending deflections and bending curvatures by $2^{nd}$ order nonlinear model leads to over-prediction of blade twist. On the other hand, geometrically exact model gives accurate twist prediction since it can also capture bending curvatures accurately.

3. More constraints on rotor blade creates larger bending curvatures which in turn leads to more nonlinearities. It is observed that $2^{nd}$ order nonlinear model is capable of accurately

predicting deflections until tip bending deflections become 15-20% of blade span, for a cantilever blade. While for a simply supported blade, it can give reasonable prediction only until bending deflection becomes 0.2% of blade span. In case of a cycloidal rotor, blades are fixed in bending at both end which creates large bending curvatures and thus, nonlinearities start much earlier. For this reason, it is essential to use a fully nonlinear geometrically exact model to analyze this types of structure.

# 4. VEHICLE RESPONSE MODEL*

## 4.1 Overview

In this chapter detail development of vehicle response model of a twin cyclocopter is discussed. Twin-cyclocopter consists of two cycloidal rotors as main thrusters and a conventional horizontal nose-rotor for pitch-torque balance. The main objective of the vehicle response model is to predict rotor blade deflections and aerodynamic loads of the complete vehicle for given sets of control inputs. Vehicle response model consists of an aeroelastic model of cycloidal rotor and an aerodynamic model of conventional nose rotor. Development of aerodynamic and structural models of cycloidal rotors were discussed in previous chapters ( Ch. 2 and Ch. 3). In the next step, an aeroelastic model of cycloidal rotor would be developed by coupling the unsteady aerodynamic model with fully nonlinear geometrically exact structural framework. Conventional rotor blades, on the other hand, being extremely smaller in size, are very stiff and goes through minimal deflections. For that reason, only an aerodynamic model of conventional rotor is developed and utilized for present analysis. In this case, it is extremely important to use the conventional rotor as nose rotor placed in front of vehicle rather than using it as a tail rotor. The detail reasoning behind these configuration is due to balancing of pitching moments in forward flight and would be discussed in detail later.

## 4.2 Aeroelastic Performance of Cycloidal Rotor

Light-weight blades are extremely important for cycloidal rotors since it would also reduce inertial load on all load bearing components of rotor hub leading to significant decrease of rotor weight. On the other hand, considerable blade deflections are inevitable for a light-weight rotor

*Part of the data reported in this chapter is reprinted with permission from "Role of Blade Flexibility on Cycloidal Rotor Hover Performance" by Halder, A., and Benedict, M., *Journal of Aircraft*, Vol. 55, No. 5, pp. 1773-1791, 2018 [30] and "Understanding the Effect of Blade flexibility on Cycloidal Rotor Performance in Hover" by Halder, A., and Benedict, M., *Proceedings of the American Helicopter Society Specialists' Meeting on Aeromechanics*, 2016 [107].

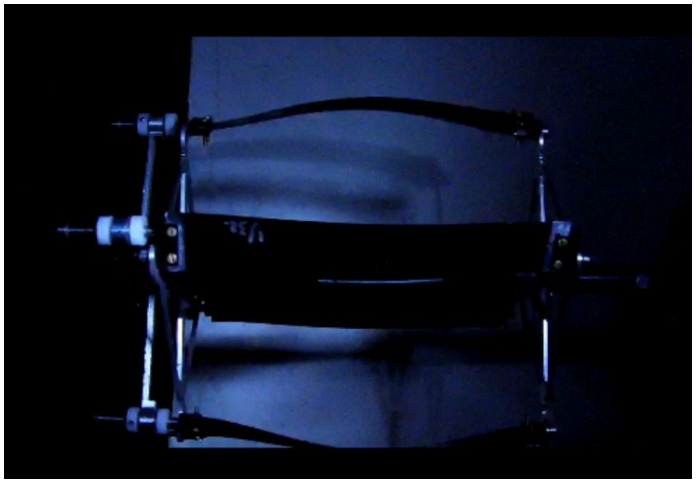

Figure 4.1: Cycloidal rotor on 3-component force balance.

blade. It is observed in previous chapter that centrifugal force of cycloidal rotor blade acts in radial direction, causing more bending and torsional deflections of rotor blade unlike conventional rotor, where centrifugal force acts axially and causes axial stiffening of the blade. It is also observed from in-house experiments (Fig. 4.1) that cyclodial rotor blades go through very large bending and torsional deflections. Previously developed structural model is capable of predicting large deflections of cycloidal rotor blade. Next step is to investigate the effect of this blade deflections on rotor aerodynamic performance. Towards this, systematic experiments are conducted with moderately flexible and highly flexible cycloidal rotors over a wide range of rotational speeds at different pitch amplitudes. Experiments show significant performance drop as the blade flexibility of cycloidal rotor is increased. To model this phenomena and further investigate it, an aeroelastic framework of cycloidal rotor is developed by coupling unsteady aerodynamic model with fully nonlinear geometrically exact structural model.

### 4.2.1 Experimental Results

Most of the previous research on cycloidal rotors were conducted using stiff rotor blades to investigate only the aerodynamic characteristics [cite]. In the present study, systematic experiments have been carried out with moderately and highly flexible rotors to understand the role of blade flexibility and deformations on the hover performance of cycloidal rotors. Experiments were

conducted with four bladed cycloidal rotor to investigate performance in terms of thrust, power requirement and power loading (thrust/power). Aluminum (E = 72 GPa, G = 26.9 GPa) and Delrin (a kind of plastic, E = 3.4 GPa, G = 1.34 GPa) blades with different stiffness have been used. Stiffness was varied by changing the thickness of the blades. All the blades are 1 inch in chord, 6.25 inch in span. Aluminum blades have thickness of 3.2%, 2% and 1.6% of chord. Delrin blades have thickness of 6.2%, 4.7% and 3.1% of chord.

| Blade thickness-to-chord ratio | $EI_y$ (Bending stiffness in radial direction), N-m$^2$ | $EI_z$ (Bending stiffness in tangential direction), N-m$^2$ | $GJ$ (Torsional stiffness), N-m$^2$ |
|---|---|---|---|
| 3.2% | 8.18e-2 | 80 | 1.2e-1 |
| 2% | 2e-2 | 50 | 3e-2 |
| 1.6% | 1e-2 | 40 | 1.5e-2 |

Table 4.1: Bending and torsional stiffness of Aluminum blades

| Blade thickness-to-chord ratio | $EI_y$ (Bending stiffness in radial direction), N-m$^2$ | $EI_z$ (Bending stiffness in tangential direction), N-m$^2$ | $GJ$ (Torsional stiffness), N-m$^2$ |
|---|---|---|---|
| 6.2% | 2.88e-2 | 7.37 | 4.5e-2 |
| 4.7% | 1.2e-2 | 5.53 | 1.9e-2 |
| 3.1% | 3.6e-3 | 3.69 | 5.7e-3 |

Table 4.2: Bending and torsional stiffness of Delrin blades

A three-component balance has been designed and built to measure the vertical force, side force and torque of the rotor. Figure 4.2 shows the test set-up. Torque, vertical and side forces are measured using load cells. A Hall-effect sensor was used to generate 1/rev signal to measure rotational speed. Power is obtained from the measured torque and rotational speed.

Figure 4.3 shows comparison of aerodynamic performance in terms of resultant thrust, power requirement and power loading, respectively, for cycloidal rotor using aluminum blades with vary-

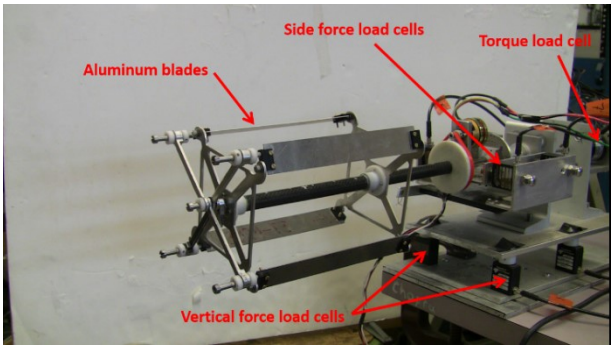


Figure 4.2: cycloidal rotor on 3-component force balance.

ing stiffness at $35^0$ pitch amplitude. The results clearly show that, total thrust decreases as stiffness of the blade is decreased, while, interestingly, power requirement increases. Since more flexible blades draw more power and generate less thrust, the power loading (thrust/power) decreases as bending and torsional stiffness of the blade is decreased. Figure 4.4 shows comparison of thrust, power requirement and power loading respectively for Delrin blades with varying stiffness at $35^0$ pitch amplitude. Figure 4.5 shows same comparison for Delrin blades at $30^0$ pitch amplitude. At both pitch amplitude, as the stiffness of the blade is decreased, net thrust decreases and power requirement increases resulting in a drop in power loading, similar to what was seen in Aluminum blades. The effect of flexibility is more significant in this case because Delrin blades are comparatively more flexible.

### 4.2.2 Aeroelastic Modeling

Experiments using flexible cycloidal rotor show significant performance drop as the blade flexibility of cycloidal rotor is increased. To further investigate this phenomenon, an aeroelastic model of cycloidal rotor is developed by coupling unsteady aerodynamic model of cycloidal rotor with beam based structural framework. For this purpose, two different structural models are utilized: 1. 2nd order nonlinear model, and 2. fully nonlinear geometrically exact beam model.

The aeroelastic governing equation of motion of cycloidal rotor can be obtained using generalized Hamilton's principle (Eq. 4.1).

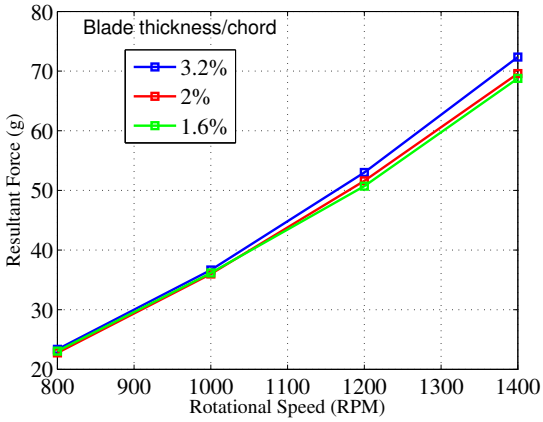


(a) Resultant Force Comparison for varying stiffness

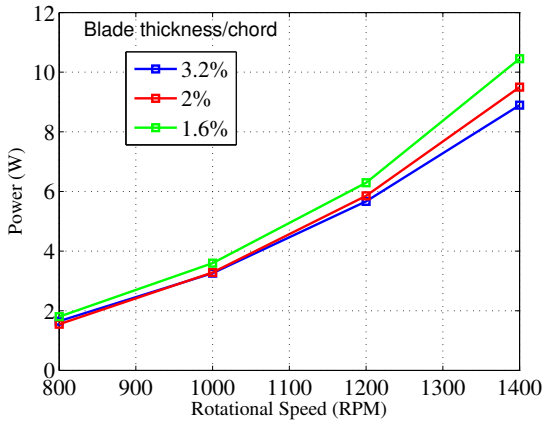


(b) Power Comparison for varying stiffness

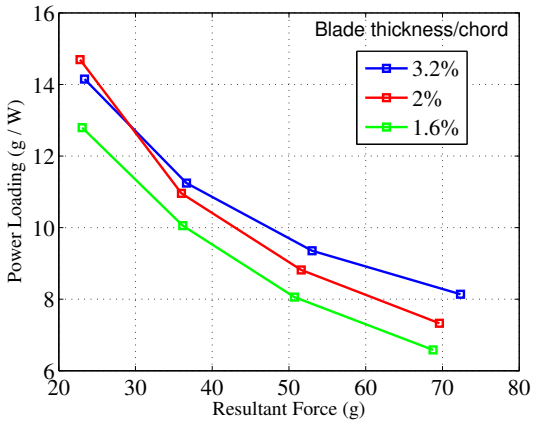


(c) Comparison of Power Loading for varying stiffness

Figure 4.3: Aluminum blades with varying stiffness for $35^0$ pitch amplitude.

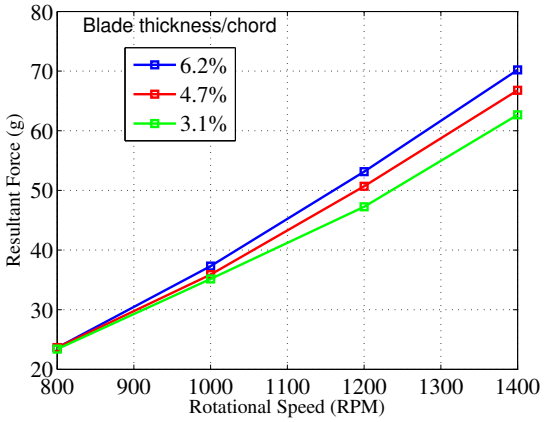


(a) Resultant Force Comparison for varying stiffness

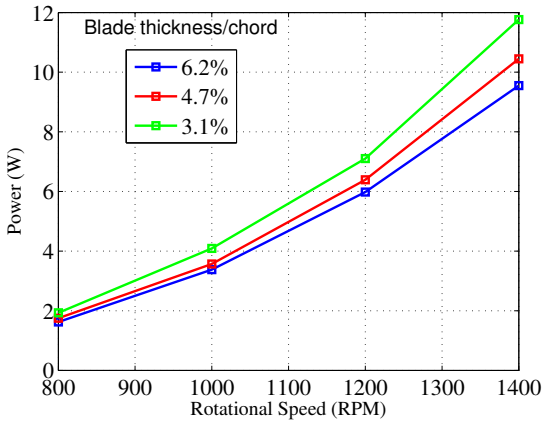


(b) Power Comparison for varying stiffness

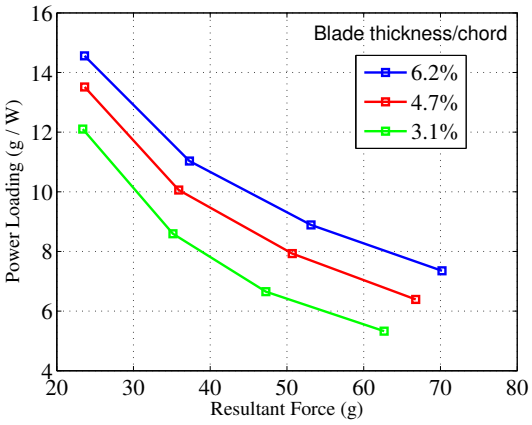


(c) Comparison of Power Loading for varying stiffness

Figure 4.4: Delrin blades with varying stiffness for $35^0$ pitch amplitude.

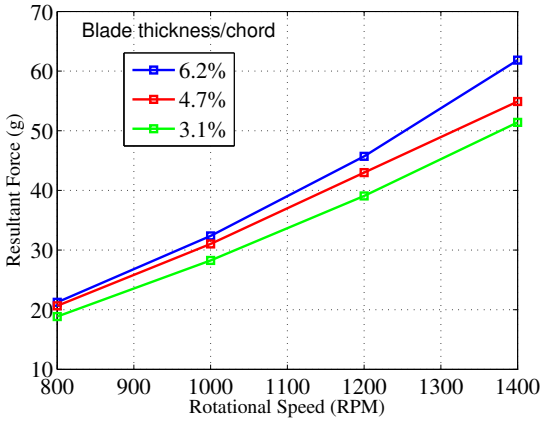


(a) Resultant Force Comparison for varying stiffness

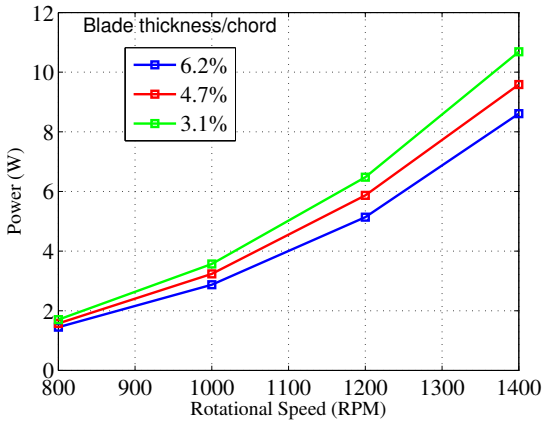


(b) Power Comparison for varying stiffness

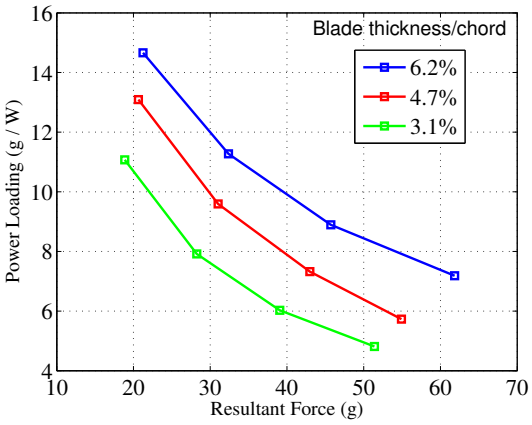


(c) Comparison of Power Loading for varying stiffness

Figure 4.5: Delrin blades with varying stiffness for $30^0$ pitch amplitude.

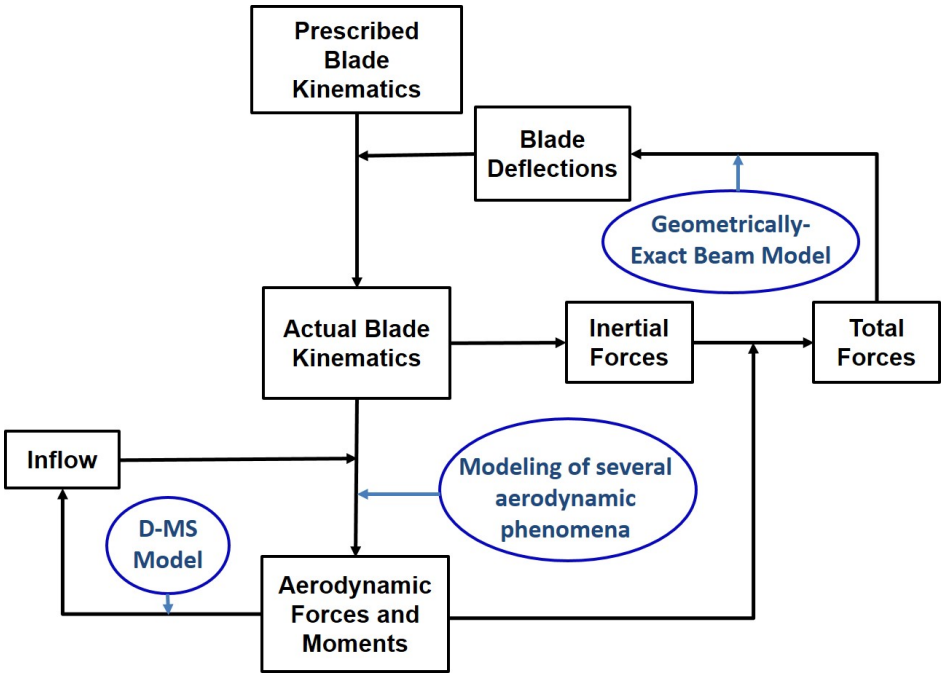


Figure 4.6: Flow-chart of Aeroelastic Model.

$$\delta\Pi = \int_{t_1}^{t_2} (\delta T - \delta U + \delta W) dt = 0 \tag{4.1}$$

In the above equation, $\delta T$ is virtual variation of kinetic energy, $\delta U$ is virtual variation of strain energy and $\delta W$ is virtual work done by the external forces. External aerodynamic forces are obtained from the aerodynamic model where the unknowns are inflow and circulation. Potential energy is obtained from the structural model where the unknowns are deflections. Kinetic energy is derived from the motion of the blade elements. Along with the prescribed rigid-body motion, the inertial position, velocity and acceleration of blade elements depend on deflections and their spatial and temporal derivatives. Thus, computation of kinetic energy itself depends on blade kinematics and the deflections obtained from the structural model. In the coupled aeroelastic model, all the unknowns (inflow, circulation and deflections) are iterated simultaneously to solve blade response equation (Eq. 4.1). A flow chart of the aeroelastic model is shown in Fig. 4.6. In the first iteration deflections are obtained from structural model by considering only the inertial

forces. These deflections are fed into aerodynamic model, and it calculates aerodynamic forces and moments based on initial inflow and circulation assumption. In the next iteration inflow and circulation are updated from aerodynamic forces. Further, the aerodynamic forces are used by structural model in the next iteration to update deflections. This cycle is repeated until inflow, circulation and deflections converge all together.

### 4.2.3 Validation of Aeroelastic Model

Complete aeroelastic model validations for moderately and highly flexible rotors are carried out in comparison with the results obtained from in-house experiments discussed before. Two aeroelastic models: 1) $2^{nd}$ order nonlinear structural beam model combined with unsteady aerodynamic model, and 2) Fully nonlinear geometrically exact beam model combined with unsteady aerodynamic model, are validated in this regard. These validations have been carried out using the experimental results discussed before from a four bladed cycloidal rotor with both Aluminum and Delrin blades with varying stiffness over a range of rotational speeds from 800 rpm to 1400 rpm and for different pitch amplitudes.

Figure 4.7 shows resultant force validation of moderately flexible 3.2% thickness-to-chord ratio Aluminum blades at pitch amplitudes ranging from $30^0$ to $40^0$. In all the cases, it is observed that both $2^{nd}$ order nonlinear model and geometrically exact model can give good prediction of thrust performance. 3.2% thickness-to-chord ratio Aluminum blades go through moderate bending and torsional deflections which is captured well by both the models.

Figure 4.8 shows same comparisons for 2% thickness-to-chord ratio aluminum blade which is even more flexible. Interestingly, in these cases, $2^{nd}$ order model gives good prediction of thrust at lower rpm. However, at higher rpms, when the deflections are larger due to larger inertial forces, this model under-predicts the thrust. As seen before (Figs. 3.4 - 3.7), $2^{nd}$ order model over-predicts bending and torsional deflections under higher loads. This over-prediction of torsional deflection causes under-prediction of net thrust (the reason for this phenomenon will be discussed in the next section). The geometrically exact model predicts thrust accurately for all the cases. This is due to the reason that even large deflections are accurately predicted by this model. Figure

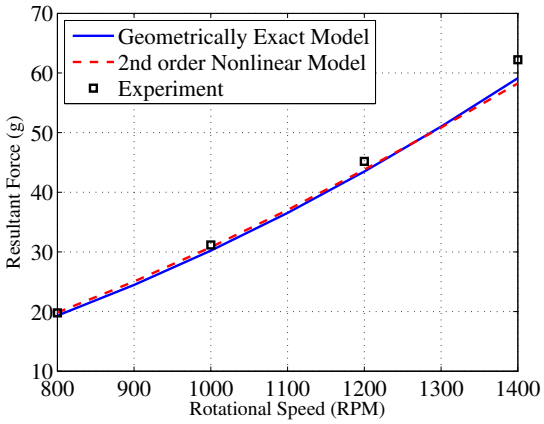


(a) Blade pitch amplitude = $30^0$.

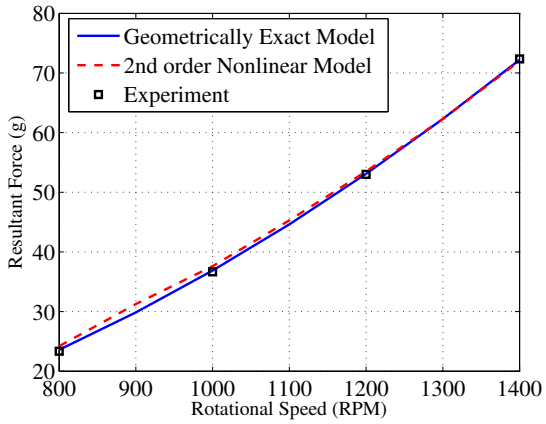


(b) Blade pitch amplitude = $35^0$.

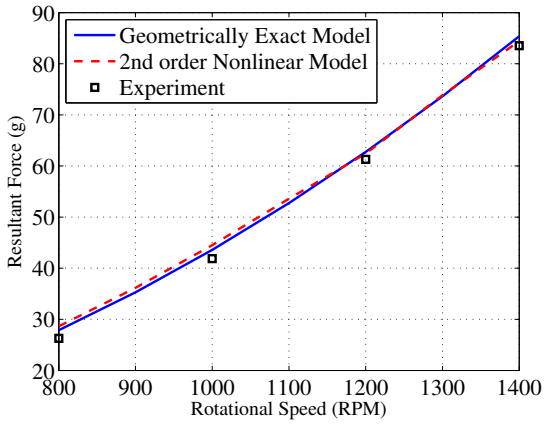


(c) Blade pitch amplitude = $40^0$.

Figure 4.7: Resultant force validation of $3.2\%$ thickness/chord Aluminum blade at different pitch amplitudes.

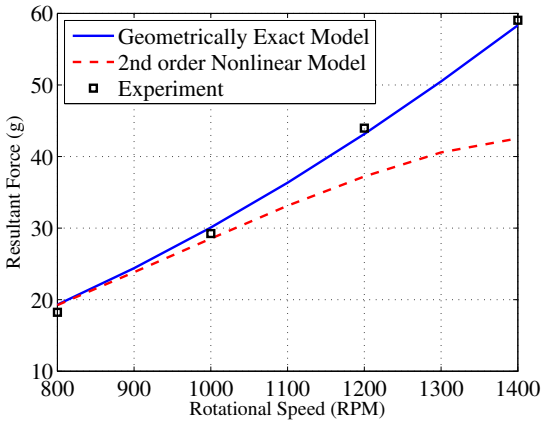


(a) Blade pitch amplitude = $30^0$.

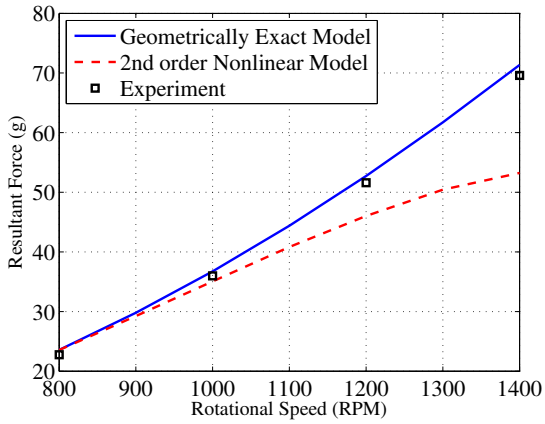


(b) Blade pitch amplitude = $35^0$.

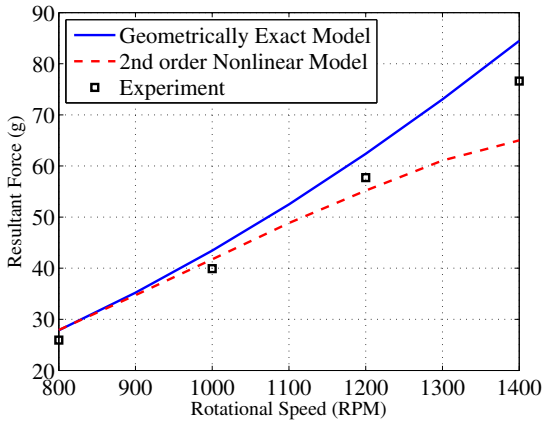


(c) Blade pitch amplitude = $40^0$.

Figure 4.8: Resultant force validation of $2\%$ thickness/chord Aluminum blade at different pitch amplitudes.

4.9 shows thrust comparison for 6.2% thickness-to-chord ratio Delrin blades at different pitch amplitudes. In all the cases, $2^{nd}$ order model again under-predicts thrust at higher rpm because Delrin blade is more flexible. However, thrust prediction of geometrically exact model is quite satisfactory for all these cases.

Figures 4.10 to 4.12 show net thrust comparison between the prediction of geometrically exact model and experimental results for extremely flexible rotor blades. Figure 4.10 shows net thrust comparison of a 1.6% thickness-to-chord ratio Aluminum blades at $40^0$ pitch amplitude. Figure 4.11 shows comparison of 4.7% thickness-to-chord ratio Delrin blades at $30^0$ pitch amplitude and Figure 4.12 shows comparison of 3.1% thickness-to-chord ratio Delrin blades at $35^0$ pitch amplitude. In all these highly flexible rotor cases, geometrically exact model can predict thrust with sufficient accuracy. These studies clearly validate the present aeroelastic analysis in terms of thrust prediction. $2^{nd}$ order nonlinear model is not able to accurately predict the performance of these highly flexible rotors. Figures 4.13 to 4.15 show power validation of extremely flexible blades at different pitch amplitude. Figure 4.13 and 4.14 show power validation of $6.2\%$ Delrin blades at $35^0$ and $40^0$ pitch amplitude respectively. Figure 4.15 shows power validation of $3.1\%$ Delrin blades at $40^0$ pitch amplitude.

### 4.2.4 Discussion

#### *4.2.4.1 Effect of Deflections*

It is observed from the in-house experimental data and aeroelastic model that resultant thrust decreases for more flexible blades. This indicates that the deflections of rotor blades negatively influence thrust performance of cycloidal rotor. The aeroelastic model is used to understand the underlying physics behind this phenomenon.

Figures 4.16a and 4.16b show tip twist of a $3.1\%$ thickness-to-chord ratio Delrin blade rotating at 1400 rpm and 2000 rpm, respectively, at $35^0$ pitch amplitude. The plot shows variation of tip twist as blade goes around different azimuth location in a complete cycle. It can be clearly seen from the figure that the blade goes through a large nose-down twist in the upper half (azimuth

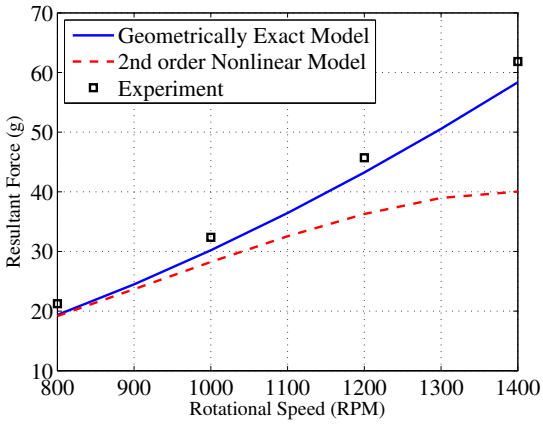


(a) a) Blade pitch amplitude = $30^0$.

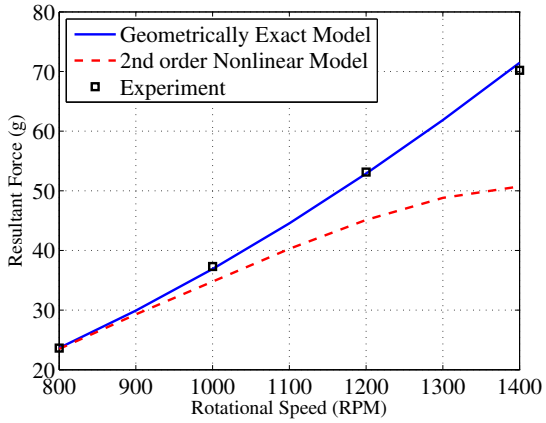


(b) b) Blade pitch amplitude = $35^0$.

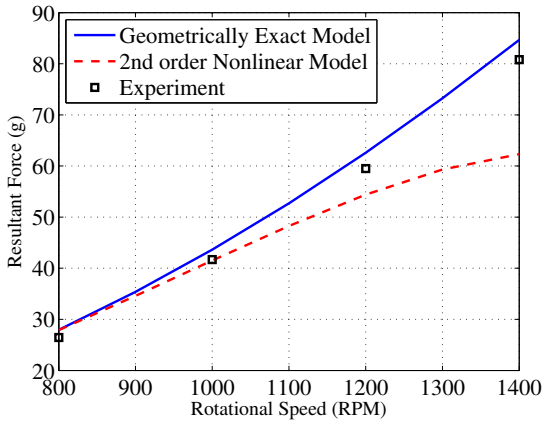


(c) c) Blade pitch amplitude = $40^0$.

Figure 4.9: Resultant force validation of $6.2\%$ thickness/chord Delrin blade at different pitch amplitudes.

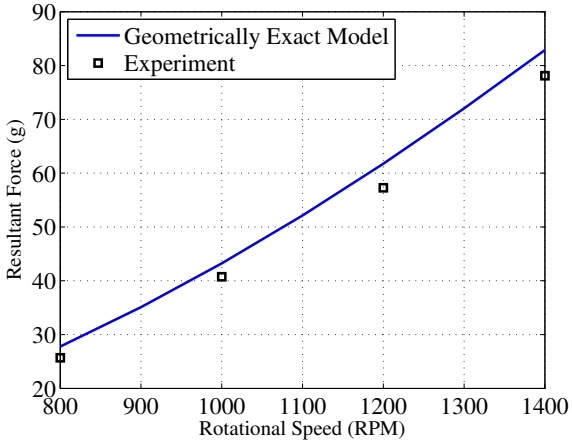


Figure 4.10: Resultant Force Validation : Aluminum blade with $1.6\%$ thickness/chord for $40^0$ pitch amplitude.

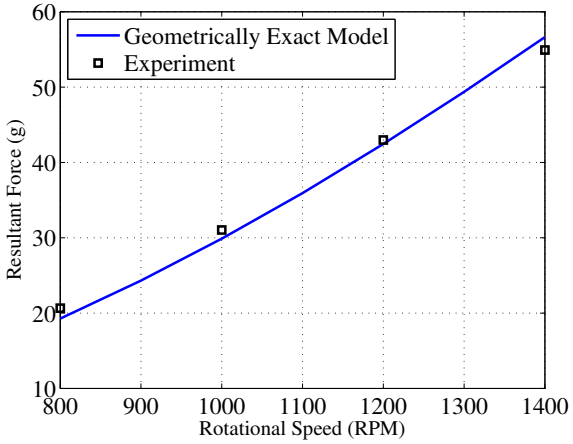


Figure 4.11: Resultant Force Validation : Delrin blade with $4.7\%$ thickness/chord for $30^0$ pitch amplitude.

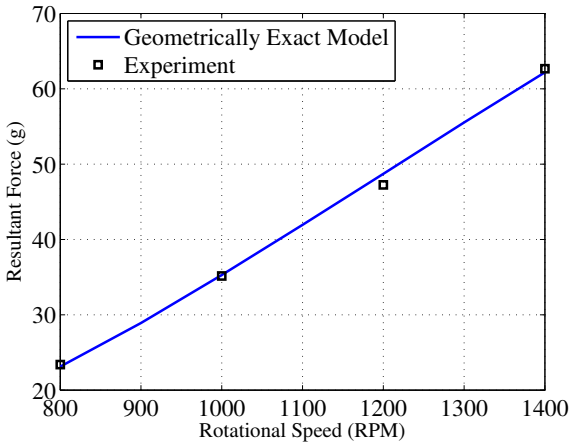


Figure 4.12: Resultant Force Validation : Delrin blade with $3.1\%$ thickness/chord for $35^0$ pitch amplitude.

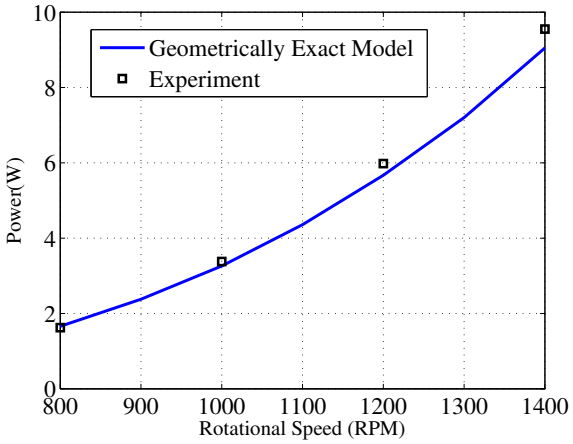


Figure 4.13: Power Validation: Delrin blade with $6.2\%$ thickness/chord for $35^0$ pitch amplitude.

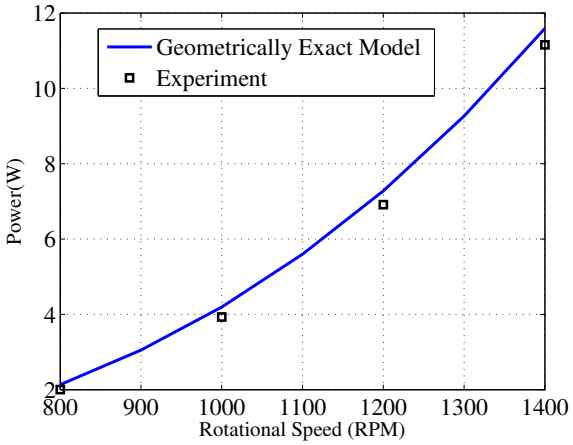


Figure 4.14: Power Validation: Delrin blade with $6.2\%$ thickness/chord for $40^0$ pitch amplitude.

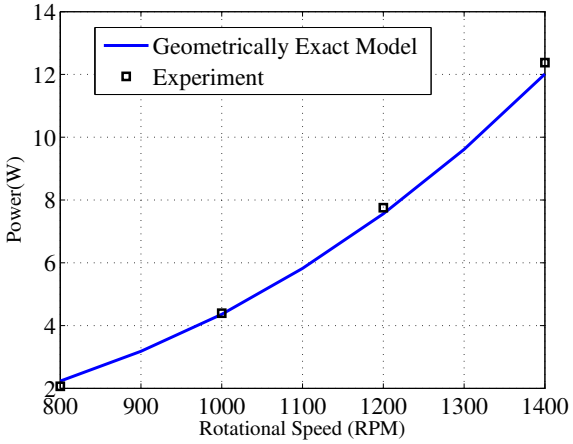


Figure 4.15: Power Validation: Delrin blade with $3.1\%$ thickness/chord for $40^0$ pitch amplitude.

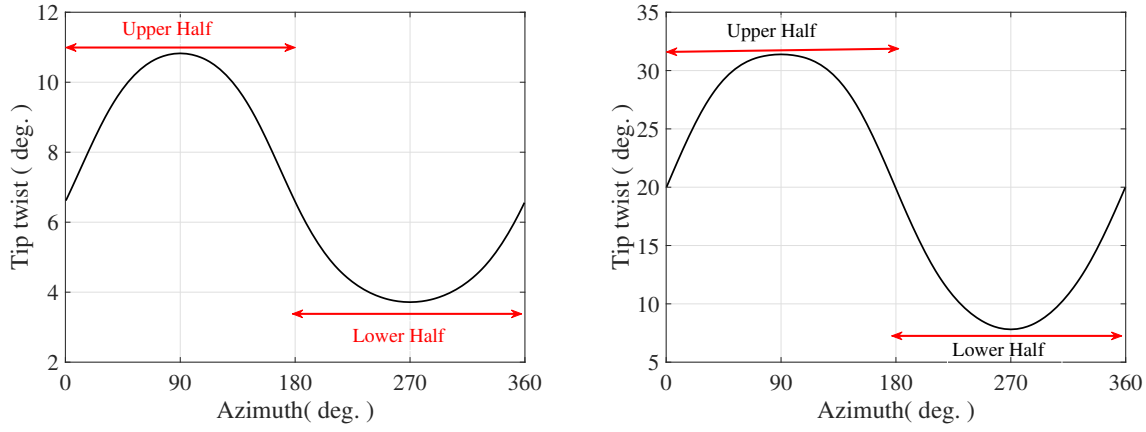


(a) 1400 RPM.

(b) 2000 RPM.

Figure 4.16: Tip twist of a $3.1\%$ Delrin blade for $35^0$ pitch amplitude at different rotational speeds.

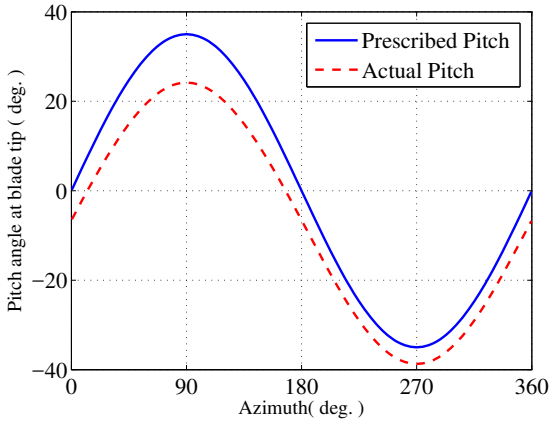


(a) 1400 RPM.

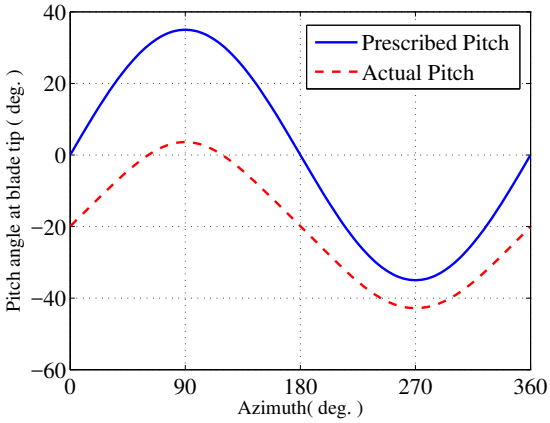


(b) 2000 RPM.

Figure 4.17: Pitch angle at the tip of a $3.1\%$ Delrin blade for $35^0$ pitch amplitude at different rotational speeds.

from $0^0$ to $180^0$), which is not compensated in the lower half (azimuth from $180^0$ to $360^0$ ). Figures 4.17a and 4.17b show pitch angle at blade tip for 1400 rpm and 2000 rpm, respectively, at $35^0$ pitch amplitude. It can be seen that there is a large drop in magnitude of actual pitch from the prescribed pitch at upper half due to large nose down tip twist. And this drop in pitch magnitude is not really compensated at the lower half. This phenomenon causes an overall decrease in the magnitude of geometric pitch angle which in turn reduces the magnitude of angle of attack and thus causes thrust reduction. So the drop in thrust performance of cycloidal rotor can be attributed to torsional deflection rather than the bending deflections. Although, a large portion of nonlinear torsional moment comes from bending curvature. Actual cyclocopter blades are fixed in bending at both ends. This highly constrained boundary condition creates large bending curvature, which leads to large nonlinear moment and high twist. For this reason it is very important for the structural part of aeroelastic model to accurately capture both torsional as well as bending deflections.

This explains the reason behind under-prediction of thrust by $2^{nd}$ order nonlinear model for flexible rotors at higher rpms. It is noticed in previous chapter (Figs. 3.4 to 3.7) that $2^{nd}$ order nonlinear model over-predicts bending and torsional deflections after a certain point when higher order nonlinearities become significant. The effect of nonlinearities start much earlier for simply-

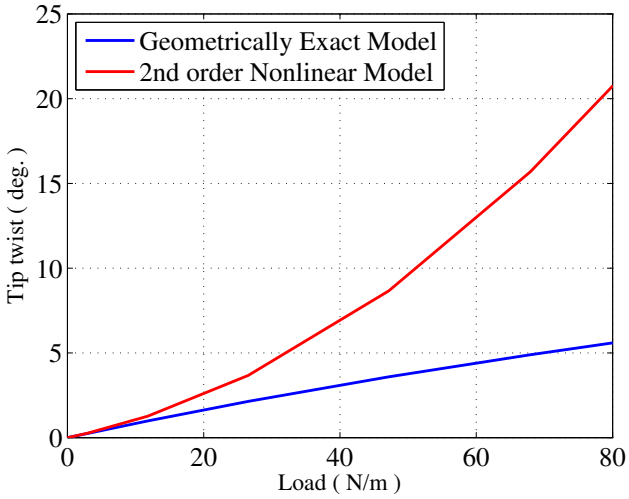


Figure 4.18: Comparison of tip twist of a cycloidal rotor blade under uniformly distributed load.

supported and fixed-fixed beam due to the additional constraints imposed on beam, as seen in Figs. 3.6 and 3.7. Bending deflections are over-predicted after $5 - 7\%$ mid beam bending in case of simply supported beam, and after $0.1 - 0.3\%$ mid-beam bending in case of beams fixed in bending at both ends. Although this bending deflections directly do not affect thrust performance of cycloidal rotor in a significant way, the bending curvature produces large amount of nonlinear moment. This nonlinear moment causes larger twist and thus drop in thrust. Since $2^{nd}$ order model over-predicts bending deflections, it also over-predicts twist caused by bending curvature. This over-prediction of twist causes under-prediction of thrust as discussed in the previous section. Figure 4.18 clearly explains this phenomenon. The figure shows comparison of $2^{nd}$ order nonlinear model and geometrically exact beam model in terms of tip-twist (Y-axis) of a cycloidal rotor blade under uniformly distributed load (X-axis). The uniformly distributed load is applied at elastic axis at an angle of $35^0$ so that both linear and nonlinear parts of the moment are produced. In this case, $6.2\%$ thickness-to-chord ratio Delrin blade with 1 inch chord and 6.25 inch span is considered. As shown in Fig. 4.18, the $2^{nd}$ order model significantly over-predicts this nonlinear twist because of the over-prediction of bending curvatures.

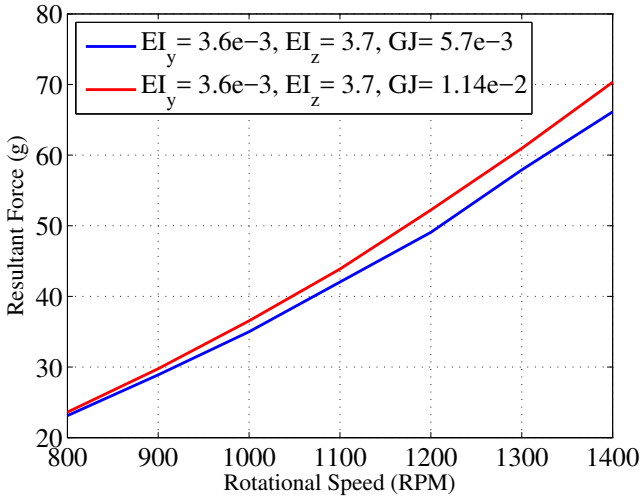


Figure 4.19: Comparison of resultant force of rotor blades with varying torsional rigidity.

#### *4.2.4.2 Effect of Blade Stiffness*

Next the aeroelastic model is used to understand the effect of torsional rigidity on the thrust performance of cycloidal rotor. Figure 4.19 shows comparison of resultant thrust (Y-axis) of rotors with varying torsional rigidity over a range of rotational speeds (X-axis). The blue line represents the thrust produced by a 4-bladed rotor at $35^0$ pitch amplitude. In this case, $3.1\%$ thickness-to-chord ratio Delrin blade is considered. The red line represents thrust produced by similar rotor in which case only torsional stiffness is increased by a factor of two while all other conditions are kept same. It can be shown from the figure that the rotor with more torsional stiffness produces more thrust. This is due to the reason that more torsional stiff blade goes through less torsional deflection under same loading compared to $3.1\%$ Delrin blade. Increased stiffness reduces the effect of both linear and nonlinear moment and produces less twist. On the other hand, for $3.1\%$ Delrin bladed rotor, torsional rigidity is less causing more twist which in turn causes drop in thrust as discussed in the previous section. It can be concluded from above study that for better aerodynamic performance blades with more torsional stiffness is preferred.

## 4.3 Aerodynamic Modeling of Conventional Nose Rotor

Unlike cycloidal rotor blades, blades of conventional rotor goes through very little blade deflections which has negligible effects on rotor performance. For this reason, only an aerodynamic model of nose rotor is developed for different flight conditions (i.e. hover, forward flight).

### 4.3.1 Hover model

For performance prediction of conventional nose rotor a modified blade element momentum theory (BEMT) based aerodynamic model is developed. In general BEMT analysis, lift coefficient ($C_L$) is assumed to be proportional to angle of attack ($\alpha$), ($C_L = C_{L_\alpha}\alpha$). This simplified formula is not applicable to small nose rotor blades operating at a high angle of attack and low Reynolds number ($10^4 < Re < 10^5$). Due to this reason, lift coefficient is obtained from look-up table generated by 2D CFD studies over a range of angles of attack and Reynolds numbers. CFD solver 2D OVERTURNS, developed at University of Maryland, is used in this purpose. Depending on the angle of attack and Reynolds number at every blade section, a linear interpolation across angles of attack and Reynolds numbers is setup to obtain the correct lift and drag coefficients from the lookup tables. On the other hand, the variation of lift with angle of attack becomes highly nonlinear at low Reynolds numbers. Due to this complexity, it becomes impossible to get a close form solution of inflow ratio ($\lambda$) since lift coefficient becomes an unknown function of inflow ratio. To solve this problem, following approach is considered.

From modified momentum theory [14], thrust ($dT_{MMT}$) generated by an annular section (Fig. 4.20) of rotor disk in hover can be represented as following equation.

$$dT_{MMT} = 4F\lambda^2 r dr \tag{4.2}$$

From blade element theory (BET), thrust ($dT_{BET}$) generated by similar annular section can be written using following blade parameters.

$$dT_{BET} = \frac{1}{2}\sigma C_L r^2 dr \tag{4.3}$$

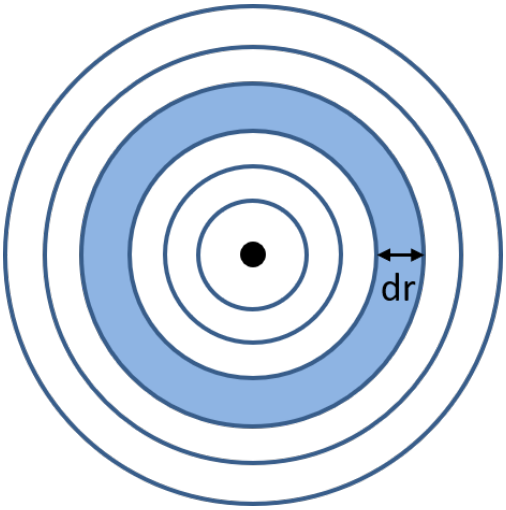


Figure 4.20: Annular rotor disc: Modified momentum theory.

In the above equation, lift coefficient ($C_L$) is a function of angle of attack and Reynolds number and obtained from CFD look-up table as discussed before. Now from blade element theory, angle of attack ($\alpha$) can be expressed in terms of inflow ratio ($\lambda$).

$$\alpha = \theta - \frac{\lambda}{r} \tag{4.4}$$

According to above equation, the lift co-efficient becomes as a function of inflow ratio ($C_L = C_L(\lambda)$). Equating Eq. 4.2 and Eq. 4.3, a nonlinear expression (Eq. 4.5) of inflow ratio is obtained.

$$f_\lambda(\lambda) = 4F\lambda^2 - 0.5\sigma C_L(\lambda)r = 0 \tag{4.5}$$

A numerical solver is developed to solve above nonlinear equation and obtain inflow ratio. For this purpose, initial value of tip loss function, F is assumed to be 1 and iterated until both tip loss function and inflow ratio converge. Once the inflow ratio is obtained, the angle of attack is computed based on Eq. 4.4. In the next step lift coefficient is obtained from angle of attack using CFD look up table. This gives elemental lift over blade section and by integrating that over whole blade, the total force and torque of the rotor blade is obtained.

### 4.3.2 Forward Fight model

In forward flight, inflow distribution of nose rotor varies with different azimuth location unlike hover. For this reason, a dynamic inflow model is developed to capture variation of inflow across different azimuth as well as radial locations. Dynamic inflow based on Pitt-Peter's model is utilized for present simulation. The total inflow ratio ($\lambda$) can be represented as summation of induced inflow ratio ($\lambda_i$) and component of forward speed ($\lambda_c$).

$$\lambda = \lambda_i + \lambda_c \tag{4.6}$$

Induced inflow ratio is dynamic in nature and can be expressed as following equation.

$$\lambda_i = \lambda_0(1 + k_x r\cos\psi + k_y r\sin\psi) \tag{4.7}$$

In the above equation, $\lambda_0$ denotes mean or average induced velocity at the center of the nose rotor, $r$ denotes radial location, $\psi$ denotes azimuth location and $k_x$ and $k_y$ are weighting factors. From momentum theory, the expression of $\lambda_0$ is computed.

$$\lambda_0 = \frac{C_T}{2\sqrt{\mu^2 + \lambda_i^2}} \tag{4.8}$$

In the above equation, $\mu$ is advance ratio and $C_T$ is thrust coefficient of nose rotor. In Eq. 4.8, $k_x$ and $k_y$ represents deviation of dynamic inflow from the uniform inflow. For Pitt-Peter's model, $k_y$ is assumed to be zero and expression of $k_x$ is given by following equation.

$$k_x = \frac{15\pi}{2}\tan\frac{\chi}{2} \tag{4.9}$$

Here, $\chi$ is the wake skew angle in forward flight. Once the inflow ratio is computed using above equations (Eq. 4.6 - 4.9), angle of attack of nose rotor is computed over all the azimuth and radial locations. Based on angle of attack, sectional lift is obtained using interpolation function

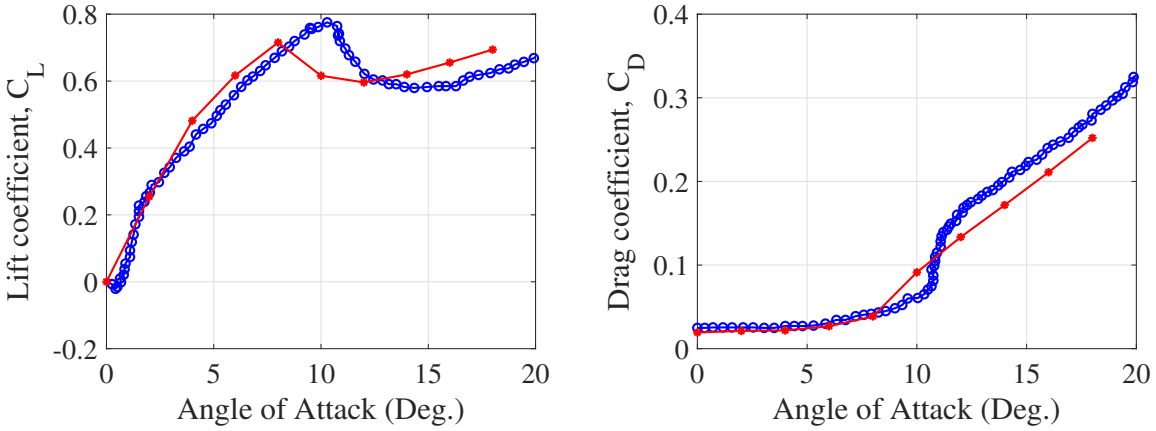


(a) Comparison of lift coefficient

(b) Comparison of drag coefficient

Figure 4.21: Comparison of lift and drag coefficient at Reynolds number = 60k

and CFD look-up table discussed before. In the next step, total forces and moments of the rotor is computed by integrating sectional forces.

### 4.3.3 Model Validation

One of the key parts of the aerodynamic model of the nose rotor is look-up table of lift and drag coefficients generated by 2D CFD over range of different angle of attacks and Reynolds numbers. CFD results are validated with previously published experiments [109]. Fig. 4.21a and 4.21b show comparison of lift and drag coefficient, respectively, at 60,000 Reynolds number. Fig. 4.22a and 4.22b show comparison of lift and drag coefficient, respectively, at 40,000 Reynolds number. All the the figures show that CFD results correlate well with experiments.

Once the CFD results are validated, the performance of small scale conventional rotors are validated in the next step. Previously published in-house experiments [109] are utilized for this validation purpose. Fig. 4.23 shows comparison of thrust coefficient vs power coefficient of small scale conventional rotor. Fig. 4.23a shows performance comparison for a rotor utilizing NACA 0012 airfoil and Fig. 4.23b shows similar comparison for a rotor utilizing NACA 6504 airfoil. Both the graphs show very well correlation of predicted performance with experimental results.

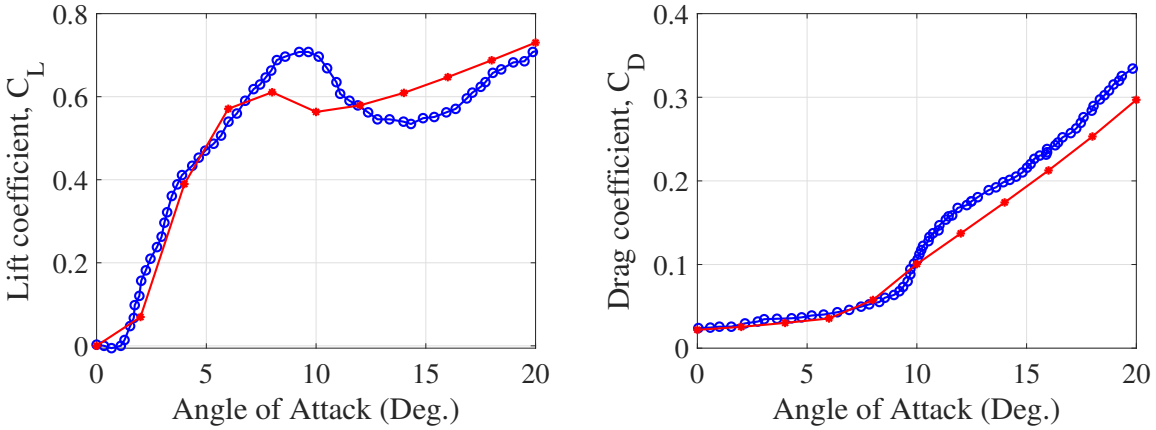


(a) Comparison of lift coefficient (b) Comparison of drag coefficient

Figure 4.22: Comparison of lift and drag coefficient at Reynolds number = 40k

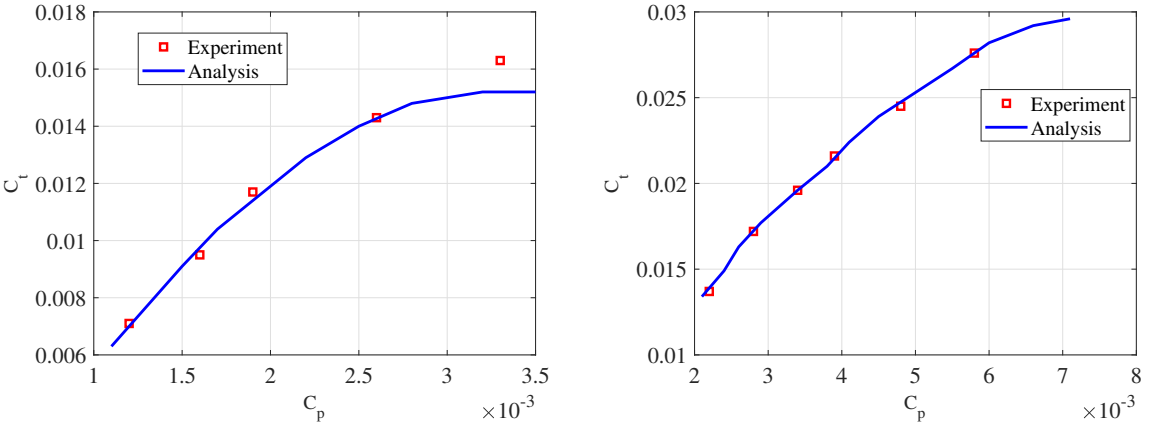


(a) Rotor with NACA 0012 airfoil (b) Rotor with NACA 6504 airfoil

Figure 4.23: Performance validation of micro scale conventional rotor

## 4.4 Conclusion

The primary objective of this chapter is to develop vehicle response model of a cycloidal rotor based vehicle (twin cyclocopter). Vehicle response model consists of modeling of cycloidal rotor, which acts as a primary thruster, and modeling of conventional nose rotor, whose main job is to balance pitching moment of the vehicle.

Structural modeling of cycloidal rotor shows that rotor blades go through large nonlinear bending and torsional deflections. Both experimental and analytical approaches are taken to investigate effect of these deflections on cycloidal rotor performance. A test set-up has been designed and built to measure the thrust, torque and rotational speed of the cycloidal rotor. Systematic experiments were conducted with a 4 bladed rotor with varying flexibility over a wide range of rotational speed at different pitch amplitudes. For experimental purpose, moderately flexible Aluminum blades and highly flexible Delrin (a type of plastic) blades are utilized. The flexibility of the rotor blade is varied by changing thickness of the blades. To further investigate effect of blade deflections on rotor performance, an aeroelastic model of cycloidal rotor is developed. Aeroelastic governing equation of motion of cycloidal rotor is obtained using generalized Hamilton's principle. In this procedure, unsteady aerodynamic model of cycloidal rotor is coupled with a fully nonlinear geometrically exact beam based structural framework. Once the model is systematically validated with in-house experiments, it is utilized for understanding effects of rotor deflections on rotor performance.

On the other hand, conventional nose rotor blades go through minimal deflections having negligible effects on performance, unlike cyclodial rotor blades. For this reason, only an aerodynamic model of nose rotor is developed for different flight conditions. Towards this, a blade element momentum theory (BEMT) based approach is taken. Several assumptions of traditional BEMT theory becomes invalid for low Reynolds number operating regime of small scale nose rotor. For this purpose, necessary modifications are made by relaxing unrealistic assumptions. Moreover, a 2-D CFD based look-up table is generated and utilized for this purpose. CFD data is validated with previously published experiments. Performance of small scale conventional rotor predicted by developed aerodynamic model is validated with in-house experiments.

Key conclusions from present study of modeling of cycloidal rotor and nose rotor, are given below:

1. The experimental results show deterioration in cycloidal rotor performance as the stiffness of the blades are decreased. It is observed that more flexible blades draw more power while producing less thrust, which significantly decreases power loading compared to stiffer blades.

2. Aeroelastic model based on $2^{nd}$ order nonlinear structural model is capable of predicting thrust of moderately flexible rotors. However, in the cases of highly flexible blades, this model underestimate thrust at higher rotational speeds. Highly flexible blades go through larger bending and torsional deflections at higher rpm due to increased centrifugal force which varies as the square of rotational speed. Second order structural model over-predicts bending deflections and axial twist, which causes under-prediction of thrust.

3. Geometrically exact model is able to accurately predict large deflections. Aeroelastic model based on this model is capable of accurately predicting the thrust of cycloidal rotors for a wide range of blade flexibilities. Inclusion of geometrically exact model has proven to be very essential in accurate prediction of thrust performance.

4. Aeroelastic analysis showed that torsional deflection decreases total magnitude of pitch angle from prescribed pitch causing overall decrease in thrust in the upper half. Although bending deflections directly does not affect thrust in considerable amount, bending curvature creates significant amount of nonlinear moment that ultimately increases twist and decreases thrust. For this reason, it is very important to accurately estimate both bending and torsional deflections. Since blade twist is the primary reason for the thrust drop, increased torsional rigidity of cycloidal rotor blade is required to counteract both linear and nonlinear part of torsional moments, thus minimize blade twist and thrust drop.

# 5. COUPLED TRIM MODELING OF CYCLOCOPTER*

## 5.1 Overview

In this chapter, detailed development of nonlinear aeroelastic coupled trim model of a twin-cyclocopter for different flight conditions (i.e. hover, forward flight) is presented [34, 35]. Twin-cyclocopter consists of two cycloidal rotors as main thrusters and a conventional horizontal nose-rotor for pitch-torque balance. It is shown that three control inputs are needed to trim the cyclocopter in hover by balancing one force (in vertical direction) and two moments (in yaw and pitch directions). In this hover scenario, forces in lateral and longitudinal directions and moment in rolling direction remain always balanced. These three sets of control inputs are mean rpm of cycloidal rotors, differential phase offset of cycloidal rotors and rpm of nose rotor. Mean rpm of cycloidal rotors is used to balance vertical forces, differential phase offset of cycloidal rotors is used to balance yawing moment and nose rotor rpm is used to balance pitching moment. Alternatively, mean pitch amplitude of cycloidal rotors can be used to balance vertical forces while keeping mean rpm of cycloidal rotors as a constant. In forward flight, it is shown that five control inputs are needed to trim cyclocopter by balancing three moments (in yaw, pitch, and roll directions) and two forces (in vertical and longitudinal directions). Forces on cyclocopter along lateral direction remains balanced at all stages. These five sets of control inputs are mean and differential rpm of cyclodial rotors, mean and differential phase offset of cycloidal rotors and rpm of nose rotor. Alternatively, mean and differential pitch amplitude of cycloidal rotors can be used as control inputs while keeping rpm of cyclodial rotors constant. Coupled trim analysis requires simultaneous computation of trim controls, vehicle orientation and blade structural responses so that both blade

*Part of the data reported in this chapter is reprinted with permission from "'Nonlinear Aeroelastic Coupled Trim Analysis of a Cyclocopter in Hover" by Halder, A., and Benedict, M., *Proceedings of 73rd Annual Forum of the American Helicopter Society*, 2017 [34] and "Nonlinear Aeroelastic Modeling of Cycloidal Rotor in Forward Flight" by Halder, A., and Benedict, M., *Proceedings of the AHS Technical Meeting on Aeromechanics Design for Transformative Vertical Lift*, 2018 [35].

response equations and vehicle trim equations are satisfied. To obtain the blade structural response and the rotor aerodynamic loads for a given set of control inputs, a nonlinear aeroelastic framework of the complete vehicle is developed. This framework consists of aeroelastic model of cycloidal rotor and aerodynamic model of conventional nose rotor, detail development and validation of which are discussed in the previous sections. Once the complete aeroelastic framework of cyclocopter is developed, coupled trim analysis is performed by simultaneously solving blade response equations and vehicle trim equations until trim controls, blade response, inflow, and circulation converge all together. Variation of control inputs required for hover and forward fight trim is investigated with change of different design parameters (i.e. gross-weight and longitudinal center of gravity location of the vehicle).

## 5.2 Methodology

Coupled trim analysis requires simultaneous computation of trim controls, vehicle orientation and blade responses so that both blade response equations and vehicle trim equations are satisfied. Trim equation represents force and moment equilibrium residuals and the proper control inputs are obtained through an iterative procedure until the trim residual goes to zero. Due to complex nonlinear behavior of trim equations, initial control estimations need to be reasonably accurate. Initial control estimates are obtained by solving uncoupled trim equation for rigid rotors. Based on the initial control estimations, vehicle response equations are solved to obtain forces and moments produced by cycloidal rotors and nose rotors. Residuals are updated using the forces and moments obtained from vehicle response equations. And control inputs are updated using proper trim Jacobian and residuals. The above iteration is continued until residuals go to zero. A flow chart of aeroelastic model is shown in Fig. 5.1.

## 5.3 Hover Analysis

In this section detail development of hover trim model of cyclocopter is discussed. The developed model is utilized systematically to investigate variation of control inputs required for hover trim with change in design parameters such as gross-weight and longitudinal center of gravity

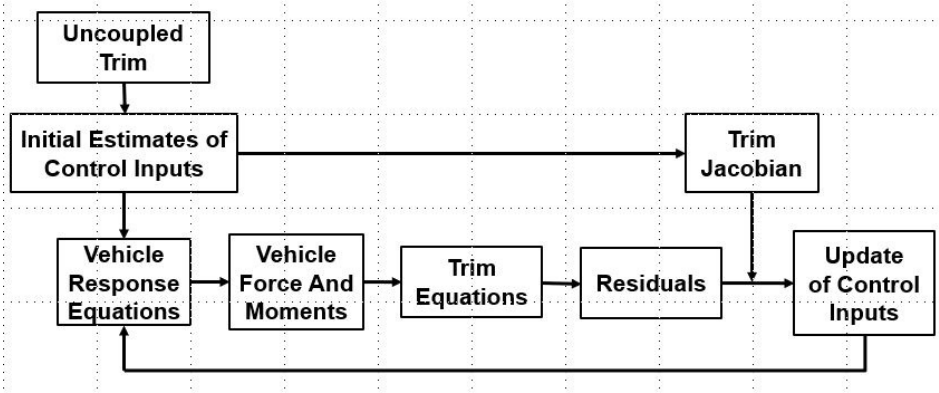


Figure 5.1: Flow-chart of coupled trim model.

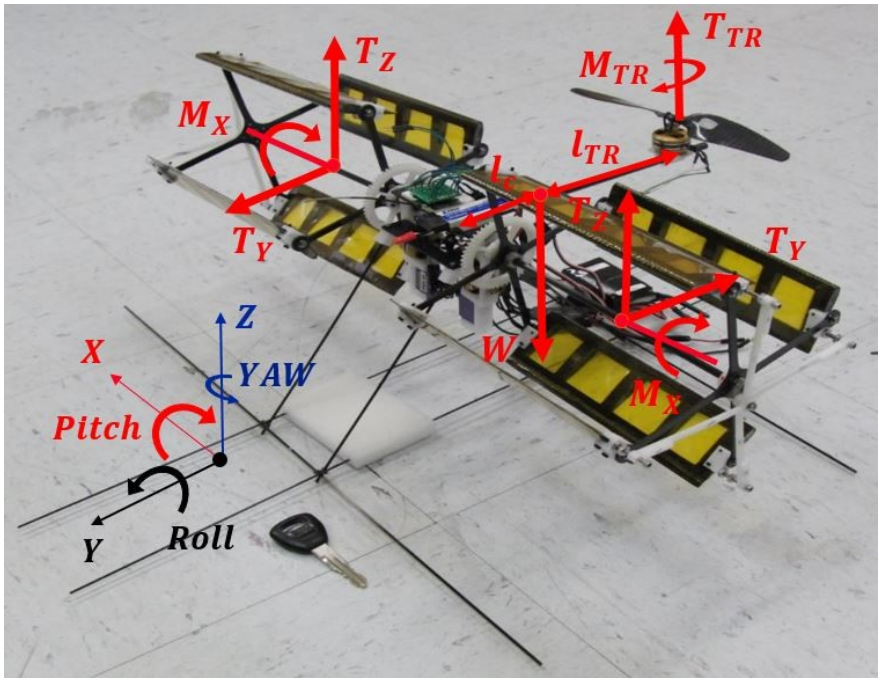


Figure 5.2: Forces and moments on a cycloidal rotor in hover

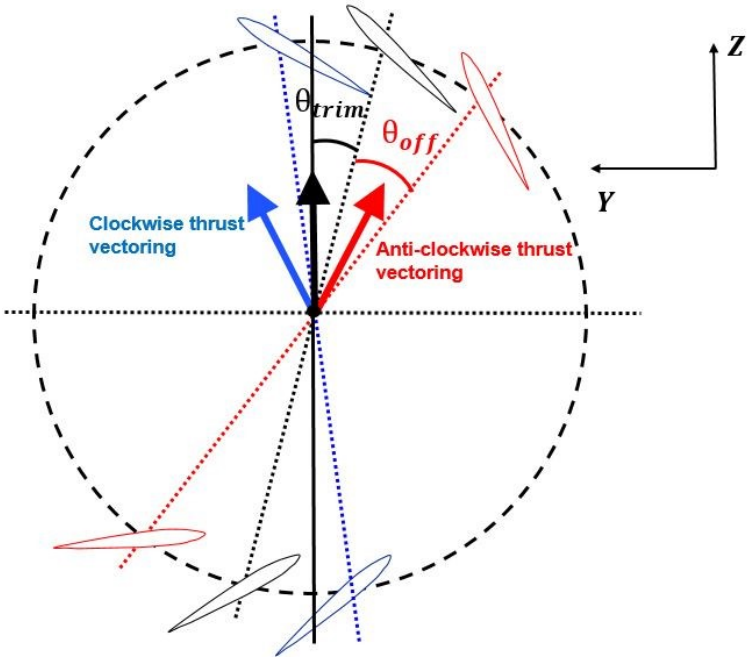


Figure 5.3: Definition of trim offset and pitch offset

location of the vehicle.

### 5.3.1 Trim Model in Hover

Trim equations are basically equilibrium equations that are obtained by balancing all the forces (vertical, longitudinal and lateral) and moments (roll, pitch and yaw) on vehicle. Figure 5.2 shows body co-ordinate frame of cyclocopter and associated forces and moments acting on cyclocopter which will be discussed in detail. In this context, Y-axis is along longitudinal direction, X-axis is along lateral direction and Z-axis is along vertical direction. Solution of trim equations gives the controls needed for sustaining steady flight for a particular flight condition. It is assumed that engine can supply all the power necessary for vehicle trim. A twin cyclocopter in hover needs only three control inputs: rotational speed of cycloidal rotor ($\Omega$), rotational speed of nose rotor ($\Omega_{TR}$) and pitch phase offsets of cycloidal rotor ($\theta_{off}$). Both the cycloidal rotors operate at same rotational speed but opposite pitch phase offsets, so that they produce same vertical forces ($T_z$), but opposite side forces ($T_y$) with same magnitude in longitudinal direction. The idea of phase

offset ($\theta_{off}$) is shown clearly in Fig. 5.3. If cycloidal rotor attains maximum pitch amplitude at $90^\circ$ and $270^\circ$ azimuthal locations, it produces both vertical and forward thrust or in other words, so the net thrust vector will be tilted forward. As shown in Fig. 5.2, an appropriate phasing ($\theta_{trim}$) needs to be applied to the pitch kinematics so that the thrust produced by cycloidal rotor acts vertically upwards. From this reference phasing of $\theta_{trim}$, an additional phasing is applied for control, which is called, pitch phase offset ($\theta_{off}$) and this is one of the control inputs. The pitch phase offset is applied in the opposite direction for the two cycloidal rotors so that they produce opposite horizontal forces of same magnitude resulting in a yawing torque for the cyclocopter to balance the yawing moment generated by nose rotor which is discussed later in detail.

If the center of gravity ($cg$) is placed in the line perfectly in between of cycloidal rotors (along Y-axis) or assuming inertial-symmetry about Y-Z plane then, the equal vertical forces produced by two cycloidal rotors balance the rolling motion automatically. For this reason, both the cycloidal rotors rotate at same rpm to produce equal vertical force. These two vertical forces of cycloidal rotors along with vertical force of nose rotor balances the vehicle weight. Operation of nose rotor creates a reaction moment in yawing direction. To balance this yaw moment, cycloidal rotors produce equal horizontal forces in opposite direction. Moreover, the opposite horizontal forces eliminate each other such that forces in longitudinal direction is always balanced. Also, no forces are being generated in lateral direction. For above mentioned reasons, two force equations in lateral and longitudinal directions and one moment equation (roll) are automatically satisfied. Rest of the three trim equations can be listed as given in Eq. 5.1.

$$F(x) = 0 \tag{5.1}$$

Where $F = [F_1,\ F_2,\ F_3]^T$ are vehicle equilibrium residuals and $x = [\Omega,\ \Omega_{TR},\ \theta_{off}]^T$ are control inputs. Expression of $F_1$, $F_2$ and $F_3$ are given below (Eq. 5.2-5.4).

$$F_1 = 2T_z + +T_{NR} - W_v \tag{5.2}$$

$$F_2 = 2l_cT_z + 2M_x - l_{NR}T_{NR} \tag{5.3}$$

$$F_3 = M_c - M_{NR} \tag{5.4}$$

Equation 5.2 is force balance in vertical direction which shows the weight of the vehicle ($W_v$) is balanced by vertical thrust generated by two cycloidal rotors ($T_z$), and one conventional nose rotor ($T_{NR}$). Equation 5.3 is pitching moment balance equation where $M_x$ is pitching moment generated by tangential forces on cycloidal rotor blade and $l_c$ is distance of cycloidal rotor ahead from cg and $l_{NR}$ is distance of nose rotor behind from cg. It shows the pitch down moment generated by cycloidal rotor is balanced by pitch up moment generated by nose rotor thrust. Equation 5.4 is yawing moment balance. Longitudinal side force ($T_y$) from each cycloidal rotor acting in opposite direction creates a yawing moment ($M_c$). $M_{NR}$ is the yawing moment created by nose rotor. $F_1$, $F_2$ and $F_3$ are vertical force residual, pitching moment residual and yawing moment residual, respectively. In coupled trim procedure, control inputs are updated in an iterative manner until all the residuals go to zero. For this purpose, trim Jacobian matrix is computed using following formula.

$$J = \frac{\partial F}{\partial x} = \begin{bmatrix} \frac{\partial F_1}{\partial \Omega} & \frac{\partial F_1}{\partial \Omega_{NR}} & \frac{\partial F_1}{\partial \theta_{off}} \\ \frac{\partial F_2}{\partial \Omega} & \frac{\partial F_2}{\partial \Omega_{NR}} & \frac{\partial F_2}{\partial \theta_{off}} \\ \frac{\partial F_3}{\partial \Omega} & \frac{\partial F_3}{\partial \Omega_{NR}} & \frac{\partial F_3}{\partial \theta_{off}} \end{bmatrix} \tag{5.5}$$

All the terms in the trim Jacobian matrix is calculated numerically using trim finite difference method. Using the trim Jacobin and residuals, control inputs are updated according to following formula.

$$x_{new} = x_{old} + \Delta x \tag{5.6}$$

Where,

$$\Delta x = -J(x_{old})^{-1}F(x_{old}) \tag{5.7}$$

During each iteration, updated control inputs are fed into vehicle response equations and residuals are calculated from forces and moments obtained from vehicle response equations. To obtain the

external forces and moments acting on the vehicle in the body frame, an aeroelastic model of cycloidal rotor and a modified BEMT based aerodynamic model of conventional rotor are utilized. This procedure is continued in a loop until control inputs are converged.

### 5.3.2 Results: Coupled Trim in Hover

The coupled trim model of cyclocopter developed in the present study is used to investigate how control inputs required for hover are affected by changing various design parameters. In the present simulation, three control inputs, rotational speed of cycloidal rotor ($\Omega$) and nose rotor ($\Omega_{NR}$), and phase offsets of cycloidal rotor ($\theta_{off}$) are used to trim a twin cyclocopter (Fig. 5.2) in hover. The cyclocopter consists of two 4-bladed cycloidal rotors with blade chord of 2 inches, radius of 3 inches and span of 6.25 inches and a conventional 2-bladed nose rotor with 0.8 inch blade chord and 6 inch diameter. The pitch amplitude of cycloidal rotors are kept fixed at 35°. The nose rotor is un-tapered and untwisted and has a collective pitch of 22°. The cyclocopter is 14.5 inches in lateral direction and 16 inches in longitudinal direction. The distance between nose rotor and cycloidal rotors is 10 inches. These specifications are very close to the 500 gram cyclocopter shown in Fig.5.2.

#### *5.3.2.1 Effects of CG Location*

In this section, effects of longitudinal position of center of gravity (cg) on rotor performance are investigated. Figure 5.4 shows variation of control inputs and required power of cyclodial rotors and conventional rotors as longitudinal position of cg is changed from cyclodial rotors to nose rotors. For the present simulation, vehicle weight is kept constant at 500 grams. $xc$ is the distance between cg and cycloidal rotors normalized by the distance between cycloidal rotors and nose rotors. $xc = 1$ denotes cg at nose rotor while $xc = 0$ indicates cg to be aligned with cycloidal rotors. As the cg comes closer to nose rotor (i.e. $xc$ increases), rpm of the cycloidal rotors decreases and that of nose rotor increases as observed in Fig. 5.4a and Fig. 5.4b, respectively. This is because closer the cg is towards nose rotor, the smaller becomes the pitching moment arm of nose rotor thrust from cg. Therefore, more thrust needs to be generated by nose rotor to balance pitch up

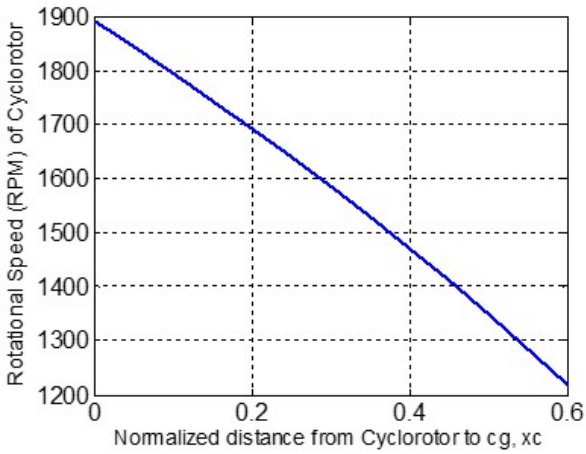


(a) Variation of rotational speed of cycloidal rotor

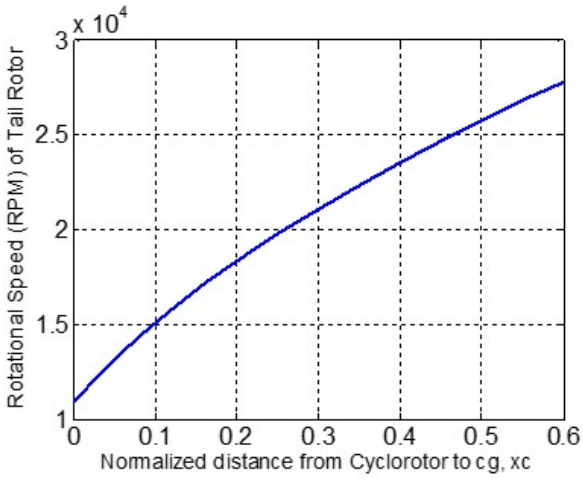


(b) Variation of rotational speed of nose rotor

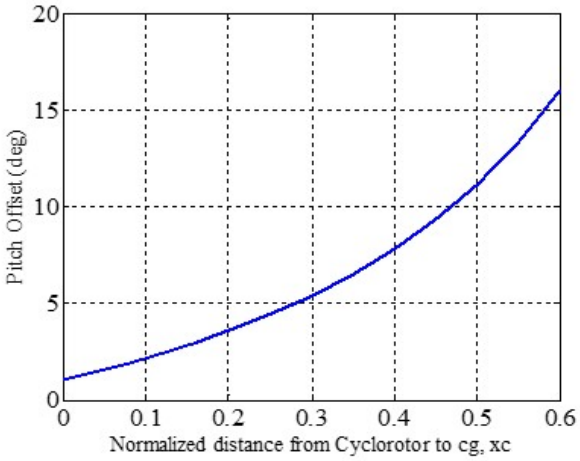


(c) Variation of pitch offset

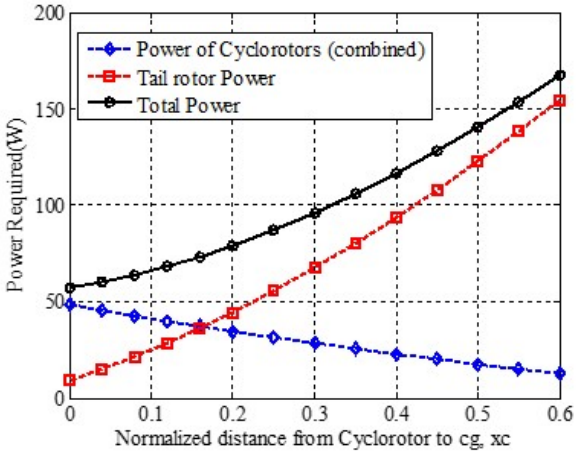


(d) Variation of required power

Figure 5.4: Variation of control inputs and required power vs weight of cyclocopter

torque of cycloidal rotors and thus rpm of nose rotor increases . Since the net vertical thrust of the rotors need to be constant to balance the constant weight, the increment of nose rotor thrust also forces decrease in cycloidal rotor thrust causing decrease in required cycloidal rotor rpm as observed in Fig. 5.4a. On this other hand, as the cg is moving closer to the nose rotor, due to lower rpm and thrust requirement, the cycloidal rotors themselves are producing less reaction torque in pitching direction, which is a counteracting effect. Increased nose rotor speed means more yawing torque of nose rotor and to balance that more side forces are required from cycloidal rotors. The decrease in vertical force requirement and the increase in horizontal force requirement of cycloidal rotors causes the thrust vector of the cycloidal rotors to tilt more in the horizontal direction as the cg moves towards nose rotor. This is obtained by increasing pitch offset of cycloidal rotors as observed in Fig. 5.4c. Figure 5.4d shows increase in nose rotor power requirement and decrease in cycloidal rotor power requirement as cg is moved towards nose rotor as expected since nose rotor thrust requirement increases while cycloidal rotor thrust requirement decreases. Interesting thing to notice here is that total power requirement increases in this process because the nose rotor power increases dramatically, when pushed to higher thrust values. This is because small conventional nose rotor are much less efficient compared to cycloidal rotor and requires comparatively more power to generate similar thrust. Also, a large part of thrust generated by cycloidal rotor is vectored sidewards to balance yawing moment of nose and power due to this is basically wasted to balance moments. Another notable observation here is that when $xc$ is zero or cg is along cycloidal rotor axis, almost entire weight of the vehicle is supported by the cycloidal rotors and the nose rotor is only producing a small thrust to balance the pitch torque produced by the cycloidal rotors. From Fig. 5.4d, this is the scenario for the least power for the cyclocopter.

#### *5.3.2.2 Effects of Weight of the Vehicle*

In this section, effects of vehicle weight on rotor performance are investigated. Figure 5.5 shows variation of control inputs and required power as weight of the vehicle is increased. In this case cg is 0.4 inches (normalized distance $xc$ = 0.04) behind cycloidal rotor and 9.6 inches ahead of nose rotor. It is observed from Fig. 5.5a and 5.5b that as the weight of the vehicle

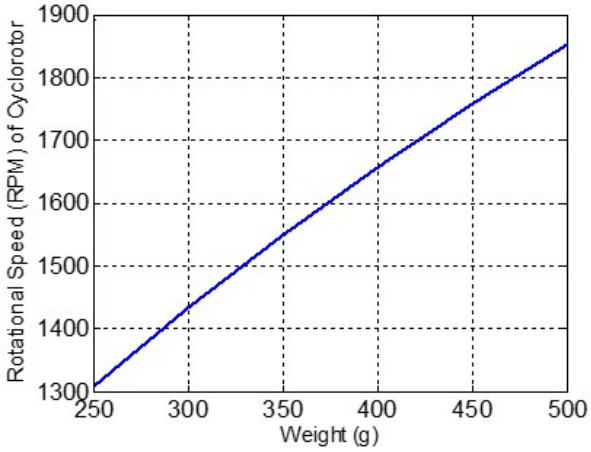


(a) Variation of rotational speed of cycloidal rotor

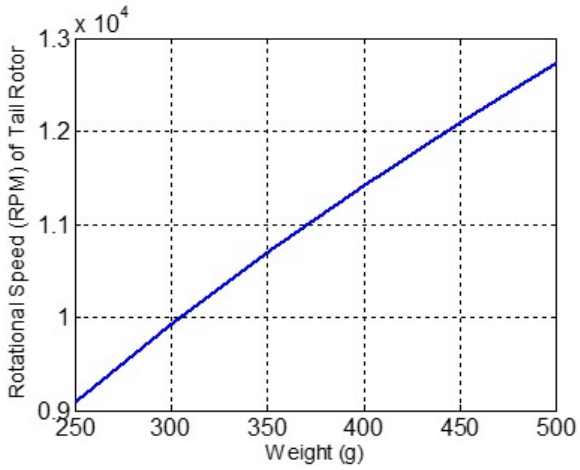


(b) Variation of rotational speed of nose rotor

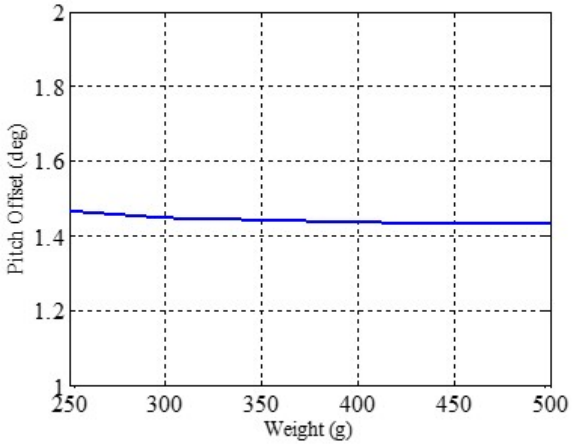


(c) Variation of pitch offset

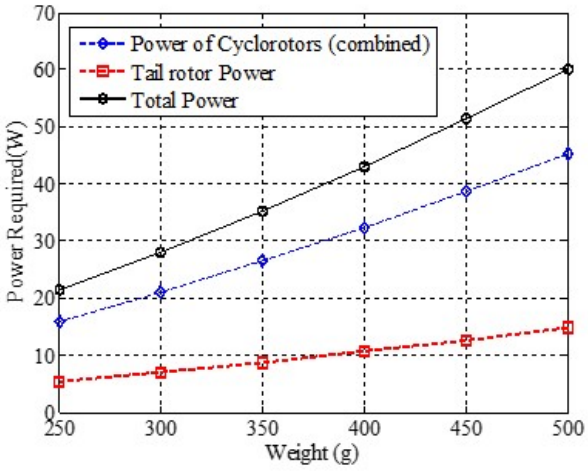


(d) Variation of required power

Figure 5.5: Variation of control inputs and required power vs weight of cyclocopter

increases, required rpms of both cycloidal rotors and nose rotor increase. This is because all the rotors need to produce more thrust as the weight of the vehicle is increased and net thrust generated by all the rotors increase quadratically with rpm of corresponding rotors . Moreover, moments due to aerodynamic forces generated by rotors also increase quadratically with rpm. To balance the nose rotor moments in yawing direction, cycloidal rotors need to produce more thrust in forward direction. So, both the forward and vertical thrust requirement of cycloidal rotors increase simultaneously with increase of vehicle weight in a similar rate. Therefore, the thrust vectoring of cyclodial rotors remain almost unchanged. Since thrust vectoring of cycloidal rotors is controlled by pitch offset ($\theta_{off}$), pitch offset also remains almost constant as weight of cyclocopter is increased, as observed in Fig. 5.5c. Figure 5.5d shows that required power for cycloidal rotors and nose rotors increases with increasing weight as expected since all the rotors produce more thrust, they would require more power to operate.

## 5.4 Forward Flight Analysis

In this section detail development of trim model of cyclocopter in forward flight is discussed. The forward flight trim model is validated with in-house experimental data obtained for a trimmed cycloidal rotor in wind tunnel. Once validated, the trim model is utilized systematically to investigate effects of various design parameters such as vehicle gross weight, pitch amplitude and longitudinal cg location on control inputs required for forward flight trim.

### 5.4.1 Trim Model in Forward Flight

As discussed in previous chapters, the cycloidal rotors have to rotate with a backspin with respect to forward speed (upper half of rotor is the retreating side) in order to generate positive vertical force due to virtual camber effect (Fig. 5.6).Therefore, rotation of cycloidal rotors creates a nose-down reaction moment (Fig. 5.7 ). The conventional rotor of the cyclocopter has to be at the front of the vehicle ahead of cg to produce nose-up moment during forward flight motion to balance the nose-down moment of cycloidal rotor and thus, it acts as a nose rotor (Fig. 5.6). If the conventional rotor was at the rear, it will have to produce a downward force to counteract

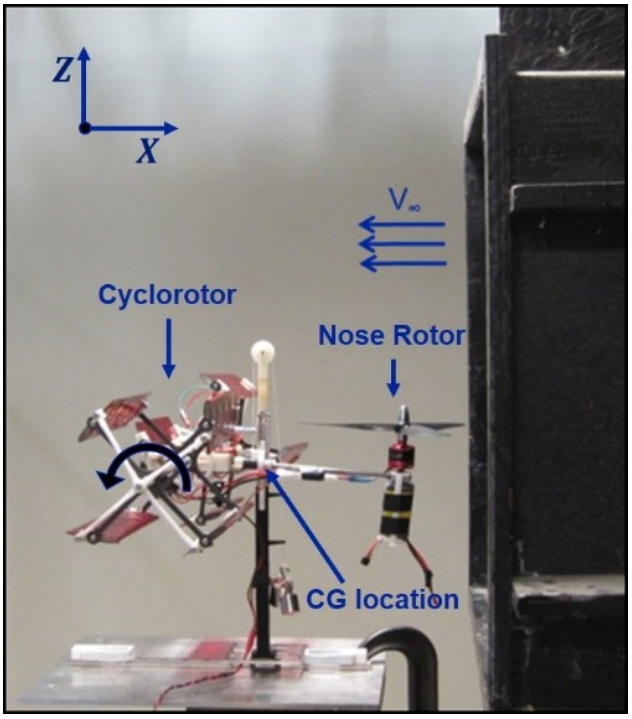


Figure 5.6: Forces and moments on a cycloidal rotor in hover

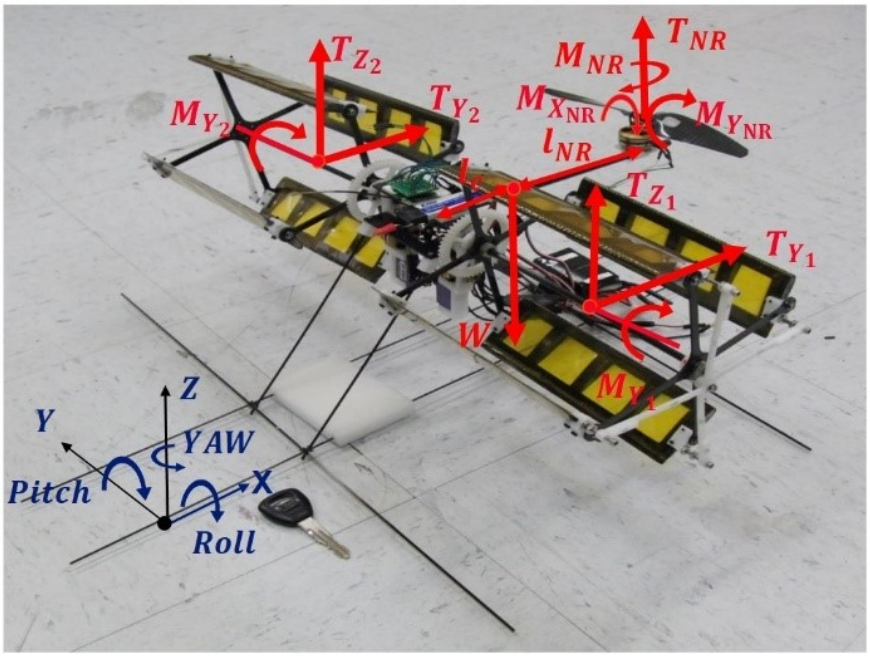


Figure 5.7: Forces and moments on a cycloidal rotor in hover

the cycloidal rotor pitch torque, which is detrimental to the total upward thrust needed to balance weight. For this reason, the most efficient way to fly a cyclocopter is to utilize the conventional rotor as nose rotor instead of tail rotor.

Figure 5.7 shows body co-ordinate frame of cyclocopter and associated forces and moments acting on the vehicle in forward flight. As shown in the figure, Y-axis is along longitudinal direction, X-axis is along lateral direction and Z-axis is along vertical direction. A twin cyclocopter in forward flight needs only five control inputs to balance three moments ( along roll, pitch and yaw directions) and two forces (along longitudinal and vertical directions) acting on cyclocopter while lateral forces remain zero at all stages. These five control inputs are mean and differential rotational speed of cycloidal rotors ($\Omega_{mean}$, $\Omega_{diff}$) and mean and differential phase offset of cycloidal rotors ($\theta_{off_{mean}}$, $\theta_{off_{diff}}$) and rotational speed of nose rotor ($\Omega_{NR}$). Weight of the cyclocopter is balanced by vertical thrust produced by cycloidal rotors ($T_z$) and nose rotor ($T_{NR}$). Magnitude of thrust generated by cycloidal rotors and nose rotor is controlled by their respective rotational speed. If the center of gravity (cg) is placed in the line perfectly in between of cycloidal rotors (along Y-axis) or assuming inertial-symmetry about Y-Z plane then, equal vertical forces produced by two cycloidal rotors balance the rolling motion automatically in hover. In forward flight, nose rotor operates with a lift offset since it is a fixed pitch propeller without any cyclic pitch control. For this reason, nose rotor in forward flight creates rolling and pitching motion. To balance the rolling moment produced by nose rotor, cycloidal rotors rotate at different rpm and produce different amount of vertical thrust. Different rotational speeds of cycloidal rotors could be represented as mean and differential values ($\Omega_{mean}$, $\Omega_{diff}$) such that rotational speed of one cycloidal rotor is $\Omega_{mean} + 0.5\Omega_{diff}$, while that of other cycloidal rotor would be $\Omega_{mean} - 0.5\Omega_{diff}$. Operation of cycloidal rotor creates a reaction moment along pitching direction and vertical thrust produced by cycloidal rotor also creates a pitching moment due to longitudinal offset of cycloidal rotors from cg. These cycloidal rotor pitching moments along with pitching moment of nose rotor due to lift offset is balanced by moments from nose rotor thrust. The drag of the aircraft body in forward flight is balanced by horizontal forces ($T_y$) produced by cycloidal rotors which is obtained by for-

ward thrust vectoring by introducing phase offset in the cyclic blade pitching kinematics. Now, operation of nose rotor produces a yawing moment which is balanced by unequal forward thrust produced by cycloidal rotors. For this reason, cycloidal rotors would have different magnitude and direction of net thrust so that horizontal force component of cycloidal rotors cancels vehicle drag and also yawing moment of nose rotor. For this reason, both the cycloidal rotors would have different rpm and phase offset. Different phase offset of cycloidal rotors could be represented as mean and differential values ($\theta_{off_{mean}}$, $\theta_{off_{diff}}$) such that phase offset of one cycloidal rotor is $\theta_{off_{mean}} + 0.5\theta_{off_{diff}}$, while that of other cycloidal rotor would be $\theta_{off_{mean}} - 0.5\theta_{off_{diff}}$. Five trim equations (2 force equations and 3 moment equations) can be listed as given in Eq. 5.8.

$$F(x) = 0 \tag{5.8}$$

Where $x = [\Omega_{mean}, \Omega_{diff}, \theta_{off_{mean}}, \theta_{off_{diff}}, \Omega_{NR}]^T$ are control inputs and $F = [F_1, F_2, F_3, F_4, F_5]^T$ are vehicle equilibrium residuals. Expression of $F_1$, $F_2$, $F_3$, $F_4$, $F_5$ are given below (Eq. 5.9 - 5.13).

$$F_1 = T_{z_1} + T_{z_2} + T_{NR} - W_V \tag{5.9}$$

$$F_2 = T_{y_1} + T_{y_2} - D \tag{5.10}$$

$$F_3 = l_c(T_{z_1} + T_{z_2}) + M_{y_1} + M_{y_2} + M_{y_{NR}} - l_{NR}T_{NR} \tag{5.11}$$

$$F_4 = M_{z_c} + M_{z_{NR}} \tag{5.12}$$

$$F_5 = M_{x_c} + M_{x_{NR}} \tag{5.13}$$

Equation 5.9 is force balance in vertical direction which shows the weight ($W_v$) of the vehicle is balanced by vertical thrust generated by two cycloidal rotors ($T_{z_1}$, $T_{z_2}$), and one conventional nose rotor ($T_{NR}$). Equation 5.10 represents force balance in longitudinal direction that shows drag of the aircraft is balanced by forward force components of cycloidal rotors ($T_{y_1}$, $T_{y_2}$). Equation 5.11 is pitching moment balance equation where $M_y$ is pitching moment generated by tangential forces

on cycloidal rotor blade, $l_c$ is distance of cycloidal rotor behind from cg, $l_{NR}$ is distance of nose rotor ahead from cg and $M_{y_{NR}}$ is nose rotor pitching moment due to longitudinal lift offset. It shows the pitch down moment generated by cycloidal rotors and pitching moment of nose rotor due to lift offset is balanced by pitch up moment generated by nose rotor thrust. Equation 5.12 is yawing moment balance. Difference in forward force ($T_y$) from each cycloidal rotor creates a yawing moment $M_{z_c}$. $M_{z_{NR}}$ is the reaction yawing moment created by nose rotor. Equation 5.13 represents rolling moment balance. $M_{x_c}$ is rolling moment generated by cycloidal rotors due to difference in vertical component of force ($T_z$) and $M_{x_{NR}}$ is rolling moment generated by nose rotor due to lateral lift offset. $F_1$ and $F_2$ are vertical and longitudinal force residuals respectively and $F_3$,$F_4$ and $F_5$ are pitching, yawing and rolling moment residuals, respectively.

In coupled trim procedure, control inputs are updated in an iterative manner until all the residuals go to zero. For this purpose, trim Jacobian matrix is computed using following formula.

$$J(i,j) = \frac{\partial F_i}{\partial x_j} \tag{5.14}$$

Where, $i$ and $j$ varies from 1 to 5.All the terms in the trim Jacobian matrix is calculated numerically using trim finite difference method.Using the trim Jacobin and residuals, control inputs are updated according to following formula.

$$x_{new} = x_{old} + \Delta x \tag{5.15}$$

Where,

$$\Delta x = -J(x_{old})^{-1} F(x_{old}) \tag{5.16}$$

During each iteration, updated control inputs are fed into vehicle response equations and residuals are calculated from forces and moments obtained from vehicle response equations. To obtain the external forces and moments acting on the vehicle in the body frame, an aeroelastic model of cycloidal rotor and an aerodynamic model of conventional rotor based on BET and dynamic inflow are utilized.

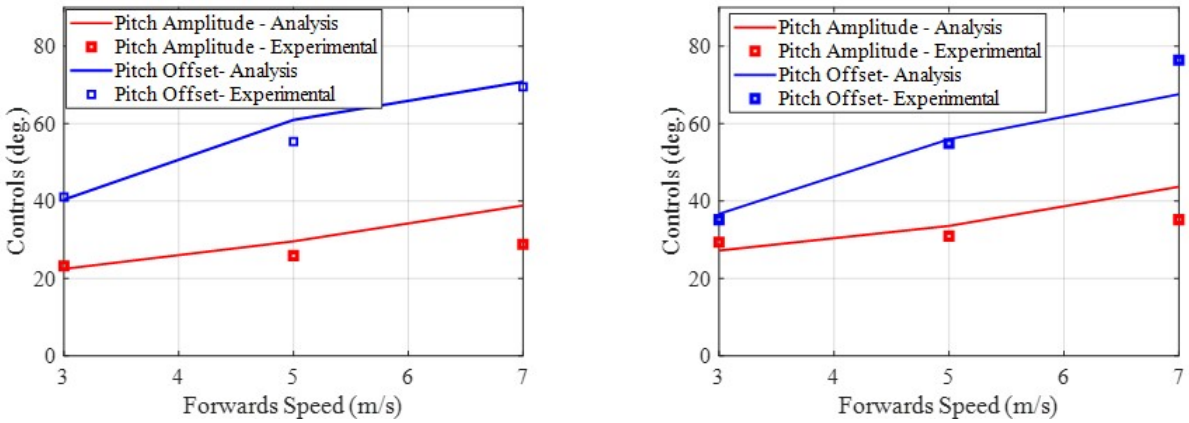


(a) RPM = 1800 (b) RPM = 1600

Figure 5.8: Variation of control inputs with forward speed for different rotational speeds

### 5.4.2 Model Validation

Since there is no flight test data available in the literature for trim control inputs required for a cyclocopter aircraft in forward flight, the developed model is validated with results from an isolated trimmed cycloidal rotor in wind tunnel. This data was obtained from in-house experiments published in Ref. 15. In this case, an isolated cycloidal rotor is trimmed by two control inputs (pitch amplitude and phase offset) in such a way that propulsive force (or net force in the horizontal direction) remains zero for a constant vertical force. Figure 5.8 shows variation of control inputs with forward speed for two different rotational speeds, 1800 rpm in Fig. 5.8a and 1600 rpm in Fig. 5.8b. In both the cases, vertical force is kept constant to be 1.96 N while propulsive force is balanced. Both the figures show reasonable correlation of model predicted results with experimental data. Figure 5.9 shows more validations comparing control inputs for different values of vertical force while keeping the net propulsive force zero. In these cases, rpm of cycloidal rotor is kept constant at 1800.Similar to the previous case, all the graphs in Fig. 5.9 show reasonable correlations between present model predictions and experimental data.

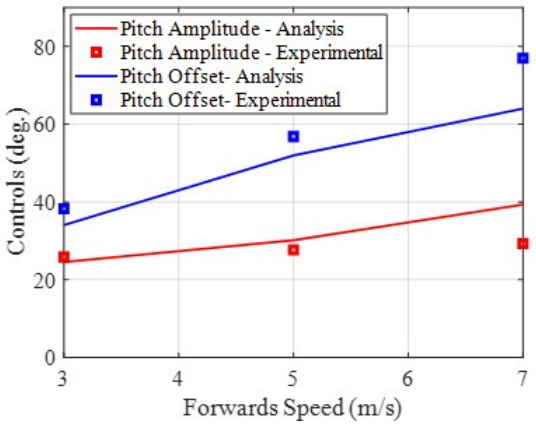


(a) Vertical force = 2.21N

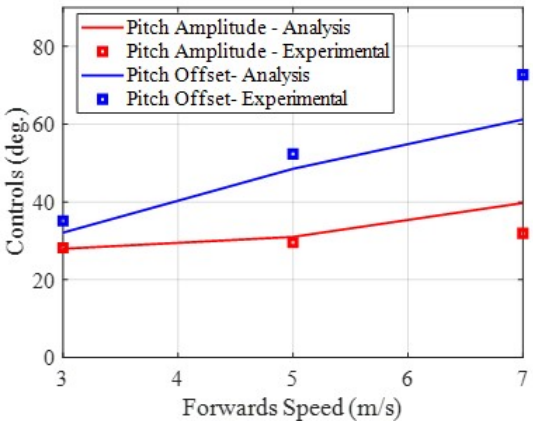


(b) Vertical force = 2.45N

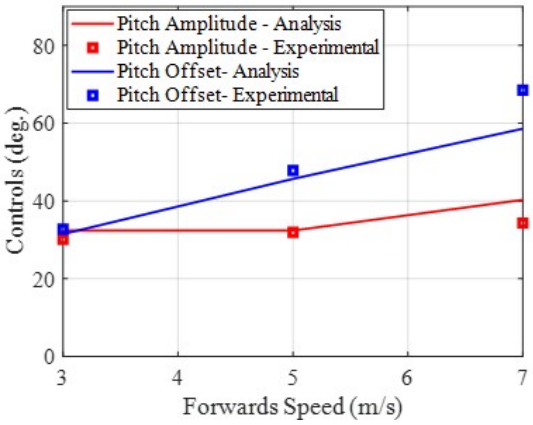


(c) Vertical force = 2.7N

Figure 5.9: Variation of control inputs with forward speed for different vertical forces

### 5.4.3 Results: Coupled Trim in Forward Flight

The coupled trim model of cyclocopter developed in the present study is used to investigate how control inputs required for forward flight at different forward speeds are affected by changing various vehicle parameters. A twin cyclocopter (Fig. 5.2 and 5.3) in forward flight needs only five control inputs. For present simulation, 4-bladed cycloidal rotors with blade chord of 2 inches, radius of 3 inches and span of 6.25 inches and a conventional 2-bladed nose rotor with 0.8 inch blade chord and 6 inch diameter are used. The nose rotor is un-tapered and untwisted and has a pitch of 22°. The cyclocopter measures 14.5 inches in lateral direction and 16 inches in longitudinal direction. The distance between nose rotor and cycloidal rotor axis is 10 inches. These specifications are very close to the 500-gram cyclocopter shown in Fig. 5.2 and previously tested in forward flight.

#### *5.4.3.1 Effects of pitch amplitude*

Figure 5.10 shows variation of control inputs as forward speed is increased for different set of cycloidal rotor pitch amplitudes. As forward speed of cyclocopter is increased, cycloidal rotor vertical force increases while propulsive force decreases due to virtual camber effects as discussed in previous chapters. For this reason, direction of cycloidal rotor thrust vector needs to be tilted forward to balance forces by increasing propulsive force and decreasing vertical force. This is done by introducing a mean phase offset in cyclic blade pitching kinematics as shown in Fig. 5.10a. Also, this mean phase offset increases with forward speed. Figure 5.10b shows that differential phase offset remains almost unchanged for different forward speeds. Figures 5.10a and 5.10b also show that pitch amplitude has very minimal effect on mean and differential phase offset. At higher forward speeds, increased pitch amplitude decreases mean phase offset slightly. This is because increased pitch amplitude increases propulsive force, so less phase offset is required to balance propulsive force. Figure 5.10c shows mean rpm of cycloidal rotor initially decreases with forward speed because of reduction in induced inflow and then increases due to increased parasitic drag at higher speeds. Moreover, as the pitch amplitude of cycloidal rotor is increased, it would require less

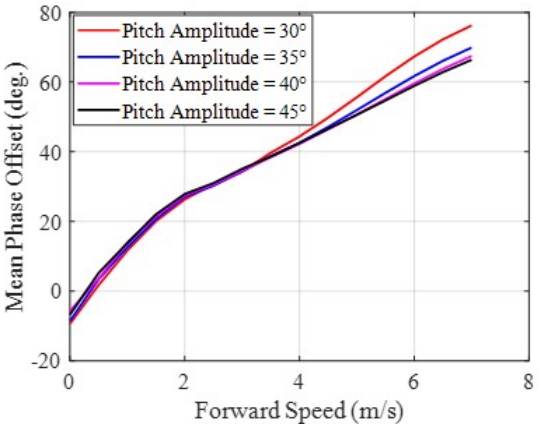


(a) Variation of mean phase offset

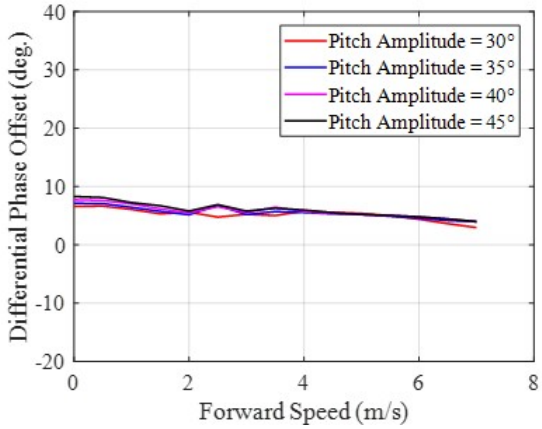


(b) Variation of differential phase offset

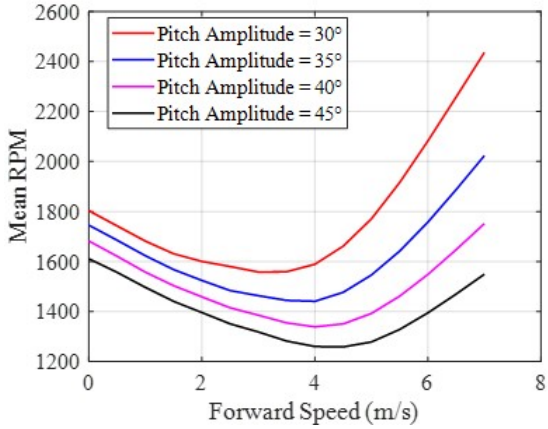


(c) Variation of mean rpm

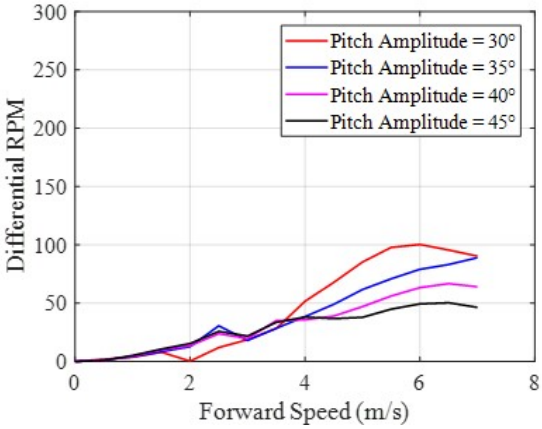


(d) Variation of differential rpm

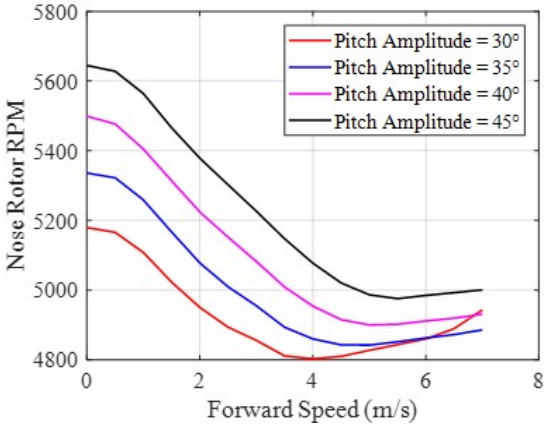


(e) Variation of nose rotor rpm

Figure 5.10: Variation of control inputs with forward speed for different pitch amplitudes

rpm to produce same amount of forces as shown in Fig. 5.10c. As the forward speed increases, nose rotor would generate more rolling moment due to lift offset which would in-turn require more balancing rolling moment from cycloidal rotor. For this reason, differential rpm of cycloidal rotor increases with forward speed as shown in Fig. 5.10d. Moreover, as the pitch amplitude of cycloidal rotors are increased, the cycloidal rotors would need lesser differential rpm to produce same amount of differential vertical thrust (to balance rolling moment) which is also observed in Fig. 5.10d.Figure 5.10e shows nose rotor rpm initially decreases with forward speed due to initial reduction of induced flow. After a certain forward speed, the nose rotor rpm remains almost constant unlike that of cycloidal rotor. This is because parasitic drag becomes dominant after certain velocity and cycloidal rotors need to overcome that by producing more thrust in horizontal direction to counter this drag. Whereas, nose rotor does not contribute towards propulsive force, it only acts to balance pitching moments. Therefore, nose rotor rpm remains almost unaffected. Moreover, fig. 5.10e shows that nose rotor rpm increases with increase in cycloidal rotor pitch amplitude at almost all forward speed. This is because increased pitch amplitude causes increased torque of cycloidal rotors (because of lower cycloidal rotor rpm at similar power) and to balance this increased pitching moment, nose rotor needs to produce more thrust.

Figure 5.11 shows variation of power as forward speed of cyclocopter is increased for different pitch amplitudes. Figure 5.11a shows that power of cycloidal rotors decreases initially with increased forward speed due to decrease in induced power, but increases after a point when parasitic power increases and becomes significant. Moreover, fig. 5.11a shows a very interesting phenomenon that the power requirement of cycloidal rotor increases along with pitch amplitude of cycloidal rotor at small forward speed only, while exactly opposite thing happens after a certain forward speed. Increase in cycloidal rotor pitch amplitude decreases rotor rpm, thus decreases profile power but increases lift induced power. At lower speed, induced power dominates over profile power. Therefore, total power increases with pitch amplitude along with increased induced power. At higher speed, profile power and parasitic becomes more significant, thus total power decreases with pitch amplitude along with decreased profile power. Figure 5.11b shows decrease

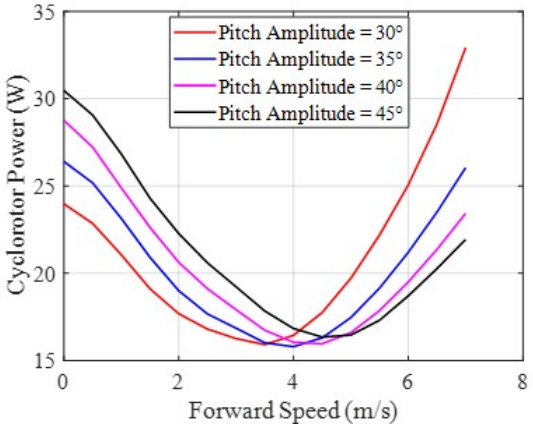


(a) Variation of power of cycloidal rotor

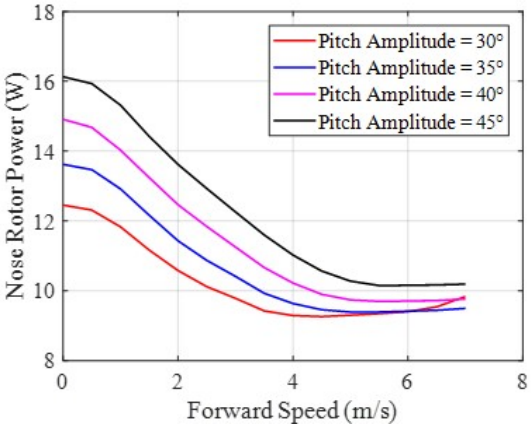


(b) Variation of power of nose rotor

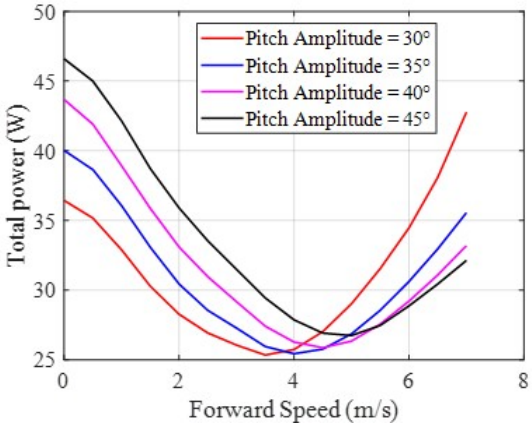


(c) Variation of total power

Figure 5.11: Variation of required power with forward speed for different pitch amplitudes

in nose rotor power with increase in speed due to decrease in induced power. Unlike cycloidal rotor power, nose rotor power does not increase after 4m/s. This is because the vehicle drag goes up with forward speed and the main rotor (in this case, cycloidal rotor) has to overcome that by producing more propulsive force causing increase in cycloidal rotor power, while the nose rotor of cyclocopter does not have to produce any propulsive thrust (zero forward shaft tilt angle) and thus, its power requirement does not increase. Moreover , figure 5.11b also shows that nose rotor power increases with increase in pitch amplitude of cycloidal rotor. This is because, as pitch amplitude of cycloidal rotor increases, it produces more torque and to balance that nose rotor need to produce more thrust. So, the nose rotor rpm increases (Fig. 5.10d) causing increase in nose rotor power. Figure 5.11c shows variation of total power along with forward speed which decreases initially and then increases after a point. The total power shows similar characteristics of cycloidal rotor power since cycloidal rotor is main thruster and generates majority of the thrust. Even though the nose rotor power is a significant fraction of the total power, unlike a conventional helicopter, it is not wasted because nose rotor is producing upward thrust to support the vehicle weight.

#### *5.4.3.2 Effects of vehicle weight*

Figure 5.12 shows variation of control inputs while weight of the vehicle is increased. Along with the increment of vehicle weight, thrust by drag ratio of the vehicle increases for a certain speed. So, the ratio of vertical force and horizontal force requirement of cycloidal rotor increases and the cycloidal rotors would need less phase offset to balance fuselage drag as shown in Fig. 5.12a. Figure 5.12b and 5.12d shows minimal effect of vehicle weight on differential phase offset and differential rpm respectively. Increased weight demands more force from rotors, so mean rpm of cycloidal rotor and rpm of nose rotor increases as shown in Fig. 5.12c and 5.12e. Figure 5.13 shows power requirement of both cycloidal rotor and nose rotor increases with increasing weight leading to increment in total power consumption, as expected.

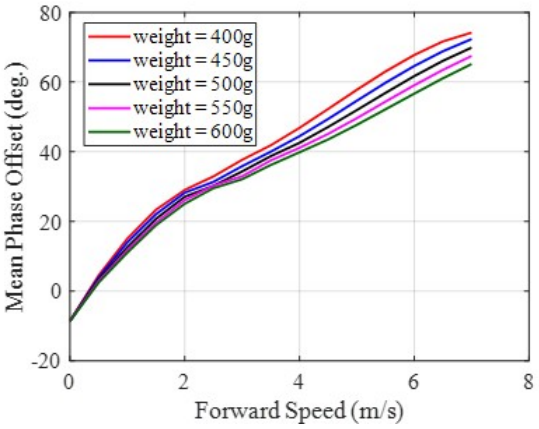


(a) Variation of mean phase offset

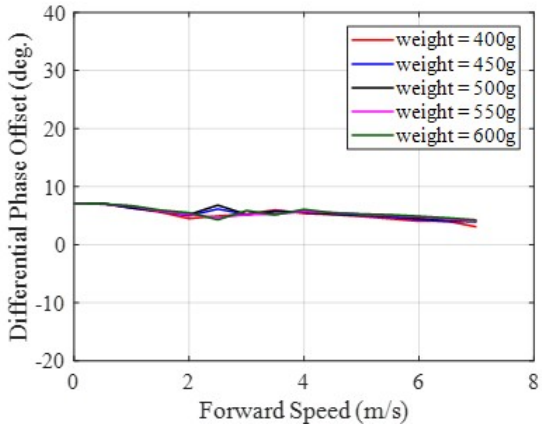


(b) Variation of differential phase offset

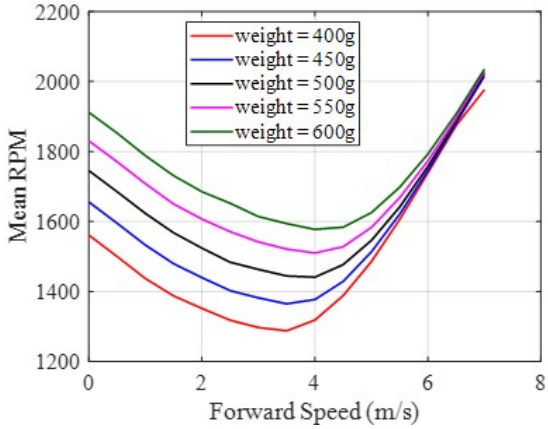


(c) Variation of mean rpm

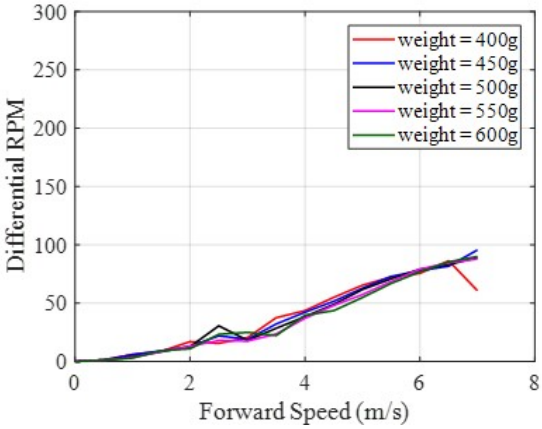


(d) Variation of differential rpm

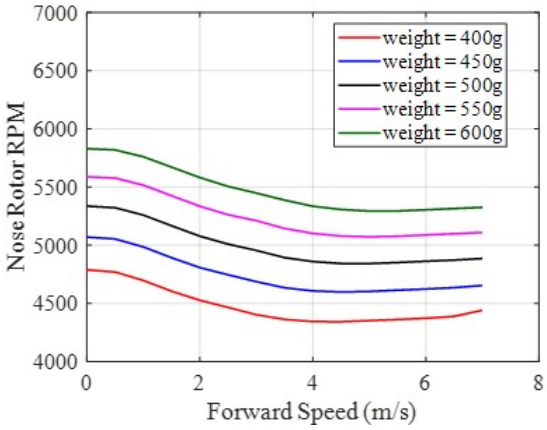


(e) Variation of nose rotor rpm

Figure 5.12: Variation of control inputs with forward speed for different vehicle weights

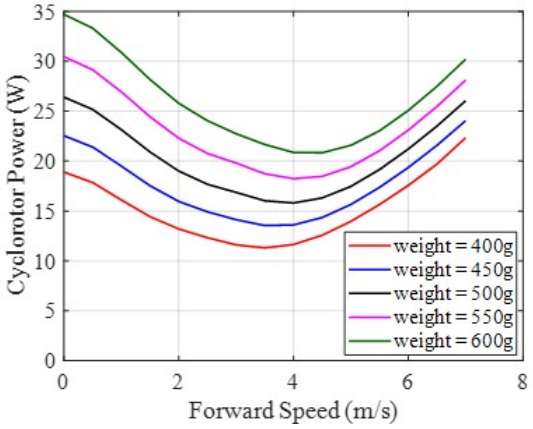


(a) Variation of power of cycloidal rotor

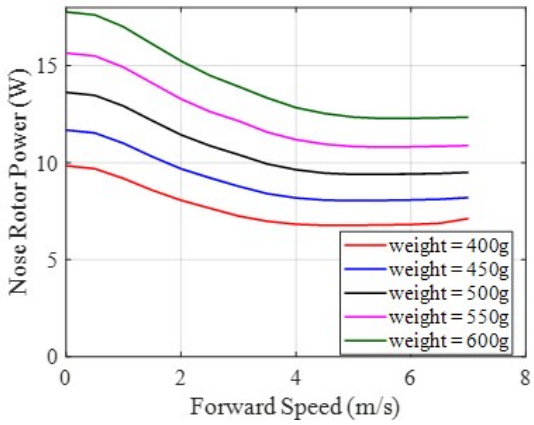


(b) Variation of power of nose rotor

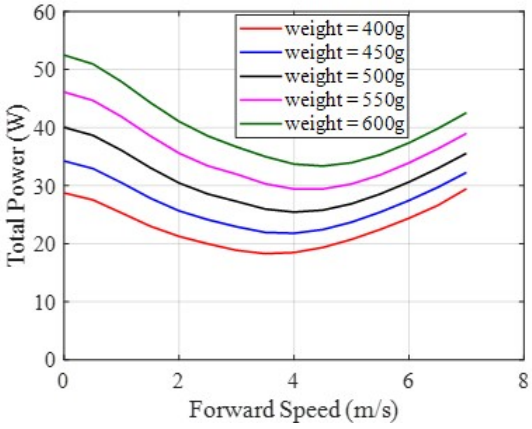


(c) Variation of total power

Figure 5.13: Variation of required power with forward speed for different vehicle weights

#### *5.4.3.3 Effects of CG location*

Figure 5.14 shows variation of control inputs as cg location of the vehicle is shifted towards nose rotor from cycloidal rotors. As cg is shifted towards nose rotor, nose rotor thrust would increase and cycloidal rotors vertical thrust would decrease to balance pitching moment. Increase in nose rotor thrust requirement increases nose rotor rpm and decrease in cycloidal rotor thrust requirement decreases cycloidal rotor rpm as shown in Figs. 5.14a and 5.14b, respectively. As nose rotor thrust increases, the rolling moment due to nose rotor lift offset also increases. For this reason, cycloidal rotors need larger differential rpm to balance this rolling moment as shown in Fig. 5.14c. With higher $xc$, the vertical force requirement of cycloidal rotor decreases while horizontal thrust requirement remains almost same to counteract the drag. Therefore, cycloidal rotors need to tilt the thrust vector more towards horizontal direction and thus, mean phase offset of cycloidal rotor increases with increasing $xc$ as shown in Fig. 5.14d. Figure 5.14e shows that differential phase offset of cycloidal rotor increases with increase in $xc$, specially at smaller speeds. This is because as cg is shifted forward, nose rotor thrust increases, which in-turn increases nose rotor yawing moment. To balance the yawing moment, cycloidal rotors need larger differential propulsive force which causes increase in differential phase offset.

Figure 5.15 shows that as the cg is shifted forward, nose rotor power increases due to increased thrust requirement while cycloidal rotor power decreases due to decreased thrust requirement. This phenomenon lead to total power increase. This is because if nose rotor produces larger force, cycloidal rotor would have to produce larger differential propulsive force to counter nose rotor torque, and this force is wasted to balance yawing moment without balancing weight or drag of the vehicle. Moreover, the conventional nose rotor is inefficient and requires more power to generate similar amount of thrust compared to cycloidal rotor.

## 5.5 Conclusion

In this chapter, detail development of nonlinear aeroelastic coupled trim models of a twin-cyclocopter in different flight conditions is discussed. Twin-cyclocopter consists of two cycloidal

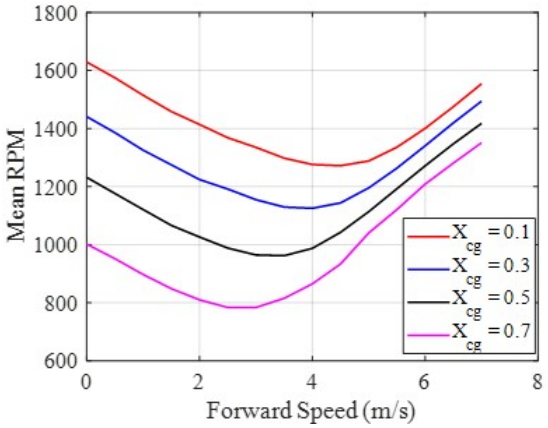


(a) Variation of mean rpm

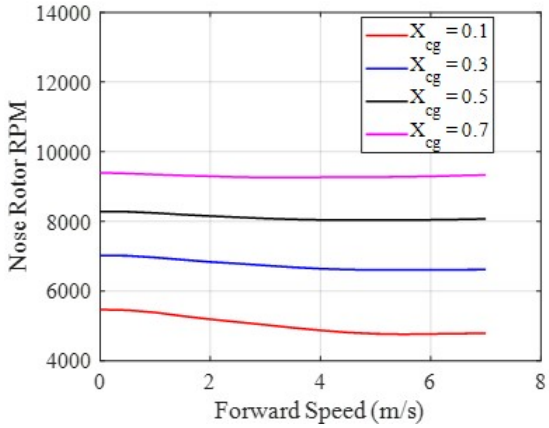


(b) Variation of nose rotor rpm

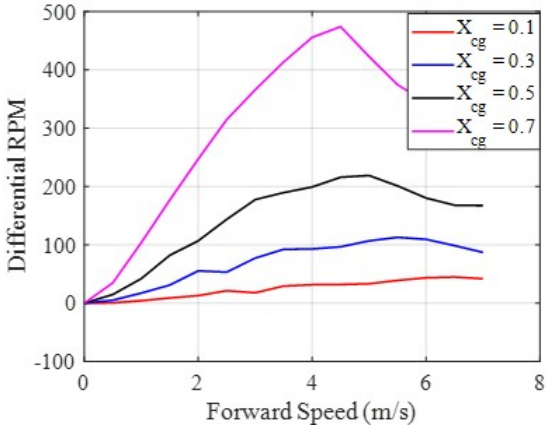


(c) Variation of differential rpm

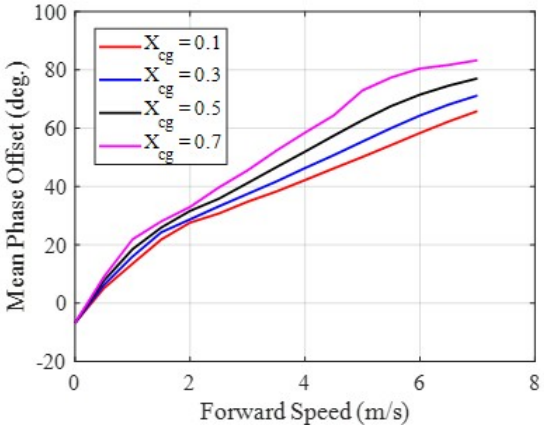


(d) Variation of mean phase offset

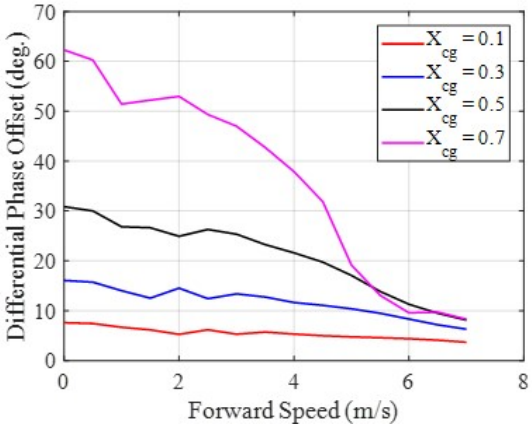


(e) Variation of differential phase offset

Figure 5.14: Variation of control inputs with forward speed for different longitudinal locations of cg

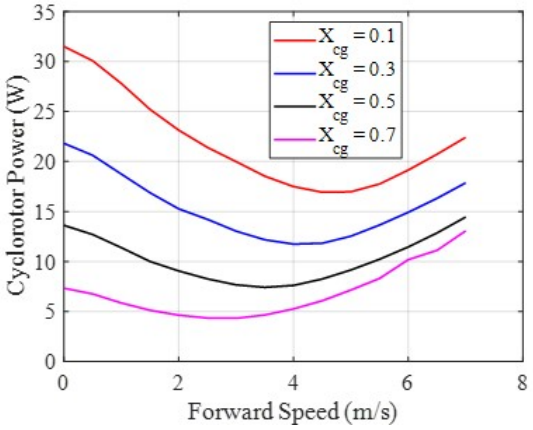


(a) Variation of power of cycloidal rotor

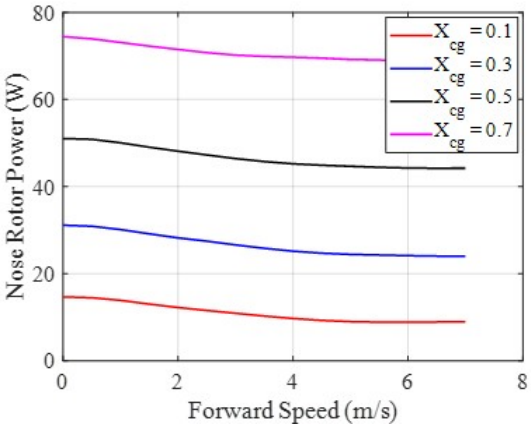


(b) Variation of power of nose rotor

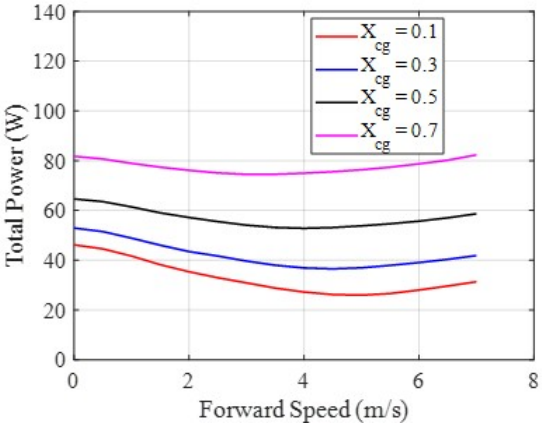


(c) Variation of total power

Figure 5.15: Variation of required power with forward speed for different longitudinal position of cg

rotors and a conventional horizontal nose rotor. Towards this, a vehicle response model and a vehicle trim model in hover and forward flight are developed and solved simultaneously to obtain coupled trim solutions. To obtain blade structural response and rotor aerodynamic forces, an aeroelastic model of cycloidal rotor and an aerodynamic model of conventional nose rotor are utilized. The developed model is validated with in-house experimental data obtained for a trimmed cycloidal rotor in wind tunnel. Once validated, the coupled trim model is utilized systematically to investigate effects of various design parameters such as vehicle gross weight, pitch amplitude and longitudinal cg location on control inputs required for vehicle trim. Key conclusions are listed below:

### 5.5.1 Conclusions from hover study

1. Vehicle trim model consist of only 3 equations since other moment (roll) and force equations (lateral and longitudinal) are automatically satisfied. These three equations include vertical force balance and yaw and pitching moment balance equations.

2. It is shown that to sustain hovering flight, a twin-cyclocopter needs only three control inputs: rotational speed of cycloidal rotor and tail rotor and pitch offset associated with cycloidal rotor. Both the cycloidal rotors need to rotate with same rpm but with opposite pitch offset.Alternatively, pitch amplitude of cycloidal rotors can be used as control input instead of rotational speed.

3. The movement of cg location towards tail rotor demands increased thrust and thus increased rotational speed of tail rotor to balance pitching moment. Moreover, increased speed of tail rotor causes increased yawing moment, which in turn requires more side force from cycloidal rotor to balance out. For this reason, pitch offset of cycloidal rotor increase as cg is shifted towards tail rotor. Moving the cg towards the tail rotor increases the power requirement for the cyclocopter.

4. The coupled trim solution results show that as the weight of the vehicle is increased, required rotational speed of both cycloidal rotors and tail rotor increases. However, the pitch offset of

cycloidal rotors required for balancing tail-rotor torque remains unchanged because both the thrust of cycloidal rotors and moment of tail rotor vary quadratically with rotational speed.

### 5.5.2 Conclusions from forward flight study

1. It is shown that to sustain steady level forward flight, a twin-cyclocopter needs five control inputs (mean and differential rpm of cycloidal rotors and mean and differential phase offset of cycloidal rotors and rpm of nose rotor) to balance five trim equations: two forces (vertical and longitudinal) and three moments (yaw, roll and pitch) equations. Forces in lateral direction remain always zero.

2. The coupled trim solution results show that mean phase offset of cycloidal rotors increases with increasing forward speed. Mean rpm and power of cycloidal rotors decreases initially due to reduced induce power and then increases once profile and propulsive power becomes dominating. Rotational speed and power of nose rotor decreases asymptotically with forward speed since it does not have to produce any propulsive force. Nose rotor rolling moment due to lift offset increases with forward speed, which causes increase in differential rpm of cycloidal rotors.

3. Increase in cycloidal rotor pitch amplitude decreases rpm, thus decreases profile power but increases lift induced power. At lower speed, induced power dominates over profile power so total cycloidal rotor power increases with pitch amplitude. At higher speed, profile power and parasitic power become more significant, thus total cycloidal rotor power decreases with increase in pitch amplitude.

4. As the weight of the vehicle is increased, required rotational speed and power of both cycloidal rotors and nose rotor increases. However, increased thrust by drag ratio of cycloidal rotors decrease mean phase offset of cycloidal rotors.

5. The movement of cg location towards nose rotor demands increased thrust and thus increased rpm and power of nose rotor while decreased thrust, rpm and power of cycloidal

rotors. Moreover, increased thrust of nose rotor causes increased yawing and rolling moment, which in turn requires more differential propulsive and vertical forces from cycloidal rotors to balance out. For this reason, differential phase offset and differential rpm of cycloidal rotors increase. Wastage of cycloidal rotor thrust to balance these moments increases total power requirement of the cyclocopter.

# 6. SUMMARY AND CONCLUSIONS

## 6.1 Summary

In last few decade, micro air vehicles or MAVs has become extremely popular among researchers and scientists due to its wide range of potential applications towards both military and civilian sectors. Although, present generation of hover-capable MAVs based on conventional rotorcraft have shown very poor performance in terms of endurance (<15 minutes), agility, and disturbance-rejection capability. Developing next generation of MAVs with performance comparable to small birds would require radical improvements in propulsion systems as well as control and guidance strategies. Cycloidal rotor is one such novel configuration which has huge potential due to its higher efficiency and maneuverability (360Âř instantaneous thrust vectoring). In the present dissertation, cycloidal rotor based MAV (cyclocopter) is proposed as an alternative to conventional rotorcraft based MAVs. First step towards building efficient MAVs based on cycloidal rotor is to develop an aeroelastic framework and coupled trim model of the vehicle, which could be utilized for design optimization and this is the main objective of the present dissertation.

The main contribution of the thesis is development of an aeroelastic coupled trim model of a twin-cyclocopter at different flight conditions (i.e hover, forward flight). Twin-cyclocopter consists of two cycloidal rotors as main thrusters and a conventional horizontal nose-rotor for pitch-torque balance. Coupled trim analysis requires simultaneous computation of trim controls, vehicle orientation and blade structural responses so that both blade response equations and vehicle trim equations are satisfied. Control strategy of the vehicle in hover and forward flight is developed. Trim model of the vehicle is developed based on the above mentioned control strategy. On the other hand, to obtain the vehicle response (blade structural response and the rotor aerodynamic loads) for a given set of control inputs, a nonlinear aeroelastic framework of the complete vehicle is developed. This framework consists of aeroelastic model of cycloidal rotor and aerodynamic model of conventional nose rotor. The nonlinear aeroelastic model of the cycloidal rotor is devel-

oped by coupling unsteady aerodynamic model with a fully nonlinear geometrically exact beam based structural framework capable of predicting large bending and torsional deflections of rotor blade. Towards this, complex aerodynamics of the cycloidal rotor is thoroughly investigated and various underlying phenomena, such as dynamic virtual camber, non-uniform inflow, effects of near and shed wake and leading-edge vortices are rigorously modeled. To obtain the performance of the conventional nose rotor, a modified BEMT based model with CFD-based airfoil lookup tables is developed. All the models and the sub-models are systematically validated with results obtained from in-house experiments. Once validated, the models are utilized to understand the physics behind the force production of cycloidal rotor.

## 6.2 Conclusions

### 6.2.1 Aerodynamic Modeling of Cycloidal Rotor

An unsteady aerodynamic model of cycloidal rotor is developed to predict its performance. Towards this, aerodynamics of a cycloidal rotor is investigated thoroughly and various underlying physical phenomena such as dynamic virtual camber, non-uniform inflow, effects of near and shed wake, leading edge vortices are rigorously modeled. All these detail modeling helped the aerodynamic model to systematically validate with not only time averaged forces, but also time-history of aerodynamic forces obtained from in-house experiments. The validated model is utilized for understanding physics behind the force production of cycloidal rotor. Key conclusions from this study is listed below.

#### *6.2.1.1 Concluding Remarks: Hover Study*

1. Chord-wise variation of incident velocity angle on cycloidal propeller blade is manifested as virtual camber/incidence effect. Virtual camber and incidence depend on curvilinear flow geometry, pitch angle, pitch-rate and inflow distribution. Considering all these effects, a generalized methodology is developed to model virtual camber.

2. Curvilinear geometry causes a static negative virtual camber at all azimuth locations while pitch, pitch rate and inflow distribution cause cyclic variation of virtual camber with blade

azimuthal location making it a dynamic virtual camber. A positive blade pitch-rate (nose-up pitch) creates positive virtual camber, while a negative pitch-rate (nose-down pitch) creates negative virtual camber.

3. Virtual camber caused by pitch rate creates asymmetry in side force due to blade lift between the right and the left halves. However, the virtual camber resulting from flow curvature creates asymmetry in side force between upper and lower halves due to blade drag. These two types of asymmetries create net time averaged side force on a cycloidal propeller even with zero phase offset.

4. Due to curvilinear flow, the cycloidal propeller blade experiences reverse or negative virtual camber in the upper half (upstream half) of its circular trajectory along with decrease in effective angle of attack due to negative virtual incidence. However, the blade experiences positive virtual camber (observed from inertial frame) and increase in effective angle of attack (due to positive virtual incidence) in the entire lower half (downstream half). For this reason, blades produce larger hydrodynamic forces in the lower or downstream half as observed from both experiments and analysis. Moreover, unsteady phenomena such as dynamic stall keep the flow attached to the cycloidal propeller blade up to very high pitch angles, which results in very high sectional force coefficients.

#### *6.2.1.2 Concluding Remarks: Forward Flight Study*

1. It is shown that forward flight velocity changes curvilinear geometry of flow associated with cycloidal rotor and this alters chord-wise variation of incident flow velocity angle on rotor blade. This chord wise variation of incident flow angle is manifested as dynamic nonlinear virtual camber effect, which is very different from what was observed previously for hover.

2. It is shown that dynamic nature of virtual camber plays an important role in the net vertical force production of cycloidal rotor in forward flight. cycloidal rotor blade experiences negative virtual camber near top of the cycle generating a negative vertical force and it experiences a positive virtual camber near bottom of the cycle generating a positive vertical force.

Since rotor blade experiences large flow speed at bottom (advancing side) compared to top (retreating side), the positive vertical force produced at the bottom dominates the negative vertical force produced at the top. These phenomena lead to net positive vertical force over a complete cycle.

3. Cycloidal rotor's capability to produce net propulsive thrust heavily depends on dynamic virtual camber as well as local angle of attack and direction of local blade forces. cycloidal rotor blade produces small negative propulsive force in the upstream half of the cycle (near 0° azimuth) due to small negative virtual camber, but it produces large positive propulsive force at the downstream half of cycle (near 180° azimuth) due to combination of large positive virtual camber and positive angle of attack. These phenomena lead to net positive propulsive force over a complete cycle.

4. It is observed that incoming flow impacts downstream of cycloidal rotor at a higher speed compared to upstream due to acceleration of induced wake after upstream. As the advance ratio of the rotor increases, effect of induced flow and induced wake becomes insignificant and flow becomes more uniform and upstream and downstream flow velocity becomes similar.

5. As the advance ratio of cycloidal rotor is increased, net vertical force increases while net propulsive decreases. Also, the additional lift due to virtual camber increases as advance ratio of cycloidal rotor is increased.

6. The study shows that it is very important for the cycloidal rotor to have a backwards rotation with respect to forward speed (blade moving away from the flow in the upper half) in order to generate positive vertically upward force. A forward spin of cycloidal rotor would generate same amount of vertical force in opposite direction. However, the direction of propulsive force is insensitive to the direction of rotation.

Although the above mentioned lower order model is computationally inexpensive and capable

of predicting rotor performance with sufficient accuracy, it can not capture the complex flow-field of cycloidal rotor with extreme accuracy. Specifically, it is extremely challenging to the capture the complex inflow distribution, blade vortex interaction and geometry of trailing vortices using a lower order model. For this reason, a high-fidelity model of cycloidal rotor based on free-wake is developed to further investigate aerodynamics of cycloidal rotor in more detail. The wake model consists of near wake and free wake region which includes trailing vortices and shed wakes. The prediction of the developed free wake model shows even better correlation with in-house experimental data compared to that of a lower model. Although, wake model is much more expensive from computational point of view which limits its application for preliminary design optimization of cycloidal rotor.

### 6.2.2 Structural Modeling of Cycloidal Rotor

To predict the deflections of cycloidal rotor blade, two independent blade structural models are developed. For traditional rotorcraft structural analysis, $2^{nd}$ order nonlinear Hodges-Dowell [106] models are widely used among scientific community. Initially similar $2^{nd}$ order nonlinear model of cycloidal rotor is developed which is capable of predicting moderate bending and torsional deflections of cycloidal rotor blades. In case of cycloidal rotor, the blades go through large centrifugal force which causes large nonlinear deflections. $2^{nd}$ order non-linear model can not capture this large bending and torsional deflections of rotor blade properly. For this reason, a fully nonlinear geometrically exact beam based structural model is developed. Both the models are systematically validated with results obtained from Abaqus, a commonly used software in scientific community. Key conclusions from the structural analysis are listed below.

1. The $2^{nd}$ order nonlinear model over-predicts bending deflections. This is because nonlinearities in bending are of third order which is not accurately captured by this $2^{nd}$ order nonlinear model. The geometrically exact model can capture large bending deflections accurately.

2. On of the major source of twist of cycloidal rotor blade is nonlinear torsional moment generated due to bending curvatures. Over-prediction of bending deflections and bending curva-

tures by $2^{nd}$ order nonlinear model leads to over-prediction of blade twist. On the other hand, geometrically exact model gives accurate twist prediction since it can also capture bending curvatures accurately.

3. More constraints on rotor blade creates larger bending curvatures which in turn leads to more nonlinearities. It is observed that $2^{nd}$ order nonlinear model is capable of accurately predicting deflections until tip bending deflections become 15-20$\%$ of blade span, for a cantilever blade. While for a simply supported blade, it can give reasonable prediction only until bending deflection becomes 0.2$\%$ of blade span. In case of a cycloidal rotor, blades are fixed in bending at both end which creates large bending curvatures and thus, nonlinearities start much earlier. For this reason, it is essential to use a fully nonlinear geometrically exact model to analyze this types of structure.

### 6.2.3 Vehicle Response Model

Vehicle response model of twin cyclocopter consists of modeling of cycloidal rotor, which acts as a primary thruster, and modeling of conventional nose rotor, whose main job is to balance pitching moment of the vehicle.

Structural modeling of cycloidal rotor shows that rotor blades go through large nonlinear bending and torsional deflections. Both experimental and analytical approaches are taken to investigate effect of these deflections on cycloidal rotor performance. Systematic experiments were conducted with a 4 bladed rotor with varying flexibility over a wide range of rotational speed at different pitch amplitudes. For experimental purpose, moderately flexible Aluminum blades and highly flexible Delrin (a type of plastic) blades are utilized. To further investigate effect of blade deflections on rotor performance, an aeroelastic model of cycloidal rotor is developed. In this procedure, unsteady aerodynamic model of cycloidal rotor is coupled with a fully nonlinear geometrically exact beam based structural framework. Once the model is systematically validated with in-house experiments, it is utilized for understanding effects of rotor deflections on rotor performance.

On the other hand, conventional nose rotor blades go through minimal deflections having neg-

ligible effects on performance, unlike cyclodial rotor blades. For this reason, only an aerodynamic model of nose rotor based on BEMT is developed for different flight conditions. Performance of small scale conventional rotor predicted by the developed aerodynamic model is validated with in-house experiments.

Key conclusions from present study of modeling of cycloidal rotor and nose rotor, are given below:

1. The experimental results show deterioration in cycloidal rotor performance as the stiffness of the blades are decreased. It is observed that more flexible blades draw more power while producing less thrust, which significantly decreases power loading compared to stiffer blades.

2. Aeroelastic model based on $2^{nd}$ order nonlinear structural model is capable of predicting thrust of moderately flexible rotors. However, in the cases of highly flexible blades, this model underestimate thrust at higher rotational speeds. Highly flexible blades go through larger bending and torsional deflections at higher rpm due to increased centrifugal force which varies as the square of rotational speed. Second order structural model over-predicts bending deflections and axial twist, which causes under-prediction of thrust.

3. Geometrically exact model is able to accurately predict large deflections. Aeroelastic model based on this model is capable of accurately predicting the thrust of cycloidal rotors for a wide range of blade flexibilities. Inclusion of geometrically exact model has proven to be very essential in accurate prediction of thrust performance.

4. Aeroelastic analysis showed that torsional deflection decreases total magnitude of pitch angle from prescribed pitch causing overall decrease in thrust in the upper half. Although bending deflections directly does not affect thrust in considerable amount, bending curvature creates significant amount of nonlinear moment that ultimately increases twist and decreases thrust. For this reason, it is very important to accurately estimate both bending and torsional deflections. Since blade twist is the primary reason for the thrust drop, increased torsional rigidity

of cycloidal rotor blade is required to counteract both linear and nonlinear part of torsional moments, thus minimize blade twist and thrust drop.

### 6.2.4 Coupled Trim Modeling of Cyclocopter

Coupled trim analysis of a twin cyclocopter is carried out by simultaneously solving blade response equations and vehicle trim equations. Twin-cyclocopter consists of two cycloidal rotors and a conventional horizontal nose rotor. Towards this, a vehicle response model and a vehicle trim model in hover and forward flight are developed. To obtain blade structural response and rotor aerodynamic forces, an aeroelastic model of cycloidal rotor and an aerodynamic model of conventional nose rotor are utilized. The developed model is validated with in-house experimental data obtained for a trimmed cycloidal rotor in wind tunnel. Once validated, the developed model is utilized systematically to investigate effects of various design parameters such as vehicle gross weight, pitch amplitude and longitudinal cg location on control inputs required for vehicle trim. Key conclusions are listed below:

#### *6.2.4.1 Concluding Remarks: Hover Study*

1. Vehicle trim model consist of only 3 equations since other moment (roll) and force equations (lateral and longitudinal) are automatically satisfied. These three equations include vertical force balance and yaw and pitching moment balance equations.

2. It is shown that to sustain hovering flight, a twin-cyclocopter needs only three control inputs: rotational speed of cycloidal rotor and tail rotor and pitch offset associated with cycloidal rotor. Both the cycloidal rotors need to rotate with same rpm but with opposite pitch offset.Alternatively, pitch amplitude of cycloidal rotors can be used as control input instead of rotational speed.

3. The movement of cg location towards tail rotor demands increased thrust and thus increased rotational speed of tail rotor to balance pitching moment. Moreover, increased speed of tail rotor causes increased yawing moment, which in turn requires more side force from cycloidal

rotor to balance out. For this reason, pitch offset of cycloidal rotor increase as cg is shifted towards tail rotor. Moving the cg towards the tail rotor increases the power requirement for the cyclocopter.

4. The coupled trim solution results show that as the weight of the vehicle is increased, required rotational speed of both cycloidal rotors and tail rotor increases. However, the pitch offset of cycloidal rotors required for balancing tail-rotor torque remains unchanged because both the thrust of cycloidal rotors and moment of tail rotor vary quadratically with rotational speed.

#### *6.2.4.2 Concluding Remarks: Forward Flight Study*

1. It is shown that to sustain steady level forward flight, a twin-cyclocopter needs five control inputs (mean and differential rpm of cycloidal rotors and mean and differential phase offset of cycloidal rotors and rpm of nose rotor) to balance five trim equations: two forces (vertical and longitudinal) and three moments (yaw, roll and pitch) equations. Forces in lateral direction remain always zero.

2. The coupled trim solution results show that mean phase offset of cycloidal rotors increases with increasing forward speed. Mean rpm and power of cycloidal rotors decreases initially due to reduced induce power and then increases once profile and propulsive power becomes dominating. Rotational speed and power of nose rotor decreases asymptotically with forward speed since it does not have to produce any propulsive force. Nose rotor rolling moment due to lift offset increases with forward speed, which causes increase in differential rpm of cycloidal rotors.

3. Increase in cycloidal rotor pitch amplitude decreases rpm, thus decreases profile power but increases lift induced power. At lower speed, induced power dominates over profile power so total cycloidal rotor power increases with pitch amplitude. At higher speed, profile power and parasitic power become more significant, thus total cycloidal rotor power decreases with increase in pitch amplitude.

4. As the weight of the vehicle is increased, required rotational speed and power of both cycloidal rotors and nose rotor increases. However, increased thrust by drag ratio of cycloidal rotors decrease mean phase offset of cycloidal rotors.

5. The movement of cg location towards nose rotor demands increased thrust and thus increased rpm and power of nose rotor while decreased thrust, rpm and power of cycloidal rotors. Moreover, increased thrust of nose rotor causes increased yawing and rolling moment, which in turn requires more differential propulsive and vertical forces from cycloidal rotors to balance out. For this reason, differential phase offset and differential rpm of cycloidal rotors increase. Wastage of cycloidal rotor thrust to balance these moments increases total power requirement of the cyclocopter.

## 6.3 Future Recommendations

Significant research is needed to improve this novel concept and utilize cyclocopter for practical applications. Some of the future recommendations in this aspect are listed below.

1. In the present dissertation, development of lower order coupled trim model of a twin cyclocopter is discussed which is ideal for preliminary design and optimization. On the other hand, a very accurate high-fidelity model needs to be developed for final design phases of cycloidal rotor based MAVs.

    (a) From aerodynamic point of view, 3-D CFD model of cycloidal rotor needs to be utilized for more accurate prediction of rotor performance. Moreover, high fidelity CFD model might reveal some key physics behind the operation of cycloidal rotor which are not explored using lower order model.

    (b) For the present structural analysis, isotropic beam based model of cycloidal rotor blade is developed. This structural analysis can to be extended for composite models of the rotor blades. On the other hand, a plate based model or 3-D model might be slightly more accurate for the analysis of low aspect ratio blades.

(c) Finally, high fidelity CFD-CSD model of cycloidal rotor needs to be developed by coupling the CFD with structural framework.

2. Scalability of this concept needs to be investigated from both aerodynamic and structural point of view. High-fidelity CFD-CSD model might be crucial in this respect.

   (a) At MAV scale, cycloidal rotor is found be aerodynamically more efficient compared to a conventional rotor. Similar performance comparison needs to be carried out for rotors with larger scales. Some key aerodynamic phenomena (such as formation of leading-edge dynamic-stall vortex, nonlinear dynamic virtual camber) behind the operation of cycloidal rotor at MAV scale might be very different at larger scales.

   (b) With increasing dimension, rotor blades tend to be more flexible. Thus, thorough structural analysis needs to be carried out to investigate upward scalability of cycloidal rotor.

3. Developed coupled trim model can be utilized to develop a flight dynamic model of twin cyclocopter. System identification of the system needs to be carried out for this purpose. Flight dynamic model might be crucial to develop advanced control strategies of the vehicle.

4. Present dissertation focuses on developing modeling tools of cycloidal rotor and cyclocopter. These tools can be utilized to develop a thorough design framework of the vehicle which would be extremely helpful for developing next generation cyclocopters.

5. Modeling tools developed at present study can be further utilized to optimize the performance of cycloidal rotor and cyclocopter. For example, the performance model of cycloidal rotor can be used to investigate the optimum pitch kinematics of cycloidal rotor at different advance ratios.

6. Thorough investigation is required to find the optimum configuration of cyclocopter (i.e. twin cyclocopter vs quad-cyclocopter etc).

   Cycloidal rotors are speculated to be very quiet compared to conventional rotor due to extremely low operating rpm. Although no scientific study is carried out to investigate the

potential acoustic advantages of cycloidal rotor. Towards this, an aeroacoustic model of cycloidal rotor needs to be developed by coupling aeroelastic model of cycloidal rotor (developed in the present thesis) with an acoustic solver.

# REFERENCES


[1] Hundley, R. O., and Gritton, E. C., "Future Technology-Driven Revolutions in Military Operations: Results of a Workshop," RAND National Defense Research Institute DB-110-ARPA, Santa Monica, CA, 1994 Defense Technical.

[2] McMichael, J. M., and Francis, USAF (Ret.), C. M. S., "Micro Air Vehicles Toward a New Dimension in Flight,"*U.S. Department of Defense Weapons Systems Technology Information Analysis Center (WSTIAC) Newsletter*, Vol. 1, No. 13, Jan 2000 Originally published online at http://www.darpa.mil/tto/MAV/mav auvsi.html, Aug. 7, 1997.

[3] Mueller, T. and DeLaurier, J., "Aerodynamics of Small Vehicles," *Annual Rev. of Fluid Mech.*, Vol. 35, 2003, pp. 89-111.

[4] Winslow, J. M., "*Understanding Of Low Reynolds Number Aerodynamics And Design Of Micro Rotary-Wing Air Vehicles*," Master's Thesis, Department of Aerospace Engineering, University of Maryland College Park, 2016.

[5] Ifju, P. G., Jenkins, D. A., Ettinger, S., Lian, Y., Shyy,W., andWaszak, M. R., "Flexible-Wing-Based Micro Air Vehicles," *AIAA 40th Aerospace Sciences Meeting and Exhibit*, Reno,NV,AIAAPaper 2002-705, Jan. 2002.

[6] Keenon, M. T., and Grasmeyer, J. M., "Development of the Black Widow and Microbat MAVs and a Vision of the Future of MAV Design," *AIAA/ICAS International Air and Space Symposium and Exposition, The Next 100 Years Proceedings*, Dayton, OH, AIAA Paper 2003-2901, July 2003.

[7] Peterson, B., Erath, B., Henry, K., Lyon, M., Walker, B., Powell, N., Fowkes, K., and Bowman, W. J., "Development of a Micro Air Vehicle for Maximum Endurance and Minimum Size," Paper AIAA-2003-416, *AIAA 41st Aerospace Sciences Meeting and Exhibit*, Reno, NV, January 6–9, 2003.

[8] Brion, V., Aki, M., and Shkarayev, S., "Numerical Simulation of Low Reynolds Number Flows Around Micro Air Vehicles and Comparison Against Wind Tunnel Data," Paper AIAA-2006-3864, *AIAA 24th Applied Aerodynamics Conference Proceedings*, San Francisco, CA, June 5–8, 2006.

[9] Grasmeyer, J. M., and Keennon, M. T., "Development of the Black Widow Micro Air Vehicle," Paper AIAA-2001-0127, *AIAA 39th Aerospace Sciences Meeting and Exhibit*, Reno, NV, January 8–11, 2001.

[10] Hrishikeshavan, V. and Chopra, I., "Design and Testing of a Shrouded Rotor MAV with Anti-Torque Vanes," *Proceedings of the 64th Annual National Forum of the American Helicopter Society*, Montreal, Canada, April 28–30, 2008.

[11] Bohorquez, F., Samuel, P., Sirohi, J., Pine, D. J., Rudd, L. and Parel, R., "Design, Analysis and Hover Peroformance of a Rotary Wing Micro Air Vehicle," *Journal of the American Helicopter Society*, Vol. 48, No. 2, April 2003, pp. 80–90.

[12] Sirohi, J., Tishchenko, M. and Chopra, I., "Design and Testing of a Micro-Aerial Vehicle with a Single Rotor and Turning Vanes," *Proceedings of 61s Annual Forum of the American Helicopter Society*, Grapevine, TX June 2005.

[13] Hein, B., and Chopra, I., "Hover Performance of a Micro Air Vehicle: Rotors at Low Reynolds Number," *Journal of American Helicopter Society*, Vol. 52, (3), July 2007, pp. 254–262.

[14] Leishman, J. G., *Principles of Helicopter Aerodynamics*, Cambridge University Press, Cambridge, UK, 2000.

[15] Anderson, J. D., *Fundamentals of Aerodynamics*, Boston: McGraw-Hill, 2001.

[16] Schmitz, F. W., "Aerodynamics of Model Aircraft wing Measurements I", R.T.P. Translation No 2460. Issued by Ministry of Aircraft Production. 1983.

[17] Abbott, I. H., and Von Doenhoff, A. E., *Theory of Airfoil sections*, Dover, New York, 1959.

[18] Riegels, F. W., *Airfoil sections*, Butterworth, London, 1961.

[19] Althaus, D., and Wortmann, F. X., "Stuttgarter profilkatalog I - Experimental results for the laminar wind tunnel of the University of Stuttgart," Friedr. Vieweg and Sohn, Braunschweig, 1972 (English version in 1981).

[20] McMasters, J. and Henderson, M., "Low-Speed Single Element Airfoil Synthesis," *Technical Soaring*, Vol. 6, 1980, pp. 1-21.

[21] Mueller, T. J., and Batill, S. M., "Experimental studies of separation on a two dimensional airfoil at low Reynolds numbers," *AIAA Journal*, Vol. 20, No.4, 1982, pp. 457-463.

[22] OMeara, M. M., and T. J. Mueller., "Laminar Separation Bubble Characteristics on an Airfoil at Low Reynolds Numbers." AIAA Journal, Vol. 25, No. 8, August 1987, pp. 1033-1041.

[23] Bastedo, W. G., Jr., and Mueller, T. J., "The Spanwise Variation of Laminar Separation Bubbles on Finite Wings at Low Reynolds Numbers," *Journal of Aircraft*, Vol. 23, No. 9, pp. 687-694, September 1986.

[24] Pelletier, A., and Mueller, T. J., "Low Reynolds number aerodynamics of low-aspect-ratio, thin/flat/cambered-plate wings," *Journal of Aircraft*, Vol. 37, No.5, 2000, pp. 825-832.

[25] Mueller, T. J., "Aerodynamic Measurements at Low Reynolds Numbers for Fixed Wing Micro-Air Vehicles," Presented at the RTO AVT/VKI Special Course on Development and Operation of UAVs for Military and Civil Applications, VKI, Belgium, September 13-17, 1999.

[26] Laitone, E. V., "Wind Tunnel Tests of Wings at Reynolds Numbers Below 70,000," *Experiments in Fluids*, Vol. 23, 1997, pp. 405-409

[27] Selig M. S., Donovan J. F., and Fraser D. B., *Airfoils at Low Speeds*, Soar Tech Publ., Virginia Beach, VA, 1989.

[28] McArthur, J., "*Aerodynamics of wings at low Reynolds numbers: Boundary layer separation and reattachment*", PhD thesis, University of Southern California, Department of Aerospace and Mechanical Engineering, 2008.

[29] Carmichael, B., "Low Reynolds Number Airfoil Survey," NASA CR165803, 1981.

[30] Halder, A., and Benedict, M., "Role of Blade Flexibility on Cycloidal Rotor Hover Performance," *Journal of Aircraft*, Vol. 55, No. 5 (2018), pp. 1773-1791.

[31] Benedict, M., "*Fundamental Understanding of the Cycloidal-Rotor Concept for Micro Air Vehicle Applications*," Ph.D Thesis, Department of Aerospace Engineering, University of Maryland College Park, December 2010.

[32] Benedict, M., Ramasamy, M., Chopra, I., and Leishman, J. G., "Performance of a Cycloidal Rotor Concept for Micro Air Vehicle Applications," *Journal of the American Helicopter Society*, Vol. 55, No. 2, April 2010, pp. 022002-1 - 022002-14.

[33] Benedict, M., Jarugumilli, T., and Chopra, I., "Effect of Rotor Geometry and Blade Kinematics on Cycloidal Rotor Hover Performance," *Journal of Aircraft*, Vol. 50, No. 5, 2013, pp. 1340 – 1352.

[34] Halder, A., and Benedict, M., "Nonlinear Aeroelastic Coupled Trim Analysis of a Cyclocopter in Hover," *Proceedings of 73rd Annual Forum of the American Helicopter Society*, Dallas, TX, May 9-11, 2017.

[35] Halder, A., and Benedict, M., "Nonlinear Aeroelastic Modeling of Cycloidal Rotor in Forward Flight," *Proceedings of the AHS Technical Meeting on Aeromechanics Design for Transformative Vertical Lift*, San Francisco, CA, Jan 16-18, 2018.

[36] Boirum, C. G., and Post, S. L., "Review of Historic and Modern Cyclogyro Design," Paper AIAA-2009-5023, *45th AIAA/ASME/SAE/ASEE Joint Propulsion Conference and Exhibit*, Denver, CO, August 2-5, 2009.

[37] "Cyclogyro History," World-Wide Web document, http://www.rotoplan.narod.ru/historye.html, May 19, 2007.

[38] Sachse, H., "Kirsten-Boeing Propeller," Technical Memorandum 351, National Advisory Committee for Aeronautics, January 1926.

[39] Kirsten, F. K., "Cycloidal Propulsion Applied to Aircraft," *Transactions of the American Society of Mechanical Engineers*, Vol. 50, (12), 1928, pp 25-47.

[40] "Flying Without Wings or Motors, an interview with F. K. Kirsten (Popular Science 1934)," World-Wide Web document, http://blog.modernmechanix.com/2007/09/04/flying-without-wings-or-motors/, Sept 4, 2007.

[41] "Voith Schneider Propeller," World-Wide Web document, http://en.wikipedia.org/wiki/VoithSchneiderPropeller, Nov 28, 2010.

[42] "Voith Schneider Propeller," World-Wide Web document, http://www.renewbl.com/2010/07/16/voith-turbo-supplying-propellers-for-two-jack-up-vessels.html, July 16, 2010.

[43] Strandgren, C., "The Theory of the Strandgren Cyclogyro," Technical Report 727, National Advisory Committee for Aeronautics, July 1933.

[44] Wheatley, J., "Simplified Aerodynamic Analysis of the Cyclogiro RotatingWing System," Technical Report 467, National Advisory Committee for Aeronautics, August 1933.

[45] Wheatley, J. B., and Windler, R., "Wind-Tunnel Tests of a Cyclogiro Rotor," NACA Technical Note No. 528, May 1935.

[46] Taniguchi, K., "An Approximate Solution of the Voith-Schneider Propeller", *Journal of Zosen Kiokai(Trans. Soc. of Naval Arch. of Japan)*, Vol. 74, 1944, pp. 153-161.

[47] Taniguchi, K., "Hydrodynonical Investigations of the Blade Wheel Propeller", *Journal of Zosen Kiokai (Trans. Soc. of Naval Arch. of Japan)*, Vol. 88, 1950, pp. 63-74.

[48] Taniguchi, K., "*Studies on a Trochoidal Propeller*", Doctor of Engineering Thesis, Tokyo University, 1960.

[49] Haberman, W. L., and Harley, E. E., "Performance of Vertical Axis (Cycloidal) Propellers Calculated by Tanuguchi's Method", Report No 1564. Department of the Navy, David Taylor Model Basin, Hydromechanics Laboratory Research and Development Report. November 1961.

[50] Boschma, J. H., "Modern Aviation Applications for Cycloidal Propulsion," Paper AIAA-2001-5267, *AIAA Aircraft, Technology Integration, and Operations Forum Proceedings*, Los Angeles, CA, October 16-18, 2001.

[51] Gibbens, R., "Improvements in Airship Control using Vertical Axis Propellers," Paper AIAA-2003-6853, *3rd AIAA Annual Aviation Technology, Integration, and Operations (ATIO) Forum Proceedings*, Denver, CO, Nov. 17-19, 2003.

[52] Gibbens, R., Boschma, J., and Sullivan, C., "Construction and Testing of a New Aircraft Cycloidal Propeller," Paper AIAA-1999-3906, *AIAA 13th LighterThan-Air Systems Technology Conference Proceedings*, Norfolk, VA, June 28- July 1, 1999.

[53] McNabb, M., "*Development of a Cycloidal Propulsion Computer Model and Comparison with Experiment*," M.S. Thesis, Department of Aerospace Engineering, Mississippi State University, December 2001.

[54] Garrick, I. E., "Propulsion of a flapping and Oscillating Airfoil", Technical Report 567, National Advisory Committee for Aeronautics, 1937, pp. 419-427.

[55] Iosilevskii, G., and Levy, Y., "Aerodynamics of the Cyclogiro", Paper AIAA2003-3473, *AIAA 33rd Fluid Dynamics Conference and Exhibit*, Orlando, FL, June 23-26, 2003.

[56] Iosilevskii, G., and Levy, Y., "Experimental and Numerical Study of Cyclogiro Aerodynamics," *AIAA Journal*, Vol. 44, (12), 2006, pp 2866-2870.

[57] Levy, Y., "Numerical Simulation of Dynamically Deforming Aircraft ConïňĄgurations Using Overset Grids," *Journal of Aircraft*, Vol. 38, No. 2, 2001, pp. 349-354.

[58] Moryossef, Y., and Levy, Y., "Effect of Oscillations on Airfoils inClose Proximity to the Ground," *AIAA Journal*, Vol. 42, No. 9, 2004, pp. 1755-1764.

[59] Adar, M., and Levy, Y., "Numerical Simulation of Flare SafeSeparation," *Journal of Aircraft*, Vol. 43, No. 4, 2006, pp. 1129-1137.

[60] Benek, J. A., Buning, P. G., and Steger, J. L., "A 3-D Chimera Grid Embedding Technique,"AIAA Paper 85-1523, July 1985.

[61] Kim, S., Yun, C., Kim, D., Yoon, Y., and Park, I., "Design and Performance Tests of Cycloidal Propulsion Systems," Paper AIAA-2003-1786, *44th AIAA/ASME/ASCE/AHS/ASC Structures, Structural Dynamics, and Materials Conference*, Norfolk, Virginia, April 7-10, 2003.

[62] Yun, C. Y., Park, I., Lee, H. Y., Jung, J. S., Hwang, I. S., Kim, S. J. and Jung, S. N., "A New VTOL UAV Cyclocopter with Cycloidal Blades System," *Proceedings of the 60th American Helicopter Society Annual Forum*, Baltimore, MD, June, 2004.

[63] Yun, C. Y., Park, I. K., Hwang, I. S., and Kim, S. J., "Thrust Control Mechanism of VTOL UAV Cyclocopter with Cycloidal Blades System," *Journal of Intelligent Material Systems and Structures*, Vol. 16, No. 11-12, December 2005, pp. 937-943.

[64] Yun, C. Y., Park, I. K., Lee, H. Y., Jung, J. S., Hwang, I. S., and Kim, S. J., "Design of a New Unmanned Aerial Vehicle Cyclocopter," *Journal of American Helicopter Society*, Vol. 52, (1), January 2007, pp. 24-35.

[65] Hwang, I. S., Min, S. Y., Kim, M. K., and Kim, S. J., "Multidisciplinary Optimal Design of Cyclocopter Blade System," *1st AIAA Multi-Disciplinary Optimization Specialist Conference*, AIAA 2005-2287, April 2005.

[66] Hwang, I. S., Hwang, C. P., Min, S. Y., Jeong, I. O., Lee, C. H., Lee., Y. H., and Kim, S. J., "Design and Testing of VTOL UAV Cyclocopter with 4 Rotors," *American Helicopter Society 62nd Annual Forum Proceedings*, Phoenix, AZ, April 29-May 1, 2006.

[67] Hwang, I. S., Min, S. Y., Lee, C. H., and Kim, S. J., "Development of a Four Rotor Cyclocopter," *Journal of Aircraft*, Vol. 45, (6), November 2008, pp. 2151-2157.

[68] Hwang, I. S., Hwang, C. S., and Kim, S. J., "Structural Design of Cyclocopter Blade System," *Paper AIAA-2005-2020, 46th AIAA/ASME/ASCE/AHS/ASC Structures, Structural Dynamics and Materials Conference Proceedings*, Austin, TX, April 18-21, 2005.

[69] Kim, S. J., Hwang, I. S., Lee, H. Y., and Jung, J. S., "Design and Development of Unmanned VTOL Cyclocopter," *Symposium on Aerospace Science and Technology Proceedings*, NC, August 12-14, 2004.

[70] STAR-CD Ver. 3.20 User Guide, CD-Adapco Group, New York, 2004.

[71] MSC.PATRAN PCL Reference Guide, MSC Software, Santa Ana, CA,2003.

[72] MSC.NASTRAN UserâĂŹs Manual, MSC Software, Santa Ana, CA,2003.

[73] "The Development of Cyclogyro," World-Wide Web document, http : //serve.me.nus.edu.sg/cyclocopter/, Feb 19, 2007.

[74] Yu, H., Bin, L. K., and Beng, T. W., "The Investigtion of Cyclogyro Design and the Performance," *Proceedings of the 25th International Congress of the Aeronautical Sciences*, Hamburg, Germany, September 3-8, 2006.

[75] Yu, H., Bin, L. K., and Rong, H. W., "The Research on the Performance of Cyclogyro," Paper AIAA-2006-7704, *AIAA 6th Aviation Technology, Integration and Operations Conference Proceedings*, Wichita, KS, September 25-27, 2006.

[76] Sirohi, J., Parsons, E., and Chopra, I., "Hover Performance of a Cycloidal Rotor for a Micro Air Vehicle," *Journal of American Helicopter Society*, Vol. 52, (3), July 2007, pp. 263-279.

[77] Clark, R., Acuity Technologies Inc., "SBIR A02.07: VTOL to Transonic Aircraft", Final technical report, July 24, 2006.

[78] Siegel, S., Seidel, J., Cohen, K., and McLaughlin, T., "A Cycloidal Propeller Using Dynamic Lift," Paper AIAA-2007-4232, *AIAA 37th Fluid Dynamics Conference and Exhibit*, Miami, FL, June 25-28, 2007.

[79] Hara, N., Tanaka, K., Ohtake, H., and Wang, H., "Development of a Flying Robot with Pantograph-based Variable Wing Mechanism," *Proceedings of the 2007 IEEE International Conference on Robotics and Automation*, Roma, Italy, April 10-14 2007, pp. 349-354.

[80] Tanaka, K., Suzuki, R., Emaru, T., Higashi, Y., and Wang HO., "Development of a Cyclogyro-based Flying Robot with Variable Attack Angle Mechanisms," *IEEE/ASME Transaction on Mechatronics*, Vol. 12, No. 5, October 2007.

[81] Nozaki, H., Sekiguchi, Y., Matsuuchi, K., Onda, M., Murakami, Y., Sano, M., Akinaga, W., and Fujita, K., "Research and Development on Cycloidal Propellers for Airships," Paper AIAA-2009-2850, *AIAA 18th Lighter-Than-Air Systems Technology Conference*, Seattle, Washington, May 4-7, 2009.

[82] Yang, K., Lakshminarayan, V. K., and Baeder, J. D., "Simulation of a Cycloidal Rotor System Using an Overset RANS Solver," *American Helicopter Society 66th Annual Forum Proceedings*, Phoenix, AZ, May 11-13, 2010.

[83] Nakaie, Y., Ohta, Y., and Hishida, K., "Flow Measurements around a Cycloidal Propeller," *Journal of Flow Visualization*, Vol. 16, No. 4, 1978, pp. 393-402.

[84] Benedict, M., Ramasamy, M., and Chopra, I., "Improving the Aerodynamic Performance of Micro-Air-Vehicle-Scale Cycloidal Rotor: An Experimental Approach," *Journal of Aircraft*, Vol. 47, No. 4, July-August 2010, pp. 1117 – 1125.

[85] Benedict, M., Jarugumilli, T., and Chopra, I., "Experimental Optimization of MAV-Scale Cycloidal Rotor Performance," *Journal of the American Helicopter Society*, Vol. 56, No. 2, April 2011, pp. 022005-1 - 022005-11.

[86] Jarugumilli, T., Benedict, M., Lind, A. H., and Chopra, I., "Performance and Flow Visualization Studies to Examine the Role of Pitching Kinematics on MAV-scale Cycloidal Rotor Performance in Forward Flight," *Proceedings of the American Helicopter Society International Specialists' Meeting on Unmanned Rotorcraft*, Scottsdale, AZ, January 22-24, 2013.

[87] Benedict, M., Jarugumilli, T., Lakshminarayan, V. K., and Chopra, I., "Effect of Flow Curvature on the Forward Flight Performance of a MAV-Scale Cycloidal Rotor," *AIAA Journal (early edition)*, 2014.

[88] Jarugumilli, T., Benedict, M., and Chopra, I., "Wind Tunnel Studies on a Micro Air Vehicle-Scale Cycloidal Rotor," *Journal of the American Helicopter Society*, Vol. 59, No. 2, April 2014, pp. 1 – 10.

[89] Jarugumilli, T., Lind, A. H., Benedict, M., Lakshminarayan, V. K., Jones, A. R., and Chopra, I., "Experimental and Computational Flow Field Studies of a MAV-scale Cycloidal Rotor in Forward Flight," *Proceedings of the 69th Annual National Forum of the American Helicopter Society*, Phoenix, AZ, May 21–23, 2013.

[90] Benedict, M., Gupta, R., and Chopra, I., "Design, Development and Flight Testing of a Twin-Rotor Cyclocopter Micro Air Vehicle," *Journal of the American Helicopter Society*, Vol. 58, No. 4, October 2013, pp. 1 – 10.

[91] Benedict, M., Shrestha, E., Hrishikeshavan, V., and Chopra, I., "Development of a Micro Twin-Rotor Cyclocopter Capable of Autonomous Hover," *Journal of Aircraft*, Vol. 51, No. 2, 2014, pp. 672 – 676.

[92] Benedict, M., Mullins, J., Hrishikeshavan, V., and Chopra, I., "Development of an Optimized Quad Cycloidal-Rotor UAV Capable of Autonomous Stable Hover," *Proceedings of the American Helicopter Society International Specialists' Meeting on Unmanned Rotorcraft*, Scottsdale, AZ, January 22-24, 2013.

[93] Zachary, H., A., Benedict, M., Hrishikeshavan, V., and Chopra, I., "Design, Development, and Flight Test of a Small-Scale Cyclogyro UAV Utilizing a Novel Cam-Based Passive Blade Pitching Mechanism," *International Journal of Micro Air Vehicles*, Vol. 5, No. 2, June 2013, pp. 145 – 162.

[94] Shrestha, E., Benedict, M., Hrishikeshavan, V., and Chopra, I., "Development of a 100 gram Micro Cyclocopter Capable of Autonomous Hover," *Proceedings of the 38th European Rotorcraft Forum*, Amsterdam, Netherlands, September 4–7, 2012.

[95] Hrishikeshavan, V., Benedict, M., and Chopra, I., "Identification of Flight Dynamics of a Cyclocopter Micro Air Vehicle in Hover," *Journal of Aircraft (early edition)*, 2014.

[96] Elena, S., Hrishikeshavan, V., Benedict, M., Yeo, D., and Chopra, I., "Development of Control Strategies and Flight Testing of a Twin-Cyclocopter in Forward Flight," *Proceedings of the 70th Annual National Forum of the American Helicopter Society*, Montreal, Quebec, Canada, May 20–22, 2014.

[97] Benedict, M., Jarugumilli, T., and Chopra, I., "Design and Development of a Hover-Capable Cyclocopter MAV," *Proceedings of the 65th Annual National Forum of the American Helicopter Society*, Grapevine, TX, May 27-29, 2009.

[98] Benedict, M., Mattaboni, M., Chopra, I. and Masarati, P., "Aeroelastic Analysis of a Micro-Air-Vehicle-Scale Cycloidal Rotor in Hover," *AIAA Journal*, Vol. 49, No. 11, November, 2011.

[99] Halder, A., Walther, C.M. and Benedict, M., "Unsteady Hydrodynamic Modeling of a Cycloidal Propeller," *Fifth International Symposium on Marine Propulsion*, smp'17, Espoo, Finland, June 12-15, 2017.

[100] Halder, A., Walther, C. M. and Benedict, M., "Hydrodynamic Modeling and Experimental Validation of a Cycloidal Propeller," *Ocean Engineering*, Vol. 154, 15 April 2018, Pages 94-105.

[101] Halder, A., and Benedict, M., "Nonlinear Aeroelastic Modeling of Cycloidal Rotor in Forward Flight," *Proceedings of the AHS Technical Meeting on Aeromechanics Design for Transformative Vertical Lift*, San Francisco, CA, Jan 16-18, 2018.

[102] Halder, A. and Benedict, M., "Free-wake Based Nonlinear Aeroelastic Modeling of Cycloidal Rotor," *AIAA Aviation 2019 Forum*, Dallas, TX, June 17-21, 2019.

[103] Walther, C.M., Coleman, D., Benedict, M. and Lakshminarayan, V., "Experimental and Computational Studies to Understand Unsteady Aerodynamics of Cycloidal Rotors in Hover at Ultralow Reynolds Number," *AHS International's 73rd Annual Forum*, 2017.

[104] Polhamus, E.C., "A Concept Of The Vortex Lift Of Sharp-Edge Delta Wings Based On a Leading Edge Suction Analogy," NASA Technical Note, 1966.

[105] Polhamus, E.C., “Application Of The Leading-Edge Suction Analogy Of Vortex Lift To The Drag Due To Lift Of Sharp-Edge Delta Wings,” NASA Technical Note, 1968.

[106] Hodges, D. H., and Dowell, E. H., “Nonlinear Equations of Motion for the Elastic Bending and Torsion of Twisted Nonuniform Rotor Blades,” NASA TN D-7818, 1974.

[107] Halder, A., and Benedict, M., “Understanding the Effect of Blade flexibility on Cycloidal Rotor Performance in Hover,” *Proceedings of the American Helicopter Society Specialists' Meeting on Aeromechanics*, San Francisco, CA, Jan 20-22, 2016.

[108] Pai, P. F., *Highly Flexible Structures: Modeling, Computation, and Experimentation*, American Institute of Aeronautics and Astronautics, Inc., Reston, Virginia, 2007.

[109] Benedict, M., Winslow, J., Hasnain, Z., and Chopra, I., “Experimental Investigation of Micro Air Vehicle Scale Helicopter Rotor in Hover,” *International Journal of Micro Air Vehicles*, Vol. 7, Sept. 2015, pp. 231- 255. doi:10.1260/1756-8293.7.3.231

[110] Gagnon, L., Morandini, M., Quaranta, G., Muscarello, V. and Masarati, P., “Aerodynamic models for cycloidal rotor analysis,” *Aircraft Engineering and Aerospace Technology*, Vol. 88 Issue: 2, pp.215-231, https://doi.org/10.1108/AEAT-02-2015-0047.

[111] Gagnon, L., Quaranta, G., Morandini, M., Masarati, P., Lanz, M., Xisto, C.M. and PÃąscoa, J.C., “Aerodynamic and Aeroelastic Analysis of a Cycloidal Rotor,” *44th AIAA Fluid Dynamics Conference, AIAA AV1AT1ON Forum*, (AIAA 2014-2450).